

ACOUSTIC TRANSDUCTION – MATERIALS AND DEVICES

Period 1 January 2000 to 31 December 2000

Annual Report

VOLUME I

**OFFICE OF NAVAL RESEARCH
Contract No: N00014-96-1-1173**

**APPROVED FOR PUBLIC RELEASE –
DISTRIBUTION UNLIMITED**

**Reproduction in whole or in part is permitted for any
purpose of the United States Government**

Kenji Uchino

PENNSTATE



**THE MATERIALS RESEARCH LABORATORY
UNIVERSITY PARK, PA**

20010817 076

REPORT DOCUMENTATION PAGE

Form Approved
OMB No. 0704-0188

Public reporting burden for this collection of information is estimated to average 1 hour per response, including the time for reviewing instructions, searching existing data sources, gathering and maintaining the data needed, and completing and reviewing the collection of information. Send comments regarding this burden estimate or any other aspect of this collection of information, including suggestions for reducing this burden, to Washington Headquarters Services, Directorate for Information Operations and Reports, 1215 Jefferson Davis Highway, Suite 1204, Arlington, VA 22202-4302, and to the Office of Management and Budget, Paperwork Reduction Project (0704-0188), Washington, DC 20503.

1. AGENCY USE ONLY (Leave blank)		2. REPORT DATE 7/12/2001	3. REPORT TYPE AND DATES COVERED ANNUAL REPORT 01/01/2000--12/31/2000	
4. TITLE AND SUBTITLE ACOUSTIC TRANSDUCTION -- MATERIALS AND DEVICES			5. FUNDING NUMBERS ONR CONTRACT NO. N00014-96-1-11173	
6. AUTHOR(S) Materials Research Laboratory The Pennsylvania State University University Park, Pa 16802				
7. PERFORMING ORGANIZATION NAME(S) AND ADDRESS(ES)			8. PERFORMING ORGANIZATION REPORT NUMBER	
9. SPONSORING/MONITORING AGENCY NAME(S) AND ADDRESS(ES) Office of Naval Research Office of Naval Research ONR 321SS Regional Office Chicago Ballston Centre Tower One 536 S. Clark Str. RM 208 800 N. Quincy Street Chicago IL 60605-1588 Arlington, VA 2217-5660			10. SPONSORING/MONITORING AGENCY REPORT NUMBER	
11. SUPPLEMENTARY NOTES				
12a. DISTRIBUTION / AVAILABILITY STATEMENT			12b. DISTRIBUTION CODE	
13. ABSTRACT (Maximum 200 words) SEE FOLLOWING PAGE				
14. SUBJECT TERMS			15. NUMBER OF PAGES	
			16. PRICE CODE	
17. SECURITY CLASSIFICATION OF REPORT UNCLASSIFIED	18. SECURITY CLASSIFICATION OF THIS PAGE UNCLASSIFIED	19. SECURITY CLASSIFICATION OF ABSTRACT UNCLASSIFIED	20. LIMITATION OF ABSTRACT	

GENERAL INSTRUCTIONS FOR COMPLETING SF 298

The Report Documentation Page (RDP) is used in announcing and cataloging reports. It is important that this information be consistent with the rest of the report, particularly the cover and title page. Instructions for filling in each block of the form follow. It is important to *stay within the lines* to meet *optical scanning requirements*.

Block 1. Agency Use Only (Leave blank).

Block 2. Report Date. Full publication date including day, month, and year, if available (e.g. 1 Jan 88). Must cite at least the year.

Block 3. Type of Report and Dates Covered. State whether report is interim, final, etc. If applicable, enter inclusive report dates (e.g. 10 Jun 87 - 30 Jun 88).

Block 4. Title and Subtitle. A title is taken from the part of the report that provides the most meaningful and complete information. When a report is prepared in more than one volume, repeat the primary title, add volume number, and include subtitle for the specific volume. On classified documents enter the title classification in parentheses.

Block 5. Funding Numbers. To include contract and grant numbers; may include program element number(s), project number(s), task number(s), and work unit number(s). Use the following labels:

C - Contract	PR - Project
G - Grant	TA - Task
PE - Program Element	WU - Work Unit Accession No.

Block 6. Author(s). Name(s) of person(s) responsible for writing the report, performing the research, or credited with the content of the report. If editor or compiler, this should follow the name(s).

Block 7. Performing Organization Name(s) and Address(es). Self-explanatory.

Block 8. Performing Organization Report Number. Enter the unique alphanumeric report number(s) assigned by the organization performing the report.

Block 9. Sponsoring/Monitoring Agency Name(s) and Address(es). Self-explanatory.

Block 10. Sponsoring/Monitoring Agency Report Number. (If known)

Block 11. Supplementary Notes. Enter information not included elsewhere such as: Prepared in cooperation with...; Trans. of...; To be published in.... When a report is revised, include a statement whether the new report supersedes or supplements the older report.

Block 12a. Distribution/Availability Statement. Denotes public availability or limitations. Cite any availability to the public. Enter additional limitations or special markings in all capitals (e.g. NOFORN, REL, ITAR).

DOD - See DoDD 5230.24, "Distribution Statements on Technical Documents."

DOE - See authorities.

NASA - See Handbook NHB 2200.2.

NTIS - Leave blank.

Block 12b. Distribution Code.

DOD - Leave blank.

DOE - Enter DOE distribution categories from the Standard Distribution for Unclassified Scientific and Technical Reports.

NASA - Leave blank.

NTIS - Leave blank.

Block 13. Abstract. Include a brief (*Maximum 200 words*) factual summary of the most significant information contained in the report.

Block 14. Subject Terms. Keywords or phrases identifying major subjects in the report.

Block 15. Number of Pages. Enter the total number of pages.

Block 16. Price Code. Enter appropriate price code (*NTIS only*).

Blocks 17. - 19. Security Classifications. Self-explanatory. Enter U.S. Security Classification in accordance with U.S. Security Regulations (i.e., UNCLASSIFIED). If form contains classified information, stamp classification on the top and bottom of the page.

Block 20. Limitation of Abstract. This block must be completed to assign a limitation to the abstract. Enter either UL (unlimited) or SAR (same as report). An entry in this block is necessary if the abstract is to be limited. If blank, the abstract is assumed to be unlimited.

ABSTRACT

This report describes research performed over the period 1st January 2000 to 31st December 2000 on a MURI under Office of Naval Research contract N00014-96-1-1173 on the topic "Acoustic Transduction Materials and Devices". This program brings together researchers from the Materials Research Laboratory (MRL), the Applied Research Laboratory (ARL) and the Center for Acoustics and Vibrations (CAV) at the Pennsylvania State University. As has become customary over many years, research on the program is detailed in the technical appendices of published work, and only a brief narrative description connecting these studies is given in the text.

The program combines a far reaching exploration of the basic phenomena contributing to piezoelectric and electrostrictive response with the highly applied thrusts necessary to produce the "pay-off" in new applications relevant to Navy needs. Polarization vector tilting in the ferroelectric phase of perovskite structure crystals at compositions close to a morphotropic phase boundary (MPB) was first underscored on this program some four years ago, and is now widely accepted as one mode for exploiting the large intrinsic spontaneous strain in the ferroelectric to produce exceedingly strong anhysteretic piezoelectric response and very large electric field controlled elastic strain. New evidence for the importance of both spontaneous (monoclinic) and electric field induced tilting on the properties of both single and polycrystal MPB systems is presented in this report.

The puzzling phenomena associated with relaxor ferroelectric response have long been a topic of study in MRL, where the micro-polar region model and the application of Vogel/Fulcher to the dielectric slowing down were first applied. The current "pay-off" is in the greatly enhanced relaxor ferroelectric electrostrictive response from high electron energy irradiated polyvinylidene difluoride: trifluoroethylene (PVDF: TrFE) co-polymer discussed in this report. This development opens a new field of high strain, high energy density actuators with tremendous practical applicability. Now the possibility of engineering this response by chemical manipulation in the terpolymer systems without irradiation further enhances the exciting possibilities.

In composite structures, the early promise of the flexensional cymbal type actuators is now being fully realized and programs exploring large area cymbal transducer arrays are progressing very well, both at MRL/ARL and at NRL. The connection with CAV at Penn State is particularly important in keeping the MURI faculty aware of problems endemic to water as our host medium and the effects of turbulence in flow and the need for many types of acoustic noise control.

New designs of piezoelectric transformers and motors are demanding materials with lower loss levels under continuous high driving, and important progress is reported in separating and understanding the components of this loss and in designing new doping schemes for ceramics which enhance power capability almost tenfold. New piezoelectric micro-motor designs look particularly attractive and appear to offer significant advantages over electromagnetics for very small-scale applications. Thick and thin film studies for MEMS are progressing well and offering new insights into fatigue and switching behavior in the ferroelectrics.

**ACOUSTIC TRANSDUCTION –
MATERIALS AND DEVICES**

Period 1 January 2000 to 31 December 2000

Annual Report

VOLUME I

OFFICE OF NAVAL RESEARCH

Contract No: N00014-96-1-1173

**APPROVED FOR PUBLIC RELEASE –
DISTRIBUTION UNLIMITED**

**Reproduction in whole or in part is permitted for any
purpose of the United States Government**

Kenji Uchino

TABLE OF CONTENTS

APPENDICES LISTING	2
ABSTRACT	10
INTRODUCTION	11
1.0 GENERAL SUMMARY PAPERS	12
2.0 MATERIALS STUDIES.....	12
2.1 Polycrystal Perovskite Ceramics	12
2.2 Single Crystal Systems	13
2.3 High Strain Polymers	13
3.0 TRANSDUCER STUDIES	14
3.1 Composite Structures	14
3.2 Piezoelectric Transformers..	14
3.3 High Power Level Materials	14
3.4 Fluid Structure Interactions	14
4.0 ACTUATOR STUDIES	15
4.1 Materials and Designs	15
4.2 Photostriction.	15
4.3 High Force Actuators	15
4.4 Piezoelectric Motors	15
4.4 Acoustic Absorbers	16
5.0 MODELING and CHARACTERIZATION..	16
5.1 Design and Simulation	16
5.2 Thin and Thick Films	16
5.3 Domain Studies	16
6.0 GRADUATE STUDENTS IN THE PROGRAM	17
7.0 HONORS and AWARDS	17
8.0 PAPERS PUBLISHED IN REFEREED JOURNALS	18
9.0 PAPERS SUBMITTED FOR PUBLICATION	23
10.0 PAPERS APPEARING IN NON REFERRED PROCEEDINGS	24
11.0 INVITED PAPERS PRESENTATIONS AT NATIONAL AND INTERNATIONAL MEETINGS	26
12.0 INVITED PAPERS PRESENTED AT UNIVERSITY, INDUSTRY, AND GOVERNMENT LABORATORIES	29
13.0 CONTRIBUTED PAPERS AT NATIONAL AND INTERNATIONAL MEETINGS	31
14.0 BOOKS (AND SECTIONS THERE OF)	36
15.0 INVENTION DISCLOSURES	37

APPENDICES

VOLUME I

GENERAL SUMMARY PAPERS

1. Uchino, K., Encyclopedia of Vibration, Partial Charge "Electrostrictive Materials", Academic Press, London (2000). [in press]
2. Uchino, K., and Y. Ito, Encyclopedia Smart Materials, J. Harvey, Edit., Partial Charge "Smart Ceramics: Transducers, Sensors and Actuators", John Wiley & Sons, New York (2000). [in press]
3. Wennu Ma, L.E. Cross, "Observation of the flexoelectric effect in relaxor PB ($\text{Mg}_{1/3}\text{Nb}_{2/3}$) O_3 ceramics", Applied Physics Letters. Volume #8 number 19 pp. 2920
4. R. Hatt and W. Cao, "Landau-Ginzburg Model for Antiferroelectric Phase Transition Based on Microscopic Symmetry", Phys. Rev. B, vol. **62**, pp. 818-823 (2000).

2.0 MATERIALS STUDIES

2.1 Polycrystal Perovskite Ceramics

5. A.S. Bhalla, R. Guo, R. Roy, "The Perovskite Structure - A Review of Its Role in Ceramic Science and Technology, "Mat. Res. Innovat., **4(1)**, 3-26, (2000)
6. E.F. Alberta, R. Guo, L.E. Cross, A.S. Bhalla, "Structure-Property Diagrams of Ferroic Solid Solutions. Part I: Perovskite Ferroelectrics with Morphotropic Phase Boundaries," *Ferroelectrics Review*, 3, 1, (2001)
7. B. Noheda, J.A. Gonzalo, L.E. Cross, R. Guo, S-E. Park, D.E. Cox, G. Shirane, "Tetragonal-to-Monoclinic Phase Transition in a Ferroelectric Perovskite: the Structure of $\text{PbZr}_{0.52}\text{Ti}_{0.48}\text{O}_3$, "Phys. Rev. B, **61(13)**, 8687-8689, (2000)
8. B. Noheda, D.E. Cox, G. Shirane, R. Guo, B. Jones, L.E. Cross, "Stability of the monoclinic phase in the ferroelectric perovskite $\text{PbZr}_{(1-x)}\text{Ti}_x\text{O}_3$, "Los Alamos Natl. Lab., Prepr. Arch., Condens. Matter, **1-8**, arXiv:cond-mat/0006152, (2000)
9. R. Guo, L.E. Cross, S-E. Park, B. Noheda, D.E. Cox, G. Shirane, "Origin of the high piezoelectric response in $\text{PbZr}_{1-x}\text{Ti}_x\text{O}_3$," *Phys. Rev. Letters*, **84(23)**, 5423-5426, (2000)
10. W. Jiang and W. Cao, "Nonlinear Elastic Properties of Lead Zirconate Titanate Ceramics", J. Appl. Phys. vol. **88**: 6684-6689 (2000).
11. Chen, Y. H., D. Viehland and K. Uchino, "Substituent Effects in $0.65\text{Pb}(\text{Mg}_{1/3}\text{Nb}_{2/3})\text{O}_3$ - 0.35PbTiO_3 Piezoelectric Ceramics" J. Electroceramics, **6**, 13-20 (2001). (First Author Supervised by Candidate).
12. W.H. Jiang and W. Cao, " Intrinsic and Coupling-induced Elastic Nonlinearity of Lanthanum-doped Lead Magnesium Niobate-Lead Titanate Electrostrictive Ceramic", Appl. Phys. Lett., vol. **77**, pp. 1387-1389 (2000).

VOLUME II

2.0 MATERIALS STUDIES

2.2 *Single Crystal Systems*

13. L.E. Cross, J. Fousek, "Engineering Multidomain Ferroic Samples", *Ferroelectrics*, 2001, Vol. 252, pp. 171-180.
14. Wada, Satoshi, Takaaki Tsurumi, Miour Osada, Masato Kakihana, Seung Eek Park, L.Eric Cross and Thomas R. Shrout. "Change of Macroscopic and Microscopic Symmetries in Relaxor PZN Single Crystal Under Bias Field." Transactions of the Material Research Society of Japan, **25** (1). 281-284 (2000).
15. Wada, Satoshi, Takaaki Tsurumi, Miour Osada, Masato Kakihana, Seung Eek Park, L.Eric Cross and Thomas R. Shrout. "Dipolar Behavior in PZN Relaxor Single crystals under Bias Fields." Transactions of the Materials Research Society of Japan **25** (1), 281-284 (2000).
16. Belegundu, U., X. Du and K. Uchino, "Switching Current in $\text{Pb}(\text{Zn}_{1/3}\text{Nb}_{2/3})\text{O}_3$ - PbTiO_3 Single Crystals," Symp. LL Proc., Mater. Res. Soc. Fall Mtg. '99, (LL.1.9, Boston, Nov. 29-Dec.3. 1999), Vol. **604**, 39-44 (2000).
17. Yu Lu, D.-Y. Jeong, Z. Y. Cheng, Q. M. Zhang, H. Luo, Z. Yin, and D. Viehland. Phase Transitional Behavior and Piezoelectric Properties of the orthorhombic Phase of PMN-PT Single Crystals. *Appl. Phys. Lett.* **78**, 3109 (2001).
18. Yu Lu, Z.-Y. Cheng, E. Park, S. F. Liu and Q. M. Zhang. Linear Electro-optic Effect of $0.88\text{Pb}(\text{Zn}_{1/3}\text{Nb}_{2/3})$ - 0.12PbTiO_3 Single Crystal. *Jpn. J. Appl. Phys.* **39**, 141-145 (2000).
19. Y. Barad, Yu Lu, Z. Y. Cheng, S. E. Park, and Q. M. Zhang. Composition, Temperature, and Crystal Orientation Dependence of Linear Electro-optic Properties of PZN-PT Single Crystals. *Appl. Phys. Lett.* **77**, 1247-1249 (2000).
20. Y. Lu, Z.-Y. Cheng, Y. Barad, and Q. M. Zhang. Photoelastic Effects in the Tetragonal PZN-PT Single Crystals near the Morphotropic Phase Boundary. *J. Appl. Phys.* **89**, 5075 (2001).

2.3 *High Strain Polymers*

21. Vivek Bharti, H. S. Xu, G. Shanthi, Q. M. Zhang, and Kuming Liang. Polarization and Structural Properties of High Energy Electron Irradiated P(VDF-TrFE) Copolymer Films. *J. Appl. Phys.* **87**, 452-461 (2000).
22. Haisheng Xu, G. Shanthi, V. Bharti, Q. M. Zhang, and T. Ramatowski. Structural, Conformational, and Polarization Changes of P(VDF-TrFE) Copolymer Induced by High Energy Electron Irradiation. *Macromolecules*, **33**, 4125-4131(2000).
23. Q. M. Zhang, Z. Y. Cheng, and Vivek Bharti. Relaxor Ferroelectric Behavior in High Energy Electron Irradiated P(VDF-TrFE) copolymers. *Appl. Phys.* **A70**, 307-312 (2000).
24. Vivek Bharti and Q. M. Zhang. Dielectric Study of Relaxor Ferroelectric P(VDF-TrFE) Copolymer System. *Phys. Rev. B.* **63**, 184103 (2001).
25. Z.Y. Cheng, Vivek Bharti, T.B. Xu, Hansheng Xu, T. Mai, and Q. M. Zhang. Electrostrictive P(VDF-TrFE) Copolymers. *Sensors and Actuators A-Phys.* **90**, 138-147 (2001)

26. Z. Y. Cheng, V. Bharti, T. Mai, T. B. Xu, Q. M. Zhang, K. Hamilton, T. Ramotowski, K. A. Wright, and R. Ting. Effect of High Energy Electron Irradiation on the Electromechanical Properties of Poly(vinylidene fluoride-trifluoroethylene) 50/50 and 65/35 Copolymers. *IEEE Trans. UFFC* **47**, 1296 (2000).
27. Vivek Bharti, Z.-Y. Cheng, T. Mai, Q. M. Zhang, T. Ramotowski, K. A. Wright. High Electromechanical Coupling Factor and Electrostrictive Strain over a Broad Frequency Range in Electrostrictive Poly(vinylidene fluoride-trifluoroethylene) Copolymer. *Jpn. J. Appl. Phys.* **40**, 672 (2001).
28. Vivek Bharti, G. Shanthi, H. Xu, Q. M. Zhang, and K. Liang. Evolution of Transitional Behavior and Structure of Electron Irradiated P(VDF-TrFE) Copolymer Films. *Mater. Lett.* **47**, 107-111 (2001).
29. F. Xia, H. Xu, F. Fang, B. Razivi, Z. Y. Cheng, Yu Lu, Baoming Xu, and Q. M. Zhang. Thickness Dependence Behavior of Ferroelectric Switching in P(VDF-TrFE) Spin Cast Films. *Appl. Phys. Lett.* **78**, 1122 (2001).
30. Q. M. Zhang, H. S. Xu, Fei Fang, Z.-Y. Cheng, Xia Feng, and H. You. Observation of Critical Thickness of Crystallization in Spin Cast Ferroelectric Thin Films. *J. Appl. Phys.* **89**, 2613 (2001).
31. Shizhuo Yin, Q. M. Zhang, K.-W. Chung, R. Yang, Z. Y. Cheng, and Yu Lu. Investigation of the Electro-optic Properties of Electron-irradiated P(VDF-TrFE) Copolymer. *Opt. Eng.* **39**, 670-672 (2000).
32. Hai-Sheng Xu, Z.-Y. Cheng, Vivek Bharti, Shexi Wang, and Q. M. Zhang. All-Polymer Electromechanical Systems Consisting of Electrostrictive Poly(vinylidene fluoride-trifluoroethylene) and Conductive Polyaniline. *J. Appl. Poly. Sci.* **75**, 945-951 (2000).
33. H. Xu, Z.Y. Cheng, D. Olson, T. Mai, Q. M. Zhang, and G. Kavarnos. Ferroelectric and Electromechanical Properties of P(VDF-TrFE-CTFE) Terpolymer. *Appl. Phys. Lett.* **78**, 2360 (2001).

3.0 TRANSDUCER STUDIES

3.1 *Composite Structures*

34. Uchino, K., "Piezoelectro Composites," Chap.5.24, *Comprehensive Composite Materials*, Elsevier Science, Oxford, UK (2000).
35. Tressler, J. and K. Uchino, "Piezoelectric Composite Sensors," Chap.5.22, *Comprehensive Composite Materials*, Elsevier Science, Oxford, UK (2000).

VOLUME III

36. Meyer, R.J. Jr., A. Dogan, C. Yoon, S. Pilgrim and R.E. Newnham, "Displacement Amplification of Electroactive Materials Using the Cymbal Flexensional Transducer," *Sensors & Actuators A*, vol.87, pp. 157-162 (2001).
37. Dogan, A., K. Uchino and R. E. Newnham, "Flexensional Composite Transducers: Designing, Fabrication and Application," *Proc. NATO- Advanced Research Workshop: Piezoelectric Materials: Advance in Science, Technology and Applications*, (Predeal, Romania, May 24-27, 1999, Kluwer Academic Publ., p.357-374 (2000).

38. Zhang, J., A.C. Hladky-Hennion, W.J. Hughes, and R.E. Newnham, "Modeling and Underwater Characterization of Cymbal Transducers and Arrays," IEEE Transactions on Ultrasonics, Ferroelectrics, and Frequency Control, vol. 48 (2), pp. 560-568 (2001).
39. Zhang, J., W. J. Hughes, R. J. Meyer Jr., K. Uchino and R. E. Newnham, "Cymbal Array: A Broad Band Sound Projector," Ultrasonics 37, 523-529 (2000).
40. Zhang, J., A.C. Hladky-Hennion, W.J. Hughes, and R.E. Newnham, "A Miniature Class V flextensional cymbal transducer with directional beam pattern: The Double-Driver," Ultrasonics, vol. 39, pp. 91-95 (2001).
41. Meyer, R.J. Jr. and R.E. Newnham, "Flextensional transducers with Shape Memory Caps for Tunable Devices," Journal of Intelligent Materials Systems and Structures, vol. 11, pp. 199-205 (2001).
42. Meyer, R.J. Jr., S. Alkoy, J. Cochran, T. Ritter, and R.E. Newnham, "Pre-focused Lead Titanate > 25 MHz Single Element Transducers from Hollow Spheres," IEEE Transactions on Ultrasonics, Ferroelectrics, and Frequency Control, vol. 48 (2), pp. 488-493 (2001).
43. Y. Bai, Z.Y. Cheng, V. Bharti, H. S. Xu, and Q. M. Zhang. High Dielectric Constant Ceramic Powder Polymer Composites. Appl. Phys. Lett. 76, 3804-3806 (2000).
44. M.R. Shen and W. Cao, "Acoustic Bandgap Formation in a Periodic Structure with Multilayer Unit Cells", J. Phys. D: Applied Physics, vol. 33, pp. 1150-1154 (2000).
45. T.B. Xu, Z-Y. Cheng, Q. M. Zhang, R. Baughman, C. Cui, A. Zakhidov, and J. Su. Fabrication and Characterization of 3-Dimensional Periodic Ferroelectric Polymer-Silica Opal Composites and Inverse Opal. J. Appl. Phys. 88(1), 405-409 (2000).

3.2 *Piezoelectric Transformers*

46. Uchino, K., B. Koc, P. Laoratanakul and A. Vazquez Carazo, "Piezoelectric Transformers -New Perspective--," Proc. 3rd Asian Mtg. Ferroelectrics, D1d.1, Hong Kong, Dec. 12-15 (2000).
47. Koc, B., and K. Uchino, "Disk Type Piezoelectric Transformer with Crescent Shape Input Electrodes," Proc. NATO- Advanced Research Workshop: Piezoelectric Materials: Advance in Science, Technology and Applications, (Predeal, Romania, May 24-27, 1999, Kluwer Academic Publ., p.375-382 (2000).

3.3 *High Power Level Materials*

48. Uchino, K. and S. Hirose, "Loss Mechanisms in Piezoelectrics: How to Measure Different Losses Separately," IEEE UFFC Transactions, 48, 307-321 (2001).
49. Uchino, K., and J. Zheng, Y. H. Chen, X. Du and S. Hirose, "Loss Mechanisms in Piezoelectrics and Resonance/ Antiresonance," Proc. 101st Annual Mtg. of Amer. Ceram. Soc., Symp. Electronic Ceramic Materials and Devices, (Indianapolis, April 25 - 28, 1999), p.79-100 (2000).
50. Uchino, K., J. Zheng, Y. H. Chen, X. Du, S. Hirose and S. Takahashi, "Loss Mechanisms in Piezoelectrics -Extrinsic and Intrinsic Losses--," Mater. Res. Soc. Fall Mtg. '99, (LL.1.6, Boston, Nov. 29-Dec.3, 1999), Vol. 604, 25-31 (2000).

51. Chen, Y. H., S. Hirose, D. Viehland and K. Uchino, "Doping Effects in $\text{Pb}(\text{Mg}_{1/3}\text{Nb}_{2/3})\text{O}_3\text{-PbTiO}_3$ Ceramics for High Power Transduction Applications," Mater. Res. Soc. Fall Mtg. '99, (LL.5.8, Boston, Nov. 29-Dec.3, 1999), Vol. **604**, 215-220 (2000).
52. Chen, Y. H., S. Hirose, D. Viehland, S. Takahashi and K. Uchino, " Mn-Modified $\text{Pb}(\text{Mg}_{1/3}\text{Nb}_{2/3})\text{O}_3\text{-PbTiO}_3$ Ceramics: Improved Mechanical Quality Factors for High-Power Transducer Applications," Jpn. J. Appl. Phys. **39**, 4843-4852 (2000).
53. Gao, Y. Y. H. Chen, J. Ryu, K. Uchino and D. Viehland, " Eu and Yb Substituent Effects on the Properties of $\text{Pb}(\text{Zr}_{0.52}\text{Ti}_{0.48})\text{O}_3\text{-Pb}(\text{Mn}_{1/3}\text{Sb}_{2/3})\text{O}_3$ Ceramics: Development of a New High-Power Piezoelectric with Enhanced Vibrational Velocity," Jpn. J. Appl. Phys., **40**, 79-85 (2001).

VOLUME IV

3.4 *Fluid Structure Interactions*

54. Lauchle, G. C., W. A. Kargus IV. Scaling of Turbulent Wall Pressure Fluctuations Downstream of a Rearward Facing Step. *J. Acoust. Soc. Am.* **107**: L1-L6 (2000).
55. Capone, D. E., G. C. Lauchle. Modeling the Unsteady Lift and Drag on a Finite-Length Cylinder in Cross Flow. *J. Fluids and Struct.* **14**: 799-817 (2000).
56. Gavin, J. R., G. C. Lauchle. Modeling the Space-Time Correlations in the Wake Region of a Turbulent Boundary Layer. *Proc. of the ASME Noise Control and Acoustics Division 2000*, NCA-Vol. 27, pp 227-241 (2000).
57. Gavin, J. R., G. C. Lauchle, M. L. Jonson. Prediction of Turbulence Ingestion Forces for Rotors with Arbitrary Rake and Skew. *Proc. of the ASME Noise Control and Acoustics Division 2000*. NCA-Vol. 27, pp 217-226 (2000).
58. Lauchle, G. C, D. K. McLaughlin. Review of: *Acoustics of Fluid Structure Interactions* by M. S. Howe in *Noise Control Eng. J.* **48**: 70-71 (2000).

4.0 ACTUATOR STUDIES

4.1 *Materials and Designs*

59. Koc, B. and K. Uchino, "Piezoelectric Ultrasonic Motors," Chap.6.34, *Comprehensive Composite Materials*, Elsevier Science, Oxford, UK (2000).
60. Uchino, K., "Recent Trend of Piezoelectric Actuator Developments –Material, Design and Drive Technique Related Issues--," Proc. Actuator 2000 (7th Int'l Conf. New Actuators, June 19-21, 2000), p.34-39 (2000).
61. Yao, K., K. Uchino, Y. Xu, S. Dong, and L. C. Lim, "Compact Piezoelectric Stacked Actuators for High Power Applications," IEEE Trans. UFFC, **47**, 819-825 (2000).
62. Liu, Rubin, L.e. Cross, Gareth Knowles, Bruce Bower, and Brookd Childers. " A Stackable Bonding-Free Flextensional Piezoelectirc Actuator" *Journal of Electroceramics* **4** (1), 201-206 92000)
63. A. E. Glazounov, Q. M. Zhang, C. Kim. Torsional Actuator Based on Mechanically Amplified Shear Piezoelectric Response. *Sensors and Actuators A79*, 22-30 (2000).

4.2 Photostriction

- 64. Poosanaas, P., K. Tonooka and K. Uchino, "Photostrictive Actuators," *J. Mechatronics* **10**, 467-487 (2000).
- 65. Uchino, K., P. Poosanaas and K. Tonooka, "Photostrictive Actuators–New Perspective-," *Proc. 3rd Asian Mtg. Ferroelectrics*, C3p.105, Hong Kong, Dec. 12-15 (2000).
- 66. Uchino, K., P. Poosanaas and K. Tonooka, "Photostrictive Actuators–New Perspective-," *Proc. 5th Euroconf. Appl. Polar Dielectrics*, O-43, Jurmala, Latvia, Aug. 27-30 (2000).
- 67. Poosanaas, P., K. Tonooka, I. R. Abothu, S. Komarneni, and K. Uchino, "Influence of Composition and Dopant on Photostriction in Lanthanum-Modified Lead Zirconate Titanate Ceramics," *J. Intelligent Mater. Systems and Structures* **10**, 439-445 (2000). (
- 68. Poosanaas, P., Dogan, A., Prasadarao, A. V., Komarneni, S. and Uchino, K., "Effect of Ceramic Processing Methods on Photostrictive Ceramics", *J. Advanced Performance Mater.* **6**, 57-69 (1999).

VOLUME V

4.3 High Force Actuators

- 69. A. E. Glazounov, Q. M. Zhang, and C. Kim. Torsional Actuator and Stepper Motor Based on Piezoelectric d_{15} Shear Response. *J. Intel. Mater. Syst. & Struct.* **11(6)**, 456-468 (2000).
- 70. Galante, T., J. Frank, J. Bernard, W. Chen, G.A. Lesieutre, and G.H. Koopmann, "A High-Force, High-Displacement Piezoelectric Inchworm Actuator," *Journal of Intelligent Materials Systems and Structures*, Vol. 10, No. 12, December, 2000, pp. 962-972.

4.4 Piezoelectric Motors

- 71. Koc, B. and K. Uchino, "Piezoelectric Ultrasonic Motors," Chap.6.34, *Comprehensive Composite Materials*, Elsevier Science, Oxford, UK (2000).
- 72. Uchino, K., and B. Koc, "Compact Piezoelectric Ultrasonic Motors," *Proc. NATO-Advanced Research Workshop: Piezoelectric Materials: Advance in Science, Technology and Applications*, (Predeal, Romania, May 24-27, 1999, Kluwer Academic Publ., p.309-320 (2000).
- 73. Koc, B., J. F. Tressler and K. Uchino, "A Miniature Piezoelectric Rotary Motor Using Two Orthogonal Bending Modes of a Hollow Cylinder," *Proc. Actuator 2000 (7th Int'l Conf. New Actuators*, June 19-21, 2000), p.242-245 (2000).
- 74. Koc, B., J. F. Tressler and K. Uchino, "A Miniature Piezoelectric Rotary Motor Using Two Orthogonal Bending Modes of a Hollow Cylinder," *Proc. Actuator 2000 (7th Int'l Conf. New Actuators*, June 19-21, 2000), p.242-245 (2000).
- 75. Bouchilloux, P., B. Koc and K. Uchino, "New Concept for Resonant Longitudinal-Shear Ultrasonic Motor," *Symp. LL Proc., Mater. Res. Soc. Fall Mtg. '99*, (LL.2.10, Boston, Nov. 29-Dec.3, 1999), Vol. **604**, 71-78 (2000).
- 76. Koc, B., P. Bouchilloux, and K. Uchino, "Piezoelectric Micromotor Using A Metal-Ceramic Composite Structure," *IEEE Trans. Ultrasonic, Ferroelectrics, and Frequency Control* **47** (4), 836-843 (2000).

4.5 *Acoustic Absorbers*

77. Davis, C.L. and G.A. Lesieutre, "An Actively Tuned Solid State Vibration Absorber Using Capacitive Shunting of Piezoelectric Stiffness," *Journal of Sound and Vibration*, Vol. 232(3), 4 May 2000, pp. 601-617.
78. Patricia L. Driesch, Hisao Iwata, Gary H. Koopmann, and Jeff Dosch. Nov. 2000. Development and evaluation of a surface acoustic intensity probe. *Review of Scientific Instruments*, 71 (11), pp. 1-6.
79. W. Huang, G. H. Koopmann, S. J. Sharp, and W. Chen. April 2000. Enhanced Low Frequency Transmission Loss of Lightweight Trim Panels. *Journal of Intelligent Material Systems and Structures*, Volume 11, No 4.
80. E.W. Constans, A.D. Belegundu, and G.H. Koopmann. 2000. Optimally Designed Shell Enclosures with Tuned Absorbers for Minimizing Sound Power. *Optimization and Engineering*, 1, 67-86, (an International Journal, Kluwer Publishers)

VOLUME VI

5.0 MODELING AND CHARACTERIZATION

5.1 *Design and Simulation*

81. K. Uchino, "Designing With Piezoelectric Devices" International Center for Actuators and Transducers, Materials Research Institute, The Pennsylvania State University, University Park, PA (2000)
82. W.K. Qi, and W. Cao, "Finite Element Study on 1-D Array Transducer Design", *IEEE Transaction, Ultra. Ferro. and Frequency Control*, vol. **47**, pp. 949-955 (2000).
83. T.A. Ritter, K. K. Shung, W. Cao and T. R. Shrout, "Electromechanical Properties of Thin Strip Piezoelectric Vibrators at High Frequency", *J. Applied Phys*, vol. **88**, pp. 394-397 (2000).
84. T.A. Ritter, K. K. Shung, W. Cao and T. R. Shrout, "Electromechanical Properties of Thin Strip Piezoelectric Vibrators at High Frequency", *J. Applied Phys*, vol. **88**, pp. 394-397 (2000).

5.2 *Thick and Thin Films*

85. Kalpat, S., X. Du, I. R. Abothu, A. Akiba, H. Goto and K. Uchino, "Effect of Crystal Orientation on Dielectric Properties of Lead Zirconate Titanate Thin Films Prepared by Reactive RF-Sputtering," *Jpn. J. Appl. Phys.*, **40**, 158-162 (2001).
86. Kalpat, S., X. Du, I. R. Abothu, A. Akiba, H. Goto, S. Trolier-McKinstry and K. Uchino, "Dielectric Properties of Highly Oriented Lead Zirconate Titanate Thin Films Prepared by Reactive RF-Sputtering," *Symp. LL Proc., Mater. Res. Soc. Fall Mtg. '99*, (LL.1.3, Boston, Nov. 29-Dec.3, 1999), Vol. **604**, 3-8 (2000).
87. S. Trolier-McKinstry, "Piezoelectric Films for MEMS Applications," *J. Ceram. Soc. Jpn.* **109** (5) S76-S79 (2001).
88. Jeong Hwan Park, Fei Xu, and Susan Trolier-McKinstry, "Dielectric and Piezoelectric Properties of Sol-Gel Derived Lead Magnesium Niobium Titanate Films with Different Textures," *J. Appl. Phys.* **89**(1) 568 - 574 (2001).

89. Q. F. Zhou, E. Hong, R. Wolf, and S. Trolier-McKinstry, "Dielectric and Piezoelectric Properties of PZT 52/48 Thick Films with (100) and Random Crystallographic Orientation," Ferroelectric Thin Films, Vol 655 (2000).
90. L.-P. Wang, R. Wolf, Q. F. Zhou, S. Trolier-McKinstry and R. J. Davis, "Wet-etch patterning of lead zirconate titanate (PZT) thick films for microelectromechanical systems (MEMS) application," *Mat. Res. Soc. Symp. Vol.657 (MEMS)*

5.3 *Domain Studies*

91. Uchino, K., and H. Aburatani, "Field Induced Acoustic Emission in Ferroelectric Ceramics," *Proc. 101st Annual Mtg. of Amer. Ceram. Soc., Symp. Electronic Ceramic Materials and Devices, SE-56, (Indianapolis, April 25 – 28, 1999), (2000).*
92. J. Fousek ^{ab}, L.E. Cross ^b, "Engineering Multidomain Ferroic Samples, Dept of Physics and International Center for Piezoelectric Research, University of Technology, Liberec, 46117 Czech Republic and ^b Materials Research Laboratory, The Pennsylvania State University, University Park, PA 16802, USA. (June 2000)
93. J.H. Yin, and W. Cao, "Domain Configurations in Domain-Engineered 0.955Pb(Zn_{1/3}Nb_{2/3})O₃-0.045PbTiO₃ Single Crystals", *J. Appl. Phys*, vol. **87**, pp. 7438-7441 (2000).
94. Rajeev Ahluwalia, "Computer Simulations of Domain Pattern Formation in Ferroelectrics", *AIP Conference Proceedings Series, © 2001 American Institute of Physics, Proceedings of the 2001 Workshop on Fundamental Physics of Ferroelectrics Williamsburg, Va, 2001*
95. R. Ahluwalia and W. Cao, "Influence of Dipolar Defects on Switching Behavior in Ferroelectrics", *Phys. Rev. B*, vol. **63**, pp. 012103 (2000)
96. Uchino, K., and H. Aburatani, "Field Induced Acoustic Emission in Ferroelectric Ceramics," *Proc. 101st Annual Mtg. of Amer. Ceram. Soc., Symp. Electronic Ceramic Materials and Devices, SE-56, (Indianapolis, April 25 – 28, 1999), (2000).*

ABSTRACT

This report describes research performed over the period 1st January 2000 to 31st December 2000 on a MURI under Office of Naval Research contract N00014-96-1-1173 on the topic "Acoustic Transduction Materials and Devices". This program brings together researchers from the Materials Research Laboratory (MRL), the Applied Research Laboratory (ARL) and the Center for Acoustics and Vibrations (CAV) at the Pennsylvania State University. As has become customary over many years, research on the program is detailed in the technical appendices of published work, and only a brief narrative description connecting these studies is given in the text.

The program combines a far reaching exploration of the basic phenomena contributing to piezoelectric and electrostrictive response with the highly applied thrusts necessary to produce the "pay-off" in new applications relevant to Navy needs. Polarization vector tilting in the ferroelectric phase of perovskite structure crystals at compositions close to a morphotropic phase boundary (MPB) was first underscored on this program some four years ago, and is now widely accepted as one mode for exploiting the large intrinsic spontaneous strain in the ferroelectric to produce exceedingly strong anhysteretic piezoelectric response and very large electric field controlled elastic strain. New evidence for the importance of both spontaneous (monoclinic) and electric field induced tilting on the properties of both single and polycrystal MPB systems is presented in this report.

The puzzling phenomena associated with relaxor ferroelectric response have long been a topic of study in MRL, where the micro-polar region model and the application of Vogel/Fulcher to the dielectric slowing down were first applied. The current "pay-off" is in the greatly enhanced relaxor ferroelectric electrostrictive response from high electron energy irradiated polyvinylidene difluoride: trifluoroethylene (PVDF: TrFE) co-polymer discussed in this report. This development opens a new field of high strain, high energy density actuators with tremendous practical applicability. Now the possibility of engineering this response by chemical manipulation in the terpolymer systems without irradiation further enhances the exciting possibilities.

In composite structures, the early promise of the flexensional cymbal type actuators is now being fully realized and programs exploring large area cymbal transducer arrays are progressing very well, both at MRL/ARL and at NRL. The connection with CAV at Penn State is particularly important in keeping the MURI faculty aware of problems endemic to water as our host medium and the effects of turbulence in flow and the need for many types of acoustic noise control.

New designs of piezoelectric transformers and motors are demanding materials with lower loss levels under continuous high driving, and important progress is reported in separating and understanding the components of this loss and in designing new doping schemes for ceramics which enhance power capability almost tenfold. New piezoelectric micro-motor designs look particularly attractive and appear to offer significant advantages over electromagnetics for very small-scale applications. Thick and thin film studies for MEMS are progressing well and offering new insights into fatigue and switching behavior in the ferroelectrics.

INTRODUCTION

This report describes the research performed over the period of 1 January 2000 to 31 December 2000 on a MURI under Office of Naval Research contract N00014-96-1-1173 on the topic "Acoustic Transduction Materials and Devices." This program commenced on 31 July 1996 and brings together activities in the Materials Research Laboratory (MRL), the Applied Research Laboratory (ARL), and the Center for Acoustic and Vibration (CAV) at The Pennsylvania State University. Principal Investigator on the program is Professor Kenji Uchino, Professor of Electrical Engineering at Penn State. The program officer for the Office of Naval Research is Dr. Jan Lindberg.

The overall objective of the program is the development of acoustic transduction materials and devices of direct relevance to U.S. Navy needs, but also with relevant application capability in commercial sector products. A continuing emphasis is upon high performance high sensitivity sensors and upon high authority high strain actuators for transducing functions. New materials and improved material systems are being developed on the program. These studies are affording new insights into the strain mechanisms in already widely used ceramics and polymers and are developing needs for new device structures and improved drive and control strategies. There is proper emphasis upon performance and reliability under a wide range of operating conditions consonant with Navy needs.

Responsibility for the program elements are assigned as follows:

MATERIAL STUDIES	A.S. Bhalla
COMPOSITE SYSTEMS	R.E. Newnham
DEVICE STRUCTURES	T.R. Shrout
MODELLING	W. Cao
DEVICE FABRICATION and TESTING	W.J. Hughes
AIR ACOUSTICS and STEP and REPEAT SYSTEMS	G. Lesieutre

Layout of the report follows long established precedent drawing upon 96 published papers that we included as appendices with a very brief narrative summary to interconnect the different studies. In this report the topics are clustered as follows:

- 1.0. GENERAL SUMMARY PAPERS
- 2.0. MATERIALS STUDIES
 - 2.1. Polycrystal Perovskite Ceramics
 - 2.2. Single Crystal Systems
 - 2.3. High Strain Polymers
- 3.0. TRANSDUCER STUDIES
 - 3.1. Composite Structures
 - 3.2. Fluid Structure Interactions
 - 3.3. Piezoelectric Transformers
 - 3.4. High Power Materials
- 4.0. ACTUATOR STUDIES
 - 4.1. Materials and Designs
 - 4.2. Photostriction

- 4.3. High Force Systems
- 4.4. Piezoelectric Motors
- 4.5. Acoustic Absorbers
- 5.0. MODELING AND CHARACTERIZATION
 - 5.1. Design and Simulation
 - 5.2. Thin and Thick Films
 - 5.3. Domain Studies
- 1.0. GENERAL SUMMARY PAPERS

Electrostriction is the fundamental driving mechanism in all the most widely used perovskite structure based sensor and actuator materials. The subject is neatly summarized by Uchino (1) who clearly identifies structurally and phenomenologically the phenomena of piezoelectricity and electrostriction and their close inter-relationship in ferroelectric and relaxor ferroelectric systems. After a brief but very useful general introduction in his contribution on Smart Ceramics (2) Uchino focuses in on electro-mechanical application of piezoelectrics covering both material issues and a wide range of applications. In a brief but ground breaking study Ma and Cross (3) highlight the huge flexoelectric effect (charge-separation by elastic strain gradient) in lead magnesium niobate relaxor ferroelectric. A second major forward step is the introduction of a Landau-Ginsburg type model for antiferroelectricity based on macroscopic symmetry and group theory by Hatt and Cao, which properly models local dipole orientation, cell doubling, domain walls, and antiphase boundaries.

2.0. MATERIALS STUDIES

2.1. Polycrystal Perovskite Ceramics

The importance of the perovskite structure for a very wide range of both scientific and technological studies is placed nicely in context by the review of Bhalla, Guo and Roy (5). Just in the area of relaxor ferroelectric perovskite solid solutions which exhibit morphotropic phase boundaries (MPBs) the huge range of interesting possible compositions and data for these compositions is summarized in (6). This reference has more than 320 pages so only the table of contents is presented here. In three papers (7) (8) (9) the preparative skills for PZT ceramics at Penn state have been allied with the exceptional X-ray and neutron diffraction skills at Brookhaven to further authenticate the presence of a monoclinic phase at the MPB composition in PZT and to demonstrate the cardinal importance to the piezoelectric behavior in this system. In (10) ultrasonic second harmonic generation is employed to explore non linearity in commercial PZT and shown to be a sensitive indicator of poling induced damage in these ceramics. Lead magnesium niobate: lead titanate ceramic at composition close to the MPB is examined in (11) which explores the beneficial influence of Manganese substitution upon the loss levels at higher electric drive fields Elastic non linearity in the more conventional 0.9PMN:0.1P is measured in (12) using ultrasonic second harmonic generation and shown to exhibit a huge $\beta \sim 30$ and possible practical field tunability.

2.2. Single Crystal Systems

In the PZN:PT and PMN:PT single crystal systems, at compositions on the rhombohedral symmetry side of (MPB) the 001 field poled polydomain sample has vastly superior piezoelectric properties. This is not the only domain engineered system with much superior properties and (13) distinguishes domain geometry engineering, domain averaged systems and domain wall dependent applications. Relaxor character of the pure PZN Crystal is brought out strongly in (14) (15) by comparing micro (Raman) and macro (optical domain) determined symmetries. These studies strongly support the dynamic micro-polar region model for the relaxor status in this system. Initial results for polarization reversal in PZN and PZN:PT crystals are given in (16) which reports both exponential and linear behavior for different composition and field orientations.

Work is now progressing well on the optical, electro optic and photo elastic effects in PZN:PT and PMN:PT. Confirming the close approach of different ferroelectric species is the finding of a field forced single domain orthorhombic state in 0.67 PMN:0.33PT together with a domain divided rhombohedral:macro orthorhombic form with piezoelectric behavior that can be directly traced to the prototypic electrostrictive constants (17). In the linear electro-optic effect r_{51} is as expected much larger than r_{33} reflecting the high transverse permittivity (18) whereas r_{13} is very small in both tetragonal and rhombohedral forms and almost independent of temperatures (19). A phase locked AC stressing system was used to measure the piezooptic constant π_{33}^E at low stress levels for both 0.9PZN:0.1PT and 0.88PZN:0.12PT in rhombohedral and tetragonal forms (20) yielding values comparable to those in the widely used acousto-optic TeO_2 .

2.3 High Strain Polymers

Work by Qiming Zhang and his group has opened up a whole new family of high strain actuator materials by the demonstration of massive electrostrictive strain in high energy electron irradiated poly (vinylidene fluoride:trifluoroethylene) copolymers. Polarization and structural properties are discussed in (21) and (22). The evidence that the effect of the irradiation is to convert the material to a relaxor ferroelectric is presented from X-ray data (23) and from dielectric studies which exhibit very clear Vogel:Fulcher type relaxational response (24). The most important massive electrostrictive response is examined in (25) and the manner in which transverse response can be tuned by stretching discussed in (26). High strain, even under high tensile stress and transverse coupling in the field induced piezoelectric form of up to 0.45 are demonstrated. That this most effective electromechanical response extends over a broad frequency range is confirmed in (27). Evolution of the transition behavior under a very broad range of electron irradiation dosage is studied in (28) confirming the onset of local polar ordering and relaxor response. A strong thickness dependence of polarization switching is observed in thin spin cast films (29) leading to a critical thickness of order 100 nm (30) traced to strongly hindered crystallinity. Preliminary studies suggest that the irradiated electrostrictive polymer may have good electro-optic properties with $r_{33} \sim 40 \text{ pm/V}$ (31). Because of the high strain, electrodes are always a problem with the polymers and it is encouraging to see conductive polyaniline (32) in an all polymer actuator.

Probably however, the most encouraging development is that a chemical route may be possible to break up the polar domains as evidenced by early studies in the poly (vinylidene fluoride – trifluoroethylene-chlorotrifluoroethylene) terpolymers (33).

3.0 TRANSDUCER STUDIES

3.1 Composite Structures

The general topic of Piezoelectric composites is very effectively introduced in (34) which discusses connectivity, sum and product properties and the piezoelectric ceramic polymer systems. Specific application of piezocomposites to sensor type systems are discussed in (35) covering both ceramic:polymer and ceramic metal composites. The cymbal flexensional transducer is proving to be an exciting single element and component for array systems. Cymbal displacement amplification is discussed (36). Design, fabrication and applications for individual elements are outlined in (37). Modeling and underwater characteristics both for single elements and array structures are discussed in (38) and detailed characteristics of a 3x3 array are reported in (39).

Exciting specialization of the cymbal is achieved by individual driving of the end caps generating a directed beam pattern (40) and a second interesting development is the use of shape memory metal end caps to achieve tunability of resonance characteristics (41). Miniature hollow spheres of PZT made by a new sacrificial core process are proving effective as pre-focused VHF single element transducers (42).

To improve the dielectric permittivity of irradiated P(VDF:TrFE) copolymer, compositing with PMT:PT powder has been successfully demonstrated (43). A most interesting theoretical study of acoustic band gaps in periodic structures is given in (44) and techniques for forming a most unusual ferroelectric polymer-silica opal composite with three-dimensional periodic structure are presented in (45).

3.2. Piezoelectric transformers

Recent work has made the piezoelectric transformer a much more interesting component for sensor, actuator and smart material systems by markedly raising the available power level in new designs. This new perspective is summarized in (46) and a new disk type transformer which satisfies some of the predictions is discussed in (47).

3.3. High Power Level Materials

Proper measurement of the combined loss processes in piezoelectric ceramics at higher drive levels is a non trivial task. The problem of measurement and separation of dielectric, mechanical and piezoelectric components is tackled in (48), (49). Differences occur between resonant and non-resonant drive conditions and an important improvement by measurement under anti-resonant condition is discussed in (50). Modifications to the perovskite material systems to lower loss level under high continuous drive by Doping are discussed in (51) using PMN:PT ceramic as a vehicle for study. The proposed methods are further explored in manganese modified PMN:PT at compositions close to the MPB (52). A new composition in the family $\text{Pb}(\text{Zr}_{0.52}\text{Ti}_{0.48})\text{O}_3\text{Pb}(\text{Mn}_{1/3}\text{Sb}_{2/3})\text{O}_3$ with Eu and Yb substituents is shown to permit vibration velocity levels up to 1.0 m/s 3X higher than commercial hard PZT (53).

3.4 Fluid Structure Interactions

Several important problems in fluid flow and unsteady lift and drag on bodies in flowing fluid are considered in this section. The scaling of turbulent wall pressure fluctuations for flow

over a surface with a rearward-facing step are discussed in (54) where a new form of the wall pressure auto correlation frequency spectrum is proposed. Unsteady lift and drag in cross flow over a finite length cylinder is considered in (55) where the calculations suggest that unsteady lift is greater than the broad band unsteady drag. The problem of turbulence ingestion for rotors in turbomachinery are examined in (56) extending earlier studies to include rotors with arbitrary rake and skew. An extension of the correlation method of Martinez is shown to give good agreement with measurements for a 10 bladed rotor. A new model is proposed for space-time correlation in the wake region of a turbulent boundary layer in (57) and has been made available for general studies. The excellent book on Acoustic Fluid-Structure Interactives by MS Howe is reviewed in detail in (58).

4.0. ACTUATOR STUDIES

4.1. Materials and Designs

The topic of actuators studies is nicely introduced by (59) which covers composites and multilayer structures, materials and reliability and a range of applications. Recent trends including singly crystals and epitaxial films are introduced in (60). Compact multilayer structures with hollow cylindrical geometry are explored in (61) and shown to offer enhanced performance in both resonant and non-resonant driving. A simple stackable flextensional element assembled from commercial multilayer actuator without glue layers is presented in (62). An elegant sheer torsional amplifier using a simple sectorized cylinder is described in (63) with application to both transducers and motors.

4.2. Photostriction

Photostrictive actuation is discussed in (64) (65) (66). A new model is proposed for the basic phenomenon of charge separation under illumination, the so called anomalous photovoltaic effect (APV), using the second order optical non-linearity evident in the poled ferroelectric. Measurements as a function of illumination intensity, sample thickness and surface roughness are used to supply support for this model. Doping effects in PLZT are explored in (67) for optimized composition near the MPB in this system. Nb^{5+} , Mo^{6+} and Gd^{3+} were found to be effective. Ceramic processing variables are also found to be important including purity, homogeneity, stoichiometry, density and fine grain size (68).

4.3. High Force Actuators

To achieve high force with useful stroke it is necessary to go to step and repeat systems. Application of the torsional actuator in stepper configuration is discussed in (69). Limitations of the force in the stepping configuration are not usually due to the actuator but due to the clamping mechanism used in the stepping process, this is very evident from the care taken with this process in a new high force inchworm (70).

4.4. Piezoelectric Motors

The general classification of piezoelectric ultrasonic motors, standing wave and traveling wave types, single element vs. multielement, piezoelements used, and reliability issues are nicely summarized in (71). Comparison to electromagnetic motors are discussed in (72) and the advantages of the piezoelectric for small scales underlined. The attractive concept of using orthogonal modes in an excited hollow cylinder is considered in (73) for a motor down to 2.8 mm in diameter. Highly compact motors are discussed also in (74) with miniature windmill,

hollow ceramic and metal tube types considered. Resonant shear is considered in (75) for an original type of linear motor. A composite metal:ceramic ring type is discussed in (76) where inner circumference metal arms provide coupling to a truncated cone.

4.5 Acoustic Absorbers

A clever method for obtaining the large advantage of a tuned absorber over a wider frequency range is described in (77) using a shunt capacitance tuned piezoelectric which also acts as the sensor. Tuning is by a switched capacitor network. Noise reduction using light stiff trim panels driven by PZT inertial actuators is discussed in (78). Using a simple analogue controller the panel produced up to 13dB reduction in vibration and noise transmission. A new type of sound intensity probe is detailed in (79) which can be placed directly on the vibrating surface to determine power radiated from specific areas. Design of shell structures enclosing tuned absorbers to minimize sound power is covered in (80).

5.0 MODELLING AND CHARACTERIZATION

5.1. Design and Simulation

The complex of issues which must be considered in designing for piezoelectric application is summarized in (81). Materials, driving technique, reliability issues and possible techniques for health monitoring are discussed. Design of one dimensional transducer arrays using finite element methods is considered in (82). Crosstalk reduction, subdicing, and baffle effects are important issues. A method to determine electromechanical properties of thin strip vibrators at 20 to 30 MHz using a Mason model is considered in (83) and gives an interesting method for assessing degradation between fabrication damage and grain size effects. An usual method for characterizing electric parameters of ultra thin ($t \ll \lambda$) layers using leaky multi-mode lamb waves is given in (84).

5.2. Thin and Thick Films

The strong effects of crystal orientation on thin film lead zirconate titanate (PZT) films are described in (85, 86). For the PZT (70/30) rhombohedral phase compositions, 001 orientation gave sharp square loops whilst 111 oriented samples gave more rounded loops. Piezoelectric ferroelectric thin films are important for MEMS applications (87) but careful control is needed in deposition to achieve optimum properties and low aging. Measurements of permittivity and piezoelectric constants for lead magnesium niobate: lead titanate thin films at the 70:30 rhombohedral ferroelectric phase composition show $d_{33} \sim 180 \text{pC/N}$ for $\langle 001 \rangle$ oriented film superior to the $\langle 111 \rangle$ orientation (88) as in the bulk single crystal. Aging for $d_{31} \sim 4$ to 10% per decade is probably due to depoling. It is interesting to compare the PMN:PT data to PZT thin films (89) where random orientation shows superior polarization and piezoelectric constants to (001) oriented texture for the 52:48 composition. Wet etch patterning of PZT using a two-step process is described in (90). Good definition and low undercutting were obtained without detriment to the dielectric or piezoelectric properties.

5.3. Domain Studies

Domain engineering in single crystal ferroelectrics is becoming a more widely practiced art. To maintain order in this developing field it is suggested to distinguish between systems using special arrangement of domains and those using the average properties induced by closely spaced domains (91, 92). The configuration in a domain average engineered 0.955

PZN:0.045PT is discussed in (93) which points up the appearance on mm2, one of the many permitted average symmetries. The crucial role of defects in the establishing of the domain structure is highlighted by computer simulation in (94). For dipolar defects (95) the simulation suggests that local 90°twins reduce the coercivity and lead to 180° switching by two 90° flips. Field induced Acoustics Emission (96) when properly practiced can distinguish deformation related to domain reorientation and that due to direct piezoelectric deformation.

6.0 GRADUATE STUDENTS IN THE PROGRAM

STUDENT	ADVISOR	STUDENT	ADVISOR
F. Jeremy	G. Koopman	J. Bernard	G. Lesieutre
Jiang Jia	G. Koopman	J. Zhang	R.E. Newnham
B. Edinger	G.Koopman	Yi Bai	Q. Zhang
D. Erickson	G. Koopman		
J. Loverich	G. Koopman		
E. Alberta	A. Bhalla		

7.0 HONORS AND AWARDS

R.E. Newnham

2000 Byron Short Lecturer, University of Texas at Austin

2000 The IEEE Third Millennium Medal for Ferroelectrics

2001 David Kingery Award, American Ceramic Society

Susan Trolier McKinstry

Wilson Teaching Award of the College of Earth and Mineral Sciences, Penn State University

Faculty Achievement Award – Materials Research Laboratory

George A. Lesieutre

Penn State Engineering Society (PSES) Outstanding Research Award, April 2000

Best Student Paper in Engineering Acoustics, 2000, Acoustical Society of America, to advisee Julien Bernard, for "The Design of Actively-Tuned Flexural Piezoceramic Bar/Disk Transducers"

American Institute of Aeronautics and Astronautics (AIAA)

Zarem Educator award, January 2001

Best Paper, AIAA/ASME/ASCE/AHS/ASC Structures, Structural Dynamics and Materials Conference, 2000. For "Modeling of Shock Propagation and Attenuation in Viscoelastic Materials," with advisee Razvan Rusovici and co-advisor Daniel Inman, April 2001.

Ruyan Guo

Elected Program Chair of Electronics Division, ACERs. for 2000-2001

Elevated to Senior Member, IEEE

Symposium and Meeting Organizer, Symp. on Piezoelectrics, Electronics Division Meeting, October 2000, Greenville, South Carolina

Organization Committee. The Third Asian Meeting on Ferroelectrics, December 2000, Hong Kong

Gary Koopman

First holder of the Chair for International Cooperation, Department of Mechanical Sciences and Engineering, Tokyo Institute of Technology, April–July 2000.

E. J. Richards Lecture, University of Southampton, United Kingdom, November 2000.

L. Eric Cross

IEEE Third Millennium Medal 2000

American Ceramic Society, Honorary Life Member 2001

8.0 PAPERS PUBLISHED IN REFEREED JOURNALS

1. Hai-Sheng Xu, Z.-Y. Cheng, Vivek Bharti, Shexi Wang, and Q. M. Zhang. All-Polymer Electromechanical Systems Consisting of Electrostrictive Poly(vinylidene fluoride-trifluoroethylene) and Conductive Polyaniline. *J. Appl. Poly. Sci.* **75**, 945-951 (2000).
2. Vivek Bharti, H. S. Xu, G. Shanthi, Q. M. Zhang, and Kuming Liang. Polarization and Structural Properties of High Energy Electron Irradiated P(VDF-TrFE) Copolymer Films. *J. Appl. Phys.* **87**, 452-461 (2000).
3. A. E. Glazounov, Q. M. Zhang, C. Kim. Torsional Actuator Based on Mechanically Amplified Shear Piezoelectric Response. *Sensors and Actuators A* **79**, 22-30 (2000).
4. Yu Lu, Z.-Y. Cheng, E. Park, S. F. Liu and Q. M. Zhang. Linear Electro-optic Effect of $0.88\text{Pb}(\text{Zn}_{1/3}\text{Nb}_{2/3})-0.12\text{PbTiO}_3$ Single Crystal. *Jpn. J. Appl. Phys.* **39**, 141-145 (2000).
5. H. S. Xu, Z. Y. Cheng, Q. M. Zhang, A. MacDiarmid. Influence of High-energy Electron Irradiation on the Conduction Behavior of Doped Polyaniline Films in the High Current Regime. *Synthetic Met.* **108**, 133-137 (2000)
6. Q. M. Zhang, Z. Y. Cheng, and Vivek Bharti. Relaxor Ferroelectric Behavior in High Energy Electron Irradiated P(VDF-TrFE) copolymers. *Appl. Phys.* **A70**, 307-312 (2000).
7. Z. Y. Cheng, V. Bharti, T. Mai, T. B. Xu, Q. M. Zhang, K. Hamilton, T. Ramotowski, K. A. Wright, and R. Ting. Effect of High Energy Electron Irradiation on the Electromechanical Properties of Poly(vinylidene fluoride-trifluorethylene) 50/50 and 65/35 Copolymers. *IEEE Trans. UFFC* **47**, 1296 (2000).
8. A. E. Glazounov, S. Wang, Q. M. Zhang, and C. Kim. Piezoelectric Stepper Motor with Direct Coupling Mechanism to Achieve High Efficiency and Precise Control of Motor. *IEEE Trans. UFFC*, **47(4)**, 1059-1068 (2000).
9. Haisheng Xu, G. Shanthi, V. Bharti, Q. M. Zhang, and T. Ramatowski. Structural, Conformational, and Polarization Changes of P(VDF-TrFE) Copolymer Induced by High Energy Electron Irradiation. *Macromolecules*, **33**, 4125-4131(2000).
10. Shizhuo Yin, Q. M. Zhang, K.-W. Chung, R. Yang, Z. Y. Cheng, and Yu Lu. Investigation of the Electro-optic Properties of Electron-irradiated P(VDF-TrFE) Copolymer. *Opt. Eng.* **39**, 670-672 (2000).
11. Y. Bai, Z.Y. Cheng, V. Bharti, H. S. Xu, and Q. M. Zhang. High Dielectric Constant Ceramic Powder Polymer Composites. *Appl. Phys. Lett.* **76**, 3804-3806 (2000).
12. T.B. Xu, Z-Y. Cheng, Q. M. Zhang, R. Baughman, C. Cui, A. Zakhidov, and J. Su. Fabrication and Characterization of 3-Dimensional Periodic Ferroelectric Polymer-Silica Opal Composites and Inverse Opal. *J. Appl. Phys.* **88(1)**, 405-409 (2000).

13. Y. Barad, Yu Lu, Z. Y. Cheng, S. E. Park, and Q. M. Zhang. Composition, Temperature, and Crystal Orientation Dependence of Linear Electro-optic Properties of PZN-PT Single Crystals. *Appl. Phys. Lett.* **77**, 1247-1249 (2000).
14. A. E. Glazounov, Q. M. Zhang, and C. Kim. Torsional Actuator and Stepper Motor Based on Piezoelectric d_{15} Shear Response. *J. Intel. Mater. Syst. & Struct.* **11**(6), 456-468 (2000).
15. F. Xia, H. Xu, F. Fang, B. Razivi, Z. Y. Cheng, Yu Lu, Baoming Xu, and Q. M. Zhang. Thickness Dependence Behavior of Ferroelectric Switching in P(VDF-TrFE) Spin Cast Films. *Appl. Phys. Lett.* **78**, 1122 (2001).
16. Vivek Bharti, Z.-Y. Cheng, T. Mai, Q. M. Zhang, T. Ramotowski, K. A. Wright. High Electromechanical Coupling Factor and Electrostrictive Strain over a Broad Frequency Range in Electrostrictive Poly(vinylidene fluoride-trifluoroethylene) Copolymer. *Jpn. J. Appl. Phys.* **40**, 672 (2001).
17. Q. M. Zhang, H. S. Xu, Fei Fang, Z.-Y. Cheng, Xia Feng, and H. You. Observation of Critical Thickness of Crystallization in Spin Cast Ferroelectric Thin Films. *J. Appl. Phys.* **89**, 2613 (2001).
18. H. Xu, Z.Y. Cheng, D. Olson, T. Mai, Q. M. Zhang, and G. Kavarnos. Ferroelectric and Electromechanical Properties of P(VDF-TrFE-CTFE) Terpolymer. *Appl. Phys. Lett.* **78**, 2360 (2001).
19. Vivek Bharti, G. Shanthi, H. Xu, Q. M. Zhang, and K. Liang. Evolution of Transitional Behavior and Structure of Electron Irradiated P(VDF-TrFE) Copolymer Films. *Mater. Lett.* **47**, 107-111 (2001).
20. Vivek Bharti and Q. M. Zhang. Dielectric Study of Relaxor Ferroelectric P(VDF-TrEF) Copolymer System. *Phys. Rev. B.* **63**, 184103 (2001).
21. Y. Lu, Z.-Y. Cheng, Y. Barad, and Q. M. Zhang. Photoelastic Effects in the Tetragonal PZN-PT Single Crystals near the Morphotropic Phase Boundary. *J. Appl. Phys.* **89**, 5075 (2001).
22. Z.Y. Cheng, Vivek Bharti, T.B. Xu, Hansheng Xu, T. Mai, and Q. M. Zhang, Electrostrictive P(VDF-TrFE) Copolymers. *Sensors and Actuators A-Phys.* **90**, 138-147 (2001).
23. Yu Lu, D.-Y. Jeong, Z. Y. Cheng, Q. M. Zhang, H. Luo, Z. Yin, and D. Viehland. Phase Transitional Behavior and Piezoelectric Properties of the orthorhombic Phase of PMN-PT Single Crystals. *Appl. Phys. Lett.* **78**, 3109 (2001).
24. Zhang, J., W. J. Hughes, R. J. Meyer Jr., K. Uchino and R. E. Newnham, "Cymbal Array: A Broad Band Sound Projector," *Ultrasonics* **37**, 523-529 (2000).
25. Poosanaas, P., K. Tonooka and K. Uchino, "Photostrictive Actuators," *J. Mechatronics* **10**, 467-487 (2000).
26. Koc. B., P. Bouchilloux, and K. Uchino, "Piezoelectric Micromotor Using A Metal-Ceramic Composite Structure," *IEEE Trans. Ultrasonic, Ferroelectrics, and Frequency Control* **47** (4), 836-843 (2000).
27. Chen, Y. H., S. Hirose, D. Viehland, S. Takahashi and K. Uchino, "Mn-Modified $\text{Pb}(\text{Mg}_{1/3}\text{Nb}_{2/3})\text{O}_3\text{-PbTiO}_3$ Ceramics: Improved Mechanical Quality Factors for High-Power Transducer Applications", *Jpn. J. Appl. Phys.* **39**, 4843-4852 (2000).
28. Poosanaas, P., K. Tonooka, I. R. Abothu, S. Komarneni, and K. Uchino, "Influence of Composition and Dopant on Photostriction in Lanthanum-Modified Lead Zirconate Titanate Ceramics," *J. Intelligent Mater. Systems and Structures* **10**, 439-445 (2000).

29. Poosanaas, P., Dogan, A., Prasadaraao, A. V., Komarneni, S. and Uchino, K., "Effect of Ceramic Processing Methods on Photostrictive Ceramics", *J. Advanced Performance Mater.* **6**, 57-69 (1999).
30. Yao, K., K. Uchino, Y. Xu, S. Dong, and L. C. Lim, "Compact Piezoelectric Stacked Actuators for High Power Applications," *IEEE Trans. UFFC*, **47**, 819-825 (2000).
31. Uchino, K. and S. Hirose, "Loss Mechanisms in Piezoelectrics: How to Measure Different Losses Separately," *IEEE UFFC Transactions*, **48**, 307-321 (2001). (Principal Author)
32. Chen, Y. H., D. Viehland and K. Uchino, "Substituent Effects in $0.65\text{Pb}(\text{Mg}_{1/3}\text{Nb}_{2/3})\text{O}_3$ - 0.35PbTiO_3 Piezoelectric Ceramics" *J. Electroceramics*, **6**, 13- 20 (2001).
33. Kalpat, S., X. Du, I. R. Abothu, A. Akiba, H. Goto and K. Uchino, "Effect of Crystal Orientation on Dielectric Properties of Lead Zirconate Titanate Thin Films Prepared by Reactive RF-Sputtering," *Jpn. J. Appl. Phys.*, **40**, 158-162 (2001).
34. Gao, Y. Y. H. Chen, J. Ryu, K. Uchino and D. Viehland, "Eu and Yb Substituent Effects on the Properties of $\text{Pb}(\text{Zr}_{0.52}\text{Ti}_{0.48})\text{O}_3$ - $\text{Pb}(\text{Mn}_{1/3}\text{Sb}_{2/3})\text{O}_3$ Ceramics: Development of a New High-Power Piezoelectric with Enhanced Vibrational Velocity," *Jpn. J. Appl. Phys.*, **40**, 79-85 (2001).
35. Belegundu, U., X. H. Du, and K. Uchino, "Switching Current Dependence on Crystal Orientation for Relaxor Based Ferroelectric Single Crystals," *J. Electroceramics* (2001).
36. Koc, B., and K. Uchino, "Disk Type Piezoelectric Transformer with Crescent Shape Input Electrodes," *Proc. NATO- Advanced Research Workshop: Piezoelectric Materials: Advance in Science, Technology and Applications*, (Predeal, Romania, May 24-27, 1999, Kluwer Academic Publ., p.375-382 (2000).
37. Uchino, K., and B. Koc, "Compact Piezoelectric Ultrasonic Motors," *Proc. NATO- Advanced Research Workshop: Piezoelectric Materials: Advance in Science, Technology and Applications*, (Predeal, Romania, May 24-27, 1999, Kluwer Academic Publ., p.309-320 (2000).
38. Dogan, A., K. Uchino and R. E. Newnham, "Flextensional Composite Transducers: Designing, Fabrication and Application," *Proc. NATO- Advanced Research Workshop: Piezoelectric Materials: Advance in Science, Technology and Applications*, (Predeal, Romania, May 24-27, 1999, Kluwer Academic Publ., p.357-374 (2000).
39. Uchino, K., and J. Zheng, Y. H. Chen, X. Du and S. Hirose, "Loss Mechanisms in Piezoelectrics and Resonance/ Antiresonance," *Proc. 101st Annual Mtg. of Amer. Ceram. Soc., Symp. Electronic Ceramic Materials and Devices*, (Indianapolis, April 25 – 28, 1999), p.79-100 (2000).
40. Uchino, K., and H. Aburatani, "Field Induced Acoustic Emission in Ferroelectric Ceramics," *Proc. 101st Annual Mtg. of Amer. Ceram. Soc., Symp. Electronic Ceramic Materials and Devices*, SE-56, (Indianapolis, April 25 – 28, 1999), (2000).
41. Kalpat, S., X. Du, I. R. Abothu, A. Akiba, H. Goto, S. Trolrier-McKinstry and K. Uchino, "Dielectric Properties of Highly Oriented Lead Zirconate Titanate Thin Films Prepared by Reactive RF-Sputtering," *Symp. LL Proc., Mater. Res. Soc. Fall Mtg. '99*, (LL.1.3, Boston, Nov. 29-Dec.3, 1999), Vol. **604**, 3-8 (2000).

42. Uchino, K., J. Zheng, Y. H. Chen, X. Du, S. Hirose and S. Takahashi, "Loss Mechanisms in Piezoelectrics –Extrinsic and Intrinsic Losses--," Mater. Res. Soc. Fall Mtg. '99, (LL.1.6, Boston, Nov. 29-Dec.3, 1999), Vol.604, 25-31 (2000).
43. Belegundu, U., X. Du and K. Uchino, "Switching Current in $\text{Pb}(\text{Zn}_{1/3}\text{Nb}_{2/3})\text{O}_3$ - PbTiO_3 Single Crystals," Symp. LL Proc., Mater. Res. Soc. Fall Mtg. '99, (LL.1.9, Boston, Nov. 29-Dec.3, 1999), Vol.604, 39-44 (2000).
44. Bouchilloux, P., B. Koc and K. Uchino, "New Concept for Resonant Longitudinal-Shear Ultrasonic Motor," Symp. LL Proc., Mater. Res. Soc. Fall Mtg. '99, (LL.2.10, Boston, Nov. 29-Dec.3, 1999), Vol.604, 71-78 (2000).
45. Chen, Y. H., S. Hirose, D. Viehland and K. Uchino, "Doping Effects in $\text{Pb}(\text{Mg}_{1/3}\text{Nb}_{2/3})\text{O}_3$ - PbTiO_3 Ceramics for High Power Transduction Applications," Mater. Res. Soc. Fall Mtg. '99, (LL.5.8, Boston, Nov. 29-Dec.3, 1999), Vol.604, 215-220 (2000).
46. Uchino, K., "Recent Trend of Piezoelectric Actuator Developments –Material, Design and Drive Technique Related Issues--," Proc. Actuator 2000 (7th Int'l Conf. New Actuators, June 19-21, 2000), p.34-39 (2000).
47. Koc, B., J. F. Tressler and K. Uchino, "A Miniature Piezoelectric Rotary Motor Using Two Orthogonal Bending Modes of a Hollow Cylinder," Proc. Actuator 2000 (7th Int'l Conf. New Actuators, June 19-21, 2000), p.242-245 (2000).
48. W. Huang, G. H. Koopmann, S. J. Sharp, and W. Chen. April 2000. Enhanced Low Frequency Transmission Loss of Lightweight Trim Panels. Journal of Intelligent Material Systems and Structures, Volume 11, No 4.
49. Patricia L. Driesch, Hisao Iwata, Gary H. Koopmann, and Jeff Dosch. Nov. 2000. Development and evaluation of a surface acoustic intensity probe. Review of Scientific Instruments, 71 (11), pp. 1-6.
50. E.W. Constans, A.D. Belegundu, and G.H. Koopmann. 2000. Optimally Designed Shell Enclosures with Tuned Absorbers for Minimizing Sound Power. Optimization and Engineering, 1, 67-86, (an International Journal, Kluwer Publishers)
51. Davis, C.L. and G.A. Lesieutre, "An Actively Tuned Solid State Vibration Absorber Using Capacitive Shunting of Piezoelectric Stiffness," Journal of Sound and Vibration, Vo. 232(3), 4 May 2000, pp 601-617
52. Galante, T., J. Frank, J. Bernard, W. Chen, G.A. Lesieutre, and G.H. Koopman, "A high-force, High-Displacement Piezoelectric Inchworm Actuator," Journal of Intelligent materials systems and Structures , Vol. 10, Mo. 12, December, 2000, pp. 962-972
53. S. Trolier-McKinstry, "Piezoelectric Films for MEMS Applications," J. Ceram. Soc. Jpn. 109 (5) S76-S79 (2001).
54. Jeong Hwan Park, Fei Xu, and Susan Trolier-McKinstry, "Dielectric and Piezoelectric Properties of Sol-Gel Derived Lead Magnesium Niobium Titanate Films with Different Textures," J. Appl. Phys. 89(1) 568 - 574 (2001).
55. Q. F. Zhou, E. Hong, R. Wolf, and S. Trolier-McKinstry, "Dielectric and Piezoelectric Properties of PZT 52/48 Thick Films with (100) and Random Crystallographic Orientation," Ferroelectric Thin Films, Vol 655 (2000).
56. L.-P. Wang, R. Wolf, Q. F. Zhou, S. Trolier-McKinstry and R. J. Davis, "Wet-etch patterning of lead zirconate titanate (PZT) thick films for microelectromechanical systems (MEMS) application," Mat. Res. Soc. Symp. Vol.657 (MEMS)

57. Jindong Zhang, W. Jack Hughes, R. J. Meyer Jr., Kenji Uchino, and R. E. Newnham, "Cymbal array: a broadband sound projector", *Ultrasonics*, vol.37, pp.523-529, 2000.
58. Dogan, A., K. Uchino, and R.E. Newnham, "Flextensional Composite Transducers: Designing, Fabrication and Application," *Piezoelectric Materials: Advances in Science, Technology and Applications*, edited by C. Galassi et al., Kluwer Academic Publishers, pp. 357-374 (2000).
59. Meyer, R.J. Jr. and R.E. Newnham, "Flextensional transducers with Shape Memory Caps for Tunable Devices," *Journal of Intelligent Materials Systems and Structures*, vol. 11, pp. 199-205 (2001).
60. Meyer, R.J. Jr., A. Dogan, C. Yoon, S. Pilgrim and R.E. Newnham, "Displacement Amplification of Electroactive Materials Using the Cymbal Flextensional Transducer," *Sensors & Actuators A*, vol.87, pp. 157-162 (2001).
61. Meyer, R.J. Jr., S. Alkoy, J. Cochran, T. Ritter, and R.E. Newnham, "Pre-focused Lead Titanate > 25 MHz Single Element Transducers from Hollow Spheres," *IEEE Transactions on Ultrasonics, Ferroelectrics, and Frequency Control*, vol. 48 (2), pp. 488-493 (2001).
62. Zhang, J., A.C. Hladky-Hennion, W.J. Hughes, and R.E. Newnham, "Modeling and Underwater Characterization of Cymbal Transducers and Arrays," *IEEE Transactions on Ultrasonics, Ferroelectrics, and Frequency Control*, vol. 48 (2), pp. 560-568 (2001).
63. Zhang, J., A.C. Hladky-Hennion, W.J. Hughes, and R.E. Newnham, "A Miniature Class V flextensional cymbal transducer with directional beam pattern: The Double-Driver," *Ultrasonics*, vol. 39, pp. 91-95 (2001).
64. Uchino, K., B. Koc and S. Dong, "Compact Piezoelectric Ultrasonic Motors," *Proc. 5th Euroconf. Appl. Polar Dielectrics*, O-1, Jurmala, Latvia, Aug. 27-30 (2000).
65. Uchino, K., P. Poosanaas and K. Tonooka, "Photostrictive Actuators—New Perspective-," *Proc. 5th Euroconf. Appl. Polar Dielectrics*, O-43, Jurmala, Latvia, Aug. 27-30 (2000).
66. Uchino, K., B. Koc, P. Laoratanakul and A. Vazquez Carazo, "Piezoelectric Transformers—New Perspective-," *Proc. 3rd Asian Mtg. Ferroelectrics*, D1d.1, Hong Kong, Dec. 12-15 (2000).
67. Uchino, K., P. Poosanaas and K. Tonooka, "Photostrictive Actuators—New Perspective-," *Proc. 3rd Asian Mtg. Ferroelectrics*, C3p.105, Hong Kong, Dec. 12-15 (2000).
68. Rajeev Ahluwalia, "Computer Simulations of Domain Pattern Formation in Ferroelectrics", *AIP Conference Proceedings series*, © 2001 American Institute of Physics, *Proceedings of the 2001 Workshop on fundamental Physics of Ferroelectrics Williamsburg, VA 2001*.
69. R. Zhang, M. Wan, X. Gong and W. Cao, "Low Frequency Multi-Mode Ultrasonic lamb Wave Method for Characterization of the ultra-thin Elastic layer", *ATCA Metrologica Sinica*, vol. 21, pp 59-67 (2000)
70. J. H. Yin, W. Cao, "Domain Configurations in Domain Engineered 0.955Pb (Zn_{1/3}Nb_{2/3})O₃-0.045PbTiO₃ Single Crystals" *J. Appl. Phys.* vol. 87, pp 7438-7441 (2000)
71. M.R. Shen and W. Cao, "Acoustic Bandgap Formation in a Periodic Structure with Multilayer Unit Cells", *J. Phys. D: Applied Physics*, vol. 33, pp. 1150-1154 (2000).

72. W.K. Qi, and W. Cao, "Finite Element Study on 1-D Array Transducer Design" IEEE Transactions on Ultra. Ferro, and Frequency Control, vol. **47**, pp. 949-955 (2000)
73. T.A. Ritter, K.K. Shung, W. Cao, and T. R. Shrout "Electromechanical Properties of Thin Strip Piezoelectric Vibrators at High Frequency", J. Applied Phys., vol. **88** pp.394-397 (2000) Phys. Rev. B. vol. 62, pp. 818-823 (2000).
74. R. Hatt and W. Cao, "Landau-Ginzburg model for Antiferroelectric Phase Transitions Based on Microscopic Symmetry". Phys. Rev. B, vol. 62, pp. 818-823 (2000).
75. W. H. Jiang and W. Cao "Intrinsic and Coupling induced Elastic Nonlinearity of Lanthanum-doped Lead Magnesium Niobate-lead Titanate Electrostrictive Ceramic", Appl. Phys. vol. **77** pp. 1387-1389 (2000).
76. W. Jiang and W. Cao, Nonlinear Properties of Lead Zirconate Titanate Piezoceramics", J. Appl. Phys. vol. **88** 6684-6689 (2000)/
77. W. Jiang and W. Cao, "Influence of Dipolar Defects on Switching Behavior in Ferroelectrics", Phys. Rev. B. vol. **63**, pp. 012103 (2000).
78. R. Guo, L.E. Cross, S-E. Park, B. Noheda, D.E. Cox, G. Shirane, "Origin of the high piezoelectric response in $\text{PbZr}_{1-x}\text{Ti}_x\text{O}_3$," *Phys. Rev. Letters*, **84(23)**, 5423-5426, (2000)
79. B. Noheda, J.A. Gonzalo, L.E. Cross, R. Guo, S-E. Park, D.E. Cox, G. Shirane, "Tetragonal-to-Monoclinic Phase Transition in a Ferroelectric Perovskite: the Structure of $\text{PbZr}_{0.52}\text{Ti}_{0.48}\text{O}_3$," *Phys. Rev. B*, **61(13)**, 8687-8689, (2000)
80. B. Noheda, D.E. Cox, G. Shirane, R. Guo, B. Jones, L.E. Cross, "Stability of the monoclinic phase in the ferroelectric perovskite $\text{PbZr}_{(1-x)}\text{Ti}_x\text{O}_3$," *Los Alamos Natl. Lab., Prepr. Arch., Condens. Matter*, **1-8**, arXiv:cond-mat/0006152, (2000)

9.0 PAPERS SUBMITTED FOR PUBLICATION

1. Bernard, J.E., G.A. Lesieutre, "Active Tuning of Acoustic Transducers for Wide Sweep Frequency-Modulated Pulse Transmission," Journal of the Acoustical Society of America, 2001. (submitted)
2. Bernard, J.E., and Lesieutre, G.A., "The Use Of Actively-Tuned Low Frequency Transducers For High Power Linear Chirp Transmission," Journal of the Acoustical Society of America, 2001. (submitted)
3. Bernard, J., G.A. Lesieutre, and G.H. Koopmann, "Active Broadband Force Isolation using a Flexural Piezoelectric Inertial Actuator," Journal of Sound and Vibration, 2000. (submitted)
4. D.M. Hatch, W. Cao and A. Saxena, "Orientational Twins in an Improper Ferroelastic Phase Transition Driven by M_5^- Zone Boundary Phonon in $\text{RAg}_{1-x}\text{In}$ ", Submitted in Phys. Rev. B (2001).
5. R. Hatt and W. Cao, " Theory of the Antiferroelectric First Order Phase Transition in Ammonium Dihydrogen Phosphate", Submitted in J. Appl. Phys. (Apr. 2000).
6. W. Jiang and W. Cao, " Second Harmonic Generation of Transverse Waves in Crystals with Cubic, Hexagonal and Trigonal Symmetries", Submitted in J. Acous. Soc. Am., (Nov. 2000).
7. Dogan A., J. Tressler and R.E. Newnham, "Solid State Ceramic Actuator Designs," Accepted by AIAA Journal. (7/30/00).

8. Newnham R.E., J. Zhang, "Cymbal Transducer: A Review," *2000 IEEE-ISAF Proceedings*, Honolulu, Hawaii (2000).
9. Newnham R.E. and L.E. Cross, "Symmetry and Antisymmetry in Electroceramics," The Proceedings Volume of the FORUM 2000, International Academy of Ceramics, Italy (2000).
10. Newnham R.E., J. Zhang, S. Alkoy, R. Meyer, W.J. Hughes, A.C. Hladky-Hennion, J. Cochran, and D. Markley, "Cymbal and BB Underwater Transducers and Arrays," Proceeding of the 10th US-Japan Seminar on Dielectric and Piezoelectric Ceramics, Sept. 27-29, 2001, Providence, R.I.
11. Jeong Hwan Park and Susan Trolier-McKinstry, "Dependence of Dielectric and Piezoelectric Properties on Film Thickness for Highly {100} Oriented PMN-PT (70/30) Thin Films," accepted by *J. Mat. Res.* (2000).
12. Feng Xia, B. Razavi, H. S. Xu, Z.-Y Cheng and Q. M. Zhang. What Determines the Critical Thickness of Crystallization in Spin Cast Poly(vinylidene fluoride- trifluoroethylene) Polymer Thin Films? Submitted. to *Phys. Rev. Lett.* (2001).
13. E.F. Alberta and A.S. Bhalla, "Low-temperature properties of lead nickel-niobate ceramics," Submitted to *Materials Letters* (2001).
14. E.F. Alberta and A.S. Bhalla, "Low-Temperature Property Investigation of The Lead Indium-Niobate : Lead Nickel-Niobate Solid Solution," Submitted to *J. Phys. Chem. Solids* (2001).
15. E.F. Alberta and A.S. Bhalla, "Piezoelectric and Dielectric Properties of Transparent $\text{Pb}(\text{Ni}_{1/3}\text{Nb}_{2/3})_{1-x-y}\text{Zr}_x\text{Ti}_y\text{O}_3$ Ceramics Prepared by Hot Isostatic Pressing," Submitted to *Int'l. J. Inorg. Mat.* (2001).

10.0 PAPERS APPEARING IN NON REFEREED PUBLICATIONS

1. M. Grissom, A. D. Belegundu, and G. H. Koopmann. 2000. Constructing Objective Functions with Preference Curves Based on Practical Design Inputs: A Vibration Reduction Application. NSF Grantees Conference, Vancouver, Canada
2. G. A. Lesieutre, G. H. Koopmann, E. M. Mockensturm, W. Chen, and J. Frank. April 2000. High Torque Piezoelectric Rotary Motors. International Center for Actuators and Transducers (ICAT) Annual Workshop, State College, PA
3. E. M. Mockensturm, J. Jiang, G. H. Koopmann, and G. A. Lesieutre. April 2000. Modeling and Simulation of a Resonant Bimorph Actuator Drive. U.S. Navy Workshop on Acoustic Transduction Materials and Devices, State College, PA.
4. G. H. Koopmann, G. A. Lesieutre, J. E. Frank, W. Chen, and E. M. Mockensturm. April 2000. A High Torque Rotary Motor with a Resonant Bimorph Actuator Drive. U.S. Navy Workshop on Acoustic Transduction Materials and Devices, State College, PA.
5. G. H. Koopmann. June 2000. Optimal Acoustic Design for Structures: Methodology and Applications. 15th Conference on the Research of Sound from Machinery, Ritsumeikan University, Kusatsu, Japan.
6. G.H. Koopmann, J. E. Frank, G. A. Lesieutre, and W. Chen. July 2000. Development of a High Torque Rotary Motor Driven by Piezoelectric Bimorphs. ICAT 2000, Tokyo.
7. J. E. Frank, G. H. Koopmann, W. Chen, E. M. Mockensturm, and G. A. Lesieutre. March 2000. Design and Performance of a Resonant Roller Wedge Actuator. SPIE

Smart Structures and Materials Conference: Smart Structures and Integrated Systems, Newport Beach, CA.

8. G. H. Koopmann. June 2000. Optimal Acoustic Design for Structures: Methodology and Applications. First International Workshop of the Department of Mechanical Sciences and Engineering, Tokyo Institute of Technology.
9. Bernard, "Detailed Design of Actively-Tuned Flexural Piezoceramic Transducers," ONR Transducer Meeting, Baltimore, MD, May 14-16, 2001.
10. Lesieutre, G.A., Koopmann, G.H., Frank, J.B., "Mechanical Diode Based, High-Torque Piezoelectric Rotary Motor," AIAA Adaptive Structures Forum, Seattle, WA, April, 2001.
11. Bernard, J.E., and Lesieutre, G.A., "The Use Of Actively-Tuned Low Frequency Transducers For High Power Linear Chirp Transmission," Acoustical Society of America meeting, November, 2000.
12. Bernard, J.E., and Lesieutre, G.A., "The Design Of Actively-Tuned Flexural Piezoceramic Bar/Disk Transducers," Acoustical Society of America meeting, December, 2000. (ASA Student Paper Award)
13. Bernard, J. and G.A. Lesieutre, "Design and Realization of Frequency Agile Piezoceramic Transducers," proceedings of the AIAA/ASME/AHS Adaptive Structures Forum, Atlanta, GA, April 3-6, 2000.
14. Bernard, J., and G.A. Lesieutre, "Design and Realization of Variable Frequency Flexural Piezoceramic Transducers," proceedings of the SPIE Smart Structures and Materials Conference: Smart Structures and Integrated Systems, Newport Beach, CA, March 1-5, 2000.
15. Bernard, J. and Lesieutre, G.A., "Variable Frequency Flexural Piezoelectric Transducers For High Power Linear Chirp Transmission," 11th ICAST, Nagoya, Japan, October 23-26, 2000.
16. Bernard, J., and G.A. Lesieutre, "Frequency Agile Acoustic Transducers," at the U.S. Navy Workshop on Acoustic Transduction Materials and Devices," State College, PA, April 11-13, 2000.
17. Q. M. Zhang, Z. Y. Cheng, V. Bharti, T. B. Xu, H. S. Xu, T. Mia, S. Gross. Piezoelectric and Electrostrictive Polymer Based Actuator Materials. Proc. of SPIE's 7th Ann. International Symp. on Smart Struct. and Mater. Vol. 3987, 34-50 (Newport Beach, CA 2000)
18. Z. Y. Cheng, T. B. Xu, V. Bharti, and Q. M. Zhang. Characterization of Electrostrictive P(VDF-TrFE) Copolymer Films for High-frequency and High-load Applications. Proc. of SPIE's 7th Ann. International Symp. on Smart Struct. and Mater. Vol. 3987, 73-81 (Newport Beach, CA 2000).
19. Q. M. Zhang, Z. Y. Cheng, V. Bharti. Electrostrictive P(VDF-TrFE) Copolymers. Proc. Materials Congress 2000, 113 (N Alford and E. Yeatman, ed., IOM Communications Ltd, UK).
20. V. Bharti, Z. Y. Cheng, and Q. M. Zhang. Dielectric Relaxation and Weak Polarization Response in Relaxor Ferroelectric P(VDF-TrFE) Copolymer. Proc. 12th IEEE International Symp. Appl. Ferro. (Hawaii, Aug. 2000).
21. Y. Bai, V. Bharti, Z. Y. Cheng, H. S. Xu, and Q. M. Zhang. A New Ceramic-Polymer Composite Using High Dielectric Constant Matrix. Proc. IEEE 12th International Symp. Appl. Ferro. (Hawaii, Aug. 2000).

22. Z.Y. Cheng, T. B. Xu, V. Bharti, S. Gross, T. Mai, Q. M. Zhang, T. Ramotowski, L. Ewart, and R. Ting. Electrostrictive Effect and Load Capability in Electron Irradiated P(VDF-TrFE) Copolymer. Proc. IEEE 12th International Symp. Appl. Ferro. (Hawaii, Aug. 2000).
23. Y. Lu, Y. barad, Z. Y. Cheng, S. E. Park, and Q. M. Zhang. Elasto-optical and Electro-optical Studies of PZN-PT Single Crystals. Proc. IEEE 12th International Symp. Appl. Ferro. (Hawaii, Aug. 2000).
24. Yu Lu, Z.-Y. Cheng, and Q. M. Zhang. Acousto-optic Properties of PZN-PT Single Crystals. Proc. 2000 IEEE Ultrasonic Symp. 651-654 (Puerto Rica, Oct. 2000).
25. T. B. Xu, Z.-Y. Cheng, M. Tian, Yu Lu, and Q. M. Zhang. Electromechanical Coupling Factors of Electrostrictive P(VDF-TrFE) Copolymer. Proc. 2000 IEEE Ultrasonic Symp. 997-1000 (Puerto Rica, Oct. 2000).

11.0 INVITED PAPER PRESENTED AT NATIONAL AND INTERNATIONAL MEETINGS

1. L.E. Cross, "Phase switching perovskites for actuator applications", SPIE 7th Annual International Symposium on Smart Structures and Materials, March, Newport Beach, CA.
2. L.E. Cross, P. Hana, "Progress in the Thermodynamic Phenomenology for the Lead Zinc Niobate : Lead Titanate Solid Solution System", (VII.3), 2000 US Naval Workshop on Acoustic Transduction Materials and Devices, April, State College, PA.
3. L.E. Cross, "PNO38: Domain and phase change contributions to response in high strain ferroelectric materials", The 6th International Symp. On Ferroic Domains and Mesoscopic Structures (ISFD-6), May, Nanjing University.
4. L.E. Cross, "Overview of Active Materials", Aero Smart 2000, Texas A&M University, September, College Station, TX.
5. L.E. Cross, "Domain and Phase Change Contributions to Response in High Strain Piezoelectric Actuators", 3rd Asia Meeting on Ferroelectrics AMF3, December, Hong, Kong,
6. R.E. Newnham, J. Zhang, A.C. Hladky-Hennion, W.J. Hughes, R.J. Meyers, and J. Tressler "Cymbal Transducers and Arrays," ONR meeting, Penn State University.
7. R.E. Newnham, J. Zhang, and R.J. Meyers, "Cymbal Transducers and Arrays," ICAT meeting, Penn State University.
8. R.E. Newnham, "Crystal Chemistry of Rare-Earth Oxide," CDS meeting, Penn State.
9. R.E. Newnham "Biomimetic Sensors and Actuators," 102nd Annual Meeting of the American Ceramic Society, April, ST. Louis, MO.
10. R.E. Newnham, "Symmetry and Antisymmetry in Electroceramics," 102nd Annual Meeting of the American Ceramic Society, April, ST. Louis, MO.
11. R.Yimnirun, R.J. Meyer, Jr., P.J. Moses, and R.E. Newnham, "Complete Determination of Electrostriction Tensor Components of CaF₂ Single Crystal Using Single Beam Interferometer," 102nd Annual Meeting of the American Ceramic Society, April, ST. Louis, MO.
12. R.E. Newnham, "Structure-Property Relations in Smart Materials," invited paper at the 10th International Metallurgy and Materials Congress and Trade Fair, Turkey.
13. R.E. Newnham, "Cymbal and BB Transducer Arrays," Naval Underwater Warfare Center (NUWC), Rhode Island.

14. R.E. Newnham, "Molecular Mechanisms in Smart Materials," Mechanical Engineering Dept. Seminar, Rice University, Houston, Texas
15. R.E. Newnham, "Molecular Mechanisms in Smart Materials," Texas Center for Superconductivity, Univ. of Houston, Houston, Texas
16. R.E. Newnham, "Symmetry and Antisymmetry in Ferroelectric Transducers," 3rd Asian Meeting on Ferroelectrics, Hong Kong, China
17. R.E. Newnham, "Molecular Mechanisms in Smart Materials," Plenary Lecture at The Sixth International Congress on Applied Mineralogy (ICAM), University of Göttingen, Germany.
18. Craven, B.M. and R.E. Newnham, "The Crystal Structure of Ettringite Mineral," American Crystallographic Association Meeting, St. Paul, MN.
19. R.E. Newnham, "Cymbal Transducer: A Review," International Symposium on Applications of Ferroelectrics (ISAF'2000), Honolulu, Hawaii.
20. G. H. Koopmann, S. J. Sharp and P. Nelson. Nov. 2000. Power Absorbing Controllers for Noise Reduction. *The 2000 ASME International Mechanical Engineering Congress and Exposition*, Orlando, FL.
21. K. Chen and G. H. Koopmann.. Active Enhancement of Low-Frequency Sound Transmission Loss Using Planar Sound Sources. *The 2000 ASME International Mechanical Engineering Congress and Exposition*, Nov, Orlando, FL.
22. M. Grissom, A. D. Belegundu, A.D. and G. H. Koopmann. Constructing Objective Functions with Preference Curves Based on Practical Design Inputs: A Vibration Reduction Application. NSF Grantees Conference, Vancouver, Canada
23. Patricia Driesch, Gary Koopmann, and Ashok Belegundu. Acoustic control in enclosures using optimally tuned absorbers. International Mechanical Engineering Congress & Exposition, Nov, Orlando, FL, NCA 13B.
24. G. A. Lesieutre, G. H. Koopmann, E. M. Mockensturm, W. Chen, and J. E. Frank. 20-21, High Torque Piezoelectric Rotary Motors. International Center for Actuators and Transducers (ICAT) Annual Workshop, April, State College, PA.
25. E. M. Mockensturm, J. Jiang, G. H. Koopmann, and G. A. Lesieutre. Modeling and Simulation of a Resonant Bimorph Actuator Drive. U.S. Navy Workshop on Acoustic Transduction Materials and Devices, April, State College, PA.
26. G. H. Koopmann, G. A. Lesieutre, J. E. Frank, W. Chen, and E. M. Mockensturm. A High Torque Rotary Motor with a Resonant Bimorph Actuator Drive, U.S. Navy Workshop on Acoustic Transduction Materials and Devices, April State College, PA.
27. G. H. Koopmann. Optimal Acoustic Design for Structures: Methodology and Applications. 15th Conference on the Research of Sound from Machinery, Ritsumeikan University, June, Kusatsu, Japan.
28. G. H. Koopmann, J. E. Frank, G. A. Lesieutre, and W. Chen. Development of a High Torque Rotary Motor Driven by Piezoelectric Bimorphs. ICAT 2000, July, Tokyo.
29. J. E. Frank, G. H. Koopmann, W. Chen, E. M. Mockensturm, and G.A. Lesieutre. Design and Performance of a Resonant Roller Wedge Actuator. SPIE Smart Structures and Materials Conference: Smart Structures and Integrated Systems, March, Newport Beach, CA.

30. G. H. Koopmann. 2000. Optimal Acoustic Design for Structures: Methodology and Applications. First International Workshop of the Department of Mechanical Sciences and Engineering, June, Tokyo Institute of Technology.
31. Newnham R.E. and L.E. Cross, "Symmetry and Antisymmetry in Electroceramics," The Proceedings Volume of the FORUM 2000, International Academy of Ceramics, Italy (2000).
32. S. Trolrier-McKinstry, V. Bornand, J-H. Park, C. A. Randall, M. Ozgul, K. Takemura, T. Yoshimura, and Z. Zhang, "Epitaxial and Oriented Relaxor Ferroelectric-PbTiO₃ Films for Memory and Transducer Applications," invited presentation at First Asian Conference on Crystal Growth and Crystal Technology, August 29-Sept. 1, 2000, Sendai, Japan
33. Uchino, K., "Loss Mechanisms in Piezoelectrics and Heat Generation," Fundamental Physics Workshop on Ferroelectrics, Aspen, Co, Feb. 13-19 (2000).
34. Uchino, K., "Crystal Orientation Dependence of Piezoelectricity in Perovskites and Related Materials," Fundamental Physics Workshop on Ferroelectrics, Aspen, Co, Feb. 13-19 (2000).
35. Uchino, K., J. H. Zheng, Y. H. Chen, X. H. Du and S. Hirose, "Heat Generation and Loss Mechanisms in Multilayer Piezoelectric Actuators," 102nd Annual Mtg. of Amer. Ceram. Soc., Symp. Advances in Dielectric Mater. & Multilayer Electronic Devices, A2-007-00, St. Louis, April 30 – May 3 (2000).
36. Uchino, K., "Recent Trend of Piezoelectric Actuator Developments –Material, Design and Drive Technique Related Issues--," Proc. Actuator 2000 (7th Int'l Conf. New Actuators, June 19-21, 2000), p.34-39 (2000).
37. Uchino, K., B. Koc and S. Dong, "Compact Piezoelectric Ultrasonic Motors," Proc. 5th Euroconf. Appl. Polar Dielectrics, O-1, Jurmala, Latvia, Aug. 27-30 (2000).
38. Uchino, K., P. Poosanaas and K. Tonooka, "Photostrictive Actuators–New Perspective-," Proc. 5th Euroconf. Appl. Polar Dielectrics, O-43, Jurmala, Latvia, Aug. 27-30 (2000).
39. Uchino, K., X. Du, S. Kalpat and U. Belegundu, "High Electromechanical Coupling Piezoelectrics - Crystal Orientation Dependence of Electromechanical Couplings in Perovskite Crystals-," Amer. Ceram. Soc. Electronics Division Mtg., Greenville, Oct. 9-11 (2000).
40. Uchino, K., Y. H. Chen, X. Du, J. Zheng, P. Ramakrishnan, S. Hirose and S. Takahashi, "High Power Piezoelectric Measurement System," Amer. Ceram. Soc. Electronics Division Mtg., Greenville, Oct. 9-11 (2000).
41. Uchino, K., B. Koc, P. Laoratanakul and A. Vazquez Carazo, "Piezoelectric Transformers –New Perspective--," 3rd Asian Mtg. Ferroelectrics, D1d.1, Hong Kong, Dec. 12-15 (2000).
42. Uchino, K., "The Dawn of Piezoelectric Composites at MRL/Penn State: Some History," 25th Annual Int'l Conf. Advanced Ceramics & Composites, S3-001-01, Jan. 21-26 (2001).
43. Q. M. Zhang, Electroactive P(VDF-TrFE) Copolymer Based High Strain Actuators. SPIE's 7th International meeting on Smart Structures and Materials, March 6, 2000 (CA) (Invited)
44. Q. M. Zhang, Electrostrictive Polymers, Materials Congress 2000, UK (April 12) (Invited).

45. R. Y. Ting and Q. M. Zhang. New Electrostrictive P(VDF-TrFE) Copolymers for Large Strain Actuation Application. The EOS/SPIE Symposium on Applied Photonics, May 22, 2000 (Glasgow, UK) (Invited).
46. Q. M. Zhang, V. Bharti, Z. Y. Cheng, H. S. Xu, T. B. Xu, T. Ramatowski, L. Ewart, and R. Ting. Electrostrictive and Relaxor Ferroelectric Behavior of P(VDF-TrFE) Based Polymers – A Review. 12th IEEE International Symp. Appl. Ferro. (Hawaii, Sept. 30-Aug. 3, 2000). (Invited)
47. Q. M. Zhang. Electrostriction and Relaxor Ferroelectric Behavior in Electron Irradiated Polymers. 4th Internat. Symp. Ionizing Radia. & Polym. (Gouvieux-Chantilly, France, Sept. 25-27, 2000). (Invited)
48. Q. M. Zhang and Z.Y. Cheng. Recent Advances in Electromechanical and Electronic Properties of P(VDF-TrFE) Based Ferroelectric Polymers. The Knowledge Foundation's International Conference on Novel Materials for Electronics Miniaturization (San Francisco, CA, Nov. 2-3, 2000). (Invited)
49. W. Cao, "Computer Simulation of Domain Formation and Switching Process in Ferroelectric Systems", The Six International Symposium on Ferroic Domains and Mesoscopic Structures, Nanjing, China, May 29-June 2, 2000.
50. W. Cao, "Mesoscopic Symmetry and Material Properties of Multi-domain PZN-PT Single Crystals", 12th IEEE International Symposium on the Applications of Ferroelectrics (ISAF 2000) Honolulu, Hawaii, July 30-August 2, 2000.
51. W. Cao, "Fundamental Issues and Methods for Characterization of Transducer Materials Over a Broad Frequency Range", Ultrasonic Transducer Engineering Conference, State College, PA, August 2-4, 2000.
52. Ruyan Guo, "Electric Boundary Conditions on Thermal Strain Behavior of Relaxor Single Crystals", *Asia Meetings on Ferroelectrics (AMF-III)*, Dec. 12-15, 2000, Hong Kong, China (invited)
53. Ruyan Guo, "Effect of Electric Field on Oxide Ferroelectric Solid Solutions Near a Morphotropic Phase Boundary", *ACerS 102nd Annual Meeting*, April 30-May 3, 2000, St. Louis, Missouri (invited)

12.0 INVITED PAPERS PRESENTED AT UNIVERSITY, INDUSTRY AND GOVERNMENT LABORATORIES

1. L.E. Cross, "Frontiers in Materials Science Lecture" Materials Research Laboratory, University of Pennsylvania, Philadelphia, PA, April
2. L.E. Cross, "High Strain Actuation Materials: Current Status and Future Prospects", Physics Colloquium, University of Nebraska, Lincoln Nebraska
3. R.E. Newnham, "Smart Composites for Sensors, Actuators, and Transducers," Byron Short Lecture, Mechanical Engineering Dept., University of Texas, Austin, TX.
4. R.E. Newnham, "Materials Science and Engineering in the 21st Century : Scaling Up and Scaling Down," R.E. Newnham, "Molecular Mechanisms in Smart Materials," The Dow Chemical Company, Midland, Michigan.
5. R.E. Newnham, "Ceramic Engineering in the 21st Century," Anadolu University, Turkey
6. R.E. Newnham, "Smart Materials," The New World of Advanced Materials Workshop, Dept. of Physics, Penn State University.
7. R.E. Newnham, "Composite Transducers," Seminars at Acoustics Dept., ISEN, Catholic University, Lille, France.

8. S. Trolier-McKinstry, V. Bornand, J-H. Park, C. A. Randall, M. Ozgul, K. Takemura, T. Yoshimura, and Z. Zhang, "Epitaxial and Oriented Relaxor Ferroelectric-PbTiO₃ Films for Memory and Transducer Applications," invited presentation at Toshiba Corporation, Sept. 1, 2000.
9. S. Trolier-McKinstry, V. Bornand, J-H. Park, C. A. Randall, M. Ozgul, K. Takemura, T. Yoshimura, and Z. Zhang, "Epitaxial and Oriented Relaxor Ferroelectric-PbTiO₃ Films for Memory and Transducer Applications," invited presentation at Tokyo Institute of Technology, Sept. 2, 2000.
10. S. Trolier-McKinstry, V. Bornand, J-H. Park, C. A. Randall, M. Ozgul, K. Takemura, T. Yoshimura, and Z. Zhang, "Epitaxial and Oriented Relaxor Ferroelectric-PbTiO₃ Films for Memory and Transducer Applications," seminar at Clemson University, Oct. 6, 2000.
11. W. Cao, "Simulation Modeling of Microwave Devices Using FDTD method", Shandong University, Jinan, China, June 9, 2000.
12. W. Cao, "Recent Progress in the Study of Ferroelectric Domains--Theory, Experiments and simulations", City University of Hong Kong, July 5, 2000.
13. W. Cao, "Design and Fabrication of Medical Ultrasonic Transducers", Chinese University of Hong Kong, July 6, 2000.
14. Cao, W. "Modeling in Materials", Department of Mathematics, Colorado State University, October 10, 2000.
15. W. Cao, "Smart Materials and Structures--The Basics and Applications", Department Physics, Indiana University of Pennsylvania, October 13, 2000.
16. Uchino, K., "Optimal Acoustic Design: The Tuning of the Liberty Bell", Golden Key Club, Yankton, S. Dakota, August 2000.
17. Uchino, K., "Emerging Technologies for Noise and Vibration Control", Komatsu Research Center, Kanagawa, Japan, June 2000.
18. Uchino, K., "Emerging Technologies for Noise and Vibration Control", Tokyo Institute of Technology Precision & Intelligence Lab (Seiken), Yokohama, Japan, June 2000.
19. Uchino, K., "Emerging Technologies for Noise and Vibration Control", Komatsu Industries, Osaka, Japan, July 2000.
20. Uchino, K., "Emerging Technologies for Noise and Vibration Control", Northwestern Polytechnical University, Xian, China, July 2000.

13.0 CONTRIBUTED PAPERS AT NATIONAL AND INTERNATIONAL MEETINGS

1. Chen, Y. H., D. Viehland and K. Uchino "Comparison of the Doping Effect in PMN-PT and PSN-PT Based Ceramics," ONR Workshop on Acoustic Transduction Materials and Devices, University Park, PA, April 11-13 (2000).
2. Chen, Y. H. and K. Uchino, "Development of PMN-PT and PZN-PT Based Ceramics for High-Power Application," 30th ICAT Smart Actuator Symposium, State College, PA, April 20-21 (2000).
3. Chen, Y. H., S. Hirose, D. D. Viehland and K. Uchino "Heat Generation and Properties of PZT under High Level Resonance Driving with Different Polings", 102th Annual Mtg. Amer. Ceram. Soc., St. Louis, April 29 - May 3, D3P-006-00 (2000).

4. Ramakrishnan, P., Y. H. Chen and K. Uchino, "High Power Measuring System for Single Crystals", 102th Annual Mtg. Amer. Ceram. Soc., St. Louis, April 29 - May 3, D3P-007-00 (2000).
5. Du, X. H. and K. Uchino, "Determination of the Complex Elastic and Piezoelectric Coefficients for Piezoelectric Materials" ONR Transducer Material and Transducers Workshop, State College, PA, April 11-13 (2000).
6. Du, X. H. and K. Uchino, "Determination of the Piezoelectric Properties in Perovskite Ferroelectrics", 30th ICAT Smart Actuator Symposium, State Collage, April 20-21 (2000).
7. Uchino, K., J. Zheng and Y. H. Chen, "Heat Generation in Piezoelectrics," ONR Transducer Material and Transducers Workshop, State College, PA, April 11-13 (2000).
8. Zheng, J. and K. Uchino, "Hysteresis in Piezoelectrics", 30th ICAT Smart Actuator Symp., State College, PA, April 20-21 (2000).
9. Laoratanakul, P., B. Koc and K. Uchino, "Disk-type Piezoelectric Transformers," 30th ICAT Smart Actuator Symp., State College, PA, April 20-21 (2000).
10. Dong, S., S. P. Lim, K. H. Lee, L. C. Lim and K. Uchino, "Compact Piezoelectric Motor," 30th ICAT Smart Actuator Symp., State College, PA, April 20-21 (2000).
11. Zheng, J., B. Sugg, and K. Uchino, "Energy Loss in Piezoelectrics", 102th Annual Mtg. Amer. Ceram. Soc, St. Louis, April 29 - May 3, D3P-005-00 (2000).
12. Zhang, J. D., W. J. Hughes, R. J. Meyer Jr., K. Uchino and R. E. Newnham, "Cymbal Array: A Broad Band Sound Projector," 102th Annual Mtg. Amer. Ceram. Soc, St. Louis, April 29 - May 3, D3-005-00 (2000).
13. Belegundu, U. and K. Uchino, "High Power Piezoelectric Characteristics of).91 PZN-0.09PT Single Crystals: Part I," 102th Annual Mtg. Amer. Ceram. Soc, St. Louis, April 29 - May 3, D3-018-00 (2000).
14. Gao, Y. K., B. Koc and K. Uchino, "Electromechanical Properties of Ce and Fe Doped $\text{PbZrO}_3\text{-PbTiO}_3\text{-Pb}(\text{Mn}_{1/3}\text{Sb}_{2/3})\text{O}_3$ Ceramics," 102th Annual Mtg. Amer. Ceram. Soc, St. Louis, April 29 - May 3, D3P-004-00 (2000).
15. Gao, Y. K., B. Koc, K. Uchino and S. Takahashi, " $\text{PbZrO}_3\text{-PbTiO}_3\text{-Pb}(\text{Mn}_{1/3}\text{Sb}_{2/3})\text{O}_3$ Ceramics for Transformer Application," 30th ICAT Smart Actuator Symp., State College, PA, April 20-21 (2000).
16. Gao, Y. K., B. Koc, K. Uchino and S. Takahashi, " $\text{PbZrO}_3\text{-PbTiO}_3\text{-Pb}(\text{Mn}_{1/3}\text{Sb}_{2/3})\text{O}_3$ Ceramics for Transformer Application," ONR Transducer Material and Transducers Workshop, State College, PA, April 11-13 (2000).
17. Kalpat, S. S., A. Akiba, H. Goto and K. Uchino, "Highly Textured PZT and BaTiO_3 Thin Films for MEMS Devices", 102th Annual Mtg. Amer. Ceram. Soc., St. Louis, April 29 - May 3, D3P-008-00 (2000).
18. Koc, B., J. F. Tressler and K. Uchino, "A Miniature Piezoelectric Rotary Motor Using Two Orthogonal Bending Modes of a Hollow Cylinder," 7th Int'l Conf. New Actuators, Bremen, Germany, June 19-21 (2000).
19. Laoratanakul, P., A. Vazquez Carazo and K. Uchino, "Piezoelectric Transformers Operating in the Transverse Extensional Vibration Mode," 55th Annual Forum of PA Ceram. Assoc., University Park, PA, September (2000).
20. Uchino, K., P. Poosanaas and K. Tonooka, "Photostrictive Actuators -New Perspective--," Proc. 3rd Asian Mtg. Ferroelectrics, C3p.105, Hong Kong, Dec. 12-15 (2000).

21. Bernard, "Detailed Design of Actively-Tuned Flexural Piezoceramic Transducers," ONR Transducer Meeting, Baltimore, MD, May 14-16, 2001.
22. Lesieutre, G.A., Koopmann, G.H., Frank, J.B., "Mechanical Diode Based, High-Torque Piezoelectric Rotary Motor," AIAA Adaptive Structures Forum, Seattle, WA, April, 2001.
23. Bernard, J.E., and Lesieutre, G.A., "The Use Of Actively-Tuned Low Frequency Transducers For High Power Linear Chirp Transmission," Acoustical Society of America meeting, November, 2000.
24. Bernard, J.E., and Lesieutre, G.A., "The Design Of Actively-Tuned Flexural Piezoceramic Bar/Disk Transducers," Acoustical Society of America meeting, December, 2000. (ASA Student Paper Award)
25. Bernard, J. and Lesieutre, G.A., "Variable Frequency Flexural Piezoelectric Transducers For High Power Linear Chirp Transmission," 11th ICAST, Nagoya, Japan, October 23-26, 2000.
26. Bernard, J., and G.A. Lesieutre, "Frequency Agile Acoustic Transducers," at the U.S. Navy Workshop on Acoustic Transduction Materials and Devices," State College, PA, April 11-13, 2000.
27. Bernard, J. and G.A. Lesieutre, "Design and Realization of Frequency Agile Piezoceramic Transducers," proceedings of the AIAA/ASME/AHS Adaptive Structures Forum, Atlanta, GA, April 3-6, 2000.
28. Bernard, J., and G.A. Lesieutre, "Design and Realization of Variable Frequency Flexural Piezoceramic Transducers," proceedings of the SPIE Smart Structures and Materials Conference: Smart Structures and Integrated Systems, Newport Beach, CA, March 1-5, 2000.
29. Q. F. Zhou, E. Hong, R. Wolf, and S. Trolier-McKinstry, "Dielectric and Piezoelectric Properties of PZT 52/48 Thick Films with (100) and Random Crystallographic Orientation," MRS Meeting, Boston (2000).
30. R. Wolf, Q. Zhou, P. Moses, S. Trolier-McKinstry, L-P. Wang, R. J. Davis, K. Chandra, K. Deng, W. Shanks, and T. Brooks, "MEMS Accelerometers using PZT films as the active piezoelectric sensing element," ISAF (2000).
31. Z.-Y. Cheng, T. B. Xu, V. Bharti, Q. M. Zhang, T. Ramotowski, R. Ting, Characterization of Electrostrictive P(VDF-TrFE) Copolymers for High Frequency and High-load Applications. SPIE's 7th International meeting on Smart Structures and Materials, March 6, 2000 (CA)
32. Vivek Bharti, Z-Y. Cheng, G. Shanthi, and Q. M. Zhang, Dielectric Response of Relaxor Ferroelectric P(VDF-TrFE) Copolymers. America Phys. Society March Meeting, March 2000 (Minnesota).
33. T. B. Xu, Z.Y. Cheng, Q. M. Zhang, R. Baughman. Fabrication and Characterization of 3-D Periodic Ferroelectric Polymer-Silica Opal Composites and Inverse Opal for Photonic Crystals. America Phys. Society March Meeting, March 2000 (Minnesota).
34. T. B. Xu, Z. Cheng, S. Gross, V. Bharti, T. Mai, and Q. M. Zhang. High Load Capability and Electrostrictive Coupling of Electron Irradiated P(VDF-TrFE) Copolymers. 2000 US Navy Workshop on Acoustic Transduction Materials and Devices. April 11-13, 2000 (Penn State University).

35. V. Bharti, Z. Cheng, and Q. M. Zhang. Relaxor Ferroelectric Behavior and Dielectric Dispersion in P(VDF-TrFE) Copolymers. 2000 US Navy Workshop on Acoustic Transduction Materials and Devices. April 11-13, 2000 (Penn State University).
36. T. Ramotowski, G. Kavanos, A. Amin, K. Gleason, P. Mabboux, Q. M. Zhang, V. Bharti. Spectroscopic and Thermal Characterization of Electron Irradiated P(VDF-TrFE) Copolymers. 2000 US Navy Workshop on Acoustic Transduction Materials and Devices. April 11-13, 2000 (Penn State University).
37. Y. Barad, Y. Lu, Z. Cheng, S. E. Park, and Q. M. Zhang. Electro-optical and Acousto-optical Properties of PZN-PT Single Crystals. 2000 US Navy Workshop on Acoustic Transduction Materials and Devices. April 11-13, 2000 (Penn State University).
38. Y. Bai, V. Bharti, Z. Y. Cheng, H. S. Xu, and Q. M. Zhang. High Dielectric Constant Polymer Ceramic Composites. 2000 US Navy Workshop on Acoustic Transduction Materials and Devices. April 11-13, 2000 (Penn State University).
39. C. Kim, A. Glazounov, Q. M. Zhang, and T. Nuyen. Piezoelectric Rotary Actuator Driven Devices and Their Applications. 2000 US Navy Workshop on Acoustic Transduction Materials and Devices. April 11-13, 2000 (Penn State University).
40. Yu Lu, Y. Barad, Z.-Y. Cheng, S.-E. Park, and Q. M. Zhang. Electro-optical Properties of PZN-PT Single Crystals. CLEO/QELS Conference (May 7-12, San Francisco)
41. Yi Bai and Q. M. Zhang. High Dielectric Constant Polymers and Composites. Passive Components for Power Electronics Workshop. Penn State University (April 27, 2000)
42. Yi Bai, V. Bharti, Z. Y. Cheng, H. Xu, and Q. M. Zhang. High Dielectric Constant Polymer Ceramic Composites. 102nd American Ceramic Society Annual Meeting, May 1, 2000 (St. Louis)
43. Q. M. Zhang. Ferroelectric Polymer Thin Films. Intel Corp, Santa Clara, CA. May 19, 2000.
44. V. Bharti, Z. Y. Cheng, and Q. M. Zhang. Dielectric Relaxation and Weak Polarization Response in Relaxor Ferroelectric P(VDF-TrFE) Copolymer. 12th IEEE International Symp. Appl. Ferro. (Hawaii, Aug. 2000).
45. Y. Bai, V. Bharti, Z. Y. Cheng, H. S. Xu, and Q. M. Zhang. A New Ceramic-Polymer Composite Using High Dielectric Constant Matrix. IEEE 12th International Symp. Appl. Ferro. (Hawaii, Aug. 2000).
46. Z.Y. Cheng, T. B. Xu, V. Bharti, S. Gross, T. Mai, Q. M. Zhang, T. Ramotowski, L. Ewart, and R. Ting. Electrostrictive Effect and Load Capability in Electron Irradiated P(VDF-TrFE) Copolymer. IEEE 12th International Symp. Appl. Ferro. (Hawaii, Aug. 2000).
47. Y. Lu, Y. Barad, Z. Y. Cheng, S. E. Park, and Q. M. Zhang. Elasto-optical and Electro-optical Studies of PZN-PT Single Crystals. IEEE 12th International Symp. Appl. Ferro. (Hawaii, Aug. 2000).
48. Q. M. Zhang. Electromechanical Properties of Modified P(VDF-TrFE) Polymer Systems. DARPA DSRC Workshop on Electrotexiles, Raleigh, NC State, Oct. 5-6, 2000
49. Yu Lu, Z.-Y. Cheng, and Q. M. Zhang. Acousto-optic Properties of PZN-PT Single Crystals. IEEE 2000 International Ultrasonic Symp. (Puerto Rico, Oct. 23-25, 2000).

50. Q. M. Zhang, T. B. Xu, Z.-Y. Cheng, M. Tian, Yu Lu. Electromechanical Coupling Factors of Electrostrictive P(VDF-TrFE) Copolymer. IEEE 2000 International Ultrasonic Symp. (Puerto Rico, Oct. 23-25, 2000).
51. R.Yimnirun, R.J. Meyer, Jr., P.J. Moses, and R.E. Newnham, "Development of a Compact, High Resolution Single Beam Interferometer for Electrostriction Measurements in Low Permittivity Dielectrics," 102nd Annual Meeting of the American Ceramic Society, April, ST. Louis, MO.
52. S. Alkoy, R.J. Meyer, Jr., A.C. Hladky-Hennion, W.J. Hughes, J.K. Cochran, and R.E. Newnham, "Arrays and Piezocomposite Transducers from Hollow Spheres," ISAF' 2000, Hawaii.
53. R.J. Meyer, Jr., S. Alkoy, T. Ritter, J. Cochran, and R.E. Newnham "Very High Frequency Focused Transducers from Hollow Spheres," ISAF'2000, Hawaii.
54. Zhang, J., W.J. Hughes, and R.E. Newnham, "Underwater Characteristics of Cymbal Transducer and Arrays," ONR meeting, Penn State University.
55. S. Alkoy, R.J. Meyer, Jr., A.C. Hladky-Hennion, W.J. Hughes, J.K. Cochran, and R.E. Newnham, "Arrays and Piezocomposite Transducers from Hollow Spheres," ONR Meeting, Penn State University.
56. R.J. Meyer, Jr., R.E. Newnham, S. Alkoy, T. Ritter, and J. Cochran, "High Frequency Pre-Focused Lead Titanate Transducers Made from Hollow Spheres," ONR Meeting, Penn State University.
57. W. Cao, S. Tavener and S. M. Xie, "Simulation of Boundary Condition Influence in a Second-Order Ferroelectric Phase Transition", March Meeting of the American Physical Society, Minneapolis, MN, March 20-24 (2000).
58. Rajeev Ahluwalia and W. Cao, "Simulation of Domain Pattern Formation in Ferroelectrics in the Presence of Dipolar Impurities", March Meeting of the American Physical Society, Minneapolis, MN, March 20-24 (2000).
59. Jianghua Yin, Bei Jiang, Seung-Eek Park and Wenwu Cao, "Physical Properties of Multidomain PZN-PT Single Crystals", March Meeting of the American Physical Society, Minneapolis, MN, March 20-24 (2000).
60. Richard Hatt and W. Cao, "A Continuum Theoretical Model for Antiferroelectric Phase Transitions", March Meeting of the American Physical Society, Minneapolis, MN, March 20-24 (2000).
61. Haifeng Wang and W. Cao, "Dispersion of Velocity and Attenuation in Ferroelectric Ceramics", March Meeting of the American Physical Society, Minneapolis, MN, March 20-24 (2000).
62. Wenhua Jiang and W. Cao, "Elastic nonlinearity of Lead Zirconate-Titanate (PZT) Ceramics", March Meeting of the American Physical Society, Minneapolis, MN, March 20-24 (2000).
63. Richard Hatt and W. Cao, "Derivation of the free Energy Density Describing Antiferroelectricity from a Microscopic Viewpoint" 2000 U.S. Navy Workshop on Acoustic Transduction Materials and Devices, The Pennsylvania State University, April 11-13 (2000).
64. Wenhua Jiang and W. Cao, "Characterization of Nonlinear Properties of Lead Zirconate-Titanate Ceramics", 2000 U.S. Navy Workshop on Acoustic Transduction Materials and Devices, The Pennsylvania State University, April 11-13 (2000).

65. H. Wang, W. Jiang, W. Cao and K. K. Shung, "Dispersion of Velocity and Attenuation in PZT Ceramics", 2000 U.S. Navy Workshop on Acoustic Transduction Materials and Devices, The Pennsylvania State University, April 11-13 (2000).
66. Jianhua Yin and Wenwu Cao, "Observation and Analysis of Domain Configurations in Domain Engineered PZN-PT Single Crystals", The Six International Symposium on Ferroic Domains and Mesoscopic Structures (ISFD-6), Nanjing, China, May 29-June 2, 2000.
67. R. A. Hatt and W. Cao, " Microscopic Origin of Two-sublattice Model for Antiferroelectric State", The Six International Symposium on Ferroic Domains and Mesoscopic Structures (ISFD-6), Nanjing, China, May 29-June 2, 2000.
68. Rajeev Ahluwalia and Wenwu Cao, "Effect of Defect Induced Nucleation and Growth on Switching behavior in Ferroelectrics", The Six International Symposium on Ferroic Domains and Mesoscopic Structures (ISFD-6), Nanjing, China, May 29-June 2, 2000.
69. Jiri Erhart, Wenwu Cao, Jan Fousek, "The Structure of S-Walls in $m\bar{3}m \rightarrow mmm$ ferroelectrics", The Six International Symposium on Ferroic Domains and Mesoscopic Structures (ISFD-6), Nanjing, China, May 29-June 2, 2000.
70. Wenhua Jiang and Wenwu Cao, "Ultrasonic nonlinearity of regular and relaxor ferroelectric ceramics", The 8th International Workshop on Modern Acoustics, Nanjing, China, Oct. 28-31, 2000.
71. Wenhua Jiang, Gonghuan Du and Wenwu Cao, "Second harmonic generation of transverse waves in electro-elastic crystals". The 8th International Workshop on Modern Acoustics, Nanjing, China, Oct. 28-31, 2000.
72. Haifeng Wang and Wenwu Cao, "Properties of Passive Transducer Materials", Ultrasonic Transducer Engineering Conference, State College, PA, August 2-4, 2000.
73. Rajeev Ahluwalia and Wenwu Cao, "Influence of Surface Induced Nucleation on Switching Behavior in Ferroelectrics", Materials Research Society 2000 Fall Meeting, Boston, MA, Nov. 27-Dec. 1 (2000).
74. Ruyan Guo, "Effect of Electric Boundary Conditions on Thermal Strain Behavior of PZN-PT Single Crystals", *presented at the ONR 2000 Transducer Materials and Transducers Workshop*, State College, PA, April 11-13, 2000.
75. E.F. Alberta and A.S. Bhalla, "The Effect of Pressure and Electric Field on the Piezoelectric Properties of $\text{Pb}[(\text{Sc}_{1/2}\text{Nb}_{1/2})_{0.58}\text{Ti}_{0.42}]\text{O}_3$ Ceramics," *presented at the 2000 US Navy Workshop on Acoustic Transduction Materials and Devices*, University Park, PA, April 11-13 2000.
76. E.F. Alberta, R. Guo, and A.S. Bhalla, "Low-Temperature Property Investigation of the Lead Indium-Niobate:Lead Nickel-Niobate Solid Solution," *presented at the 102nd Annual Meeting of The American Ceramic Society*, St. Louis, MO, April 30-May 5, 2000.
77. E.F. Alberta and A.S. Bhalla, "Dielectric and Piezoelectric Properties of the $\text{Pb}(\text{In}_{1/2}\text{Nb}_{1/2})\text{O}_3$ - PbZrO_3 Solid Solution System," *presented at the 12th IEEE international Symposium on the Applications of Ferroelectrics*, Honolulu, Hawaii, July 30- August 2, 2000.
78. Ruyan Guo, "Inside the Morphotropic Phase Boundary in PZT Ceramics", *presented at the Electronics Division Meeting, ACerS*, Clemson, South Carolina, Oct. 8-11, 2000.

79. E.F. Alberta and A.S. Bhalla, "Dielectric and Piezoelectric Properties of the $\text{Pb}(\text{In}_{1/2}\text{Nb}_{1/2})\text{O}_3\text{-PbZrO}_3$ Solid Solution System," *presented at the 2000 Amer. Cer. Soc. Electronics Division Meeting*, Clemson, SC, October 8-11, 2000.
80. E.F. Alberta and A.S. Bhalla, "Piezoelectric and Dielectric Properties of the Lead Indium-Niobate:Lead Titanate Solid Solution," *presented at the 2000 Amer. Cer. Soc. Electronics Division Meeting*, Clemson, SC, October 8-11, 2000.
81. E.F. Alberta and A.S. Bhalla, "Piezoelectric and Dielectric Properties of The Lead Indium-Niobate : Lead Titanate Solid Solution," *presented at the 2001 Amer. Cer. Soc. Annual Meeting*, Ind. IN, April 22-25, 2001

14.0 BOOKS AND SECTIONS OF BOOKS

1. Uchino, K., *Ferroelectric Devices*, Marcel Dekker, NY (2000).
2. Kelly, A., R. Davidson and K. Uchino, "Smart Composite Materials Systems," Chap.5.20, *Comprehensive Composite Materials*, Elsevier Science, Oxford, UK (2000).
3. Tressler, J. and K. Uchino, "Piezoelectric Composite Sensors," Chap.5.22, *Comprehensive Composite Materials*, Elsevier Science, Oxford, UK (2000).
4. Uchino, K., "Piezoelectro Composites," Chap.5.24, *Comprehensive Composite Materials*, Elsevier Science, Oxford, UK (2000).
5. Uchino, K., "Piezoelectric Actuators," Chap.6.35, *Comprehensive Composite Materials*, Elsevier Science, Oxford, UK (2000).
6. Koc, B. and K. Uchino, "Piezoelectric Ultrasonic Motors," Chap.6.34, *Comprehensive Composite Materials*, Elsevier Science, Oxford, UK (2000).
7. Uchino, K., *Encyclopedia of Vibration*, Partial Charge "Electrostrictive Materials", Academic Press, London (2000). [in press]
8. Uchino, K., and Y. Ito, *Encyclopedia Smart Materials*, J. Harvey, Edit., Partial Charge "Smart Ceramics: Transducers, Sensors and Actuators", John Wiley & Sons, New York (2000). [in press]
9. Uchino, K., "Designing with Piezoelectric Devices," Partial Contribution to Designing with Engineering Ceramics, Amer. Ceram. Soc., PA (2001). [in press]
10. PVDF and Its Copolymer with TrFE, Q. M. Zhang, V. Bharti, and G. Kavarnos, in *The Encyclopedia of Smart Materials* (John Wiley & Sons, Inc. 2001).
11. *Electric Polymers*, Q. M. Zhang and J. Scheinbeim, in *Electroactive Polymer Actuators as Artificial Muscles* (Ed. Y. Bar-Cohen, SPIE Optical Engineering Press, WA, 2001).
12. G. H. Koopmann, John B. Fahnline. (Published in 2000) *Acoustic Source Methods*. McGraw-Hill Yearbook of Science and Technology, 2001, pgs. 3-6.
13. Winnie Wong-Ng, T. Holesinger, G. Riley, Ruyan Guo, "Perovskite oxides for electronic, energy conversion, and energy efficiency applications", *Ceramic Transactions, AcerS, Westerville, OH, 104*, pp.284, (2000).(Editors)
14. Rustum Roy, R. Guo and A.S. Bhalla, "Perovskite - Lessons from its History and Its Crystal Chemistry," *Ceramic Transactions, ACerS, Westerville, OH, 104*, 3-39, (2000). (Invited review article)
15. W. Cao, "Phenomenological Theory of Ferroelectrics", *Encyclopedia of Materials*, (2001)

15.0 INVENTION DISCLOSURES

1. Robert E. Newnham, Joseph K. Cochran Jr. and Sedat Alkoy, "Hollow sphere transducers", PSU Inv. Disc. No. 98-1929, *U.S. Patent* No. 6,215,231, 10 April 2001.
2. Jindong Zhang and R. E. Newnham, "A Process for Fabricating Hollow Electroactive Devices", PSU invention disclosure 2000-2324, *U.S. Patent Provisional Application* No. 60/221,859, 7 July 2000.
3. Jindong Zhang, W.J. Hughes, R.J. Meyer, Jr., and R.E. Newnham, "A Miniaturized Directional Flextensional Transducer", PSU invention disclosure 2000-2325.
4. J.A. McConnell, G. C. Lauchle, T. B. Gabrielson. Two-Geophone Underwater Acoustic Intensity Probe. Disclosed: Sept. 21, 1995; patent granted January 9, 2001; U.S. Patent # 6,172,940 B1.
5. D. C. Swanson, G. C. Lauchle, R. S. McGuinn. Adaptive Flow Noise Cancellation Device for Acoustic Sensors. Disclosed: April 5, 1996; **patent application filed** April 16, 1998.
6. G. C. Lauchle, T. B. Gabrielson, J. A. McConnell. Underwater Acoustic Vector Sensor. Disclosed August 10, 1998 to Penn State, College of Engineering (provisional filed in April 2000; turned over to U. S. Navy in March 2001).
7. G. C. Lauchle, M. W. McBride, S. Park. Porous Forebody for Sensor Self Noise Reduction. Disclosed July 5, 2000, ARL Penn State Invention Disclosure #714.

GENERAL SUMMARY PAPERS

APPENDIX 1

Vibration Encyclopedia

Academic Press

ELECTROSTRICTIVE MATERIALS

Kenji Uchino, Ph.D.

Professor, Electrical Engineering

Director, International Center for Actuators and Transducers

134 Materials Research Laboratory

The Pennsylvania State University

University Park, PA 16802

Phone: 814-863-8035

Fax: 814-865-2326

E-mail: kenjiuchino@psu.edu

Keywords

electrostriction, hysteresis-free, secondary effect, anharmonicity, electromechanical coupling, complex perovskite, relaxor ferroelectrics, paraelectric phase, microdomain, lead magnesium niobate, precision positioning, converse piezoelectric effect, crystal symmetry

1. INTRODUCTION

The word "electrostriction" is used in a general sense to describe electric-field induced strain, and hence frequently also implies the "converse piezoelectric effect." However, in solid state theory, the converse piezoelectric effect is defined as a primary electromechanical coupling effect, i. e. the strain is proportional to the applied electric field, while the electrostriction is a secondary coupling in which the strain is proportional to the square of the electric field. Thus, strictly speaking, they should be distinguished. However, the piezoelectricity of a ferroelectric which has a centro-symmetric prototype (high temperature) phase is considered to originate from the electrostrictive interaction, and hence the two effects are related.

In this section, first the origin of piezoelectricity and electrostriction are explained microscopically and phenomenologically. Then, electrostrictive materials are described in details, and finally their applications are introduced.

2. MICROSCOPIC ORIGINS OF ELECTROSTRICTION

Solids, especially ceramics (inorganic materials), are relatively hard mechanically, but still expand or contract depending on the change of the state parameters. The strain (defined as the displacement ΔL / initial length L) caused by temperature change and stress are known as thermal expansion and elastic deformation. In insulating materials, the application of an electric field can also cause deformation. This is called electric field induced strain.

Why a strain is induced by an electric field is explained herewith. For simplicity let us consider an ionic crystal such as NaCl. Figures 1(a) and 1(b) show a one-dimensional

rigid-ion spring model of the crystal lattice. The springs represent equivalently the cohesive force resulting from the electrostatic Coulomb energy and the quantum mechanical repulsive energy. Figure 1(b) shows the centrosymmetric case, whereas Fig. 1(a) shows the more general non-centrosymmetric case. In (b), the springs joining the ions are all the same, whereas in (a), the springs joining the ions are different for the longer or shorter ionic distance, in other words, hard and soft springs existing alternately are important. Next consider the state of the crystal lattice (a) under an applied electric field. The cations are drawn in the direction of the electric field and the anions in the opposite direction, leading to the relative change in the inter-ionic distance. Depending on the direction of the electric field, the soft spring expands or contracts more than the contraction or expansion of the hard spring, causing a strain x (i. e. unit cell length change) in proportion to the electric field E . This is the converse piezoelectric effect. When expressed as

$$x = d E, \quad (1)$$

the proportionality constant d is called the piezoelectric constant.

On the other hand, in Fig. 1(b), the amounts of extension and contraction of the spring are nearly the same, and the distance between the two cations (i. e. lattice parameter) remains almost the same, hence, there is no strain. However, more precisely, ions are not connected by such idealized springs (those are called harmonic springs, in which (force F) = (spring constant k) \times (displacement Δ) holds). In most cases, the springs possess anharmonicity ($F = k_1\Delta - k_2\Delta^2$), i. e. they are somewhat easy to extend, but hard to contract. Such subtle differences in the displacement causes a change in the lattice parameter, producing a strain which is independent of the direction of the applied electric

field, and hence is an even-function of the electric field. This is called the electrostrictive effect, and can be expressed as

$$x = M E^2, \quad (2)$$

where M is the electrostrictive constant.

Fig. 1

3. PHENOMENOLOGY OF ELECTROSTRICTION

3.1 Devonshire Theory

In a ferroelectric whose prototype phase (high temperature paraelectric phase) is centrosymmetric and non-piezoelectric, the piezoelectric coupling term PX is omitted and only the electrostrictive coupling term P^2X is introduced into the phenomenology (P and X are the spontaneous polarization and stress). This is almost accepted for discussing practical electrostrictive materials with a perovskite structure. The theories for electrostriction in ferroelectrics were formulated in the 1950's by Devonshire and Kay. Let us assume that the elastic Gibbs energy should be expanded in a one-dimensional form:

$$G_1(P, X, T) = (1/2)\alpha P^2 + (1/4)\beta P^4 + (1/6)\gamma P^6 \\ - (1/2)s X^2 - Q P^2 X, \quad (3)$$

$$\alpha = (T - T_0)/\epsilon_0 C, \quad (4)$$

where P , X , T are polarization, stress and temperature, respectively, and s and Q are called the elastic compliance and the electrostrictive coefficient. This leads to Eqs. (5) and (6) for the electric field E and strain x :

$$E = (G_1/P) = \alpha P + \beta P^3 + \gamma P^5 - 2Q P X \quad (5)$$

$$x = -(G_1/X) = sX + QP^2 \quad (6)$$

3.1.1 Case I: $X = 0$

When an external is zero, the following equations are derived:

$$E = \alpha P + \beta P^3 + \gamma P^5 \quad (7)$$

$$x = QP^2 \quad (8)$$

$$1/\epsilon_0 \epsilon = \alpha + 3\beta P^2 + 5\gamma P^4 \quad (9)$$

If the external electric field is equal to zero ($E = 0$), two different states are derived;

$$P = 0 \text{ and } P^2 = (\beta^2 - 4\alpha\gamma - \beta)/2\gamma.$$

(i) Paraelectric phase: $P_S = 0$ or $P = \epsilon_0 \epsilon E$ (under small E)

$$\text{Permittivity: } \epsilon = C/(T - T_0) \text{ (Curie-Weiss law)} \quad (10)$$

$$\text{Electrostriction: } x = Q \epsilon_0^2 \epsilon^2 E^2 \quad (11)$$

Therefore, the previously mentioned electrostrictive coefficient M in Eq. (2) is related to the electrostrictive Q coefficient through

$$M = Q \epsilon_0^2 \epsilon^2 \quad (12)$$

Note that the electrostrictive M coefficient has a large temperature dependence like $\propto 1/(T - T_0)^2$, supposing that Q is almost constant.

(ii) Ferroelectric phase: $P_S^2 = (\beta^2 - 4\alpha\gamma - \beta)/2\gamma$ or $P = P_S + \epsilon_0 \epsilon E$ (under small E)

$$x = Q(P_S + \epsilon_0 \epsilon E)^2 = QP_S^2 + 2 \epsilon_0 \epsilon QP_S E + Q \epsilon_0^2 \epsilon^2 E^2 \quad (13)$$

$$\text{Spontaneous strain: } x_S = QP_S^2 \quad (14)$$

$$\text{Piezoelectric constant: } d = 2 \epsilon_0 \epsilon QP_S \quad (15)$$

Thus we can understand that piezoelectricity in a perovskite crystal is equivalent to the electrostrictive phenomenon biased by the spontaneous polarization.

3.1.2 Case II: $X \neq 0$

When a hydrostatic pressure p ($X = -p$) is applied, the inverse permittivity is changed in proportion to p :

$$\begin{aligned} 1/\epsilon_0 \epsilon &= \alpha + 3 \beta P^2 + 5 \gamma P^4 + 2Qp && \text{(Ferroelectric state)} \\ \alpha + 2Qp &= (T - T_0 + 2Q\epsilon_0 C_p)/(\epsilon_0 C) && \text{(Paraelectric state)} \end{aligned} \quad (16)$$

Therefore, the pressure dependence of the Curie-Weiss temperature T_0 or the transition temperature T_C is derived as follows:

$$(\partial T_0 / \partial p) = (\partial T_C / \partial p) = -2Q\epsilon_0 C \quad (17)$$

In general, the ferroelectric Curie temperature is decreased with increasing hydrostatic pressure (i. e. $Q_h > 0$).

3.2 Converse Effects of Electrostriction

So far we have discussed the electric field induced strains, i. e. piezoelectric strain (converse piezoelectric effect, $x = d E$) and electrostriction (electrostrictive effect, $x = M E^2$). Let us consider here the converse effect, i. e. the response to the external stress, which is applicable to sensors. The direct piezoelectric effect is the "increase of the spontaneous polarization by an external stress," and expressed as

$$\Delta P = d X. \quad (18)$$

On the contrary, since the electrostrictive material does not have the spontaneous polarization, it does not exhibit any charge under stress, but change the permittivity (see Eq. (16)):

$$\Delta(1/\epsilon_0 \epsilon) = 2QX \quad (19)$$

This is the converse electrostrictive effect.

3.3 Temperature Dependence of Electrostrictive Coefficient

Several expressions for the electrostrictive coefficient Q have been given so far. From the data obtained by independent experimental methods such as

- 1) electric-field induced strain in the paraelectric phase,
- 2) spontaneous polarization and spontaneous strain (x-ray diffraction) in the ferroelectric phase,
- 3) d constants from the field induced strain in the ferroelectric phase or from the piezoelectric resonance,
- 4) pressure dependence of permittivity in the paraelectric phase,

nearly equal values of Q were obtained. Figure 2 shows the temperature dependence of the electrostrictive coefficients Q_{33} and Q_{31} of the complex perovskite $\text{Pb}(\text{Mg}_{1/3}\text{Nb}_{2/3})\text{O}_3$, whose Curie temperature is near 0°C . It is seen that there is no significant anomaly in the electrostrictive coefficient Q through the temperature range from a paraelectric to a ferroelectric phase, in which the piezoelectricity appears. Q is almost temperature independent.

Fig. 2

4. ELECTROSTRICTION IN OXIDE PEROVSKITES

4.1 Perovskites and Complex Perovskites

Among the practical piezoelectric/electrostrictive materials, many have the perovskite type crystal structure ABO_3 . This is because many such materials undergo a phase transition on cooling from a high-symmetry high temperature phase (cubic paraelectric phase) to a non-centrosymmetric ferroelectric phase. Materials with a high ferroelectric transition temperature (Curie temperature) show piezoelectricity at room temperature, whereas those with a transition temperature near or below room temperature exhibit the electrostrictive

effect. For the latter, at a temperature right above the Curie temperature, the electrostriction is extraordinarily large because of the large anharmonicity of the ionic potential. Besides, simple compounds such as barium titanate (BaTiO_3) and lead zirconate (PbZrO_3), solid solutions such as $\text{A}(\text{B},\text{B}')\text{O}_3$, and complex perovskites such as $\text{A}^{2+}(\text{B}^{3+}_{1/2}\text{B}'^{5+}_{1/2})\text{O}_3$ and $\text{A}^{2+}(\text{B}^{2+}_{1/3}\text{B}'^{5+}_{2/3})\text{O}_3$ can be easily formed; such flexibility is important in materials design. Figure 3 shows the crystal structures of the above-mentioned complex perovskites with B-site ordering. When B and B' ions are randomly distributed the structure becomes a simple perovskite.

Fig. 3

4.2 Electrostrictive Effect in Simple Perovskites

Yamada has summarized the electromechanical coupling constants of not only perovskite type oxides but also tungsten bronze and LiNbO_3 types, which contain oxygen octahedra. Following the DiDomenico-Wemple treatment for the electrooptic effect, by expressing the electrostrictive tensor Q_{ijkl} of LiNbO_3 with a trigonal symmetry $3m$ in a coordinate system based on the 4-fold axis of the oxygen octahedron, and making a correction for the packing density ξ by

$$Q^{\text{P}}_{ijkl} = \xi^2 Q_{ijkl}, \quad (20)$$

Yamada obtained the electrostrictive coefficient Q^{P} normalized to a perovskite unit cell. It could be concluded that the electrostrictive coefficients Q^{P} 's of the simple perovskite type oxides with one kind of B ion have nearly equal values. The average values are:

$$\begin{aligned}
Q_{11}^P &= 0.10 \text{ m}^4\text{C}^{-2} \\
Q_{12}^P &= -0.034 \text{ m}^4\text{C}^{-2} \\
Q_{44}^P &= 0.029 \text{ m}^4\text{C}^{-2}
\end{aligned}
\tag{21}$$

4.3 Electrostrictive Effect in Complex Perovskites

Uchino et al. extended these investigations to complex perovskite type oxides to obtain the electrostrictive coefficient Q_h and Curie-Weiss constant C . The results are summarized in Table 1. It is important to note that the magnitude of the electrostrictive coefficient does not depend on the polar state whether it is ferroelectric, antiferroelectric or paraelectric, but strongly depends on the crystal structure such as whether the two kinds of B and B' ions are randomly distributed in the octahedron or ordered like B - B' - B - B' (1:1 ordering). The electrostrictive coefficient Q increases with increasing degree of cation order and follows the sequence disordered, partially ordered, simple, and finally ordered type perovskites. For the polar materials, their Curie-Weiss constants are also listed in Table 1, showing a completely opposite trend to the Q_h values. It was consequently found that the invariant for the complex perovskite type oxides is not Q itself, but the product of the electrostrictive coefficient and the Curie-Weiss constant (Uchino's constant):

$$Q_h C = 3.1 (\pm 0.4) \times 10^3 \text{ m}^4\text{C}^{-2}\text{K} \tag{22}$$

Table 1

This "QC constant rule" can be understood intuitively, if we accept the assumption that the material whose dielectric constant changes easily with pressure, also exhibits a large change

of the dielectric constant with temperature, i. e. the proportionality between the following two definitions:

$$Q_h = [(1/\epsilon) / p] / 2 \epsilon_0, \quad (23)$$

$$1/C = [(1/\epsilon) / T]. \quad (24)$$

Another intuitive crystallographic "rattling ion" model, has also been proposed. Figures 4(a) and 4(b) illustrate two models of $A(B_{I1/2}B_{II1/2})O_3$ perovskite, one being ordered and the other disordered. If the rigid ion model is assumed, in the disordered lattice, the larger B_I ions locally prop open the lattice, and there is some "rattling" space around the smaller B_{II} ion. On the contrary, in the ordered lattice, the larger neighboring ions eliminate the excess space around the B_{II} ion, and the structure becomes close-packed. The close packing in an ordered arrangement as shown in Fig. 4(a) has been confirmed by Amin et al. in $0.9Pb(Mg_{1/2}W_{1/2})O_3-0.1Pb(Mg_{1/3}Nb_{2/3})O_3$.

When an electric field is applied to the disordered perovskite, the B_{II} ions with a large "rattling space" can shift easily without distorting the oxygen octahedron. Thus, large polarizations per unit electric field, in other words, large dielectric constants, Curie-Weiss constants can be expected (recall that $\epsilon = C/(T - T_0)$). Strain per unit polarization, i. e. electrostrictive Q coefficients are also expected to be small. In the case of the ordered arrangement, neither B_I nor B_{II} ions can shift without distorting the oxygen octahedron. Hence, small polarizations, dielectric constants and Curie-Weiss constants, and large electrostrictive Q coefficients can be expected.

Fig. 4

Here, we summarize the empirical rules for the electrostrictive effect of perovskite-type oxides.

1. The value of the electrostrictive coefficient Q (defined as $x = Q P^2$) does not depend on whether the material is ferroelectric, antiferroelectric or non-polar, but is affected greatly by the degree of ordering of the cation arrangement. The Q value increases in the sequence from disordered, partially ordered, then simple, and finally to ordered perovskite crystals.
2. In perovskite solid solutions with a disordered cation arrangement, the electrostrictive coefficient Q decreases with increasing phase transition diffuseness, or with increasing dielectric relaxation.
3. The product of the electrostrictive coefficient Q and the Curie-Weiss constant C is about the same for all perovskite crystals ($Q_h \cdot C = 3.1 \times 10^3 \text{ m}^4 \text{C}^{-2} \text{K}$).
4. The electrostrictive coefficient Q is nearly proportional to the square of the thermal expansion coefficient α .

These empirical rules lead to the following important result. Since the figure of merit of electrostriction under a certain electric field is given by $Q \epsilon^2$ (ϵ : dielectric constant) or $Q C^2$ (excluding the temperature dependence), and the product QC is constant, it is more advantageous to use the disordered perovskite ferroelectrics (relaxor ferroelectrics) which have a large Curie-Weiss constant C and hence a small electrostrictive coefficient Q than the normal ferroelectrics ($\text{Pb}(\text{Zr},\text{Ti})\text{O}_3$, BaTiO_3 based ceramics etc.).

4.4 Electrostrictive Materials

Electrostrictive materials do not, in principle, exhibit the domain-related problems observed in piezoelectrics. A common practical ceramic system is the $\text{Pb}(\text{Mg}_{1/3}\text{Nb}_{2/3})\text{O}_3$ based compound. So-called relaxor ferroelectrics such as $\text{Pb}(\text{Mg}_{1/3}\text{Nb}_{2/3})\text{O}_3$ and $\text{Pb}(\text{Zn}_{1/3}\text{Nb}_{2/3})\text{O}_3$ have been developed also for very compact chip capacitors. The reasons why these complex perovskites have been investigated intensively for applications are 1) their very high polarization and permittivity, and 2) temperature-insensitive characteristics (i.e. diffuse phase transition) in comparison with the normal perovskite solid solutions.

The phase transition diffuseness in the relaxor ferroelectrics has not been satisfactorily clarified as yet. We introduce here a widely accepted "microscopic composition fluctuation" model applicable even in a macroscopically disordered structure. Considering the Kanczig region (the minimum size region in order to cause a cooperative phenomenon, ferroelectricity) to be in the range of 100 - 1000 Å, the disordered perovskite such as $\text{Pb}(\text{Mg}_{1/3}\text{Nb}_{2/3})\text{O}_3$ reveals a local fluctuation in the distribution of Mg^{2+} and Nb^{5+} ions in the B sites of the perovskite cell. Figure 5 shows a computer simulation of the composition fluctuation in the $\text{A}(\text{B}_{\text{I}1/2}\text{B}_{\text{II}1/2})\text{O}_3$ -type crystal calculated for various degrees of short-range ionic ordering. The fluctuation of the $\text{B}_{\text{I}}/\text{B}_{\text{II}}$ fraction x obeys a Gaussian error distribution, which may cause Curie temperature fluctuation. H. B. Krause reported the existence of short-range ionic ordering in $\text{Pb}(\text{Mg}_{1/3}\text{Nb}_{2/3})\text{O}_3$ by electron microscopy. The high resolution image revealed somewhat ordered (ion-ordered) islands in the range of 20 - 50 Å, each of which might have a slightly different transition temperature.

Fig. 5

Another significant characteristic of these "relaxor" ferroelectrics is dielectric relaxation (frequency dependence of permittivity) from which their name is originated. The temperature dependence of the permittivity in $\text{Pb}(\text{Mg}_{1/3}\text{Nb}_{2/3})\text{O}_3$ is plotted in Fig. 6 for various measuring frequencies. With increasing measuring frequency, the permittivity in the low-temperature (ferroelectric) phase decreases and the peak temperature near 0°C shifts towards higher temperature; this is contrasted with the normal ferroelectrics such as BaTiO_3 where the peak temperature hardly changes with the frequency. The origin of this effect has been partly clarified in $\text{Pb}(\text{Zn}_{1/3}\text{Nb}_{2/3})\text{O}_3$ single crystals. Figures 7(a) and 7(b) show the dielectric constant and loss versus temperature for an unpoled and a poled PZN sample, respectively. The domain configurations are also inserted. The macroscopic domains were not observed in an unpoled sample even at room temperature, only in which state large dielectric relaxation and loss were observed below the Curie temperature range. Once the macrodomains were induced by an external electric field, the dielectric dispersion disappeared and the loss became very small (i. e. dielectric behavior became rather normal!) below 100°C . Therefore, the dielectric relaxation is attributed to the microdomains generated in this material.

Fig. 6

Fig. 7

Thus, the PMN is easily electrically-poled when an electric field is applied around the transition temperature, and depoled completely without any remanent polarization because the domain is separated into micro-domains when the field is removed. This provides extraordinarily large apparent electrostriction, though it is a secondary phenomenon related to the electromechanical coupling ($x = \text{ME}^2$). If the phase transition temperature can be raised near room temperature, superior characteristics can be expected.

Figure 8(a) shows the longitudinal induced strain curve at room temperature in such a designed material 0.9PMN-0.1PbTiO₃. Notice that the magnitude of the electrostriction (10^{-3}) is about the same as that of a piezoelectric PLZT under unipolar drive as in Fig. 8(b). An attractive feature of this material is the near absence of hysteresis.

Other electrostrictive materials include (Pb,Ba)(Zr,Ti)O₃ and the PLZT systems. In order to obtain large (apparent) electrostriction, it is essential to generate ferroelectric microdomains (several 100 Å). It may be necessary to dope ions with a different valence or an ionic radius, or to create vacancies so as to introduce the spatial microscopic inhomogeneity in the composition.

Fig. 8

Here, the characteristics of piezoelectric and electrostrictive ceramics are compared and summarized from a practical viewpoint:

1. Electrostrictive strain is about the same in magnitude as the piezoelectric (unipolar) strain (0.1 %). Moreover, almost no hysteresis is an attractive feature.
2. Piezoelectric materials require an electrical poling process, which leads to a significant aging effect due to the depoling. Electrostrictive materials do not need such pretreatment, but, require a proper DC bias field in some applications because of the non-linear behavior.
3. Compared with piezoelectrics, electrostrictive ceramics do not deteriorate easily under severe operation conditions such as high temperature storage and large mechanical load.

4. Piezoelectrics are superior to electrostrictors, with regard to temperature characteristics.
5. Piezoelectrics have smaller dielectric constants than electrostrictors, and thus show faster response.

5. APPLICATIONS OF ELECTROSTRICTIONS

5.1 Classification of Ceramic Actuators

Piezoelectric and electrostrictive actuators may be classified into two categories, based on the type of driving voltage applied to the device and the nature of the strain induced by the voltage: (1) rigid displacement devices for which the strain is induced unidirectionally along an applied dc field, and (2) resonating displacement devices for which the alternating strain is excited by an ac field at the mechanical resonance frequency (ultrasonic motors). The first category can be further divided into two types: servo displacement transducers (positioners) controlled by a feedback system through a position-detection signal, and pulse-drive motors operated in a simple on/off switching mode, exemplified by dot-matrix printers. Figure 9 shows the classification of ceramic actuators with respect to the drive voltage and induced displacement.

Fig. 9

The AC resonant displacement is not directly proportional to the applied voltage, but is, instead, dependent on adjustment of the drive frequency. Although the positioning accuracy is not as high as that of the rigid displacement devices, very high speed motion due to the high frequency is an attractive feature of the ultrasonic motors. Servo displacement transducers, which use feedback voltage superimposed on the DC bias, are

used as positioners for optical and precision machinery systems. In contrast, a pulse drive motor generates only on / off strains, suitable for the impact elements of dot-matrix or ink-jet printers.

The materials requirements for these classes of devices are somewhat different, and certain compounds will be better suited for particular applications. The ultrasonic motor, for instance, requires a very hard piezoelectric with a high mechanical quality factor Q , in order to minimize heat generation. The servo-displacement transducer suffers most from strain hysteresis and, therefore, a PMN electrostrictor is preferred for this application. Notice that even in a feedback system the hysteresis results in a much lower response speed. The pulse-drive motor requires a low permittivity material aiming at quick response with a limited power supply rather than a small hysteresis, so that soft PZT piezoelectrics are preferred to the high-permittivity PMN for this application.

5.2 Deformable Mirrors

Precise wave front control with as small a number of parameters as possible and compact construction is a common and basic requirement for adaptive optical systems. For example, continuous surface deformable mirrors may be more desirable than segmented mirrors from the viewpoint of precision.

5.2.1 Multimorph Type Deformable Mirror

Sato et al. proposed a multimorph deformable mirror, simply operated by a micro-computer. In the case of a 2-D multimorph deflector, the mirror surface can be deformed by changing the applied voltage distribution and the electrode pattern on each electroactive ceramic layer.

The mirror surface contour is occasionally represented by Zernike aberration polynomials in optics. An arbitrary surface contour modulation $g(x,y)$ can be expanded as follows:

$$g(x,y) = C_r (x^2 + y^2) + C_c^1 x (x^2 + y^2) + C_c^2 y (x^2 + y^2) + \dots \quad (25)$$

Notice that the Zernike polynomials are orthogonal to each other, i. e. can be completely controlled independent of each other. The C_r and C_c terms are called refocusing and coma aberration, respectively. The aberration, up to the second order, can provide a clear image apparently to the human; this is analogous to the eye examination. The optometrist checks the degree of your lens, initially, then the astigmatism is corrected; no further correction will be made for the human glasses.

As examples, let us consider the cases of refocusing and coma aberration. Uniform whole area electrodes can provide a parabolic (or spherical) deformation. In the case of the coma aberration, the pattern obtained is shown in Fig. 10, which consists of only six divisions and has the fixed ratio of supply voltages.

The deflection measurement of the deformable mirror was carried out using the interferometric system with a hologram. The introduction of a hologram is to cancel the initial deformation of the deformable mirror. Typical experimental results are summarized in Fig. 11, where the three experimentally obtained interferograms of refocusing aberration, coma aberration, and a combination of the two are compared with the corresponding ideal ones. Good agreement is seen in each case. These results demonstrate the validity of the superposition of deformations and the appropriateness of the method of

producing the electrode patterns. It was also observed that the deformable mirror responds linearly up to 500 Hz for sinusoidal input voltages.

Figure 12 shows the fringe patterns observed for several applied voltages for the conventional PZT piezoelectric and PMN electrostrictive deformable mirrors. It is worth noting that for a PZT device a distinct hysteresis is observed optically on a cycle with rising and falling electric fields; but no discernible hysteresis is observed for the PMN device.

Fig. 10

Fig. 11

Fig. 12

5.2.2 Hubble Space Telescope

Fanson and Ealey have developed a space qualified active mirror called Articulating Fold Mirror. Three Articulating Fold Mirrors are incorporated into the optical train of the Jet Propulsion Laboratory's Wide Field and Planetary Camera-2, which was installed into the Hubble Space Telescope in 1993. As shown in Fig. 13, each Articulating Fold Mirror utilizes six PMN electrostrictive multilayer actuators to precisely position a mirror in tip and tilt in order to correct the refocusing aberration of the Hubble Telescope's primary mirror.

Fig. 13

Figure 14 shows the images of the core of M100, a spiral galaxy in the Virgo cluster, before and after the correction of the refocusing aberration. Both contrast and limiting magnitude have been greatly improved, restoring Hubble to its originally specified performance.

Fig. 14

5.3 Oil-Pressure Servo Valves

For oil pressure servo systems, an electric-oil pressure combination (electrohydraulic) is necessary in order to obtain large power and quick response. Quicker response has been requested for this electrohydraulic system, and the present target is 1 kHz, which is categorized in an "impossible" range using the conventional actuation. Ikabe et al. simplified the valve structure by using a piezoelectric PZT flapper. However, since pulse width modulation was employed for controlling the device to eliminate PZT hysteresis, the flapper was always vibrated by a carrier wave, and the servo valve exhibited essential problems in high frequency response and in durability. To overcome this problem, Ohuchi et al. utilized an electrostrictive PMN bimorph for the flapper instead of a piezoelectric bimorph.

5.3.1 Construction of Oil-Pressure Servo Valves

Figure 15 is a schematic drawing of the construction of a two-stage four-way valve, the first stage of which is operated by a PMN electrostrictive flapper. The second stage spool is 4 mm in diameter, which is the smallest spool with a nominal flow rate of 6 liter/min.

An electrostrictive material 0.45 PMN - 0.36 PT - 0.19 BZN was utilized because of its large displacement and small hysteresis. A flapper was fabricated using a multimorph structure, in which two PMN thin plates were bonded on each side of a phosphor bronze shim (Fig. 16). The multimorph structure increases the tip displacement, generative force and response speed. The top and bottom electrodes and the metal shim were taken as ground, and a high voltage was applied on the electrode between the two PMN plates. The

tip deflection showed a quadratic curve for the applied voltage because of the electrostriction. Thus, in order to obtain a linear relation, a push-pull driving method was adopted, which is demonstrated in Fig. 17. Notice that the displacement hysteresis in the PMN ceramic is much smaller than in the PZT piezoelectric. The resonance frequency of this flapper in oil was about 2 kHz.

Fig. 15

Fig. 16

Fig. 17

Since the conventional force feedback method has a structure connecting the flapper tip and the spool with a spring, limiting the responsivity, Ohuchi et al. has utilized an electric feedback method. The feedback mechanism using an electric position signal corresponding to the spool position, has various merits such as easy change in feedback gain and availability of speed feedback. A compact differential transformer (50 kHz excitation) was employed to detect the spool position.

5.3.2 Operating Characteristics of the Oil-Pressure Servo Valve

Figure 18 shows a static characteristic of the spool displacement for a reference input. The slight hysteresis and nonlinearity observed in Fig. 17 was completely eliminated in Fig. 18 through the feedback mechanism. Figure 19 shows a dynamic characteristic of the spool displacement. The 0 dB gain was adjusted at 10 Hz. The gain curve showed a slight peak at 1800 Hz and the 90° retardation frequency was about 1200 Hz. The maximum spool displacement at 1 kHz was ± 0.03 mm, which results in the quickest servo valve at present.

Fig. 18

Fig. 19

FURTHER READING

Uchino K (1996) *Piezoelectric Actuators and Ultrasonic Motors*. Kluwer Academic Publishers, MA, USA.

Uchino K (1986) *Electrostrictive Actuators: Materials and Applications*. Ceramic Bull. **65** (4), 674-652.

Uchino K (1993) *Ceramic Actuators: Principles and Applications*. MRS Bull. XVIII (4), 42-48.

TABLE AND FIGURE CAPTIONS

Table 1 Electrostrictive coefficient Q_h and Curie-Weiss constant C for various perovskite crystals.

Fig. 1 Microscopic explanation of the piezoestriction and electrostriction.

Fig. 2 Temperature dependence of the electrostrictive constants Q_{33} and Q_{13} in $\text{Pb}(\text{Mg}_{1/3}\text{Nb}_{2/3})\text{O}_3$.

Fig. 3 Complex perovskite structures with various B ion arrangements: (a) simple, (b) 1:1 ordered and (c) ordered.

Fig. 4 "Ion rattling" crystal model of $\text{A}(\text{B}_\text{I} 1/2 \text{B}_\text{II} 1/2)\text{O}_3$. (a) ordered and (b) disordered arrangement of B_I and B_II .

Fig. 5 Computer simulation of the composition fluctuation in the $\text{A}(\text{B}_\text{I} 1/2 \text{B}_\text{II} 1/2)\text{O}_3$ type calculated for various degree of the ionic ordering (Kanzig region size 4×4).

Fig. 6 Temperature dependence of the permittivity in $\text{Pb}(\text{Mg}_{1/3}\text{Nb}_{2/3})\text{O}_3$ for various frequencies (kHz): (1) 0.4, (2) 1, (3) 45, (4) 450, (5) 1500, (6) 4500.

Fig. 7 Dielectric constant vs. temperature for a depoled (a) and a poled $\text{Pb}(\text{Zn}_{1/3}\text{Nb}_{2/3})\text{O}_3$ single crystal (b) measured along the $\langle 111 \rangle$ axis.

Fig. 8 Field induced strain curve in an electrostrictor $0.9 \text{ Pb}(\text{Mg}_{1/3}\text{Nb}_{2/3})\text{O}_3 - 0.1 \text{ PbTiO}_3$ (a) and in a piezoelectric PLZT 7/62/38 (b) at room temperature.

Fig. 9 Classification of piezoelectric/electrostrictive actuators.

Fig. 10 2D multimorph deformable mirror with refocussing and coma aberration functions.

Fig. 11 Interferograms showing deformation by the multilayer deformable mirror.

Fig. 12 Comparison of the function between the PZT and PMN deformable mirrors.

Fig. 13 Articulating fold mirror using PMN actuators.

Fig. 14 M100 galaxy comparison. (a) Prior to activation, and (b) after activation of the PMN.

Fig. 15 Construction of the oil pressure servo valve.

Fig. 16 Multimorph electrostrictive falpper.

Fig. 17 Push-pull drive characteristics of the electrostrictive flapper.

Fig. 18 Static characteristics of the servo valve.

Fig. 19 Normalized frequency characteristics of the serve valve.

	Ordering	Material	Q_h ($\times 10^{-2} \text{ m}^4 \text{ C}^{-2}$)	C ($\times 10^6 \text{ K}$)	$Q_h C$ ($\times 10^3 \text{ m}^4 \text{ C}^{-2} \text{ K}$)	Reference
Ferroelectric	Disorder	Pb ($\text{Mg}_{1/2} \text{Nb}_{2/3}$) O_3	0.60	4.7	2.8	Uchino (1980a) Nomura (1979a)
		Pb ($\text{Zn}_{1/3} \text{Nb}_{2/3}$) O_3	0.66	4.7	3.1	Nomura (1979b) Kuwata (1979)
	Partial order	Pb ($\text{Sc}_{1/2} \text{Ta}_{1/2}$) O_3	0.83	3.5	2.9	Setter (1980)
	Simple	BaTiO ₃	2.0	1.5	3.0	Yamada (1972) Johnson (1965)
		PbTiO ₃	2.2	1.7	3.7	Gavrilyachenko (1970) Fesenko (1970)
		SrTiO ₃	4.7	0.77	3.6	Samara (1966) Bell (1963)
		KTiO ₃	5.2	0.5	2.6	Uwe (1975) Uwe (1973)
	Partial order	Pb ($\text{Fe}_{2/3} \text{U}_{1/3}$) O_3	--	2.3	--	Uchino (1977)
	Simple	PbZrO ₃	2.0	1.6	3.2	Uchino (1980b) Samara (1970)
	Order	Pb ($\text{Ca}_{1/2} \text{W}_{1/2}$) O_3	--	1.2	--	Bokov (1965)
Antiferroelectric		Pb ($\text{Mg}_{1/2} \text{W}_{1/2}$) O_3	6.2	0.42	2.6	Uchino (1980b) Nomura (1979a)
	Disorder	($\text{K}_{3/4} \text{Bi}_{1/4}$)($\text{Zn}_{1/6} \text{Nb}_{5/6}$) O_3	0.55 ~ 1.15	--	--	Uchino (1980c)
Non polar	Simple	BaZrO ₃	2.3	--	--	Uchino (1980c)

Table 1 K. Uchino

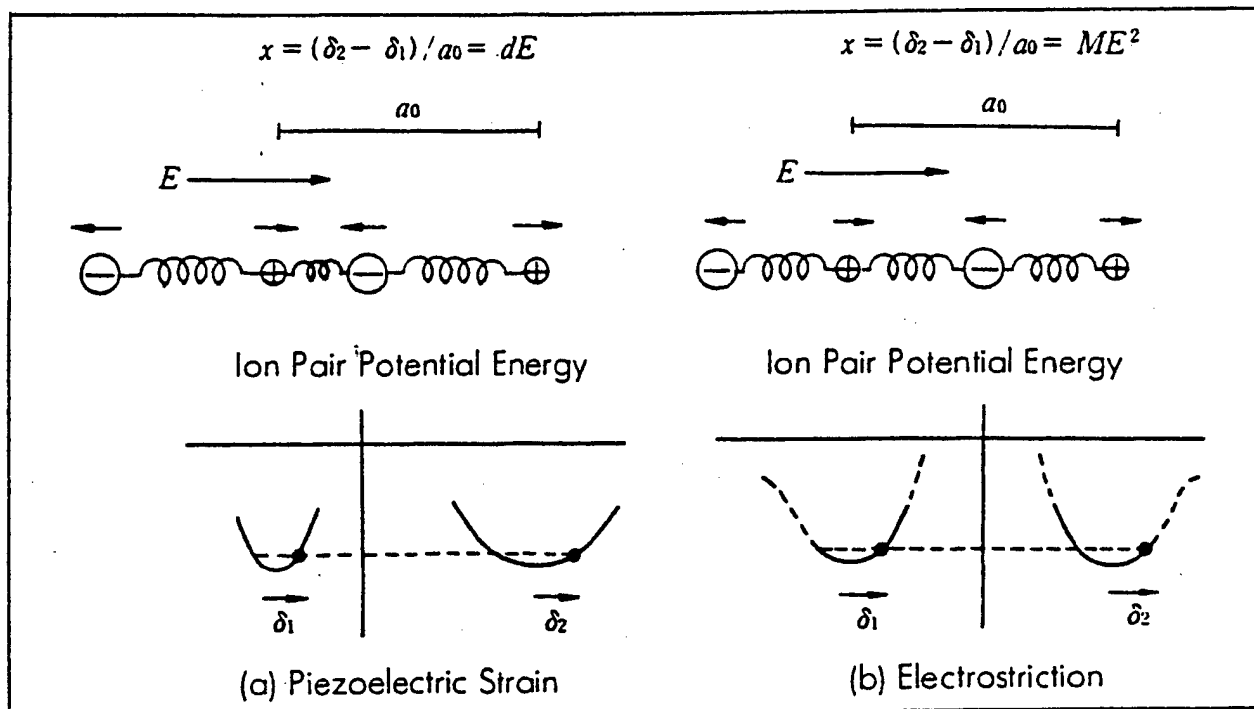


Fig 1 K. Uchino

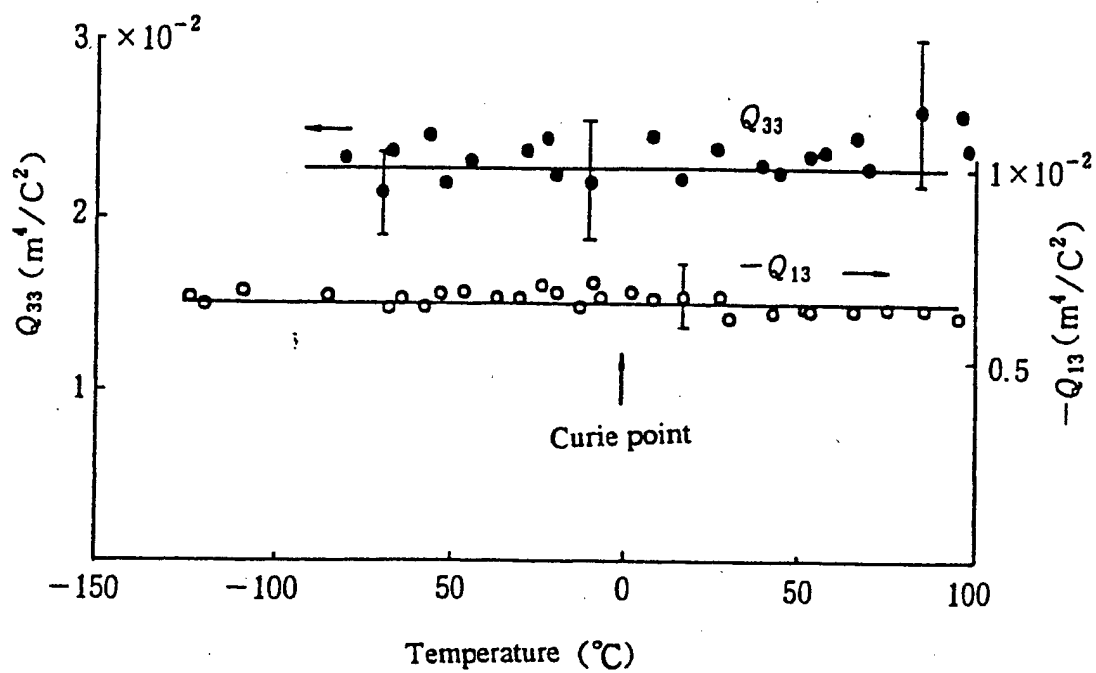


Fig 2 K. Uchino

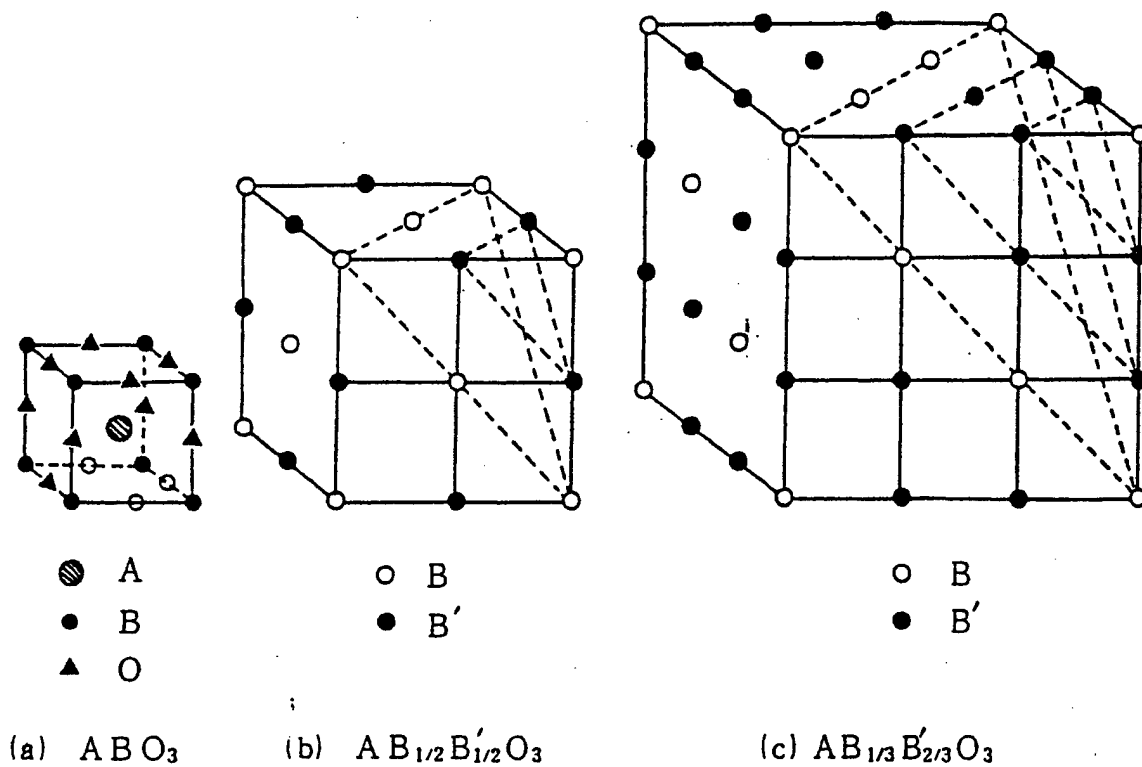


Fig 3 K. Uchino

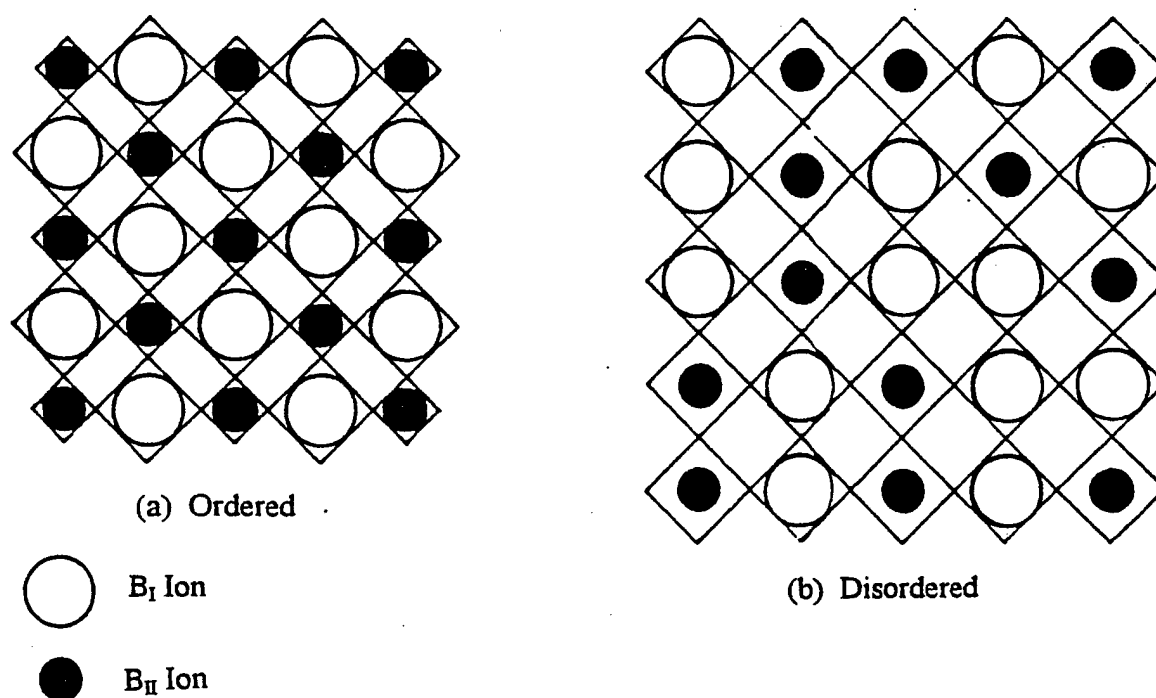


Fig 4 K. Uchino

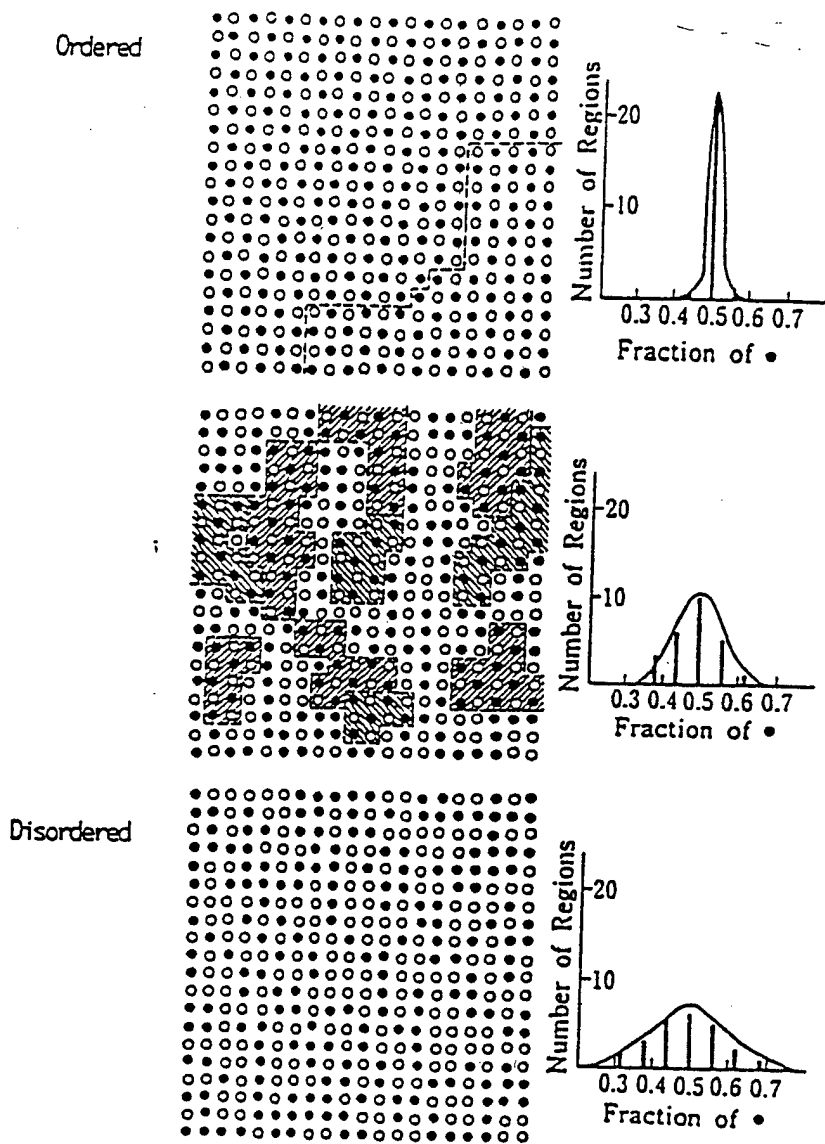


Fig 5 K. Uchino

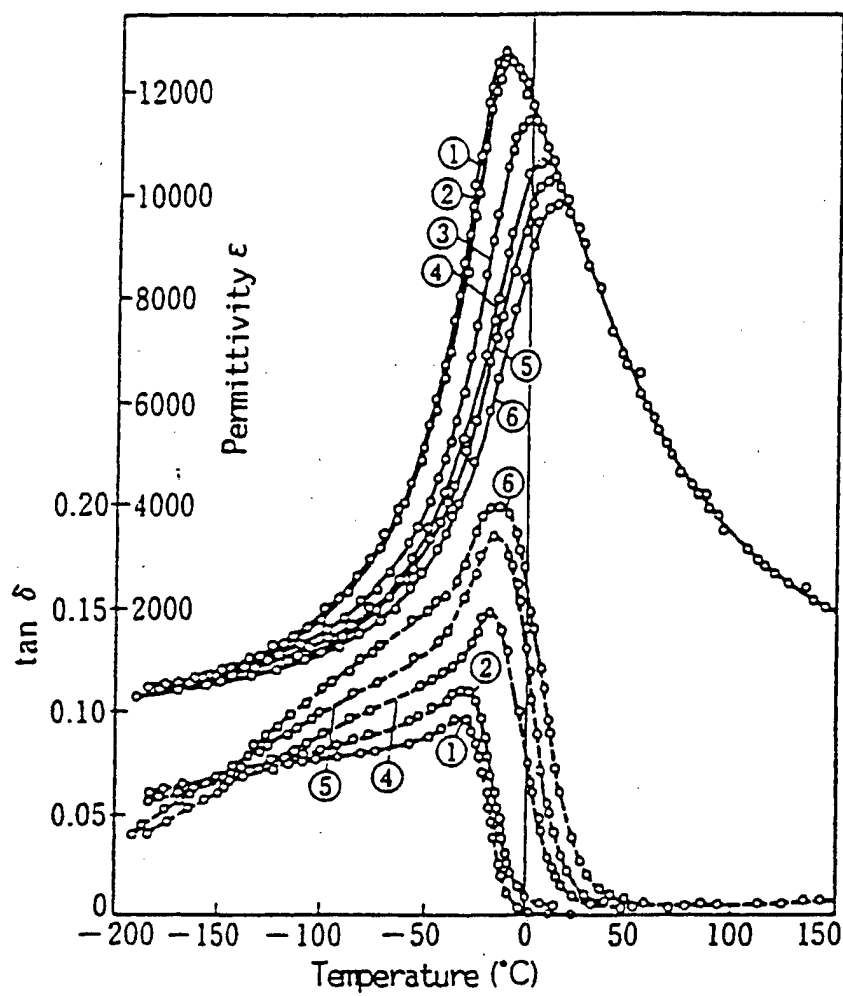
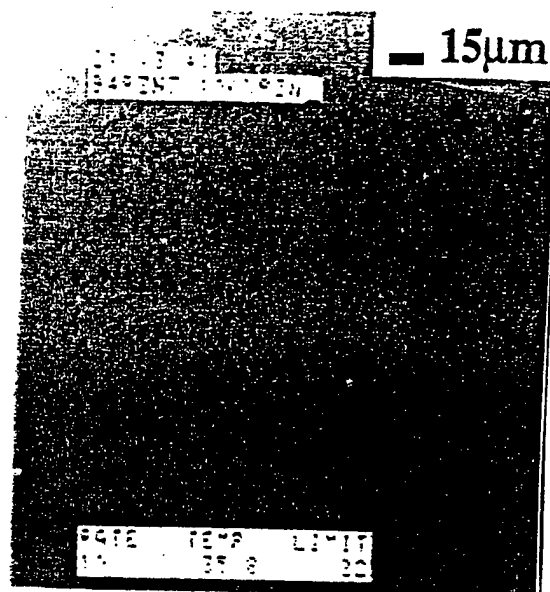
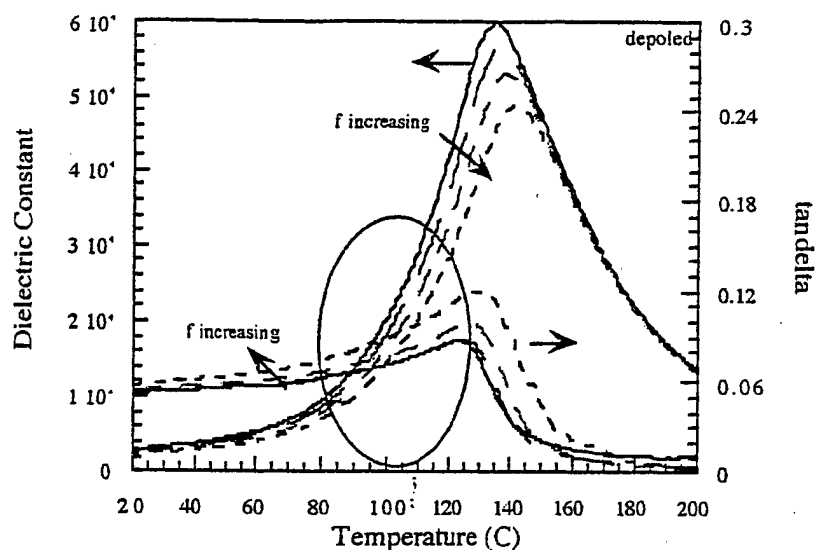


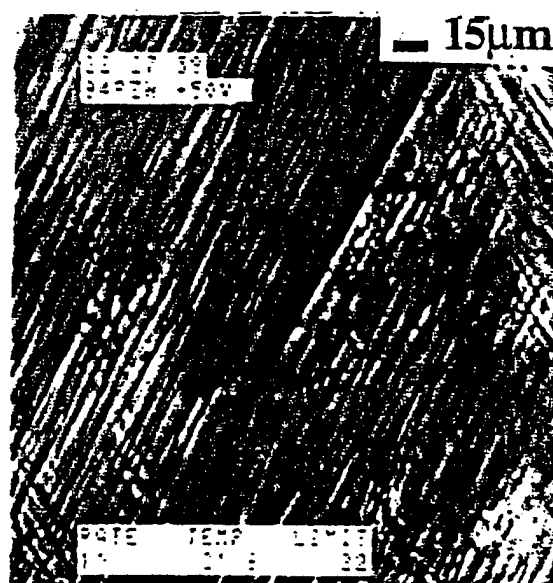
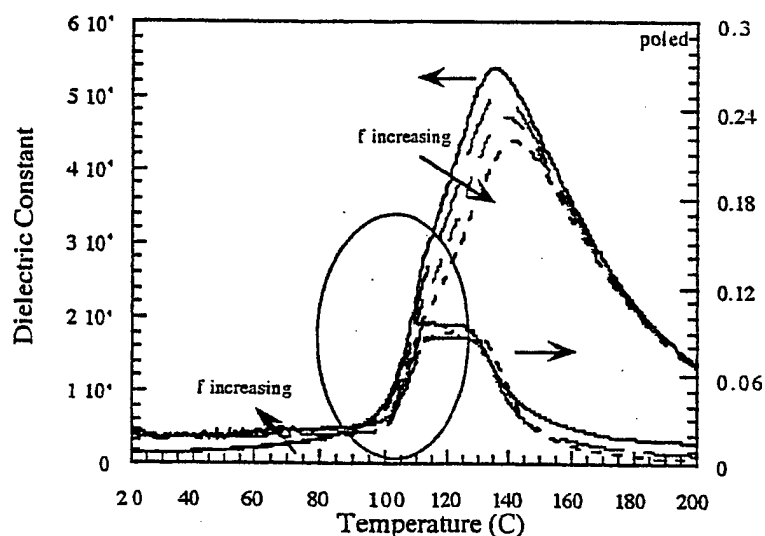
Fig 6 K. Uchino

a.) A depoled 100%PZN single crystal measured on the $\langle 111 \rangle$.



No field, 25°C

b.) A poled 100% PZN single crystal measured on the $\langle 111 \rangle$.



+6.3kV/cm DC, 25°C

Fig 7 K. Uchino

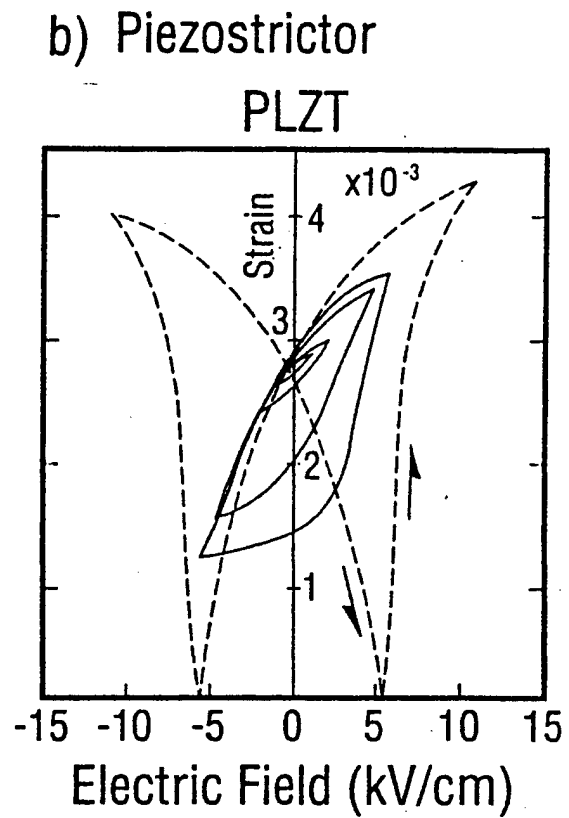
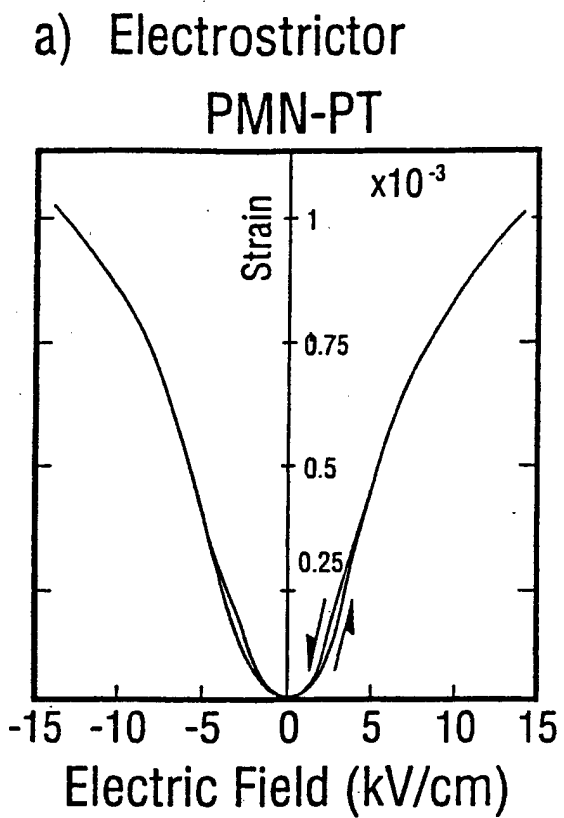


Fig 8 **K. Uchino**

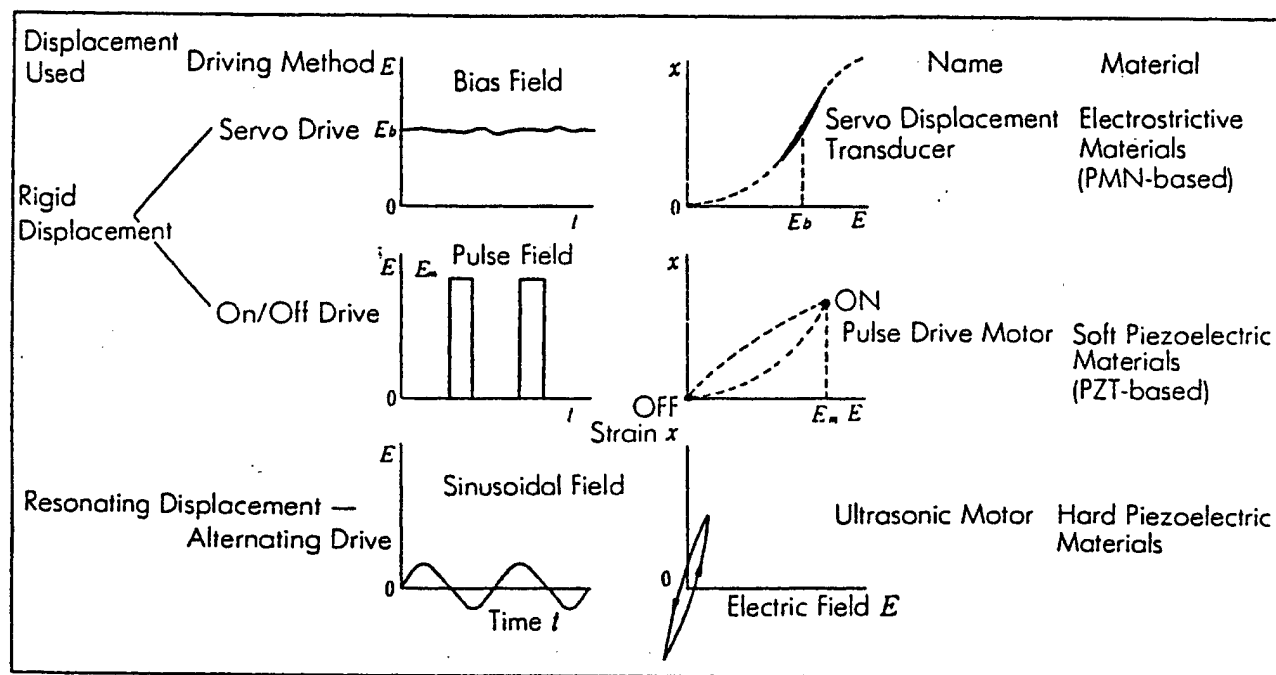


Fig 9 K. Uchino

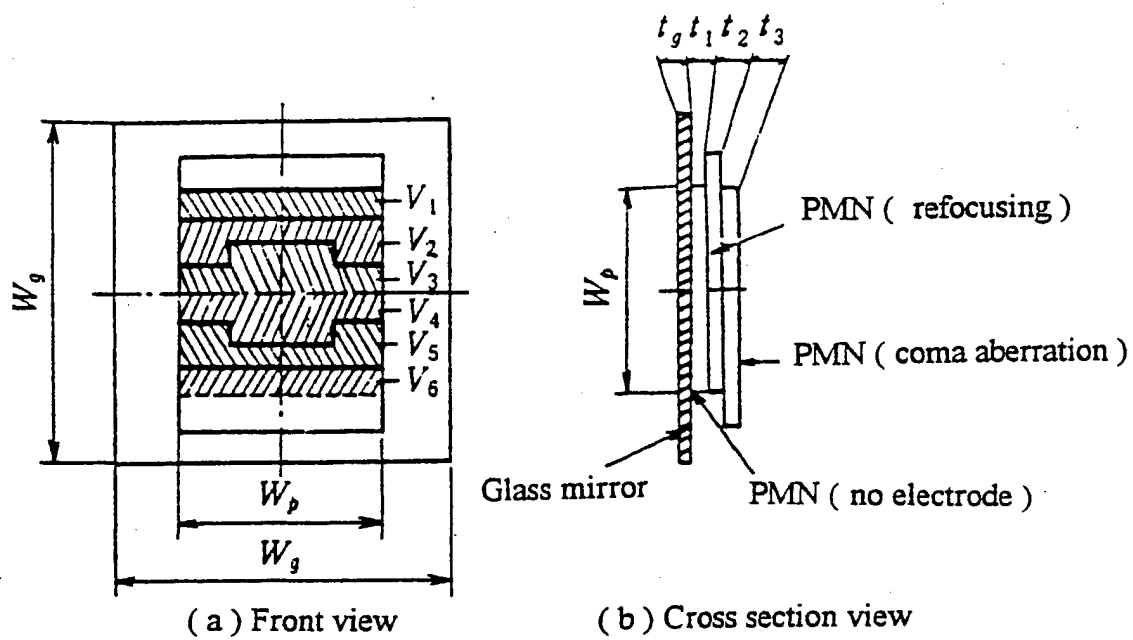
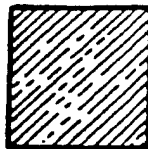
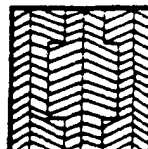
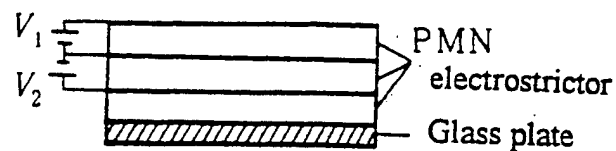


Fig 10 K. Uchino

Layer	Electrode configuration
First	
Second	



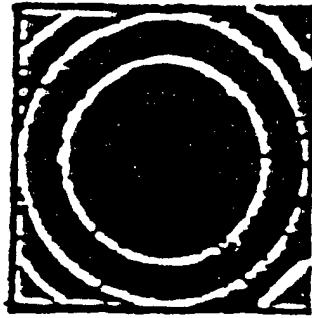
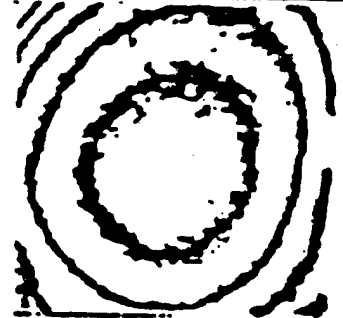



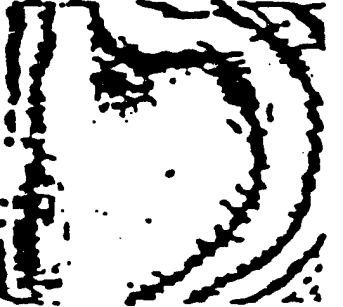
Aberration	Desired wavefronts	Generated wave fronts
Refocusing $x^2 + y^2$		
Coma $x^3 + x y^2$		
Refocusing and coma $C_R (x^2 + y^2) + C_C (x^3 + x y^2)$		

Fig 11 K. Uchino

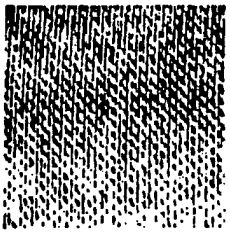
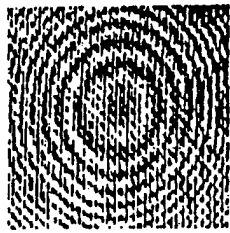
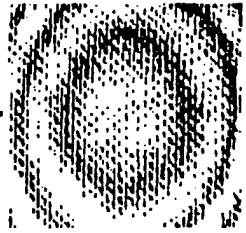


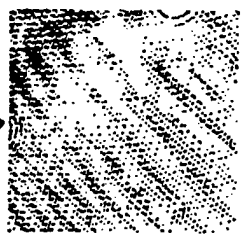
(a)	Electric Field (kV/cm)	0	3.0	0
	P Z T Interferogram of Generated Wavefronts			
(b)	Electric Field (kV/cm)	0	8.6	0
	P M N Interferogram of Generated Wavefronts			

Fig 12 K. Uchino

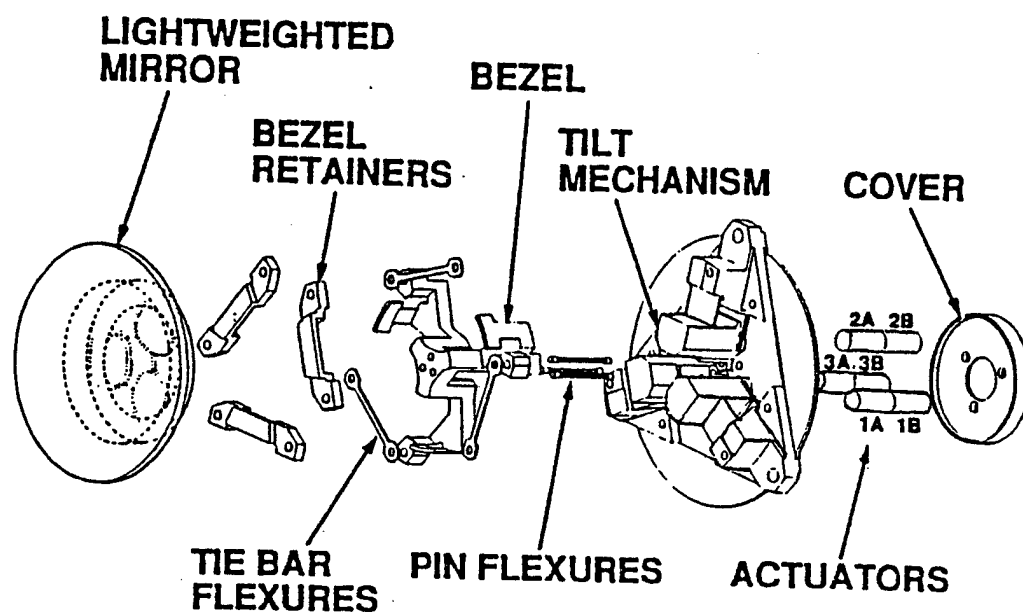
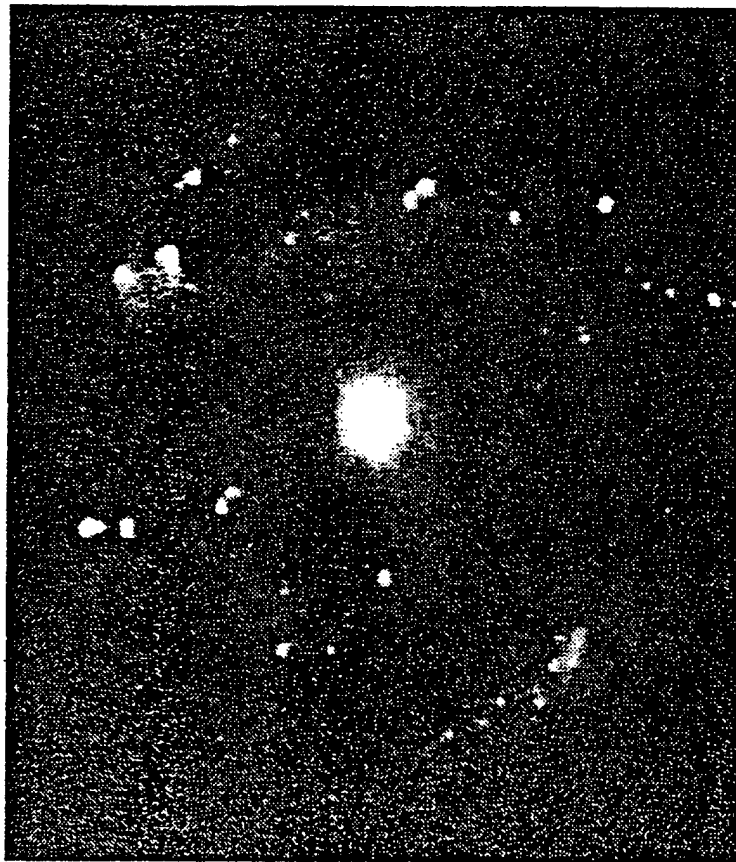
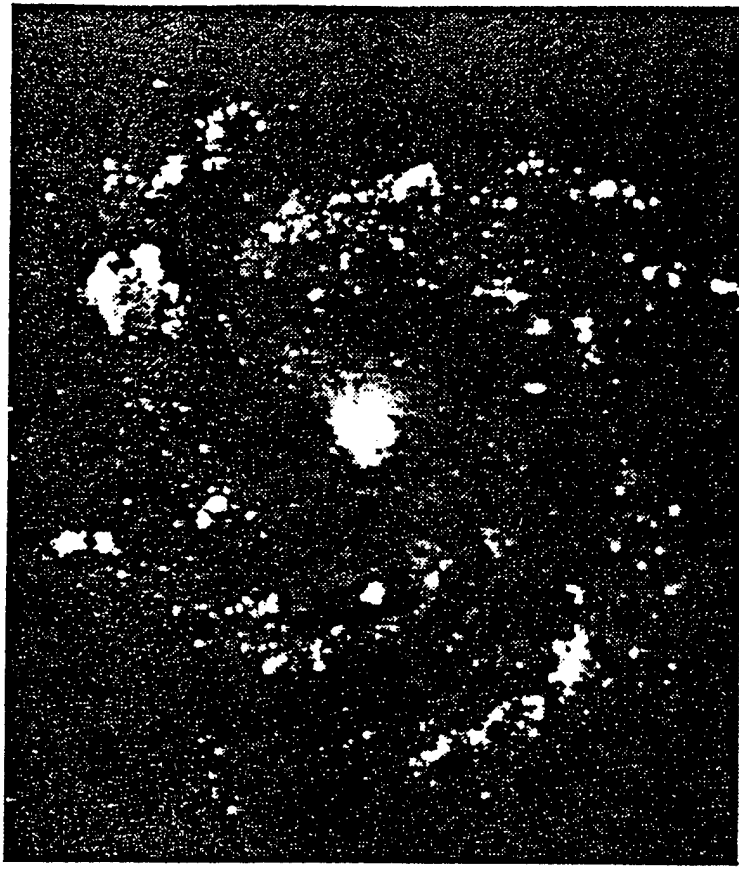


Fig 13 **K. Uchino**

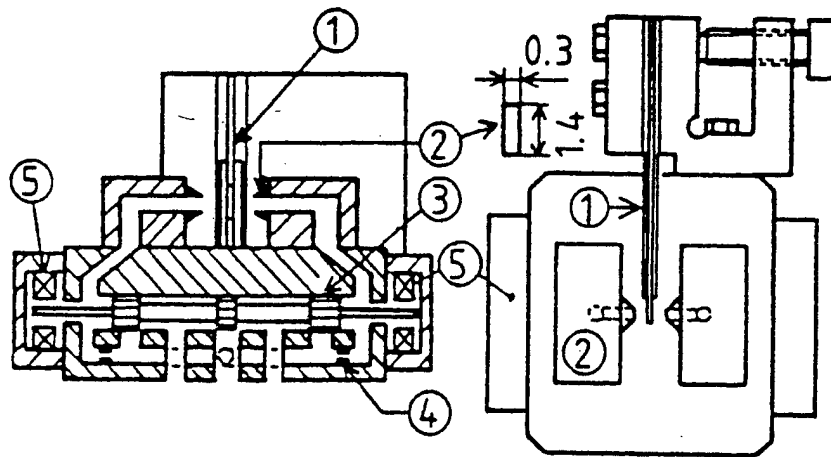


(a)



(b)

Fig 14 K. Uchino



(a) front (section) view

(b) top view

- ① PMN - flapper ② nozzle ③ spool
 ④ fixed orifice ⑤ spool position sensor

Fig 15 K. Uchino

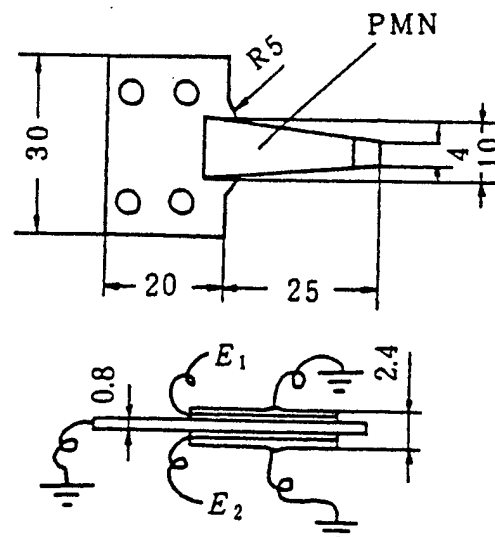


Fig 16 K. Uchino

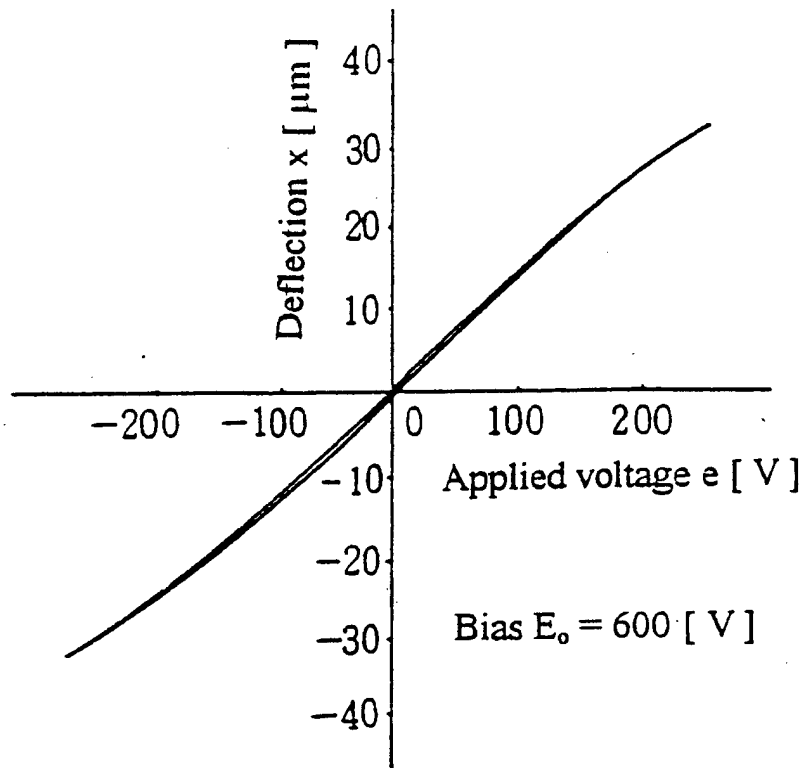


Fig 17 K. Uchino

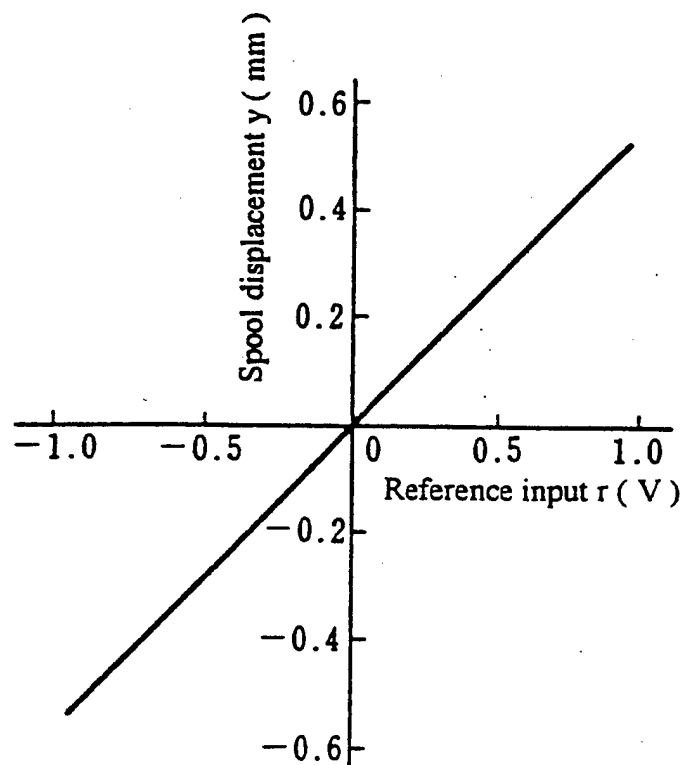


Fig 18 K. Uchino

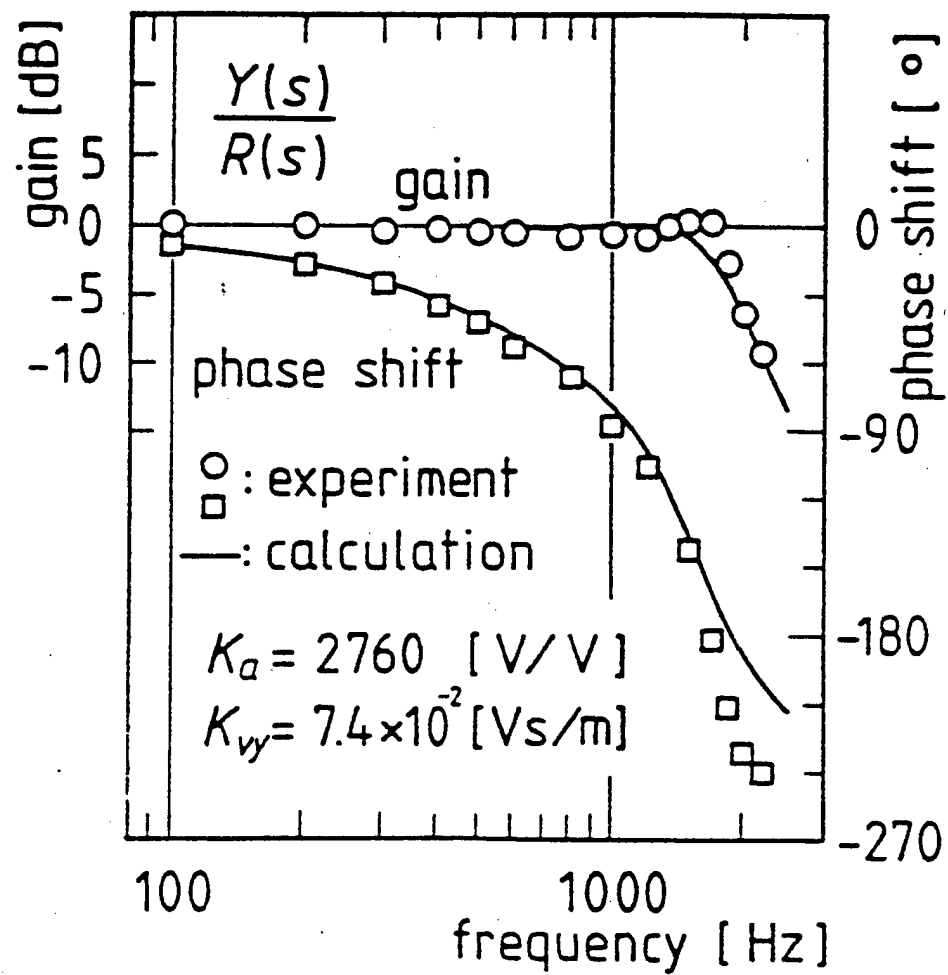


Fig 19 K. Uchino

APPENDIX 2

Contribution to ENCYCLOPEDIA SMART MATERIALS

Smart Ceramics: Transducers, Sensors and Actuators

Kenji Uchino

Professor, Electrical Engineering

Director, International Center for Actuators and Transducers

134 Materials Research Laboratory

The Pennsylvania State University

University Park, PA 16802

Phone: 814-863-8035, Fax: 814-865-2326, E-mail: kenjiuchino@psu.edu

Introduction

Smart Material

Let us start from the "smartness" of the material. Table 1 lists the various effects relating the input - electric field, magnetic field, stress, heat and light with the output - charge/current, magnetization, strain, temperature and light. The conducting and elastic materials, which generate current and strain outputs, respectively, for the input, voltage or stress (well-known phenomena!), are sometimes called "trivial" materials. On the contrary, the pyroelectric and piezoelectric, which generate an electric field for the input of heat or stress (unexpected phenomena!), are called "smart" materials. These off-diagonal couplings have a corresponding converse effect such as electrocaloric and converse-piezoelectric effects, and both "sensing" and "actuating" functions can be realized in the same materials. "Intelligent" materials should possess a "drive/control" or "processing" function which is adaptive to the environmental condition change, in addition to the actuation and sensing functions. You can notice that the ferroelectric materials exhibit most of these effects except the magnetic-related phenomena. Thus, the ferroelectrics are said to be very "smart" materials.

The "actuator" in a narrow meaning stands for materials or devices which generate mechanical strain (or stress) output. As indicated by a solid columnar border in Table 1, solid state actuators utilize converse piezoelectric, magnetostriction, elasticity, thermal expansion or photostriction phenomena. Shape memory alloy is a kind of thermal expansion material. On the other hand, the "sensor" requires charge/current output in most cases. Thus, conducting/semiconducting, magneto-electric, piezoelectric, pyroelectric, and photovoltaic materials are used for detecting electric field, magnetic field, stress, heat, and light, respectively (see a dashed columnar border in Table 1).

From this sense, piezoelectric materials are most popularly used in smart structures and systems, because the same material is applicable for both sensors and actuators, in principle. We treat with piezoelectric transducers, sensors and actuators mainly in this chapter. Even though "transducers", in general, stand for devices which can convert an input energy to a different energy type output, the piezoelectric "transducer" is often used to express the device which possesses both sensing and actuating functions, exemplified by an underwater sonar.

Piezoelectric Effect

Certain materials produce electric charges on their surfaces as a consequence of applying mechanical stress. When the induced charge is proportional to the mechanical stress, it is called direct piezoelectric effect, and was discovered by J. and P. Curie in 1880. Materials showing this phenomenon also conversely have a geometric strain generation proportional to an applied electric field. This is the converse piezoelectric effect. The root of the word "piezo" came from "pressure"; hence the original meaning of the word piezoelectricity implied "pressure electricity". (1)(2)

Piezoelectric materials provide coupling between electrical and mechanical parameters. The material used earliest for its piezoelectric properties was single-crystal quartz. Quartz crystal resonators for frequency control appear today at the heart of clocks and are also used in TVs, computers etc. Ferroelectric polycrystalline ceramics such as barium titanate and lead zirconate titanate exhibit piezoelectricity when electrically poled. Since these ceramics possess significant and stable piezoelectric effects, i.e. high electromechanical coupling, they are capable of producing large strains / forces and hence are extensively used as transducers. Piezoelectric polymers, notably polyvinyliden difluoride and its copolymers with trifluoroethylene and piezoelectric composites combining a piezoelectric ceramic with a passive polymer have been developed which offer a high potential.

Recently, thin films of piezoelectric materials are being paid attention due to their potential utilization in micro-devices (sensors and MEMSs). Piezoelectricity is being extensively utilized in the fabrication of various devices such as transducers, sensors, actuators, surface acoustic wave devices, frequency control and so on.

We describe the fundamentals of piezoelectric effect firstly, then brief history of piezoelectricity, followed by present day piezoelectric materials that are used, and finally various potential applications of piezoelectric materials are presented.

Piezoelectricity

Relationship between Crystal Symmetry and Properties

All crystals can be classified into 32 point groups according to their crystallographic symmetry. These point groups are divided into two classes; one has a center of symmetry and another lacks it. There are 21 non-centrosymmetric point groups. Crystals belonging 20 of these point groups exhibits piezoelectricity. The cubic class 432, although lacking a center of symmetry, does not permit piezoelectricity. Of these 20 point groups, there are 10 polar crystal classes containing a unique axis, along which an electric dipole moment is oriented in the unstrained condition.

Pyroelectric effect appears in any material that possesses a polar symmetry axis. The material in this category develops electric charge on the surface owing to the change in dipole moment with temperature. Among the pyroelectric crystals whose spontaneous polarization are reorientable by application of an electric field of sufficient magnitude (not exceeding the breakdown limit of the crystal) are called ferroelectrics. (3)(4) Table 2 shows the crystallographic classification of the point groups.

Piezoelectric Coefficients

Materials are deformed by stresses and the resulting deformations are represented by strains ($\Delta L/L$). When the stress X (force per unit area) causes a proportional strain x ,

$$x = s X, \quad (1)$$

where all quantities are tensors; x and X are second rank and s is fourth rank.

Piezoelectricity creates additional strains by an applied field E . The piezoelectric equation is given by

$$x_{ij} = s_{ijkl} X_{kl} + d_{ijk} E_k, \quad (2)$$

where E is the electric field and d is the piezoelectric constant which is the third rank tensor. This equation can be also expressed in a matrix form such as given for the case in a poled ceramics:

$$\begin{array}{l} |x_1| \\ |x_2| \\ |x_3| \\ |x_4| \\ |x_5| \\ |x_6| \end{array} = \begin{array}{ccc} |0 & 0 & d_{31}| \\ |0 & 0 & d_{31}| \\ |0 & 0 & d_{33}| \\ |0 & d_{15} & 0| \\ |d_{15} & 0 & 0| \\ |0 & 0 & 0| \end{array} \begin{array}{l} |E_1| \\ |E_2| \\ |E_3| \end{array} \quad (3)$$

Another frequently used piezoelectric constant is 'g' which gives the electric field produced when a stress is applied ($E = gT$). The 'g' constant is related to the 'd' constant through the permittivity ϵ :

$$g = d / \epsilon. \quad (4)$$

A measure of the effectiveness of the electromechanical energy conversion is the electromechanical coupling factor 'k', which measures the fraction of the electrical energy converted to mechanical energy when an electric field is applied or vice versa when a material is stressed (5):

$$k^2 = (\text{Stored mechanical energy} / \text{Input electrical energy}) \quad (5)$$

or

$$= (\text{Stored electrical energy} / \text{Input mechanical energy}) \quad (6)$$

Let us calculate Eq.(5), when an electric field E is applied to a piezoelectric material. Since the input electrical energy is $(1/2) \epsilon_0 \epsilon E^2$ per unit volume and the stored mechanical energy per unit volume under zero external stress is given by $(1/2) x^2 / s = (1/2) (d E)^2 / s$, k^2 can be calculated as

$$\begin{aligned} k^2 &= [(1/2) (d E)^2 / s] / [(1/2) \epsilon_0 \epsilon E^2] \\ &= d^2 / \epsilon_0 \epsilon s. \end{aligned} \quad (7)$$

Note that k is always less than 1. Typical values of k are 0.10 for quartz, 0.4 for BaTiO_3 ceramic, 0.5 - 0.7 for PZT ceramic and 0.1 - 0.3 for PVDF polymer. Another important material parameter is the mechanical quality factor Q_m which determines the frequency characteristics. The Q_m is given by an inverse value of mechanical loss:

$$Q_m = 1 / \tan \delta. \quad (8)$$

Low Q_m is preferred for sensor applications in general in order to cover a wide frequency range. On the contrary, high Q_m is most desired for ultrasonic actuation (e. g. ultrasonic motors) in order to suppress heat generation through the loss.

History of Piezoelectricity

As stated already, the discovery of piezoelectricity in quartz was done by Piere and Jacques Curie in 1880. The discovery of ferroelectricity accelerated the creation of useful piezoelectric materials. Rochelle salt was the first ferroelectric discovered in 1921. Till 1940 only two types of ferroelectric were known, Rochelle salt and potassium dihydrogen phosphate and its isomorph. In 1940 to 1943, unusual dielectric properties such as abnormally high dielectric constant were found in barium titanate BaTiO_3 independently by Wainer and Salmon, Ogawa, and Wul and Golman. After the discovery, compositional modifications for BaTiO_3 led to improvement in the temperature stability or the high voltage

output. Piezoelectric transducers based on BaTiO_3 ceramics were becoming well established in a number of device applications.

In 1950's Jaffe and co-workers established the lead zirconate - lead titanate system (called PZT system) as suitable for inducing strong piezoelectric effects. The maximum piezoelectric response was found for PZT compositions near the morphotropic phase boundary between rhombohedral and tetragonal phases. Since then, the PZT system with various additives has become the dominant piezoelectric ceramics for various applications. The development of PZT based ternary solid solution systems provided the major success of piezoelectric industries for the present applications.

Kawai et al. discovered in 1969 that certain polymers, notably polyvinyliden difluoride (PVDF), are piezoelectric when stretched during fabrication. Such piezoelectric polymers are also useful for some transducer applications. In 1978 Newnham et al., improved composite piezoelectric materials by combining a piezoelectric ceramic with a passive polymer whose properties can be tailored to the requirements of various piezoelectric devices.

There is another class of ceramic material which recently has become important; relaxor-type electrostrictors such as lead magnesium niobate [PMN], typically doped with 10% lead titanate [PT], which are potentially used for applications in the piezoelectric actuator field. Recent breakthrough in the growth of high quality large single crystal relaxor piezoelectric compositions has brought the interest in these materials for wide applications ranging from high strain actuators to high frequency transducers for the medical ultrasound devices due to their superior electromechanical characteristics. More recently, thin films of piezoelectric materials such as zinc oxide [ZnO], or PZT have been extensively investigated and developed for use in micro electromechanical (MEMS) device applications.

Piezoelectric Materials

This section summarizes the current status of piezoelectric materials: single crystal materials, piezoceramics, piezopolymers, piezocomposites and piezofilms. Table 3 shows the material parameters of some representative piezoelectric materials described below.

(6)(7)

Single Crystals

The piezoelectric ceramics are widely used at present for a large number of applications. However, single crystal materials retain their utility, being essential for application field such as frequency stabilized oscillators and surface acoustic devices. The most popular single-crystal piezoelectric materials are quartz, lithium niobate (LiNbO_3) and lithium tantalate (LiTaO_3). The single crystals are anisotropic in general, which gives different material properties depending on the cut of the materials and the direction of bulk or surface wave propagation.

Quartz is a well-known piezoelectric material. α -quartz belongs to the triclinic crystal system with point group 32 and has a phase transition at 537°C to β -type which is not a piezoelectric. Quartz has the cut with a zero temperature coefficient of the resonance frequency change. For instance, quartz oscillators using thickness shear mode of AT-cut are extensively used for clock sources in computers, frequency stabilized ones in TVs and VCRs. On the other hand, an ST-cut quartz substrate with X-propagation has a zero temperature coefficient for surface acoustic wave and so are used for SAW devices with high-stabilized frequencies. The another distinguished characteristic of quartz is its extremely high mechanical quality factor $Q_m > 10^5$.

Lithium niobate and lithium tantalate belong to an isomorphous crystal system and are composed of oxygen octahedron. The Curie temperatures of LiNbO_3 and LiTaO_3 are 1210 and 660°C, respectively. The crystal symmetry of the ferroelectric phase of these single crystals is 3m and the polarization direction is along c-axis. These materials have high electromechanical coupling coefficients for surface acoustic wave. In addition, large single crystals can easily be obtained from their melt using the conventional Czochralski technique. Thus both materials occupy very important positions in the SAW device application field.

Perovskite Ceramics

Most of the piezoelectric ceramics have perovskite structure ABO_3 , as shown Fig.1. This ideal structure consists of a simple cubic unit cell with a large cation A on the corner, a smaller cation B in the body center, and oxygens O in the centers of the faces. The structure is a net-work of corner-linked oxygen octahedra surrounding B cations. Piezoelectric properties of perovskite-structure materials can be easily tailored depending on their applications by incorporating various cations in the perovskite structure.

Barium titanate

Barium titanate BaTiO_3 is one of the most thoroughly studied and most widely used piezoelectric materials. Figure 2 shows the temperature dependence of dielectric constants in BaTiO_3 demonstrating the phase transition in BaTiO_3 single crystals. Three anomalies can be observed. The discontinuity at the Curie point (130°C) is due to a transition from a ferroelectric to a paraelectric phase. The other two discontinuities are accompanied with transitions from one ferroelectric phase to another. Above the Curie point the crystal structure is cubic and has no spontaneous dipole moments. At the Curie point the crystal becomes polar and the structure changes from a cubic to a tetragonal phase. The tetragonal axis is in the direction of the dipole moment and thus along the spontaneous polarization.

Just below the Curie temperature, the vector of the spontaneous polarization points in the [001] direction (Tetragonal phase), below 5°C it reorients to the [011] (Orthrhombic phase) and below - 90°C to the [111] (Rhombohedral phase). The dielectric and piezoelectric properties of ferroelectric ceramic BaTiO₃ can be affected by its own stoichiometry, microstructure, and by dopants entering into the A or B site solid solution. Modified ceramic BaTiO₃ with dopants such as Pb or Ca ions have been used as commercial piezoelectric materials.

Lead zirconate- lead titanate

Piezoelectric Pb(Ti,Zr)O₃ solid solutions [PZT] ceramics have been widely used because of their superior piezoelectric properties. The phase diagram of the PZT system (Pb(Zr_xTi_{1-x})O₃) is shown in Fig. 3. The crystalline symmetry of this solid-solution system is determined by the Zr content. Lead titanate has also a tetragonal ferroelectric phase of perovskite structure. With increasing Zr content, x , tetragonal distortion decreases and when $x > 0.52$ the structure changes from tetragonal 4mm phase to another ferroelectric phase of rhombohedral 3m symmetry. Figure 4 shows the dependence of several d constants on composition near the morphotropic phase boundary. The d constants have their highest values near the morphotropic phase boundary. This enhancement in piezoelectric effect is attributed to the increased ease of reorientation of the polarization under electric field. Doping the PZT material with donors or acceptor changes the properties dramatically. Donor doping with ions such as Nb⁵⁺ or Ta⁵⁺ provides soft PZTs like PZT-5, because of the facility of a domain motion due to the charge compensation of Pb-vacancy which is generated during sintering. On the other hand, acceptor doping such as Fe³⁺ or Sc³⁺ leads to hard PZTs such as PZT-8, because oxygen vacancies will pin the domain wall motion.

Lead titanate

PbTiO_3 has a tetragonal structure at room temperature with a large tetragonality $c/a = 1.063$. The Curie temperature is 490°C . Densely sintered PbTiO_3 ceramics can not be obtained easily, because they break up into a powder when cooled through the Curie temperature. This is partly due to the large spontaneous strain which occurs at the transition. Lead titanate ceramics modified by adding small amount of additives which exhibits a high piezoelectric anisotropy. Either $(\text{Pb}, \text{Sm})\text{TiO}_3$ (8) or $(\text{Pb}, \text{Ca})\text{TiO}_3$ (9) has extremely low planar coupling, that is, large k_t / k_p ratio. Here, k_t and k_p are thickness-extensional and planar electromechanical coupling factors, respectively. $(\text{Pb}, \text{Nd})(\text{Ti}, \text{Mn}, \text{In})\text{O}_3$ ceramics with a zero temperature coefficient of surface acoustic wave delay have been developed as a superior substrate materials for SAW device applications. (10)

Relaxor ferroelectrics

Relaxor ferroelectrics differ from normal ferroelectrics in terms of having broad phase transition from paraelectric to ferroelectric state, strong frequency dependence of dielectric constant (i.e. dielectric relaxation) and weak remanent polarization. Lead based relaxor materials have complex disordered perovskite structures with a general formula $\text{Pb}(\text{B}_1, \text{B}_2)\text{O}_3$ ($\text{B}_1 = \text{Mg}^{2+}, \text{Zn}^{2+}, \text{Sc}^{3+}$, $\text{B}_2 = \text{Nb}^{5+}, \text{Ta}^{5+}, \text{W}^{6+}$). The B site cations are distributed randomly in the crystal. The characteristic of a relaxor is a broad and frequency dispersive dielectric maximum. In addition, relaxor-type materials such as lead magnesium niobate $\text{Pb}(\text{Mg}_{1/3}\text{Nb}_{2/3})\text{O}_3$ - lead titanate PbTiO_3 solid solution [PMN-PT] exhibit electrostrictive phenomena, very suitable for actuator applications. Figure 5 shows an electric field induced strain curve observed for 0.9PMN-0.1PT, reported by Cross et. al in 1980. Note that a strain of 0.1% can be induced by an electric field as small as 1 kV/mm, and that hysteresis is negligibly small for this electrostriction.(11)

Since the electrostriction is the secondary electromechanical coupling observed in cubic structures, in principle, the charge is not induced under applied stress. The converse electrostrictive effect, which can be used as a sensor, means that the permittivity (first derivative of polarization with respect to electric field) will change by stress.

The relaxor ferroelectric can also induce piezoelectric effect under a bias field. That is, the electromechanical coupling factor k_t varies with the applied DC bias field. As the DC bias field increases, the coupling increases and saturates. These materials would be applied for ultrasonic transducers which can be tunable by the bias field. (12)

The recent development on single crystal piezoelectrics started in 1981, when Kuwata, Uchino and Nomura firstly reported an enormously large electromechanical coupling factor $k_{33} = 92 - 95\%$ and piezoelectric constant $d_{33} = 1500$ pC/N in solid solution single crystals between relaxor and normal ferroelectrics, $\text{Pb}(\text{Zn}_{1/3}\text{Nb}_{2/3})\text{O}_3\text{-PbTiO}_3$. (13) After about 10 years, Y. Yamashita et al. (Toshiba) and T. R. Shrout et al. (Penn State) have independently reconfirmed that these values are true, and much more improved data were obtained in these a couple of years, aiming at medical acoustic applications. Moreover, important data have been accumulated for these materials ($\text{Pb}(\text{Mg}_{1/3}\text{Nb}_{2/3})\text{O}_3$ [PMN], $\text{Pb}(\text{Zn}_{1/3}\text{Nb}_{2/3})\text{O}_3$ [PZN] and binary systems of these materials combined with PbTiO_3 [PMN-PT and PZN-PT]) from an actuator application viewpoint; strains as large as 1.7% can be induced practically for a morphotropic phase boundary composition of the PZN-PT solid solution single crystals. Figure 6 shows the field induced strain curve for [001] oriented 0.92PZN-0.08PT. (14) It is notable that the highest values are observed for a rhombohedral composition only when the single crystal is poled along the perovskite [001] axis, not along the [111] spontaneous polarization axis.

Polymers

Polyvinylidene difluoride, PVDF or PVF₂, is piezoelectric when stretched during fabrication. Thin sheets of the cast polymer are then drawn, stretched, in the plane of the sheet in at least one direction, and frequently also in the perpendicular direction, to make the material into its microscopically polar phase. Crystallization from melt forms non-polar α -phase, which can be converted into another polar β -phase by a uniaxial or biaxial drawing operation; these dipoles are then reoriented through electric poling. Large sheets can be manufactured and thermally formed into complex shapes. The copolymerization of vinylidene difluoride with trifluoroethylene (TrFE) results in random copolymer (PVDF-TrFE) with a stable, polar β -phase. This polymer need not be stretched; it can be poled directly as formed. The thickness-mode coupling coefficient of 0.30 has been reported. Such piezoelectric polymers are used for directional microphones and ultrasonic hydrophones.

Composites

Piezocomposites comprised of piezoelectric ceramic and polymer are promising materials because of excellent and tailored properties. The geometry for two-phase composites can be classified according to the connectivity of each phase (1, 2 or 3 dimensionally) into 10 structures; 0-0, 0-1, 0-2, 0-3, 1-1, 1-2, 1-3, 2-2, 2-3 and 3-3. (15) A 1-3 piezocomposite, or PZT-rod / polymer-matrix composite is identified as a most promising candidate. The advantages of this composite are high coupling factors, low acoustic impedance (square root of the product of its density and elastic stiffness), good matching to water or human tissue, mechanical flexibility, broad bandwidth in combination with low mechanical quality factor and the possibility of making undiced arrays by only structuring the electrodes. The thickness-mode electromechanical coupling of the composite can exceed the k_t (0.40-0.50) of the constituent ceramic, approaching almost the value of the rod-mode electromechanical coupling, k_{33} (0.70-0.80) of that ceramic. (16) The acoustic match to tissue or water (1.5

Mrayls) of the typical piezoceramics (20-30 Mrayls) is significantly improved by forming a composite structure, that is, by replacing heavy and stiff ceramic by light and soft polymer. Piezoelectric composite materials are especially useful for underwater sonar and medical diagnostic ultrasonic transducer applications.

Thin-films

Both zinc oxide [ZnO] and aluminum nitride [AlN] are simple binary compounds with a Wurtzite-type structure, which can be sputter-deposited in a c-axis oriented thin film on a variety of substrates. ZnO has reasonable piezoelectric coupling and its thin films are widely used in bulk acoustic and surface acoustic wave devices. The fabrication of highly c-axis oriented ZnO films have been extensively studied and developed. The performance of ZnO devices is, however, limited due to their small piezoelectric coupling (20 - 30%). PZT thin films are expected to exhibit higher piezoelectric properties. At present the growth of PZT thin film is being carried out for use in micro-transducers and micro-actuators.

Applications of Piezoelectricity

Piezoelectric materials can provide coupling between electrical and mechanical energy and thus have been extensively used in a variety of electro-mechanical device applications. The direct piezoelectric effect is most obviously used in the generation of charge at high voltage such as for the spark ignition of gas in space heaters, cooking stoves and cigarette lighters. Using the converse effect, mechanical small displacements and vibrations can be produced for actuators by applying a field. Acoustic and ultrasonic vibrations can be generated by an alternating field tuned at the mechanical resonance frequency of a piezoelectric device, and can be detected by amplifying the field generated by vibration incident on the material, which is usually used for ultrasonic transducers. The other important application field of

piezoelectricity include the control of frequency. The application of piezoelectric materials ranges over many technology fields including ultrasonic transducers, actuators and ultrasonic motors, electronic components such as resonators, wave filters, delay lines, SAW devices and transformers, and high voltage applications; gas ignitors, ultrasonic cleaning and machining. Piezoelectric-based sensors, for instance, accelerometers, automobile knock sensors, vibration sensors, strain gages and flow meters have been developed, because pressure and vibration can be directly sensed as electric signals through piezoelectric effect. Examples of these applications are given in the following sections.

Pressure Sensor/Accelerometer/Gyroscope

One of very basic applications of piezoelectric ceramics is a gas igniter. Very high voltage generated in a piezoelectric ceramic under applied mechanical stress can cause sparking and ignite the gas.

Piezoelectric ceramics can be employed as stress sensors and acceleration sensors, because of their original "direct piezoelectric effect." Kistler is manufacturing a 3-D stress sensor by combining an appropriate number of quartz crystal plates (extensional and shear types), the multilayer device can detect three-dimensional stresses. (17)

Figure 7 shows a cylindrical gyroscope commercialized by Tokin (Japan). (18) The cylinder has six divided electrodes, one pair of which are used to excite the fundamental bending vibration mode, while the other two pairs are used to detect the acceleration. When rotation acceleration is applied around the axis of this gyro, the voltage generated on the electrodes is modulated by the Coriolis force. By subtracting the signals between the two sensor electrode pairs, a voltage directly proportional to the acceleration can be obtained. This type of gyroscope has been widely installed in handy-type video cameras to

monitor the inevitable hand vibration during operation, and to compensate it electronically on a display using the sensed signal.

Ultrasonic Transducer

One of the most important applications of piezoelectric materials is based on ultrasonic echo field. (19)(20) Ultrasonic transducers convert electrical energy into mechanical form when generating an acoustic pulse and convert mechanical energy into an electrical signal when detecting its echo. Now-a-days, piezoelectric transducers are being used in medical ultrasound for clinical applications ranging from diagnosis to therapy and surgery. They are also used for underwater detection, such as sonars and fish finders, and nondestructive testing.

The ultrasonic transducers operate often in a pulse-echo mode. The transducer converts electrical input into acoustic wave output. The transmitted waves propagate into a body and echoes are generated which travel back to be received by the same transducer. These echoes vary in intensity according to the type of tissue or body structure, thereby creating images. An ultrasonic image represents the mechanical properties of the tissue, such as density and elasticity. We can recognize anatomical structures in an ultrasonic image since the organ boundaries and fluid-to-tissue interfaces are easily discerned. The ultrasonic imaging process can also be done in real time. This means we can follow rapidly moving structures such as heart without motion distortion. In addition, ultrasound is one of the safest diagnostic imaging techniques. It does not use ionizing radiation like X-rays and thus is routinely used for fetal and obstetrical imaging. Useful areas for ultrasonic imaging include cardiac structures, the vascular systems, the fetus and abdominal organs such as liver and kidney. In brief, it is possible to see inside the human body without breaking the skin by using a beam of ultrasound.

There are various types of transducers used in ultrasonic imaging. Mechanical sector transducers consist of single, relatively large resonators and can provide images by its mechanical scanning such as wobbling. Multiple element array transducers permit discrete elements to be individually accessed by the imaging system and enable electronic focusing in the scanning plane to various adjustable penetration depths through the use of phase delays. Two basic types of array transducers are linear and phased (or sector): linear array transducers are used for radiological and obstetrical examinations, while phased array transducers are useful for cardiology applications where positioning between the ribs is necessary.

Figure 8 shows the basic ultrasonic transducer geometry. The transducer is mainly composed of matching, piezoelectric material and backing layers. (21) One or more matching layers are used to increase sound transmissions into tissues. The backing is attached to the transducer rear in order to damp the acoustic backwave and to reduce the pulse duration. Piezoelectric materials are used to generate and detect ultrasound. In general, broadband transducers should be used for medical ultrasonic imaging. The broad bandwidth response corresponds to a short pulse length, resulting in better axial resolution. Three factors are important in designing broad bandwidth transducers. The first is acoustic impedance matching, that is, effectively coupling acoustic energy to the body. The second is a high electromechanical coupling coefficient of the transducer. The third is electrical impedance matching, that is, effectively coupling electrical energy from the driving electronics to the transducer across the frequency range of interest. These pulse echo transducers operate based on thickness mode resonance of the piezoelectric thin plate. The thickness mode coupling coefficient, k_t , is related to the efficiency of converting electric energy into acoustic and vice versa. Further, a low planar mode coupling coefficient, k_p , is beneficial for limiting energies being expended in nonproductive lateral mode. A large

dielectric constant is necessary to enable a good electrical impedance match to the system, especially with tiny piezoelectric sizes.

Table 4 compares the properties of ultrasonic transducer materials. (7)(22) Ferroelectric ceramics, such as lead zirconate titanate and modified lead titanate, are almost universally used as ultrasonic transducers. The success of ceramics is due to their very high electromechanical coupling coefficients. In particular, soft PZT ceramics such as PZT-5A and 5H type compositions are most widely used because of their exceedingly high coupling properties and because they can be relatively easily tailored, for instance, in the wide dielectric constant range. On the other hand, modified lead titanates such as samarium doped materials have high piezoelectric anisotropy: the planar coupling factor k_p is much less than the thickness coupling factor k_t . Since the absence of lateral coupling leads to reduced interference from spurious lateral resonances in longitudinal oscillators, this is very useful in high-frequency array transducer applications. One disadvantage to PZT and other lead based ceramics is their large acoustic impedance (approximately $30\text{-kgm}^{-2}\text{s}^{-1}$ (Mrayls) compared to body tissue (1.5 Mrayls). Single or multiple matching layers with intermediate impedances needed to be used in PZT to improve acoustic matching.

On the other hand, piezoelectric polymers, such as polyvinyliden-difluoride-trifluoroethylene, have much lower acoustic impedance (4 - 5 Mrayls) than the ceramics and thus provide better matching with soft tissues. However, piezopolymers are less sensitive than the ceramics and they have relatively low dielectric constants, requiring large drive voltage and giving poor noise performance due to electrical impedance mismatching.

An alternative to ceramics and polymers is piezoelectric ceramic/polymer composites. Piezocomposites having 2-2 or 1-3 connectivity are commonly used in ultrasonic medical

applications. These combine the low acoustic impedance advantage of polymers with the high sensitivity and low electrical impedance advantages of ceramics.

The design frequency of a transducer depends on the penetration depth imposed upon by the application. Resolution is improved with increasing frequency. Although a high frequency transducer is capable of producing a high resolution image, higher frequency acoustic energy is more readily attenuated by the body. A lower frequency transducer is used as a compromise when imaging deeper structures. Most of medical ultrasound imaging systems operate in the frequency range from 2 to 10 MHz and can resolve objects approximately 0.2 to 1 mm in size. At 3.5 MHz, imaging to a depth of 10 -20 cm is possible, while at 50 MHz, increased losses limit the depth to less than 1 cm. Higher-frequency transducers (10 - 50 MHz) are used for endoscope-based imaging and for catheter-based intravascular imaging. At a higher frequency over 100 MHz applications are being done in the field of ultrasound microscopy. The operating frequency of the transducer is directly related to the thickness and velocity of sound in piezoelectric materials employed. As frequency increases, resonator thickness decreases. For a 3.5 MHz transducer, PZT ceramic thickness needs to be roughly 0.4 mm. Conventional ceramic transducers, such as PZT are limited to frequencies below nearly 80 MHz because of the difficulty of fabricating thinner devices.(23) For microscopic applications at a frequency over 100 MHz, corresponding to the thickness of less than 20 μm piezoelectric thin-film transducers such as ZnO have to be used. (24)

Resonator and Filter

When a piezoelectric body vibrates at its resonant frequency it absorbs considerably more energy than at other frequencies resulting in the fall of impedance. This phenomenon enables piezoelectric materials to be used as a wave filter. A filter is required to pass a certain selected frequency band or to stop a given band. The band width of a filter

fabricated from a piezoelectric material is determined by the square of the coupling coefficient k . Quartz crystals with very low k value of about 0.1 can pass very narrow frequency bands of approximate 1% of the center resonance frequency. On the other hand, PZT ceramics with a planar coupling coefficient of about 0.5 can easily pass a band of 10% of the center resonance frequency. The sharpness of the passband is dependent on the mechanical quality factor Q_m of the materials. Quartz has also a very high Q_m of about 10^6 which results in a sharp cut-off to the passband and well-defined frequency of the oscillator.

A simple resonator is a thin disc type, electroded on its plane faces and vibrating radially for applications in filters with a center frequency ranging from 200 kHz to 1 MHz and with a bandwidth of several percent of the center frequency. For a frequency of 455 kHz the disc diameter needs to be about 5.6 mm. However, if the required frequency is higher than 10 MHz, other modes of vibration such as the thickness extensional mode are exploited, because of its smaller size disc. The trapped-energy type filters made from PZT ceramics have been widely used in the intermediate frequency range for such as 10.7 MHz for FM radio receiver and transmitter. By employing the trapped-energy phenomena, the overtone frequencies are suppressed. The plate is partly covered with electrodes of a specific area and thickness. The fundamental frequency of the thickness mode beneath the electrode is less than that of the unelectroded portion, because of the extra inertia of the electrode mass. The longer wave characteristic of the electrode region cannot propagate in the unelectroded region. The higher-frequency overtones can propagate away into the unelectroded region. This is called as trapped-energy principle. Figure 9 shows a schematic drawing of trapped-energy filter. In this structure the top electrode is split so that coupling between the two parts will only be efficient at resonance. More stable filters suitable for telecommunication systems have been made from single crystals such as quartz or LiTaO_3 .

Piezoelectric Transformer

The transfer of vibration energy from one set of electrodes to another on a piezoelectric ceramic body can be used for voltage transformation. This device is called a piezoelectric transformer. Recently, the office automation equipments with liquid crystal displays are successively commercialized such as notebook type personal computers and car navigation systems. These equipments with a liquid crystal display require a very thin, no electromagnetic-noise transformer to start the glow of a fluorescent back-lamp. This application has recently accelerated the development of the piezoelectric transformers. Figure 10 shows a fundamental structure by where two differently-poled parts coexist in one piezoelectric plate. The plate has electrodes on half its major faces and on an edge, which is then poled in its thickness direction at one end and parallel to the long axis over most of its length. A low-voltage AC supply is applied to the large-area electrodes at a frequency that excites a length extensional mode resonance. A high-voltage output can then be taken from the small electrode and one of the larger electrodes. After the proposal by C.A. Rosen such as mentioned above, piezoelectric transformers with several different structures have been reported. (25) A multilayer type transformers are proposed in order to increase the voltage rise ratio. (26) The input part is of the multilayer structure with internal electrodes and the output electrodes are formed at the side surface of the half part of rectangular plate. This transformer uses piezoelectric transverse mode for the input and output part.

SAW device

A surface acoustic wave (SAW) also called a Rayleigh wave is composed of a coupling between longitudinal and shear waves in which the SAW energy is confined near the surface. An associated electrostatic wave exists for a SAW on a piezoelectric substrate, which allows electroacoustic coupling via a transducer. The advantages of SAW technology are: the wave can be electroacoustically accessed and trapped at the substrate

surface and its velocity is approximately 10^4 times slower than an electromagnetic wave. The SAW wavelength is on the same order of magnitude as line dimensions which can be photolithographically produced and the lengths for both short and long delays are achievable on reasonable size substrates. (27)(28)

There are a very broad range of commercial system applications which include front-end and IF (Intermediate Frequency) filters, CATV (Community Antenna Television) and VCR (Video Cassette Recorder) components, synthesizers, analyzers and navigators etc. In SAW transducers, finger electrodes provide the ability to sample or tap the wave and the electrode gap gives the relative delay. A SAW filter is composed of a minimum of two transducers. A schematic of a simple SAW bi-directional filter is shown in Fig. 11. A bi-directional transducer radiates energy equally from each side of the transducer. Energy not being received is to be absorbed to eliminate spurious reflection.

Various materials are currently being used for SAW devices. The most popular single-crystal SAW materials are lithium niobate and lithium tantalate. The materials have different properties depending on the cut of the material and the direction of propagation. The fundamental parameters are SAW velocity, temperature coefficients of delay (TCD), electromechanical coupling factor and propagation loss. Surface acoustic waves can be generated and detected by a spatially periodic, interdigital electrodes on the plane surface of a piezoelectric plate. A periodic electric field is produced when an RF source is connected to the electrode, thus permitting piezoelectric coupling to a traveling surface wave. If an RF source with a frequency, f , is applied to the electrode having periodicity, p , energy conversion from an electrical to mechanical form will be maximum when

$$f=f_0=V_s/p \quad (9)$$

Here, V_s is the SAW velocity and f_0 is the center frequency of the device. SAW velocity is an important parameter determining the center frequency. Another important parameter for

many applications is temperature sensitivity. For example, the temperature stability of the center frequency of SAW bandpass filters is a direct function of temperature coefficient for the velocity and delay for the material used. The first-order temperature coefficient of delay is given by

$$(1/t) (dt/dT) = (1/L) (dL/dT) - (1/V_s) (dV_s/dT) , \quad (10)$$

where $t = L/V_s$ is the delay time and L is the SAW propagation length. The surface wave coupling factor, k_s^2 , is defined in terms of the change in SAW velocity which occurs when the wave passes across a surface coated with a thin massless conductor, so that the piezoelectric field associated with the wave is effectively shorted-circuited. The coupling factor, k_s^2 , is expressed by

$$k_s^2 = 2 (V_f - V_m) / V_f \quad (11)$$

where V_f is the free surface wave velocity, V_m the velocity on the metallized surface. In actual SAW applications, the value of k_s^2 relates to the maximum bandwidth obtainable and the amount of signal loss between input and output, determining the fractional bandwidth versus minimum insertion loss for a given material and filter. Propagation loss is one of the major factors that determine the insertion loss of a device and is caused by wave scattering at crystalline defects and surface irregularities. Materials which show high electromechanical coupling factors combined with small temperature coefficients of delay are likely to be required. The free surface velocity, V_0 , of the material is a function of cut angle and propagation direction. The TCD is an indication of the frequency shift expected for a transducer due to a temperature change and is also a function of cut angle and propagation direction. The substrate is chosen based on the device design specifications such as operating temperature, fractional bandwidth, and insertion loss.

Table 5 shows some important material parameters for representative SAW materials. Piezoelectric single crystals such as 128°Y-X (128°-rotated-Y-cut and X-propagation) - LiNbO₃ and X-112°Y (X-cut and 112°-rotated-Y-propagation) - LiTaO₃ have been

extensively employed as SAW substrates for applications in VIF filters. A c-axis oriented ZnO thin films deposited on a fused quartz, glass or sapphire substrate are also commercialized for SAW devices.

Actuators

Currently another important application of piezoelectric materials exists in actuator fields. (29) Using the converse piezoelectric effect, small displacement can be produced by applying a field to a piezoelectric materials. Vibrations can be generated by applying an alternating field. In advanced precision engineering, there is a demand for a variety of types of actuators which can adjust positions precisely (micropositioning devices), suppress noise vibrations (dampers), or drive objects dynamically (ultrasonic motors). These devices are used in broad areas including optics, astronomy, fluid control and precision machinery. For actuator applications, piezoelectric strain and electrostriction induced by an electric field are used.

Figure 12 shows the design classification of ceramic actuators. Simple devices composed of a disk or a multilayer type directly use the strain induced in a ceramic by the applied electric field. Complex devices do not use the induced strain directly but use the amplified displacement through a special magnification mechanism such as unimorph, bimorph and moonie. The most popularly used multilayer and bimorph types have the following characteristics: The multilayer type does not show a large displacement ($10\text{ }\mu\text{m}$), but has advantages in generation force (1 kN), response speed (10 μsec), life time (10^{11} cycles) and the electromechanical coupling factor k_{33} (0.70). The bimorph type exhibits a large displacement (300 μm), but shows disadvantages in generation force (1 N), response speed (1 msec), life time (10^8 cycles) and the electromechanical coupling factor k_{eff} (0.10). For instance, in a 0.65 PMN- 0.35 PT multilayer actuator with 99 layers of 100-mm thick sheets ($2 \times 3 \times 10\text{ mm}^3$), a 8.7 μm displacement is generated by a 100 V voltage,

accompanied by a slight hysteresis. The transmit response of the induced displacement after the application of a rectangular voltage is as quick as 10 μ sec. In conclusion, the multilayer exhibits the field induced strain of 0.1% along the length.

Unimorph and bimorph devices are defined by the number of piezoelectric ceramic plates: only one ceramic plate is bonded onto an elastic shim., or two ceramic plates are bonded together. The bimorph causes bending deformation because each piezoelectric plate bonded together produces extension or contraction under an electric field. In general, there are two types of piezoelectric bimorph: antiparallel polarization type and parallel polarization type, as shown in Fig. 13. Two poled piezoelectric plates with $t/2$ in thickness and L in length are bonded with their polarization directions opposite or parallel to each other. In cantilever bimorph configuration whose one end is clamped, the tip displacement δ_z under an applied voltage V is provided as follows;

$$\delta_z = (3/2)d_{31} (L^2/t^2) V \quad (\text{antiparallel type}) \quad (12)$$

$$\delta_z = 3d_{31} (L^2/t^2) V \quad (\text{parallel type}) \quad (13)$$

The resonance frequency f_r for both types is given by

$$f_r = 0.16 t / L^2 (\rho s_{11}^E)^{-1/2} \quad (14)$$

where ρ is density and s_{11}^E is elastic compliance. A metallic sheet (called shim) is occasionally sandwiched between the two piezoelectric plates to increase the reliability, that is, the structure can be maintained even if the ceramics fracture. Using the bimorph structure, a large magnification of the displacement is easily obtainable. However, the disadvantages include a low response speed (1 kHz) and low generative force.

A composite actuator structure called "moonie" has been developed to amplify the small displacements induced in a piezoelectric ceramic. The moonie consists of a thin multilayer element and two metal plates with a narrow moon-shaped cavity bonded together. This device has intermediate characteristics between the conventional multilayer and bimorph

actuators; this shows an order of magnitude larger displacement ($100\text{ }\mu\text{m}$) than the multilayer, and much larger generative force (100 N) with quicker response ($100\text{ }\mu\text{sec}$) than the bimorph.

Some examples of applications of piezoelectric and electrostrictive actuators are described below. The piezoelectric impact dot-matrix printer is the first mass-produced device using multilayer ceramic actuators (Fig. 14). The advantage of the piezoelectric printer head compared to the conventional magnetic types are: low energy consumption, low heat generation and fast printing speed. The longitudinal multilayer actuators do not exhibit a large displacement and thus a suitable displacement magnification mechanism is necessary. The displacement induced in a multilayer actuator pushes up the force point, and its displacement magnification is carried out through hinge levers so as to generate a large wire stroke. When the displacement in the piezoactuator is $8\text{ }\mu\text{m}$, the wire stroke of $240\text{ }\mu\text{m}$ can be obtained, that is the magnification rate is 30 times.

Bimorph structures are commonly used for VCR head tracking actuators, because of their large displacements. An auto tracking scan system uses the piezoelectric actuators so that the head follows the recording track even driven at both still and quick modes. As can be anticipated, the bimorph drive is inevitably accompanied by a torsional motion. To obtain a perfect parallel motion a special mechanism has to be employed. Piezoelectric pumps for gas or liquid utilizing an alternating bending motion of bimorph have been developed for intravenous drip injection in hospitals and for medication dispensers in chemotherapy, chronic pain and diabetes. Piezoelectric fans for cooling electronic circuits are made from a pair of bimorphs which are driven out of phase so as to blow effectively. Furthermore, piezo-bimorph type camera shutters have been widely commercialized by Minolta.

In optical control systems, lenses and mirrors require micropositioning and even the shapes of mirrors are adjusted to correct image distortions. For instance, a space qualified active mirror called articulating fold mirror utilizes six PMN electrostrictive multilayer actuators to precisely position a mirror tip and tilt in order to correct the focusing aberration of the Hubble Space Telescope.

Piezoelectric actuators are also useful for vibration suppression systems of an automobile. An electronic controlled shock absorber was developed by Toyota. The piezoelectric sensors detecting a road roughness is composed of 5 layers of 0.5 mm thick PZT discs. The actuator is made of 88 layers of 0.5 mm thick discs. Applying 500 V generates about 50 μm displacement, which is magnified by 40 times through a piston and plunger pin combination. This stroke pushes the change valve of the damping force down, then opens the bypass oil route, leading to decrease in the flow resistance. This electronically controlled shock absorber has both controllability and comfortability simultaneously.

The US Army is interested in developing a rotor control system in helicopters, because slight change of the blade angle provides drastic enhancement of controllability. Figure 15 shows a bearingless rotor flexbeam with attached piezoelectric strips. Various types of PZT-sandwiched beam structures have been investigated for such a flexbeam application and for active vibration control.

Ultrasonic Motors

An ultrasonic motor (USM) is an example of piezoelectric actuators using a resonant vibration. In ultrasonic motors linear motion is obtained from the elliptical vibration through frictional force. The motor basically consists of a high-frequency power supply, a vibrator and a slider. The vibrator is composed of a piezoelectric driving component and an elastic vibratory part, and the slider is composed of an elastic moving part and a friction

coat. The characteristics of the ultrasonic motors are low speed and high torque compared to the conventional electromagnetic motors with high speed and low torque. (29)(30)

The ultrasonic motors are classified into two types: a standing-wave type and a propagating-wave type. The standing wave is expressed by

$$x_s(x, t) = A \cos(kx) \cos(\omega t), \quad (15)$$

while the propagation wave is given by

$$\begin{aligned} x_p(x, t) &= A \cos(kx - \omega t) \\ &= A \cos(kx) \cos(\omega t) + A \cos(kx - \pi/2) \cos(\omega t - \pi/2). \end{aligned} \quad (16)$$

A propagating wave can be generated by superimposing two standing waves whose phases differ by 90 degree to each other both in time and in space. The standing-wave type is sometimes called as a vibratory-coupler or a "woodpecker" type, where a vibratory piece is connected to a piezoelectric driver and the tip portion generates flat-elliptic movement. Figure 16 shows a vibratory coupler type motor. A vibratory piece is attached to a rotor or a slider with a slight cant angle. The standing-wave type has high efficiency up to 98% theoretical. However, a problem of this type is lack of control in both clockwise and counter-clockwise directions. The principle of the propagation type is shown in Fig. 17. In the propagating-wave type, also called "surfing-type", in which a surface particle of the elastic body draws an elliptic locus due to the coupling of longitudinal and transverse waves. This type generally requires two vibration sources to generate one propagating wave, leading to low efficiency (not more than 50%), but is controllable in both the rotational directions. An ultrasonic rotatory motor is successfully used in autofocus camera to produce precise rotational displacements. The advantages of this motor over the conventional electromagnetic motor are: silent drive (inaudible), thin motor design and energy saving.

Regarding conventional electromagnetic motors, tiny motors smaller than 1 cm are rather difficult to produce with sufficient energy efficiency. Therefore, the ultrasonic motor is gaining wide spread attention. Ultrasonic motors whose efficiency is insensitive to size are superior in the mini-motor area. A compact ultrasonic rotory motor as tiny as 3 mm in diameter has been developed by Uchino et al. (31) The stator consists of a piezoelectric ring and two concave/convex metal endcaps with "windmill" shaped slots bonded together, so as to generate a coupled vibration of up-down and tortional type. Since the component number and the fabrication process were minimized, the fabrication price would be decreased remarkably, and it would be adaptive to the disposable usage. When driven at 160 kHz, the maximum revolution 600 rpm and the maximum torque 1 mN·m were obtained.

In the development of the reliable ultrasonic motors, the following themes should be systematically studied: 1. low loss and high vibration velocity piezoelectric materials development, 2. piezo-actuator designs taking account of heat generation and degradation mechanisms, 3. USM designs including displacement magnification mechanisms and frictional contact parts.

Bibliography

1. B. Jaffe, W. Cook and H. Jaffe, *Piezoelectric Ceramics*, London: Academic Press, 1971.
2. W. G. Cady, *Piezoelectricity*, New York: McGraw-Hill, Rev. Edit. by Dover, 1964.
3. F. Jona and G. Shirane, *Ferroelectric Crystals*, London: Pergamon Press, 1962.
4. M. E. Lines and A. M. Glass, *Principles and Applications of Ferroelectric Materials*, Oxford: Clarendon Press, 1977.
5. IEEE Standard on Piezoelectricity, New York, IEEE, Inc., 1978.
6. Landold and Boernstein, *Numerical Data and Functional Relationships in Science and Technology: Crystal and Solid State Physics*, vol.11, Berlin: Springer-Verlag, 1979.
7. W. A. Smith, *Proc. SPIE - The International Society for Optical Engineering* 1733, 1992.
8. H. Takeuchi, S. Jyomura, E. Yamamoto and Y. Ito, *J. Acoust. Soc. Am.*, 74, 1114, 1982.
9. Y. Yamashita, K. Yokoyama, H. Honda and T. Takahashi, *Jpn. J. Appl. Phys.*, 20, Suppl. 20-4, 183, 1981.
10. Y. Ito, H. Takeuchi, S. Jyomura, K. Nagatsuma and S. Ashida, *Appl. Phys. Lett.*, 35, 595, 1979
11. L. E. Cross, S. J. Jang, R. E. Newnham, S. Nomura and K. Uchino, *Ferroelectrics* 23, 187, 1980.
12. H. Takeuchi, H. Masuzawa, C. Nakaya and Y. Ito, *Proc. IEEE 1990 Ultrasonics Symposium*, 697, 1990.
13. J. Kuwata, K. Uchino and S. Nomura, *Jpn. J. Appl. Phys.*, 21, 1298, 1982.
14. T. R. Shrout, Z. P. Chang, N. Kim and S. Markgraf, *Ferroelectric Letters*, 12, 63, 1990.

15. R. E. Newnham, D. P. Skinner and L. E. Cross, *Materials Research Bulletin*, 13, 525, 1978.
16. W. A. Smith, *Proc. 1989 IEEE Ultrasonic Symposium*, 755, 1989.
17. Kistler, *Stress Sensor, Production Catalog*, Switzerland.
18. Tokin, *Gyroscope, Production Catalog*, Japan.
19. B. A. Auld, *Acoustic Fields and Waves in Solids*, 2nd ed., Melbourne: Robert E. Krieger, 1990.
20. G. S. Kino, *Acoustic Waves: Device Imaging and Analog Signal Processing*, Englewood Cliffs, N. J.: Prentice-Hall, 1987.
21. C. S. Desilets, J. D. Fraser and G. S. Kino, *IEEE Trans. Sonics Ultrason.*, SU-25, 115, 1978.
22. T. R. Gururaja, *Am. Ceram. Soc. Bull.*, 73, 50, 1994.
23. F. S. Foster, L. K. Ryan and D. H. Turnbull, *IEEE Trans. Ultrason. Ferroelec. Freq. Cont.*, 38, 446, 1991.
24. Y. Ito, K. Kushida, K. Sugawara and H. Takeuchi, *IEEE Trans. Ultrason. Ferroelec. Freq. Cont.*, 42, 316, 1995.
25. C. A. Rosen, *Proc. Electronic Component Symp.*, p.205, 1957.
26. S. Kawashima, O. Ohnishi, H. Hakamata, S. Tagami, A. Fukuoka, T. Inoue and S. Hirose, *Proc. IEEE Int'l Ultrasonic Symp.* '94, France, Nov., 1994.
27. C. Campbell, *Surface Acoustic Wave Devices and Their Signal Processing Applications*, San Diego, Calif. Academic Press, 1989.
28. H. Matthews, *Surface Wave Filters*, New York: Wiley Interscience, 1977.
29. K. Uchino, *Piezoelectric Actuators and Ultrasonic Motors*, Boston: Kluwer Academic Publishers, 1997.
30. S. Ueha and Y. Tomikawa, *Ultrasonic Motors*, Oxford, Clarendon Press, 1993.
31. K. Uchino, *J. Medical Ultrasonics*, 24, 1191, 1997.

Table & Figure Captions

- Table 1 Various effects in ferroelectric and ferromagnetic materials.
- Table 2 Crystallographic classification according to crystal centro-symmetry and polarity.
- Table 3 Material parameters of representative piezoelectric materials.
- Table 4 Comparison between the properties of ultrasonic transducer materials.
- Table 5 Material parameters for representative SAW materials.
-
- Figure 1 Perovskite structure ABO_3 .
- Figure 2 Dielectric constants of BaTiO_3 as a function of temperature.
- Figure 3 Phase diagram of the PZT system.
- Figure 4 Piezoelectric d strain coefficients versus composition for the PZT system.
- Figure 5 Field induced electrostrictive strain in 0.9PMN-0.1PT.
- Figure 6 Field induced strain curve for [001] oriented 0.92PZN-0.08PT.
- Figure 7 Cylindrical gyroscope commercialized by Tokin (Japan).
- Figure 8 Fundamental transducer geometry for acoustic imaging.
- Figure 9 Trapped-energy type filter.
- Figure 10 Typical SAW bi-directional filter consisting of two interdigital transducers.
- Figure 11 Piezoelectric transformer
- Figure 12 Structures of ceramic actuators.
- Figure 13 Two types of piezoelectric bimorphs: (a) antiparallel polarization type and (b) parallel polarization type.
- Figure 14 Impact dot-matrix printer head.
- Figure 15 Bearingless rotor flexbeam with attached piezoelectric strips.
- Figure 16 Vibratory coupler type ultrasonic motor.
- Figure 17 Principle of the propagating wave type ultrasonic motor.

Table 1

INPUT → MATERIAL
DEVICE → OUTPUT

OUTPUT INPUT	CHARGE CURRENT	MAGNETIZATION	STRAIN	TEMPERATURE	LIGHT
ELEC. FIELD	Permittivity Conductivity	Electro-mag. effect	Converse piezo-effect	Elec. caloric effect	Elec.-optic effect
Mag. FIELD	Mag.-electric effect	Permeability	Magneto- striction	Mag. Caloric effect	Magneto- optic effect
STRESS	Piezoelectric effect	Piezomag. effect	Elastic constant	—	Photoelastic effect
HEAT	Pyroelectric effect	—	Thermal expansion	Specific heat	—
LIGHT	Photovoltaic effect	—	Photostriction	—	Refractive index

Diagonal Coupling Smart Material Sensor
 Off-diagonal Coupling Actuator

Table 2

Polarity	Symmetry	Crystal system										
		Cubic		Hexagonal		Tetragonal		Rhombic		Orthorhombic	Monoclinic	Triclinic
Non-polar (22)	Centro (11)	m3m	m3	6/mmm	6/m	4/mmm	4/m	3m	3	mmm	2/m	
	Non-centro (21)	432	23	622	6	422	4	32		222		
		32m		6m2		42m						
Polar (Pyroelectric) (10)				6mm	6	4mm	4	3m	3	mm2	2 m	1

Table 3

Parameter	Quartz	BaTiO ₃	PZT 4	PZT 5H	(Pb,Sm)TiO ₃	PVDF-TrFE
d_{33} (pC/N)	2.3	190	289	593	65	33
g_{33} (10^{-3} Vm/N)	57.8	12.6	26.1	19.7	42	380
k_t	0.09	0.38	0.51	0.50	0.50	0.30
k_p		0.33	0.58	0.65	0.03	
$\epsilon_{33}^T/\epsilon_0$	5	1700	1300	3400	175	6
Q_m	$> 10^5$		500	65	900	3 - 10
T_c (°C)		120	328	193	355	

Table 4

	PZT ceramic	PVDF polymer	PZT-polymer composite	ZnO film
k_t	0.45 - 0.55	0.20 - 0.30	0.60 - 0.75	0.20 - 0.30
Z (Mray/s)	20 - 30	1.5 - 4	4 - 20	35
$\epsilon_{33}^T/\epsilon_0$	200 - 5000	10	50 - 2500	10
$\tan\delta$ (%)	< 1	1.5 - 5	< 1	< 1
Q_m	10 - 1000	5 - 10	2 - 50	10
ρ (g/cm ³)	5.5 - 8	1 - 2	2 - 5	3 - 6

Table 5

	Material	Cut - Propagation direction	k^2 (%)	TCD (ppm/°C)	V_0 (m/s)	ϵ_r
Single crystal	Quartz	ST - X	0.16	0	3158	4.5
	LiNbO ₃	128°Y - X	5.5	-74	3960	35
	LiTaO ₃	X112° - Y	0.75	-18	3290	42
	Li ₂ B ₄ O ₇	(110) <001>	0.8	0	3467	9.5
Ceramic	PZT-In(Li _{3/5} W _{2/5})O ₃		1.0	10	2270	690
	(Pb,Nd)(Ti,Mn,In)O ₃		2.6	< 1	2554	225
Thin film	ZnO / glass		0.64	-15	3150	8.5
	ZnO / Sapphire		1.0	-30	5000	8.5

Fig. 1

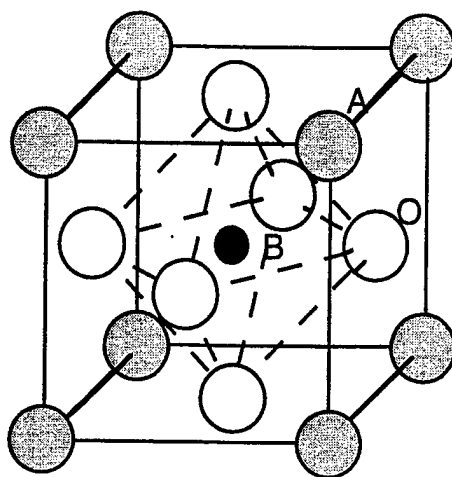


Fig. 2

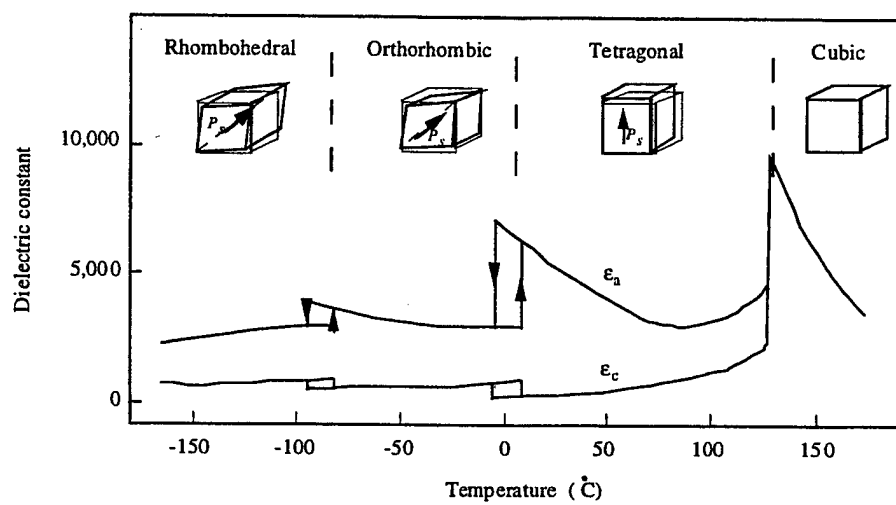


Fig. 3

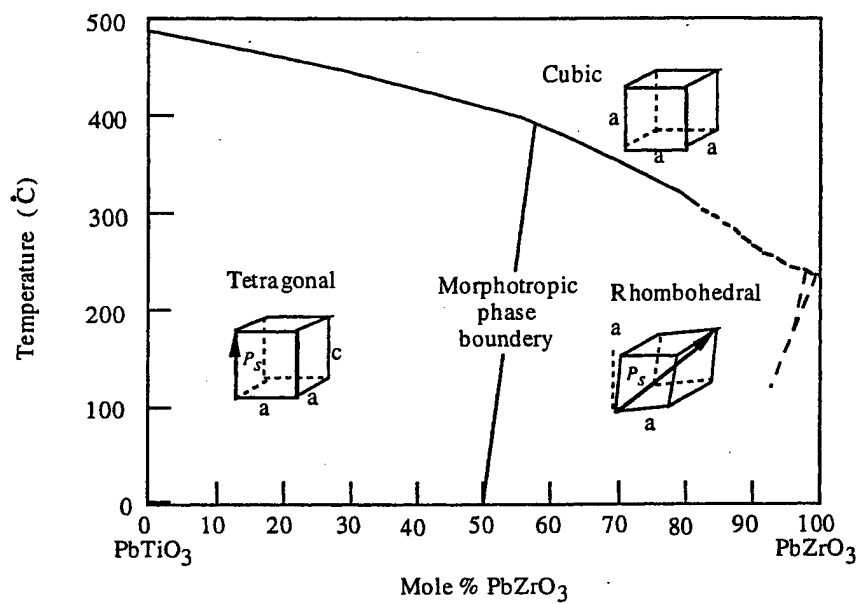


Fig. 4

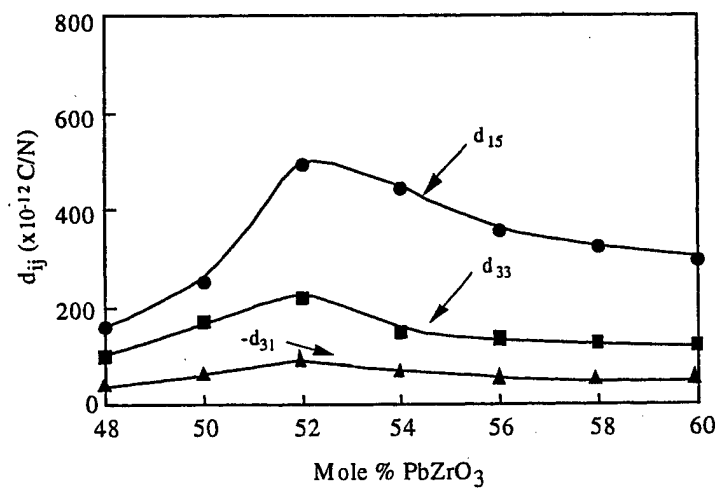


Fig. 5

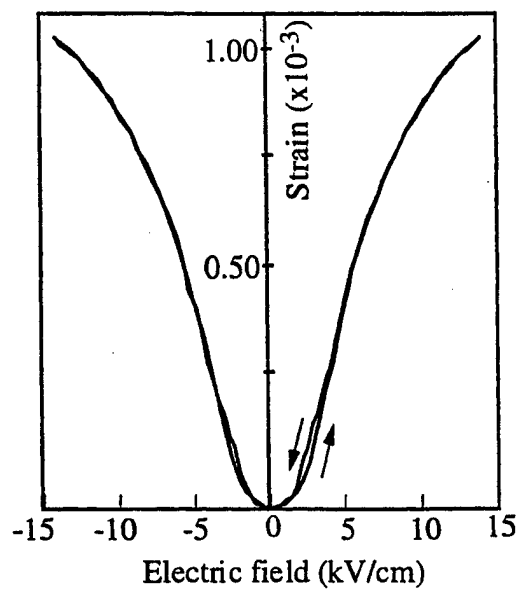


Fig. 6

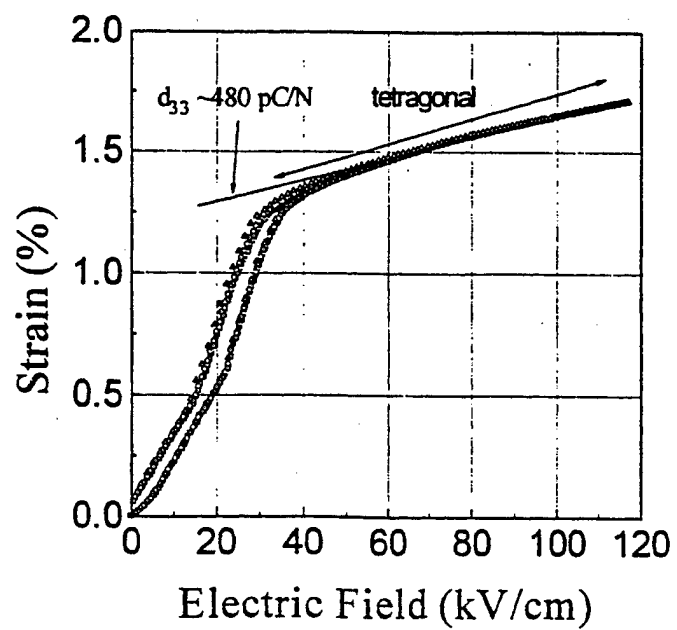


Fig. 7

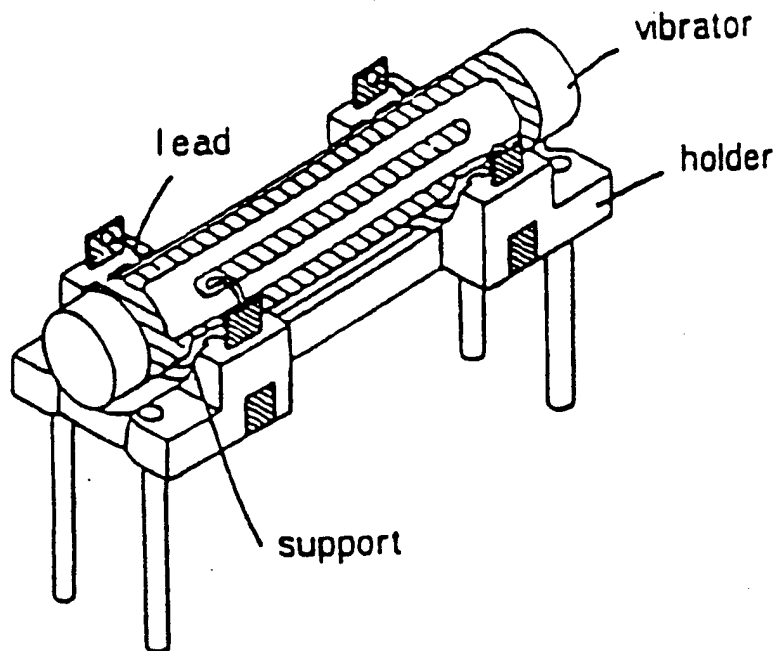


Fig. 8

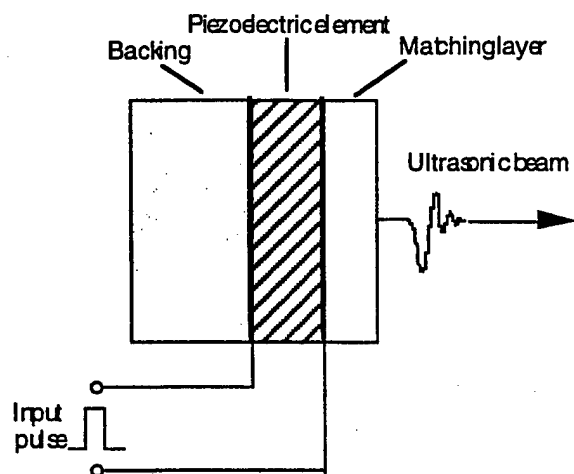


Fig. 9

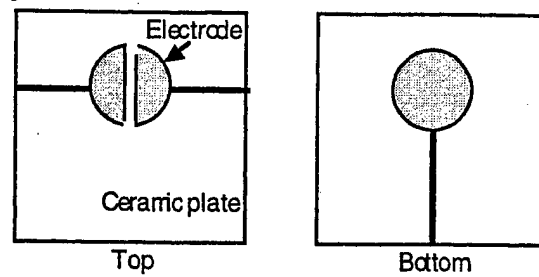


Fig. 10

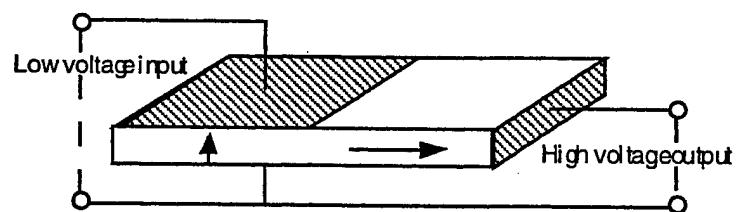


Fig. 11

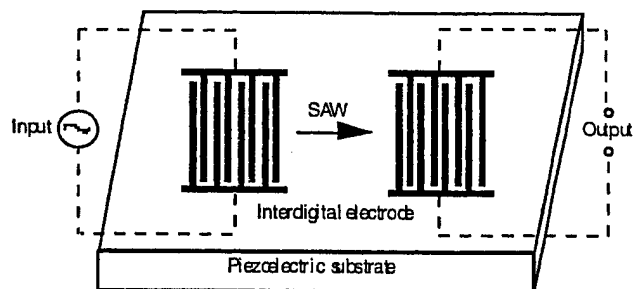


Fig. 12

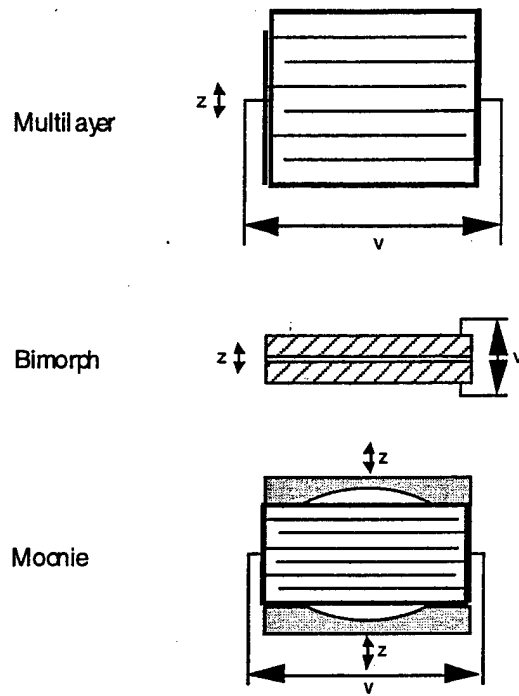


Fig. 13

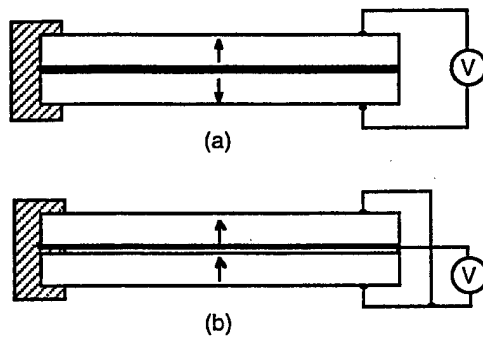


Fig. 14

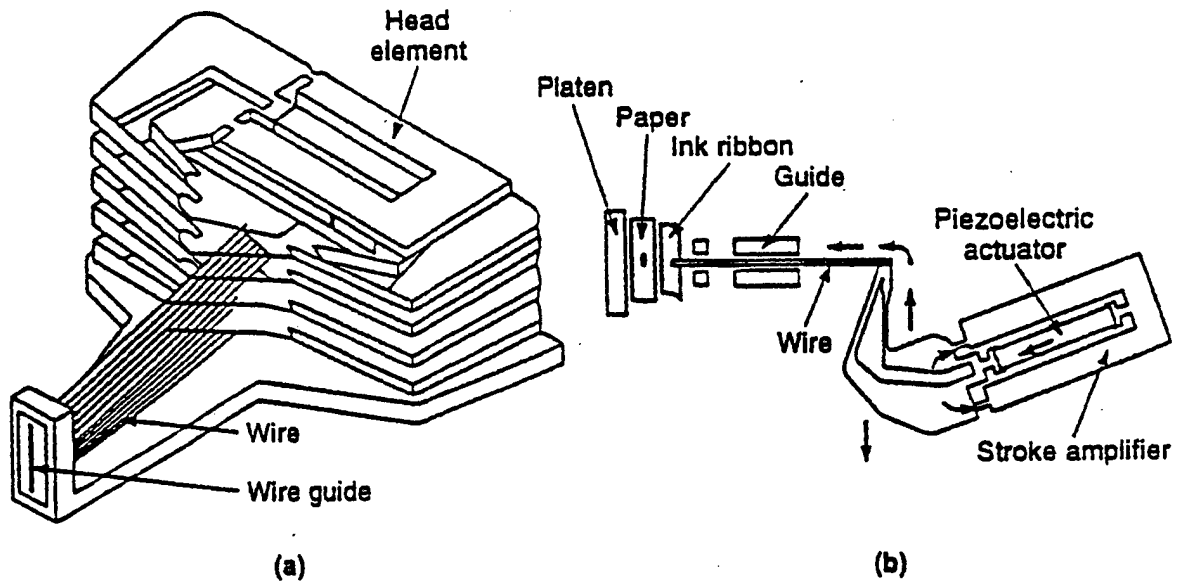


Fig. 15

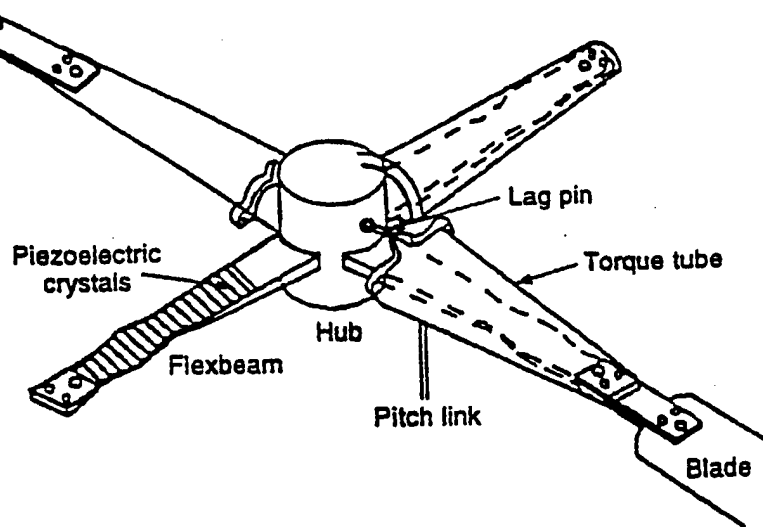


Fig. 16

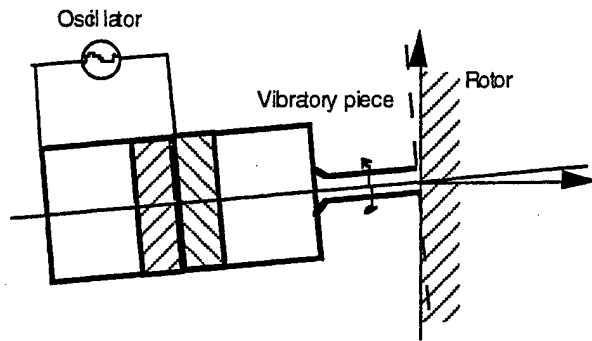
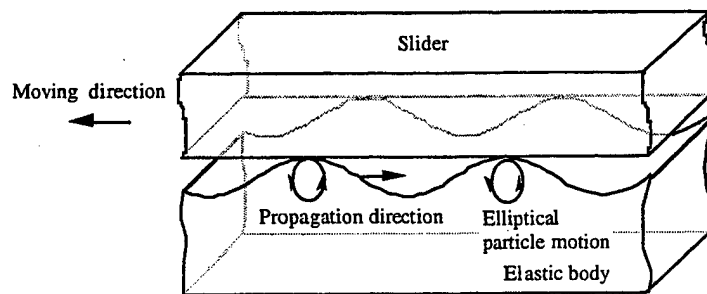


Fig. 17



APPENDIX 3

Observation of the flexoelectric effect in relaxor $\text{Pb}(\text{Mg}_{1/3}\text{Nb}_{2/3})\text{O}_3$ ceramics

Wenhui Ma and L. Eric Cross^{a)}

Materials Research Laboratory, Pennsylvania State University, University Park, Pennsylvania 16802

(Received 31 October 2000; accepted for publication 22 January 2001)

The relationship between elastic strain gradient and electric polarization was investigated in the relaxor ferroelectric lead magnesium niobate ceramic. Experimental studies indicated that flexoelectric polarization is linearly proportional to the applied strain gradient, and the flexoelectric coefficient μ_{12} is calculated to be 4×10^{-6} C/m, which is much higher than the early phenomenological estimations. © 2001 American Institute of Physics. [DOI: 10.1063/1.1356444]

The piezoelectric effect is the linear relationship between electric polarization and applied elastic stress (direct effect) or between elastic strain and applied electric field (converse effect). Due to the symmetry requirements, the piezoelectric effect may only exist in 20 crystal point groups where center of symmetry is absent. More than three decades ago, phenomenological analysis¹ stated that electric polarization might be induced by inhomogeneous strain in the materials. Later the term flexoelectric was coined to describe such an effect in analogy to an effect discovered in the nonpiezoelectric liquid crystals,² and tensor property³ and microscopic theory⁴ were investigated theoretically for single crystals. The flexoelectric effect is defined by the following relation:

$$P_i = \mu_{ijkl} \frac{\partial \epsilon_j}{\partial x_k} \quad (1)$$

where P_i is the i th component of flexoelectric polarization, μ_{ijkl} is the flexoelectric coefficient, ϵ_{ij} is the elastic strain, and x_k is the position coordinate. Flexoelectricity is controlled by a fourth-rank tensor, and thus is a property of all insulating solids, but so far no flexoelectric coefficients have in fact been measured. In the late 1960s, attempts were made to investigate the electrical polarization in nonpiezoelectric CaWO_4 crystals during torsional deformation, which might be closely associated with the flexoelectric effect,⁵ but the polarization had been attributed to the disappearance of the center of symmetry after torsion, rather than the effect of the strain gradient. In the late 1980s, a tiny flexoelectric effect was observed in an isotropic elastomer with a static flexoelectric coefficient of the order of magnitude of 10^{-11} – 10^{-10} C/m.⁶

Recently, an idea was developed for designing 0–3 piezoelectric composites based on the flexoelectric effect where none of the components are piezoelectric.⁷ If the flexoelectric coefficients are large enough for practical applications a range of properly engineered flexoelectric composite structures could provide completely new piezoelectric capability. Recent studies^{8,9} have indicated that the relaxor ferroelectric perovskites like $\text{Pb}(\text{Mg}_{1/3}\text{Nb}_{2/3})\text{O}_3$ (PMN) are exceedingly sensitive to elastic stress in the region of temperature between the dielectric permittivity maximum T_m

and the freezing temperature T_f from the Vogel–Fulcher relationship. In this letter, we report the investigation of flexoelectric effect in relaxor PMN ceramics.

The flexoelectric measurements were carried out at room temperature by using an experimental setup shown schematically in Fig. 1. The PMN ceramic bars (76.3 mm length, 12.7 mm width, and 2.5 mm thickness) were provided by the TRS company of State College, Pennsylvania. A very thin layer of sputtered gold was used as electrode, the bottom surface of the sample is fully covered with gold while on the top a series of 3 mm diameter electrodes were prepared. Strain gradient was generated in the samples along the thickness direction by a loudspeaker. A MicroStrain DVRT transducer was used to measure the displacement at several positions along the sample bar. The loudspeaker was driven by an HP467A power amplifier with a 1 Hz sinusoidal signal from an SR830 DSP lock-in amplifier. The generated current was monitored by the lock-in amplifier. The generated polarization may be calculated using the following equation:

$$P_3 = \frac{i}{2\pi f A} \quad (2)$$

where i is the alternating current, A is the electrode area, and f is the driving frequency of the loudspeaker.

The macroscopic symmetry of PMN between T_m and T_f is cubic $m3m$, while the unpoled ceramics are regarded as isotropic. Thus, the flexoelectric tensor matrices may be written as

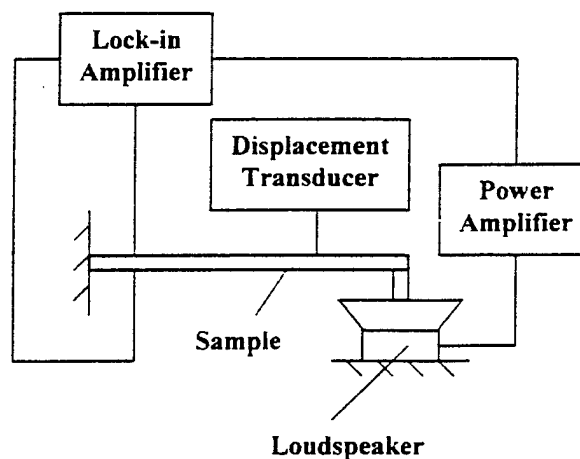


FIG. 1. Experimental setup for the measurement of the flexoelectric effect.

^{a)}Electronic mail: lec3@psu.edu

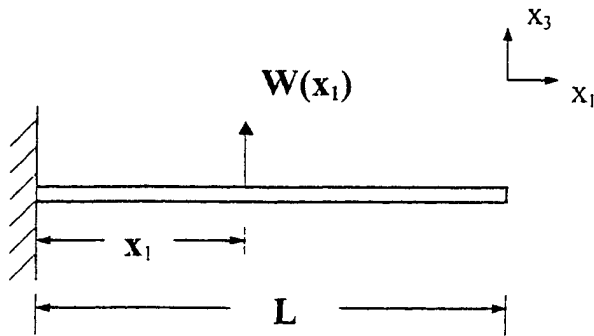


FIG. 2. Schematic diagram of a cantilevered beam and the axial arrangement.

$$\begin{pmatrix} \mu_{11} & \mu_{12} & \mu_{12} & 0 & 0 & 0 \\ \mu_{12} & \mu_{11} & \mu_{12} & 0 & 0 & 0 \\ \mu_{12} & \mu_{12} & \mu_{11} & 0 & 0 & 0 \\ 0 & 0 & 0 & \mu_{44} & 0 & 0 \\ 0 & 0 & 0 & 0 & \mu_{44} & 0 \\ 0 & 0 & 0 & 0 & 0 & \mu_{44} \end{pmatrix}.$$

For the present situation in Fig. 1, only the transverse effect exists, so the flexoelectric equation may be simplified as

$$P_3 = \mu_{12} \frac{\partial \epsilon_{11}}{\partial x_3}. \quad (3)$$

The strain in the PMN ceramic bar was calculated by assuming the natural vibration of a cantilevered beam shown in Fig. 2. The mode shape¹⁰ can be written as

$$\begin{aligned} W_r(x_1) = & A_r [(\sin \beta_r L - \sinh \beta_r L)(\sin \beta_r x_1 \\ & - \sinh \beta_r x_1) + (\cos \beta_r L + \cosh \beta_r L) \\ & \times (\cos \beta_r x_1 - \cosh \beta_r x_1)], \end{aligned} \quad (4)$$

where $A_r = C_1 / (\sin \beta_r L - \sinh \beta_r L)$, $r = 1, 2, \dots$

Here we only consider the fundamental mode ($r=1$), therefore we have $\beta_1 L = 1.875$. C_1 can be determined from the boundary condition, i.e., the measured vertical displacement of the PMN bar.

The gradient of transverse strain along the thickness direction can be written as¹¹

$$\frac{\partial \epsilon_{11}}{\partial x_3} = \frac{\partial^2 W(x_1)}{\partial x_1^2}. \quad (5)$$

Figure 3 showed the experimental results of the strain gradient induced polarization at two positions of the PMN bar, one is near the clamped end ($x_1/L=0.18$) where the strain gradient is supposed to be higher, while the other is near the free end ($x_1/L=0.67$). It is seen that the flexoelectric polarization is proportional to the strain gradient. The slopes of the polarization versus strain gradient curve obtained at two positions are very close. At the same driving voltage, the clamped end generated higher polarization than the free end. Based on the experimental results, μ_{12} was calculated to be about 4×10^{-6} C/m.

The temperature dependence of dielectric permittivity and tangent loss at various frequencies ranging from 1 kHz

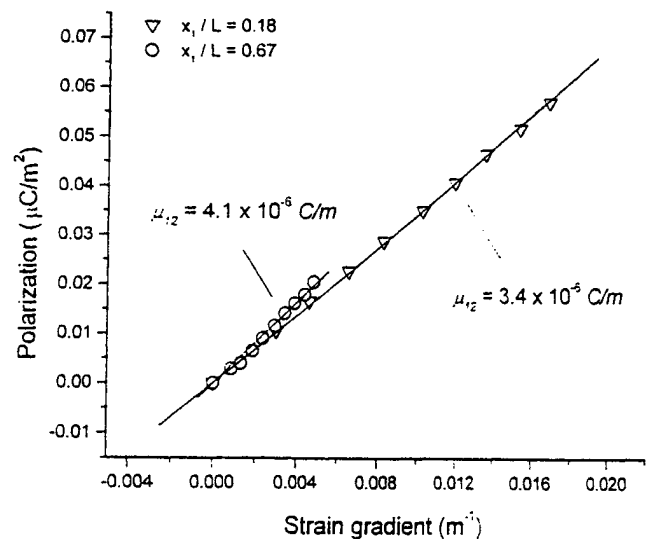


FIG. 3. The relationship between flexoelectric polarization and strain gradient in the relaxor $\text{Pb}(\text{Mg}_{1/3}\text{Nb}_{2/3})\text{O}_3$ ceramics.

to 1 MHz have been investigated and the dielectric peak temperatures are well below room temperature. At room temperature, the materials should be cubic and the unpoled ceramics are isotropic and should not exhibit any piezoelectric effect in principle. Furthermore, for the current measurement configuration, the upper and lower parts of the sample endure strain of opposite sign. So even if there is any remnant piezoelectric effect, the net effect in the whole sample should be zero because the piezoelectric polarization generated in the upper and lower halves would cancel.

Former theoretical analysis estimated the flexoelectric coefficient to be of the order of magnitude of e/a ,^{1,3,4} where e is the absolute value of electron charge and a is the lattice parameter. Generally, e/a is around 10^{-10} C/m for almost all materials, which is very small. The current experimental results on the relaxor PMN ceramics are much higher than the phenomenological estimations and are very encouraging. Such high flexoelectric effect observed in the relaxor PMN ceramics may be associated with the high dielectric constant (around 13 000 at 1 kHz and room temperature), so the charge separation becomes much easier than those in the low permittivity materials.

In summary, a flexoelectric effect has been investigated in the relaxor ferroelectric PMN ceramic, the measured flexoelectric coefficient is about four orders of magnitude higher than the earlier theoretical estimation.

¹Sh. M. Kogan, Sov. Phys. Solid State 5, 2069 (1964).

²R. B. Meyer, Phys. Rev. Lett. 22, 918 (1969).

³V. L. Indenbom, E. B. Loginov, and M. A. Osipov, Sov. Phys. Crystallogr. 26, 656 (1981).

⁴A. K. Tagantsev, Sov. Phys. JETP 61, 1246 (1985).

⁵I. S. Zheludev, Yu. S. Likhacheva, and N. A. Lileeva, Sov. Phys. Crystallogr. 14, 425 (1969).

⁶M. Marvan and A. Havránek, Prog. Colloid Polym. Sci. 78, 33 (1988).

⁷J. Fousek, L. E. Cross, and D. B. Litvin, Mater. Lett. 39, 287 (1999).

⁸L. Eric Cross, Ferroelectrics 76, 241 (1987).

⁹D. Viehland, Ph.D. dissertation, The Pennsylvania State University, 1991.

¹⁰L. Meirovitch, Principles and Techniques of Vibrations (Prentice Hall, Upper Saddle River, NJ, 1997).

¹¹R. L. Bisplinghoff, J. W. Mar, and T. H. H. Pian, Statics of Deformable Solids (Addison-Wesley, Reading, MA, 1965).

APPENDIX 4

Landau-Ginzburg model for antiferroelectric phase transitions based on microscopic symmetry

Richard A. Hatt

Materials Research Laboratory, The Pennsylvania State University, University Park, Pennsylvania 16802

Wenwu Cao

Materials Research Laboratory and Department of Mathematics, The Pennsylvania State University, University Park, Pennsylvania 16802

(Received 15 February 2000)

The only Landau-type model for antiferroelectric phase transitions was proposed by Kittel, in which two interpenetrating sublattices with opposite polarizations of equal amplitude were assumed. The theory, however, did not include any mechanism to specify the relative spatial positions of the two sublattices, and therefore could not address the cell doubling during antiferroelectric phase transitions. We propose a Landau-Ginzburg-type model based on microscopic symmetry and group theory, which can, without having to assume sublattices, account for all aspects of antiferroelectric states, including local dipole orientation and cell doubling. The average of these dipoles naturally leads to the Kittel model. The inclusion of gradient terms in the free energy allows the modeling of multidomain structures and domain walls in antiferroelectric states.

INTRODUCTION

Kittel¹ proposed a macroscopic Landau-type model for the antiferroelectric (AFE) state by introducing two interpenetrating sublattices with opposite polarizations. His model describes a second-order transition from the paraelectric state to the antiferroelectric state, by truncating the free energy at the fourth order:

$$F = \alpha_1(P_1^2 + P_2^2) + \alpha_2 P_1 P_2 + \alpha_{11}(P_1^4 + P_2^4), \quad (1)$$

where P_1 and P_2 are the polarizations of the sublattices. If $\alpha_2 > 0$, the transition will favor P_1 and P_2 being antiparallel, making the low-temperature phase antiferroelectric. On the other hand, if $\alpha_2 < 0$, the transition will favor P_1 and P_2 being parallel, and the transition will lead to a ferroelectric state.¹⁻²

This model has the intrinsic limitation that it contains only local interactions. In other words, there is no mechanism to fix the spatial relationship between the two sublattice polarizations within the crystal. This local model creates uncertainty in the antiferroelectric state. For example, the sublattice polarizations P_1 and P_2 are assumed at the same location in space (or can be anywhere in space), which leads to the cancellation of P_1 and P_2 . Such a situation does not fully describe the antiferroelectric state in which adjacent primitive cells acquire opposite dipole moments and the local polarization at any space point is actually nonzero. Using group-theoretical techniques, we propose a continuum model for the antiferroelectric state built upon microscopic symmetry. The symmetry allowed distortions associated with the soft mode are given in our model, which accounts for the formation of antiparallel dipoles in adjacent cells. The free energy has also been expanded to include gradient terms of the order parameter so that multidomain structures, such as orientation twins and antiphase walls, can be modeled using the same formulation. Specifically, in this paper we will use ammonium dihydrogen phosphate ($\text{NH}_4\text{H}_2\text{PO}_4$) (commonly

referred to as ADP) as a prototype system to illustrate the procedure and the characteristics of the antiferroelectric phase transition.

ANTIFERROELECTRIC PHASE TRANSITION

The high-temperature phase of ADP is tetragonal with space group $I\bar{4}2d$.³⁻⁶ Following the notation of the *International Tables for Crystallography*,⁷ the conventional (non-primitive) unit cell contains four formula units. Two of the formula units are in the primitive cell while the other two are related by the centering translation $(\frac{1}{2}, \frac{1}{2}, \frac{1}{2})$. At $T_C \approx -125^\circ\text{C}$, the material undergoes an antiferroelectric transition to an orthorhombic phase with space group $P2_12_12_1$.^{6,8} The transition is driven by a zone-boundary M -point soft mode and results in ionic displacements that create one dipole moment in each formula unit (four dipoles per AFE unit cell) as shown in Fig. 1. These dipole moments form a net antiferroelectric polarization along the $[100]$ or $[010]$ of the parent phase. This means that the fourfold rotational inversion axis of the parent paraelectric phase is lost during the transition, which leads to two rotationally related, energetically equivalent orientation domain states in the low-temperature phase. Moreover, the transition causes a primitive-cell doubling (equivalently, the centering point in the conventional parent cell is lost), leading to two additional

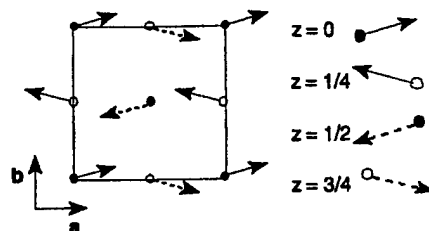


FIG. 1. Dipoles formed in the antiferroelectric phase of ADP in a conventional cell. The lattice displacement pattern can be generated from group theory.

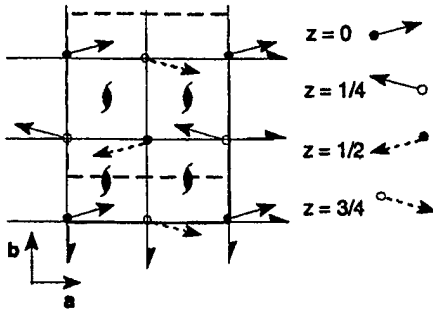


FIG. 2. Microscopic positions of the symmetry elements, creating the antiferroelectric polarization. The AFE unit cell is shown by the dashed line, with origin at $(0, \frac{1}{4}, \frac{3}{8})$. The screw axes parallel to \mathbf{a} are at $z = \frac{3}{8}$, and the screw axes parallel to \mathbf{b} are at $z = \frac{1}{4}$.

antiphase states that are translationally related to the two orientation states. Overall, there are four possible domains in the AFE state of ADP.

GROUP THEORETICAL DESCRIPTION OF THE TRANSITION

Once the structures and space groups of the high- and low-temperature phases have been determined, the microscopic positions of the symmetry elements are fixed (we will use the settings of Ref. 7), as shown in Fig. 2. Specifically, we note that the three mutually perpendicular twofold screw axes in the AFE phase do not allow a net dipole moment for the unit cell of the low-temperature phase, although they do allow antiferroelectric polarizations.

The M -point soft mode driving the transition in ADP may be described by the physically irreducible M_3M_4 representation,⁴ which is simply the direct sum $M_3 \oplus M_3^*$ (here we use the labeling of Miller and Love⁹). This representation carries a two-component order parameter (OP), (p_1, p_2) , whose values are listed in Table I. Physically, the OP corresponds to the molecular dipole moments within the \mathbf{a} - \mathbf{b} plane; p_1 represents the component along the \mathbf{a} direction, and p_2 represents the component along the \mathbf{b} direction. This OP is a continuum field, which is equal to the dipole moment at the sites of each formula unit.

Knowing the irreducible representation allows the lattice distortions that arise in the transition to be calculated using the ISOTROPY¹⁰ software package. For simplicity we will restrict our discussion to distortions arising at Wyckoff sites only, which are listed in Table II. These distortions can be used to construct the dipole arrangement within the low-temperature unit cell. As an example, consider the distortions that arise in domain S_1 , for which the OP is $(p_1, p_2) = (p_a, p_b)$. If $p_a > p_b$, the distortions result in the configu-

TABLE I. Values of the order parameter for different domain states.

Domain	Order parameter
S_1	(p_a, p_b)
S_2	$(p_b, -p_a)$
S_3	$(-p_a, -p_b)$
S_4	$(-p_b, p_a)$

TABLE II. Group theoretically allowed distortions at Wyckoff sites in domain S_1 .

Position	Distortions	Relationship to $(0,0,0)$ site
$(0,0,0)$	$p_a(1,0,0) + p_b(0,-1,0)$	$\{E 000\}$
$(\frac{1}{2}, \frac{1}{2}, \frac{1}{2})$	$p_a(-1,0,0) + p_b(0,1,0)$	$\{C_{2z} \frac{1}{2}\frac{1}{2}\frac{1}{2}\}$
$(0, \frac{1}{2}, \frac{1}{4})$	$p_a(-1,0,0) + p_b(0,-1,0)$	$\{C_{2y} \frac{1}{2}1\frac{3}{4}\}$
$(\frac{1}{2}, 1, \frac{3}{4})$	$p_a(1,0,0) + p_b(0,1,0)$	$\{C_{2x} \frac{1}{2}1\frac{3}{4}\}$

ration shown in Fig. 1, which agree well with the observed dipolar distribution by Blinc *et al.*⁸

Figure 1 was constructed based only on the microscopic positioning of the symmetry elements and the allowed distortions from group theoretical considerations, as in Fig. 2. For example, a dipole moment at position $(0, 0, 0)$ necessarily means, by action of the screw axis parallel to the z axis, an oppositely directed dipole moment at the parent cell centering point of $(\frac{1}{2}, \frac{1}{2}, \frac{1}{2})$. The screw axis parallel to the x axis further implies, from these two dipoles, that the other two antialigned dipoles within the AFE unit cell must be present. Hence, there is no need for defining sublattices and no need to explain why such sublattices would adopt exactly equal magnitudes but opposite orientation. More importantly, the spatial relationship between the two sublattices naturally comes out of our model. If a single dipole moment is formed within a parent formula unit, one can generate its counterparts by symmetry requirements to form the antiferroelectric polarization of the whole unit cell of the low-temperature phase. Also, since the dipole moment at the centering point $(\frac{1}{2}, \frac{1}{2}, \frac{1}{2})$ is opposite to the dipole moment at $(0,0,0)$, the doubling of the unit cell size is naturally explained.

HYSTERESIS AND THE RELATION TO THE SUBLATTICES PROPOSED BY KITTEL

A well-known characteristic of antiferroelectrics is the double hysteresis loop, as shown in Fig. 3. In the one-dimensional antiferroelectric model proposed by Kittel, there is no net polarization. However, if an external electric field is applied, the sublattice polarization parallel to the field grows and the other sublattice polarization opposite to the field shrinks, resulting in a net polarization. When the field strength becomes sufficiently large, the polarization in the direction opposite to the field abruptly switches orientation to become parallel to the field, resulting in a ferroelectric state. Because of symmetry constraints, a double hysteresis

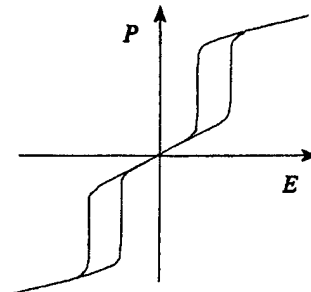


FIG. 3. Double hysteresis loop, a characteristic of the antiferroelectric state.

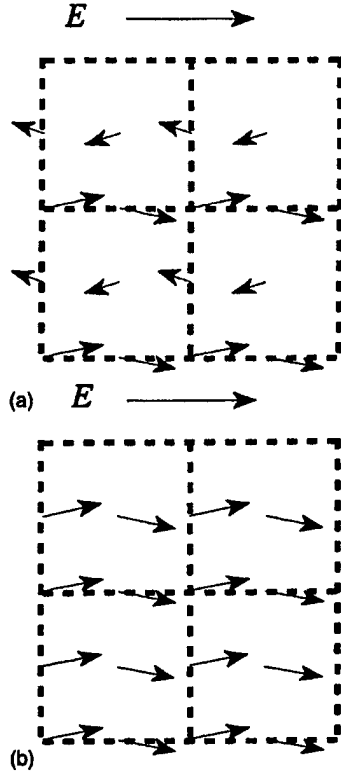


FIG. 4. Molecular dipole moments in the presence of an external electric field, (a) before switching and (b) after switching.

will be produced during such a switching process.²

In our model, we describe the hysteresis in terms of the dipole moments associated with each of the four formula units in an AFE unit cell. Consider an external electric field applied to domain S_1 , parallel to the $+a$ direction. This field will interact with the dipoles, causing $p_a > 0$ to increase in magnitude and $p_a < 0$ to decrease in magnitude, as shown in Fig. 4(a). Note that p_b is not affected in our model. At sufficiently large field strength, the dipoles with p_a antiparallel to the external field will flip so that p_a becomes parallel to $+a$, as shown in Fig. 4(b). This results in a state in which the dipole components are parallel along the a direction and antiparallel along the b direction. It is a ferroelectric state with the polarization along a , but with a cell size twice that of the Kittel model.

In order to make the connection between our microscopic model and the Kittel macroscopic model, we use the definition of the polarization, which is an average of molecular dipole moments over a given volume $P = (1/V)\sum p_i$. The sublattice polarizations P_1 and P_2 in the Kittel one-dimensional model can then be defined, in terms of the molecular dipole moments in our model, as

$$P_1 = \frac{1}{V} \sum_{(p_a > 0)} p_{ai}, \quad P_2 = \frac{1}{V} \sum_{(p_a < 0)} p_{ai}. \quad (2)$$

In other words, in the AFE state the formula units containing a positive dipole-moment component in the a direction form one sublattice with polarization P_1 , and the formula units containing a negative dipole-moment component in the a direction form the other sublattice with polarization P_2 . The

TABLE III. Invariants for the antiferroelectric transition driven by a soft mode corresponding to the M_3M_4 irreducible representation.

$\phi^{(2)} = p_1^2 + p_2^2$	$\delta_1 = \left(\frac{\partial p_1}{\partial x}\right)^2 + \left(\frac{\partial p_2}{\partial y}\right)^2$
$\phi_1^{(4)} = (p_1^2 + p_2^2)^2$	$\delta_2 = \frac{\partial p_1}{\partial x} \frac{\partial p_2}{\partial x} - \frac{\partial p_1}{\partial y} \frac{\partial p_2}{\partial y}$
$\phi_2^{(4)} = p_1^4 + p_2^4$	$\delta_3 = \left(\frac{\partial p_1}{\partial y}\right)^2 + \left(\frac{\partial p_2}{\partial x}\right)^2$
$\phi_3^{(4)} = p_1^3 p_2 - p_1 p_2^3$	

difference between the microscopic theory presented here and macroscopic continuum theory of Kittel is that the latter cannot provide the spatial relationships among dipoles of adjacent cells, and cannot account for the dipole tilt which occurs in the ADP system.

LANDAU-GINZBURG FREE ENERGY BASED ON MICROSCOPIC SYMMETRY

Adding OP gradient terms to the free energy, i.e., using the Landau-Ginzburg-type free energy, will allow us to describe inhomogeneous structures, such as orientational twins and antiphase walls. The invariant polynomials of the OP and its derivatives can also be obtained using the ISOTROPY program. In this paper, we have truncated the free energy at the fourth power of the OP to limit our discussions to a second-order transition. We also assume that the OP field varies slowly in space so that only the first derivatives of the OP are included in the free energy. We write

$$F = A\phi^{(2)} + B_i\phi_i^{(4)} + D_i\delta_i \quad (i=1,2,3), \quad (3)$$

where the invariant polynomials $\phi^{(2)}$, $\phi_i^{(4)}$, and δ_i are given in Table III. The coefficients $A = A_0(T - T_c)$, B_i , and D_i are constants.

For single domain states, all derivatives of the OP must vanish; i.e., $\delta_i = 0$. Considering the single domain state S_1 , the two component OP is (p_a, p_b) with both p_a and p_b non-zero. Since the symmetry of the low-temperature phase is known, the ionic displacements and dipole moments in each unit cell can be determined experimentally from neutron scattering. In other words, the ratio of the amplitudes $\kappa = p_a/p_b$ can be measured in the antiferroelectric state

$$p_b = \kappa p_a. \quad (4)$$

Because all derivatives of the OP vanished in the single domain state, energy minimization of Eq. (3) leads to

$$\begin{aligned} \left. \frac{\partial F}{\partial p_1} \right|_{p=(p_a, \kappa p_a)} &= 2Ap_a + [4B_1(l + \kappa^2) + 4B_2 \\ &\quad + B_3(3\kappa - \kappa^3)]p_a^3 = 0, \end{aligned} \quad (5a)$$

$$\left. \frac{\partial F}{\partial p_2} \right|_{p=(p_a, \kappa p_a)} = 2A\kappa p_a + \left[4B_1(1+\kappa^2) + 4B_2\kappa^2 + B_3 \left(\frac{1}{\kappa} - 3\kappa \right) \right] \kappa p_a^3 = 0. \quad (5b)$$

In order for Eqs. (5a) and (5b) to give the same solution for p_a , the sum involving the B_2 and B_3 terms must be equal,

$$4B_2 + B_3(3\kappa - \kappa^3) = 4B_2\kappa^2 + B_3 \left(\frac{1}{\kappa} - 3\kappa \right), \quad (6)$$

which can be written as a fourth-degree polynomial equation in κ :

$$\kappa^4 + b\kappa^3 - 6\kappa^2 - b\kappa + 1 = 0 \quad (7)$$

with $b = 4B_2/B_3$. This equation has four roots,

$$\left(\kappa_1, -\frac{1}{\kappa_1}, \kappa_2, -\frac{1}{\kappa_2} \right), \quad (8)$$

where

$$\kappa_1 = -\frac{b}{4} - \frac{1}{4} \sqrt{16+b^2} + \frac{1}{2\sqrt{2}} (16+b^2)^{1/4} \sqrt{b + \sqrt{16+b^2}}, \quad (9a)$$

$$\kappa_2 = -\frac{b}{4} + \frac{1}{4} \sqrt{16+b^2} + \frac{1}{2\sqrt{2}} (16+b^2)^{1/4} \sqrt{-b + \sqrt{16+b^2}}. \quad (9b)$$

One of the above solutions, Eq. (9a), will be less than 1 and greater than 0 (i.e., $0 < \kappa < 1$), which is the solution we seek since it corresponds to the OP in domain S_1 , with $p_a > p_b$ (see Fig. 1). Because Eq. (7) does not contain any temperature-dependent terms, the solution κ will be temperature independent.

Once κ is determined, Eq. 5(a) allows the value of p_a to be determined as a function of the expansion coefficients in Eq. (3):

$$p_a^2 = \frac{-2A}{4B_1(1+\kappa^2) + 4B_2 + B_3(3\kappa - \kappa^3)}. \quad (10)$$

We note that the expansion coefficient A is temperature dependent, $A = A_0(T - T_c)$, so that the amplitude of the order parameter satisfies the universal relation for a second order phase transition, i.e.,

$$p_b \propto p_a \propto \sqrt{T_c - T}.$$

ORDER-PARAMETER PROFILES FOR TWINS AND ANTIPHASE STRUCTURES

The Landau-Ginzburg free energy, Eq. (3), allows us to describe inhomogeneous structures. We will study both orientation twins and antiphase structures in the AFE phase, each composed of two different domains separated by a domain wall. Since there are four possible domains in the AFE state, there will be $4 \times 4 = 16$ possible pairings of domains from which we can construct orientation twins or antiphase walls. However, using the idea of equivalence in group

TABLE IV. Equivalence classes of two-domain (twins and antiphase) structures.

Domain pair	Type	Relation to S_1
(S_1, S_2)	orientation twin	$\{\sigma_{bd} 0 \frac{1}{2} \frac{1}{4}\}$
(S_1, S_4)	orientation twin	$\{\sigma_{bd} \frac{1}{2} 1 \frac{3}{4}\}$
(S_1, S_3)	antiphase structure	$\{E \frac{1}{2} \frac{1}{2} \frac{1}{2}\}$

theory, the pairing set can be much reduced. We find three classes of two-domain structures to be considered, as listed in Table IV along with the type of structure represented (the trivial degenerate structure that has the same domain on both sides of the wall is actually a single domain structure): two orientation twins, and one antiphase structure.

We will first consider the orientation twin formed by domains S_1 and S_2 . The domain wall orientation for such a twin can be determined by strain matching,^{11,12} noting that this transition belongs to the Aizu¹³ species $\bar{4}2mF222$. The strain allowed domain walls are the planes $x = \pm y$ (see Fig. 5). Since properties of the crystal will change only along the direction normal to this wall, we will rotate to a new coordinate system so that x' is normal to the wall. The OP components (and any other properties of the twin) then will be functions of x' only. This means that the derivatives in the gradient part of the free energy, Eq. (3), can be rewritten as

$$\frac{\partial p}{\partial x} \rightarrow \pm \frac{1}{\sqrt{2}} \frac{\partial p}{\partial x'}, \quad \frac{\partial p}{\partial y} \rightarrow \pm \frac{1}{\sqrt{2}} \frac{\partial p}{\partial x'}. \quad (11)$$

For such a twin structure, the OP varies across the wall from its value in S_1 to its value in S_2 ,

$$p_1 = \begin{cases} p_a, & x' \rightarrow -\infty \\ p_b, & x' \rightarrow +\infty \end{cases}, \quad p_2 = \begin{cases} p_b, & x' \rightarrow -\infty \\ -p_a, & x' \rightarrow +\infty \end{cases}. \quad (12)$$

In order to match the boundary conditions in Eq. (12), it is convenient to change the dependent variables

$$p_1 = p_a f_1 + p_b f_2,$$

$$p_2 = p_b f_1 - p_a f_2. \quad (13)$$

Here, the functions f_1 and f_2 are normalized order-parameter components and have simpler boundary conditions

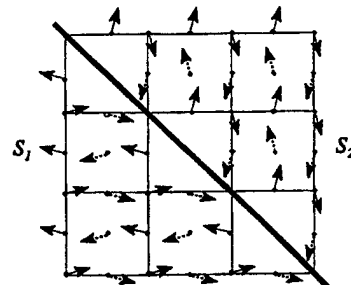


FIG. 5. Twin structure with a domain wall oriented parallel to the $(1\bar{1}0)$ lattice plane.

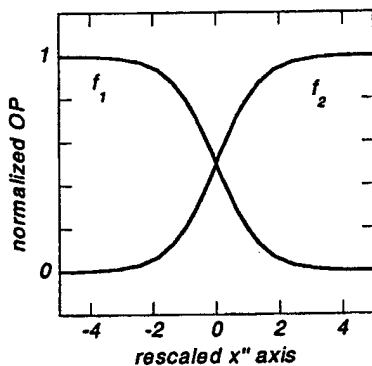


FIG. 6. Numerical solution for the order parameter profile of an orientation twin with $\gamma' = 3.0$.

$$f_1 = \begin{cases} 1, & x' \rightarrow -\infty \\ 0, & x' \rightarrow +\infty \end{cases}, \quad f_2 = \begin{cases} 0, & x' \rightarrow -\infty \\ 1, & x' \rightarrow +\infty \end{cases} \quad (14)$$

We now apply the Euler-Lagrange equations

$$\frac{d}{dx'} \frac{\partial F}{\partial f_{i,x'}} = \frac{\partial F}{\partial f_i} \quad (i=1,2) \quad (15)$$

and obtain a coupled set of ordinary differential equations

$$\begin{aligned} D \frac{d^2 f_1}{dx'^2} &= \alpha f_1 + \beta f_1^3 + \gamma f_1 f_2^2, \\ D \frac{d^2 f_2}{dx'^2} &= \alpha f_2 + \beta f_2^3 + \gamma f_1^2 f_2, \end{aligned} \quad (16)$$

where

$$\begin{aligned} D &= (1 + \kappa^2)(D_1 + D_3), \\ \alpha &= (1 + \kappa^2)A, \end{aligned} \quad (17)$$

$$\beta = p_a^2 [4(1 + \kappa^2)^2 B_1 + 4(1 + \kappa^4) B_2 + 4\kappa(1 - \kappa^2) B_3],$$

$$\gamma = p_a^2 [4(1 + \kappa^2)^2 B_1 + 24\kappa^2 B_2 - 12\kappa(1 - \kappa^2) B_3].$$

In order to meet the boundary conditions in Eq. (14), we must have

$$\alpha + \beta = 0. \quad (18)$$

The x' axis can be rescaled to

$$x'' = x' \sqrt{\frac{\beta}{D}} \quad (19)$$

to arrive at a simplified set of dimensionless equations

$$\begin{aligned} \frac{d^2 f_1}{dx''^2} &= -f_1 + f_1^3 + \gamma' f_1 f_2^2, \\ \frac{d^2 f_2}{dx''^2} &= -f_2 + f_2^3 + \gamma' f_1^2 f_2, \end{aligned} \quad (20)$$

where $\gamma' = \gamma/\beta$ is temperature independent. Equations (20) have been solved for other systems¹⁴ and the solutions for the choice of $\gamma' = 3.0$ are illustrated in Fig. 6.

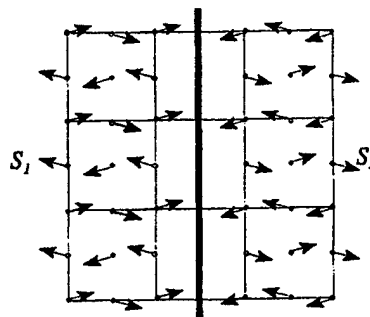


FIG. 7. Dipole arrangement in the vicinity of an antiphase wall between S_1 and S_3 .

For the second type of orientation twin involving domains S_1 and S_4 , the boundary conditions are

$$p_1 = \begin{cases} p_a, & x' \rightarrow -\infty \\ -p_b, & x' \rightarrow +\infty \end{cases}, \quad p_2 = \begin{cases} p_b, & x' \rightarrow -\infty \\ p_a, & x' \rightarrow +\infty \end{cases} \quad (21)$$

We make the following change of variables

$$\begin{aligned} p_1 &= p_a f_1 - p_b f_2, \\ p_2 &= p_b f_1 + p_a f_2. \end{aligned} \quad (22)$$

The same set of equations, Eqs. (20), for the functions f_1 and f_2 can be derived and similar solutions can be obtained.

For the antiphase structures, we cannot use the strain compatibility relations to predict the orientation of the wall since the strain compatibility relations are automatically satisfied. However, we can simplify the equations to quasi-one-dimensional using the same procedure described above. Again, we rotate the coordinate system such that x' is perpendicular to the wall. The derivatives in the gradient part of the free energy can again be expressed in terms of derivatives in the x' direction. By defining the new normalized order parameter g ,

$$p_1 = p_a g, \quad p_2 = p_b g \quad (23)$$

and using a rescaling of the space variable similar to Eq. (19) (but dependent upon the specific orientation of the wall), we can simplify the system to a single differential equation for the function g ,

$$\frac{d^2 g}{dx''^2} = -g + g^3. \quad (24)$$

For the antiphase structure formed by domains S_1 and S_3 (see Fig. 7), the boundary conditions are

$$p_1 = \begin{cases} -p_a, & x' \rightarrow -\infty \\ p_a, & x' \rightarrow +\infty \end{cases}, \quad p_2 = \begin{cases} -p_b, & x' \rightarrow -\infty \\ p_b, & x' \rightarrow +\infty \end{cases} \quad (25)$$

or

$$g = \begin{cases} -1, & x'' \rightarrow -\infty \\ 1, & x'' \rightarrow +\infty \end{cases} \quad (26)$$

Equation (24) has the analytic solution

$$g = \tanh\left(\frac{x''}{\sqrt{2}}\right). \quad (27)$$

SUMMARY AND CONCLUSIONS

We have proposed a Landau-Ginzburg model based on microscopic symmetry to describe a second-order antiferroelectric phase transition. The OP field used is directly correlated to the local dipole moments of the formula units, instead of the macroscopically averaged polarization. Our model not only can derive the macroscopic model proposed by Kittel but also can address the dipole tilt and cell doubling in the antiferroelectric transition. There is no need to assume separate sublattices in our model.

When the antiferroelectric state is switched to a ferroelectric state by an external electric field, our model predicts a unit cell size twice as large as that of the macroscopic picture obtained from previous investigations.² This picture is more consistent with the microscopic picture observed experimen-

tally that the dipoles are actually tilted from the **a** and **b** directions.

There are four domain states in the antiferroelectric phase and they form two distinct orientation twins and one type of antiphase structure. The addition of gradient energy terms in the free energy allows us to model multidomain inhomogeneous structures. Numerical solutions for the inhomogeneous OP profiles describe the gradual change of the dipole amplitude and orientation across the domain walls. We find that if, in the free energy, only the coefficient of the quadratic term is assumed to be temperature dependent, the local dipoles have a fixed orientation independent of temperature, while the amplitude of the dipole moment is a function of temperature.

ACKNOWLEDGMENTS

This work was sponsored by the Office of Naval Research under the MRUI Grant and the Grant for Piezocrystal Resource.

¹C. Kittel, Phys. Rev. **82**, 729 (1951).

²L. E. Cross, J. Phys. Soc. Jpn. **23**, 77 (1967).

³H. Meister *et al.*, Phys. Rev. **184**, 550 (1969).

⁴H. Konwent and J. Lorenc, Phys. Status Solidi B **88**, 747 (1978).

⁵L. Tenzer, B. C. Frazer, and R. Pepinsky, Acta Crystallogr. **11**, 505 (1958).

⁶R. O. Keeling, Jr. and R. Pepinsky, Z. Kristallogr. **106**, 236 (1955).

⁷*International Tables for Crystallography*, edited by T. Hahn (Reidel, Dordrecht, 1983).

⁸R. Blinc, J. Slak, and I. Zupančič, J. Chem. Phys. **61**, 988 (1974).

⁹S. C. Miller and W. F. Love, *Tables of Irreducible Representa-*

tions of Space Groups and Co-Representations of Magnetic Space Groups (Pruett, Boulder, 1967).

¹⁰H. T. Stokes and D. M. Hatch, *Isotropy Subgroups of the 230 Crystallographic Space Groups* (World Scientific, Singapore, 1988). Internet and DOS (PC) versions of this software are available at URL <http://www.physics.byu.edu/~stokesh/isotropy.html>

¹¹J. Sapriel, Phys. Rev. B **12**, 5128 (1975).

¹²J. Fousek and V. Janovec, J. Appl. Phys. **40**, 135 (1969).

¹³K. Aizu, J. Phys. Soc. Jpn. **27**, 387 (1969).

¹⁴W. Cao and G. R. Barsch, Phys. Rev. B **41**, 4334 (1990).

MATERIALS STUDIES

Polycrystal Perovskite Ceramics

APPENDIX 5

REVIEW

A.S. Bhalla · Ruyan Guo · Rustum Roy

The perovskite structure – a review of its role in ceramic science and technology

Received: 29 November 1999 / Accepted: 3 July 2000

Abstract Starting with the history of the fundamental science of the relation of structure to composition delineated completely by Goldschmidt, we use the perovskite structure to illustrate the enormous power of crystal chemistry-based intelligent synthesis in creating new materials.

The perovskite structure is shown to be the single most versatile ceramic host. By appropriate changes in *composition* one can modify the most significant electroceramic dielectric (BaTiO_3 and its relatives) phase in industry, into metallic conductors, superconductors or the highest pressure phases in the earth. After an historical introduction of the science, detailed treatment of the applications is confined to the most recent research on novel uses in piezoelectric, ferroelectric and related applications.

Keywords Perovskite · Crystal-chemistry · Tolerance factor · Ferroics · Electro-ceramics

1 Introduction: Prewar history of the emergence of perovskite as the key ternary ceramic phase

1.1 The short list of important ceramic phases

Ceramics (processed inorganic materials) are by far the highest volume and highest tonnage materials made and used by humankind. Yet, there are only a half dozen specific ceramic *phases* that dominate human use of such materials not only in terms of volume, weight, etc., but also in terms of technological significance. Any list of such would contain at least the following:

- Quartz – which as sand is ubiquitous in rocks, beaches, soil, buildings, and roads.

- Mullite – the principal component both of crude and refined pottery of all kinds, or bricks, and of a great deal of high tech ceramics.
- Calcium silicates – “ Ca_3SiO_5 , Ca_2SiO_4 and $\text{Ca}_3\text{Al}_2\text{O}_6$ ” – and their hydration products, the key constituents of cement and concrete, which at 1500 million tons/year is humankind’s largest tonnage manufactured product.
- “ Al_2O_3 ” – the key unary oxide of ceramic technologies from hard grinding materials to all kinds of refractory ceramics, to laser hosts and gems (rubies and sapphires).
- “ TiO_2 ” – the required high refractive index material in a variety of high volume (e.g., paint) uses and the key ingredient in electroceramics.

Each of these phases – defined by *both* crystal *structure* and *composition* – is useful because it has one or two special properties and applications. Well may one ask: Are there ternary structures that are multifunctional, that is, that can serve as the appropriate crystallographic host for a wide variety of useful properties and functions? Examination of lists of the main ternary crystal structures [1] reveals that among thousands of complex structures there are only a dozen or so structures which dominate the entire world of useful ceramics. Among these the A_2BX_4 structure, spinel; and the ABX_3 structure, perovskite, stand out by a wide margin, and perovskite is far ahead of spinel as the single structure which, with skilled chemical manipulation, can produce an incredibly wide array of phases with totally different functions (Fig. 1).

1.2 Perovskite proves the error of the structure-property cliché of early materials scientists

The emphasis on the importance of the “structure-property” relation as the key to the understanding of “materials science” was a curious half-truth of the 1950s mistakenly imposed on generations of students. In trying to emphasize the

A.S. Bhalla (✉) · R. Guo · R. Roy
Materials Research Laboratory,
The Pennsylvania State University,
University Park, PA 16802, USA
e-mail: asb2@psu.edu
Tel.: +1-814-8659232. Fax: +1-814-8637846

Fig. 1 Perovskite – the maximum multifunctional structure

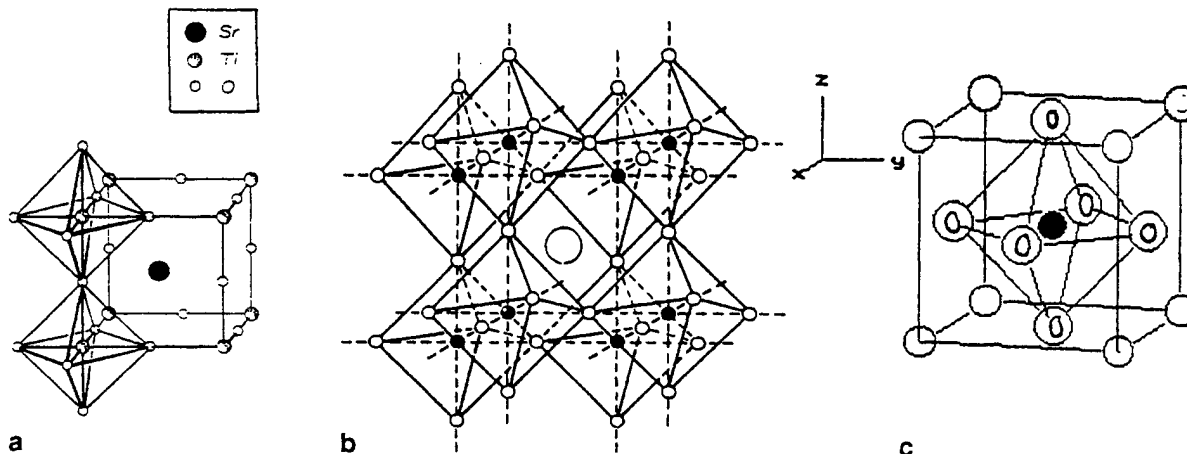
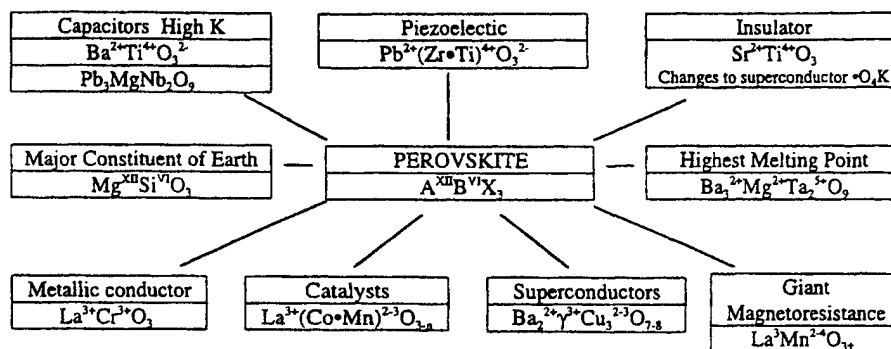


Fig. 2 (a) The [ideal perovskite] structure, illustrated for $SrTiO_3$ [2–4]. Note the corner-shared octahedra extending in three dimensions. (b) and (c) Some other ways of presenting perovskite structure

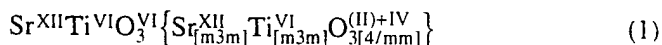
importance of crystal or atomic structure or microstructure as opposed merely to gross composition, this facile expression led to the opposite error that structure was *the* necessary (but by implication also sufficient) predictor of properties. That is, of course, manifestly absurd. The perovskite structure stands as the outstanding example proving the error of this over-simplistic cliché.

1.3 Mineral discovery

Perovskite is the name for a structural family, in addition to being the name for a particular mineral with the composition, $CaTiO_3$. This confusion between the structural name, and a compositional entity is overweening in materials science, but very rarely dealt with explicitly. In Muller and Roy's textbook [1] this nomenclature issue is dealt with extensively, and a formalism developed that when used as a structural descriptor (see [1] p 8 for detailed treatment of nomenclature) the original mineral composition would be enclosed in square brackets. Thus $[CaTiO_3]$ stands for the perovskite structures not the composition $CaTiO_3$. This formalism has not been widely adopted and confusion continues.

1.4 The structure

The [ideal perovskite] has a very simple arrangement of ions that is illustrated in Fig. 2. The cubic (isometric) structure is typified not by $CaTiO_3$ but by $SrTiO_3$ with $a=3.905$ Å, $Z=1$, and space group $O_h-Pm\bar{3}m$. The Ti atoms are located at the corners, and the Sr atoms at the center of the cube. The oxygen is placed at the centers of the twelve cube edges, giving corner-shared strings of TiO_6 octahedra, which extend infinitely in three dimensions. The TiO_6 octahedra are perfect with 90° angles and six equal Ti-O bonds at 1.952 Å. Each Sr atom is surrounded by twelve equidistant oxygen at 2.761 Å. The structural formula written explicitly with coordination number of each ion and local symmetry (see Muller and Roy) is as follows:



The [ideal perovskite] can also be regarded as a cubic close-packed structure in which the oxygen and the Sr atoms are stacked in cubic close-packed layers along the cubic [111] direction. Some of the resulting octahedral holes are occupied by Ti atoms. Some other ways of presenting the structure are shown in Fig. 2(b) and 2(c).

1.5 Crystal chemistry begins

Historically however, perovskite would have remained a mineralogical curiosity were it not for V.M. Gold-

schmidt, the founder of the science of crystal chemistry, and his school of geochemists in Oslo. Goldschmidt made and studied a large number of the first synthetic perovskites with different compositions, including BaTiO_3 , in 1924–26 [5]. This quotation is taken from Goldschmidt's classic, the single most important reference in the entire history of materials synthesis, entitled "Geochemische Verteilungsgesetze der Elemente":

In unserem Institut sind mehrere Reihen von Verbindungen ABX_3 untersucht worden, um die Morphotropie-Beziehungen dieser Stoffe festzustellen. Ich hoffe, bei späterer Gelegenheit ausführlicher auf diese Verbindungen zurückkommen zu können. An dieser Stelle seien die Struktur-Daten eines speziellen ABX_3 -Typus nach unsern Messungen zusammengestellt, nämlich die Daten des Perowskit-Typus.

But not only did Goldschmidt synthesize a large number of such isostructural phases but he started what was to become the world's first school of *crystal* chemistry, by determining the crystal *structures* of each of the phases, of the ABX_3 *compositions*. This, in an era when powder x-ray diffraction was in its infancy.

A second quotation from this monograph records the fact that Goldschmidt himself made all the compounds and that he, Tom Barth and Willy Zachariasen each did some of the x-ray structures, and measured lattice parameters which prove to be amazingly accurate today.

Perowskit-Struktur:

Die Perowskit-Struktur wurde von T. Barth (in [5]) am Perowskit, CaTiO_3 , am NaNbO_3 , sowie am Dysanalyt (Mischkristall $\text{CaTiO}_3\text{--NaNbO}_3$) studiert. Eine große Anzahl von Substanzen mit Perowskit-Struktur wurde 1925 und 1926 von mir dargestellt, und teils von mir selbst, teils von T. Barth, teils von W. Zachariasen untersucht; die meisten dieser Stoffe sind bereits in 6. Erwähnt.

Goldschmidt then went on to establish what remains after seventy-five years the first (and lasting) principles of materials synthesis:

- The radius of the ions is fundamental (his table of radii was the first) to structure.
- The radius ratio R_c/R_a determines the coordination number of the cation (= the polyhedron formed.)
- The packing of polyhedra follows simple rules (later codified by Pauling [6]).

That the perovskite structure was central to the birth of these ideas may be found in the next paragraph where Goldschmidt introduces the concept of the "tolerance factor" (T.F.) for the perovskite arrangement of interpenetrating dodecahedra and octahedra, i.e., how far from ideal packing can the ionic sizes move and still be "tolerated" by the perovskite structure?

Ich fand dabei die Entstehung der Perowskit-struktur an bestimmte numerische Beziehungen zwischen den Radien der Krystallbausteine geknüpft ist. Für unsere Betrachtungen hier ist wesentlich die Toleranzfaktor

Table 1 Bestimmungen der Gitterdimensionen liegen an folgenden Crystallen dieser Art Vor:

Verbindung	a	Literature (no. referring to that of in [5])
CaTiO_3^1	3.80 ± 0.02	6, 10
SrTiO_3	3.92 ± 0.02	6
BaTiO_3	3.97 ± 0.02	6
KIO_3	4.46 ± 0.02	6
RbIO_3	4.52 ± 0.02	6
NaNbO_3	3.98 ± 0.02	10
KNbO_3	4.01 ± 0.02	6
CaZrO_3	3.99 ± 0.10	6

$$t = \frac{R_a + R_x}{\sqrt{2} \cdot (R_b + R_x)} \quad (2)$$

Bei Perowskitstrukturen einen Wert zwischen 0,8 und 1,00 besitzt.

It should be noted that the reason why Goldschmidt's (and Pauling's) crystal chemistry has been so successful in guiding the intelligent materials synthesis of literally thousands of new and many useful phases, is that their rules and laws are based on hundreds of empirical measurements which do not change. Thirty years before each III-V and II-VI semiconductor was "discovered," Goldschmidt had listed them *all* casually on one table in the same volume referred to above.

1.6 The first *useful* property in a perovskite (BaTiO_3) – dielectric constant

The next set of key events in the history of the emergence of the perovskite structure as the preeminent high-tech ceramic materials occurred during WWII, and the history is partly lost in wartime secrecy and lack of open publications.

Nevertheless, the history of BaTiO_3 is closely tied to a very different material-muscovite mica $\text{KMg}_3(\text{AlSi}_3)\text{O}_{10}(\text{OH})_2$. Mica was the key insulator in most capacitors (with a κ of 10) and had to be imported by the Allies, Germany, Russia, and Japan mainly from India (and Brazil). Supply lines were tenuous. Demand was skyrocketing. A key wartime R/D goal for all those countries was to find a substitute dielectric (with a κ of 80 as the starting point). Our colleague W.R. Buessem, then the Director of Science Research in Siemens, Germany reported that by 1940–1941 various alkaline earth titanates were in production. Shot-down fighter planes became the source of this intelligence for the West. But whether from this source or directly from their own backgrounds, in Cleveland in The TAM labs, Wainer and Solomon had identified BaTiO_3 [7] as possibly having the highest κ .

In 1945 Wul and Goldman [8] in Moscow also found the same compound as being the most promising, and in Tokyo Ogawa [9] identified the same winner: BaTiO_3 (see history by Cross and Newnham [10]). The historians of science may find this to be an example of Rupert

Sheldrake's morphogenetic field [11] where the ideas are pregnant in the atmosphere worldwide, and crystallize out at the same time in different places. Or else one may simply see it as the result of systematic analysis of the same problem by different scientists all over the world. A final historic footnote is that one of the authors (R.R.) arrived in the US in 1945 with the objective of saving India's mica industry from the inroads of substitutes. By 1950 he was fully involved in the synthesis and crystal chemistry of the material. BaTiO_3 – which almost totally displaced mica!

1.7 The link to ferroelectricity

It was von Hippel and the MIT Laboratory for Insulation Research [12] which recognized the reason for the extraordinary values of ' κ ' which were being found. In quick succession, Ginsburg, 1946 [13], Megaw, 1946 [14], and Blattner, Matthias and Merz, 1947 [15] in Europe confirmed the theory, re-did the structure, and grew a few single crystals to prove the point. By 1948 several authors [16–20] had studied the optical domain structure and improved on the phenomenology and the structure and change involved. Several major industry groups entered the field, notably Bell Telephone Labs. In 1950 two separate groups at Penn State entered the scene. Pepinsky and his large group in the Physics Department on ferroelectricity, which during the next four years included major figures in the field (Merz, Matthias, Megaw, Shirane, Jona, etc.) and Roy and

Osborn in Geochemistry who embarked on the systematic synthesis and crystal chemistry and phase equilibria of complex oxides. Samples which were sent back and forth for measurement was the link between the groups.

1.8 Two perovskite "functions": ferroelectricity and superconductivity compared

To bracket and to conclude the history of the utility of perovskite we jump ahead forty years to the discovery of high T_C superconductivity. Whereas for years the Penn State group was literally the only one working on the synthesis and systematic crystal chemistry of the ferroelectrics, literally hundreds of groups jumped in within months of the discovery to study the superconductors.

Tables 2 and 3 make an interesting comparison to debate both the nature of advances in science and science policy, and especially investment in science. The actual advance in the key functions – dielectric constant in one case and transition temperature in the other was certainly greater in BaTiO_3 (a factor of 100) than in $\text{YBa}_2\text{Cu}_3\text{O}_{7.8}$ (factor of 3). The ratio of the speed and magnitude of the impact on technology was of course even more greatly in favor of BaTiO_3 . Yet both the absolute amount and the rate of research effort put into the superconductor was in the opposite ratio, much, much higher. The pay-off so far at least has been vastly smaller for superconductors.

Table 2 Discoveries (past) – comparative research history and strategy

	Ferroelectricity TiO_2 - MgTiO_3 BaTiO_3	Superconductivity LaBaCuO_4 $\text{YBa}_2\text{Cu}_3\text{O}_{7.8}$
Discovery	USA ~ Simultaneously: USA, USSR, Japan 1944–1946 $\kappa=10$	Switzerland-Japan ~ Simultaneously: Huntsville, Beijing, Bangalore 1986–1987 $T_C=23\text{K}$
Property advance	$\rightarrow 100$ $\rightarrow 30,000$	$\rightarrow 36\text{K}$ $\rightarrow 90\text{K}$
Research effort for Proof of	100 p.y. to major payoff	(1000 p.y. and far to go to ??)

Table 3 Comparison, history and strategy – BaTiO_3 :HTSC

	Ferroelectricity TiO_2 - MgTiO_3 BaTiO_3	Superconductivity LaBaCuO_4 $\text{YBa}_2\text{Cu}_3\text{O}_{7.8}$
US Position	Industry in commanding position	Industry very weak. Universities very weak in relevant fields
Technological	Drop-in replacement	~ No products.
Prospects	into existing	Short-term prospects unclear
Technological	enormous	Major Impact <i>Improbable</i>
Reality	capacitor industry, Piezoelectrics, Pyroelectrics, Electrooptics	in 10–15 year frame

2 Synthesis, crystal chemistry, and phase diagrams

2.1 Synthesis

All the usual ceramic reaction methods are used for synthesizing the most used perovskite phases.

2.1.1 Solid state reaction

By far the most commonly used process is that of thoroughly mixing oxides (or carbonates and oxides) and firing at temperatures of $>2/3$ m.p. for periods up to ten hours. The process poses special problems for the cases where one oxide, especially a toxic one like Pb, may vaporize in part during the long reaction times.

2.1.2 Solution technologies – sol-gel and others

Starting in 1950 several perovskites phases were probably the first such nonsilicate ceramics ever made by the sol-gel techniques which had been developed by Roy at Penn State in 1948 [21]. Sol-gel methods were routinely applied to many of the aluminate, titanate, and complex mixed cation phases (see later) made by one of the authors (R.R.) and his students [22–25] by the mid 1950s.

In the last decade or two, sol-gel techniques have finally attracted wider attention especially for making thin films at low temperatures. In our own rather extensive work we have been able to grow many highly oriented perovskites such as SrTiO_3 on SrTiO_3 "single crystals" as low as 600 °C from thin gel layers spun on to the substrates. References [26–30] give examples of some of these synthesis and processing studies on various perovskites.

2.1.3 Hydrothermal

This method [31] was also used very early on to synthesize and check the thermodynamic stability of BaTiO_3 and many other perovskites in the fifties [32]. Recently there has been considerable activity in making BaTiO_3 at very low temperatures by this route [33–35].

2.1.4 Hydrothermal-electrochemical

Following the work of Hawkins and Roy [36] on using an electric field to lower hydrothermal synthesis temperature, Yoshimura et al. have demonstrated the ability to synthesize BaTiO_3 by using such an electric field in a hydrothermal bomb at temperatures between 100 and 200 °C [37].

2.1.5 Microwave synthesis

In a conventional furnace $\text{BaCO}_3 + \text{TiO}_2$ reacts in a few hours at 1200 °C to form first Ba_2TiO_4 and then very

Table 4 Phase sequences and times of reaction in synthesis of BaTiO_3 (starting precursors: BaCO_3 and TiO_{2-x})

Conditions Temp/Time	Phases identified by XRD and relative peak intensities in %			
	BaCO_3	TiO_{2-x}	$\text{Ba}_2\text{TiO}_4^a$	Tet.- $\text{BaTiO}_3^{b,c}$
Conventional:				
900 °C/2 min	57	43	–	–
950 °C/2 min	67	33	–	–
950 °C/1 h	62	23	14	–
1100 °C/1 h	36	37	26	–
1200 °C/1 h	30	37	33	–
1300 °C/1 h	–	–	100	–
Microwave Method:				
250 °C/0 min	45	51	4	–
400 °C/0 min	25	22	48	5
500 °C/1 min	12	10	54	24
600 °C/5 min	11	13	29	47
700 °C/5 min	6	8	16	70
900 °C/5 min	–	1	–	99

^a Compare 4% BaTiO_3 (hex.) 0 min (microwave)

^b Compare 0% BaTiO_3 after 1 h (conventional)

^c Compare 99% BaTiO_3 (tet.) 5 min (microwave)

slowly the assemblage react to give increasing amounts of BaTiO_3 .

In a 2.450 GHz microwave field we find the most remarkable differences, especially when we work in systems using slightly reduced titanates or tantalates, etc. [38]. Thus one can observe the formation of BaTiO_3 in *one to two minutes*, and also note completely new reaction paths. For example appearance of hexagonal BaTiO_3 (unheard of at these temperatures) and the fact that no Ba_2TiO_4 is ever formed. Data are shown in Table 4 on a very effective and likely to be commercialized process for most electroceramics. Because of its simplicity and speed, microwave sintering is especially attractive for Pb-containing perovskites, because it minimizes the Pb-loss.

2.1.6 PVD methods – laser ablation, MBE

As the movement towards integration of the capacitive function into silicon circuitry grows, all the well-developed thin film methods are, of course, routinely being applied to perovskites. Thin film ferroelectrics are a major field of research and references to two or three symposium proceedings and journals will show how extensive this work is [39–41].

2.2 Crystal chemistry

Just as Goldschmidt had pioneered in building the foundation of crystal chemistry on the basis of extensive synthesis, so also Roy and his students took the crystal chemistry of perovskites to the next level, especially involving *multiple ion* substitution on the same site – a ba-

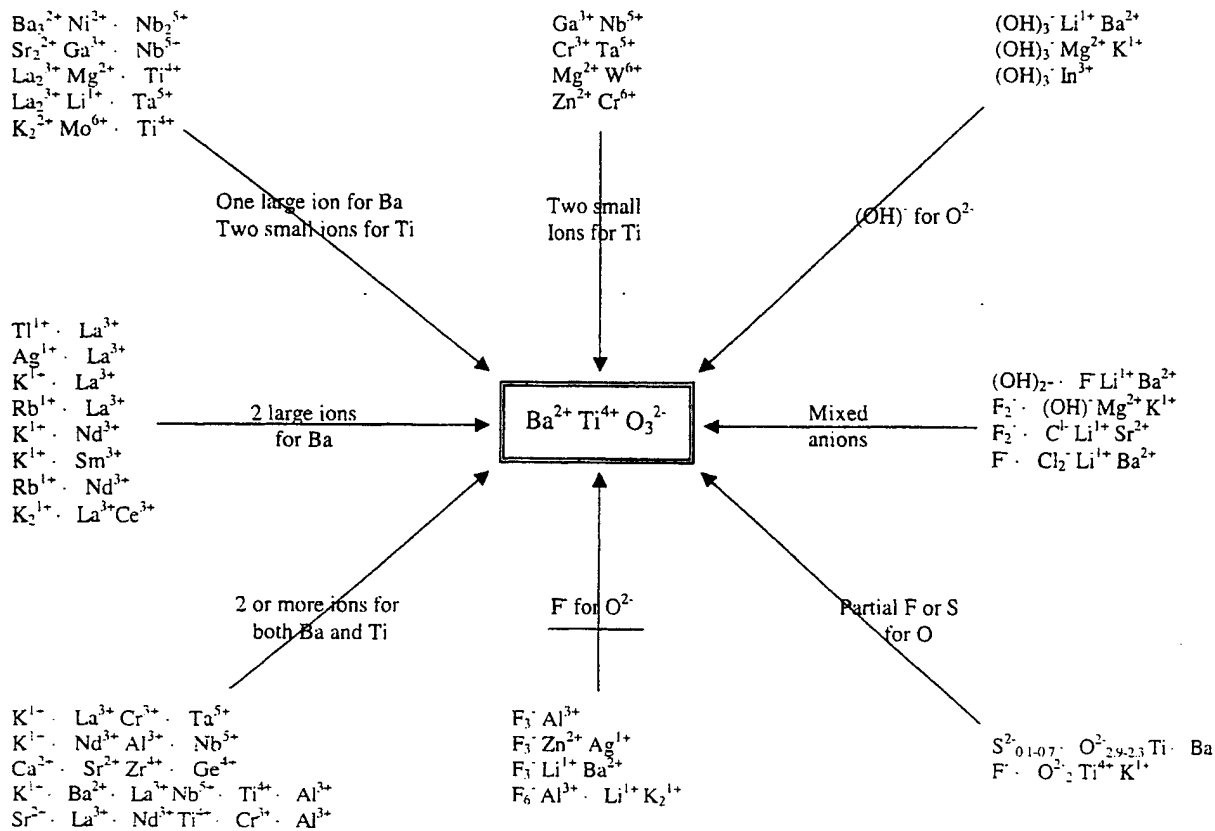


Fig. 3 Crystal chemistry of multiple ion substitution in perovskite (Roy 1954)

sic advance not envisaged by Goldschmidt. Thus Roy et al. were able to make many "half-breed derivatives" on the A site, B site, and mixed (M.J. Buerger terminology).

Figure 3 is taken from Roy's summary of this work in 1954 [42]. This list of materials synthesized, viewed in retrospect is remarkable. The prototype of virtually every useful substitution made in the perovskite structure is illustrated by *real* examples in this figure. For example, the $\text{A}_3\text{B}^{2+}\text{B}_2^{5+}\text{O}_9$ is the prototype of the PMN relaxor material, typified by its prototype $\text{Sr}_3\text{NiNb}_2\text{O}_9$. This map serves even today as a template for the novice interested in introducing any particular ion into the perovskite structure. The one major limitation is that unlike the garnet and spinel structures, no small ions $< \approx 0.6 \text{ \AA}$ can be accommodated since there are no tetrahedral sites in the perovskite structure.

But just as Goldschmidt had worked on the relations of two structures [Perovskite] – [Ilmenite], [NaCl] – [CsCl], etc., Roy turned his attention to the general problem of how structures of ternary phases change with the cation radius of the two ions involved. His very first work was on the ABO_3 phases (Keith and Roy [43]) and in this paper the first (crude) examples of Structure Field Maps are presented, showing the relation of perovskite to neighboring structures; and it was in this paper that the discovery of ferromagnetic rare earth garnets was first reported.

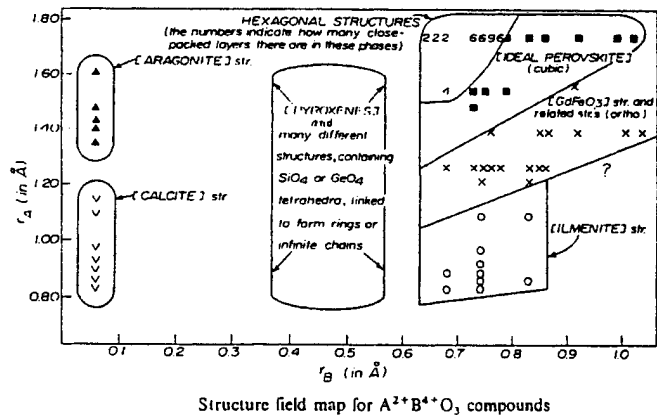
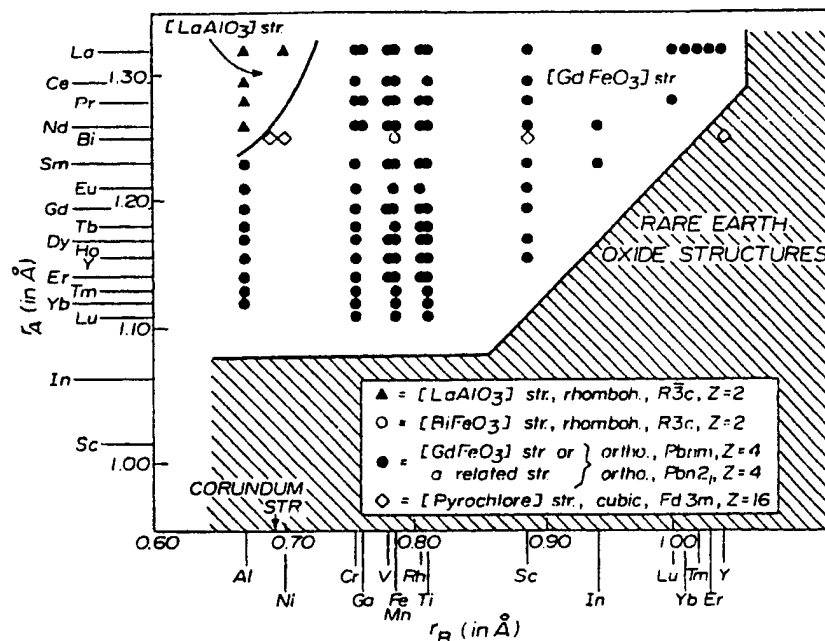


Fig. 4 Structure-field map for $\text{A}^{2+}\text{B}^{4+}\text{O}_3$ compounds

2.2.1 Structure field maps

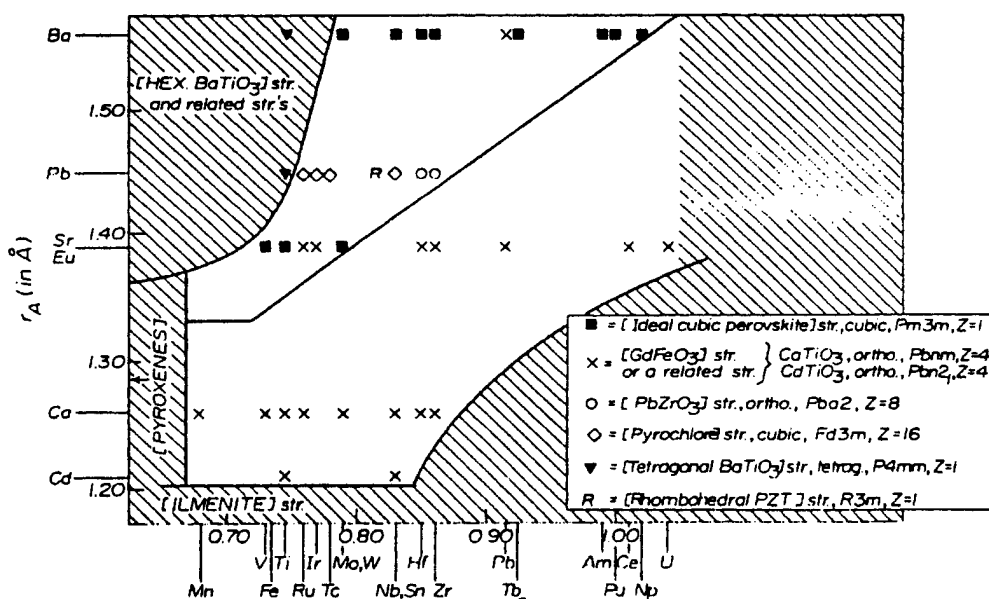
In the subsequent decades Roy and his students developed the Goldschmidt approach much further and produced a large number of "structure field maps." The limitations of such an approach are clearly recognized. The zeroth order approximation of the structure of a real material is a hard sphere model, with each ion having simple integral charges involving only *s* and *p* electrons in purely electrostatic bonding. Of course none of these boundary conditions exists in practice, but nevertheless the deviations prove to be minor. The absolute dominance of composition on structure, as indicated by Goldschmidt, is demonstrated by the segregation of allowed

Fig. 5 Structure-field map for $A^{3+}B^{3+}O_3$ [perovskites]



Structure field map for $A^{3+}B^{3+}O_3$ [perovskites]

Fig. 6 Structure-field map for $A^{2+}B^{4+}O_3$ [perovskites]



Structure field map for $A^{2+}B^{4+}O_3$ [perovskites]

structures for any particular stoichiometry: ABX_3 , A_2BX_4 , ABX_4 , etc. Among all ternary phases the actual numbers of structures are possible very limited. Ninety-five percent of all such phases on the earth probably fall into less than a couple of dozen structures. In their book "The Major Ternary Structural Families" Muller and Roy [1] have collected such information into one place and presented dozens of such structure field maps. Galasso [44] has also provided a valuable similar compilation of data. Figs. 4-6 show the kind of information which is conveyed in such SFM. These maps show the extent of

the domain of occurrence of a particular structure or substructure (for example rhombohedrally or tetragonally distorted perovskites) in radius space of the two cations A and B in any ternary phase. While from Goldschmidt's earliest work it was clearly recognized that the effect of radius was modulated by "polarization," or what became in Pauling's approach the "percentage covalency (ionicity)." So far it has not been usefully reduced to simple presentations in complex ionic compounds. In the simpler case of metallic structures it was Brewer and Engels [45] who took this approach by adding in a term for the

effects of 'd' and 'f' electrons participating in the bonding. In the "covalent" approximation to carbon, silicon, germanium and the partially ionic III-V and II-VI compounds, the theoretical physics community (A. Zunger [46]; J.C. Phillips [47, 48]) has attempted (what are labeled) "first principles" calculations to relate composition to structure. After enormous efforts, the results are marginally more precise than Goldschmidt's 1926 results which require no more effort than reading off radii from a table. Moreover, virtually no such efforts have been attempted for ternary or quaternary structures.

2.2.2 Point defects – substitution (solid solutions) and vacancies

The only defects which affect the bulk crystal structure are those which affect the chemical composition. *Solid* (more accurately, *crystalline*) solutions are universal. All solid matter deviates (i.e., is defective), with respect to the deviation of ionic content, from the formal ratios of say 1:1:3 in ABX_3 . In many well-known structures (e.g., in the case of $TiO_{(1\pm x)}$ the deviation can be 20–30 percent). In perovskite it can be 100%. Thus the phase ReO_3 should be written $Re^{6+}O_3^{2+}$, because while its structure is that of perovskite, the A sites are 100% vacant. The so-called tungsten bronzes based on " $NaW^{5+}O_3$ " in fact are heavily defective (i.e., lacking in A ions) along a formula which simply drops out Na^{1+} ions, $Na_{1-x}W_{1-x}^{5+}W_x^{6+}O_3$ by balancing out the partial oxidation of W^{5+} to W^{6+} . A special category of 'defect' that Goldschmidt recognized was the charge "model." He argued that if one dropped the formal charge of O^{2-} to F^- , one could substitute K^+ for Ba^{2+} and Mg^{2+} for Ti^{4+} and retain the perovskite structure. Indeed the prediction of the structures of chemically utterly different phases such as $KMgF_3$, Na_2BeF_4 and BeF_2 by involving the model structure theory must be regarded as one of the spectacular triumphs of crystal chemistry – and this was 1926.

The immeasurable number of solid solutions, which are used in technology daily, are quite simply limited by the radius considerations in the structure field maps. Especially relevant often are cases where a designed composition may switch from the pyrochlore to the perovskite structure [1] as the defect concentration changes (see examples in [50]).

2.2.3 Defects: Order-disorder

Another important consideration in complex-composition perovskites are in the half-breed compositions of Roy [42]. Here say $K^{1+} + La^{3+}$ are substituted for $2Ba^{2+}$; or $Mg^{2+} + Nb_2^{5+}$ are substituted for $3Ti^{4+}$. The possibilities of order-disorder structural changes become obvious. In the disordered state the ions are statistically distributed over the 2 (or 3) A (or B) sites. However at lower temperature, a lower free energy possibility is often assured whereby a superstructure is formed with a larger unit-

cell and the ions segregated into chemically homogeneous sublattices. These order-disorder changes cause very significant electrical and optical changes and the systematization is very valuable.

2.3 Phase diagrams: Stable and metastable

While crystal chemistry relates composition to structure, thermodynamics relates structure and composition to the intensive variables principally of temperature and pressure. It is a fact that in contradistinction from other structures say [NaCl] or [Diamond], the usual laboratory pressure variable (up to say 100 kbars) causes virtually no phase transition in any perovskites; (see later for $MgSiO_3$ in the earth) hence it is only the T-x diagrams which are of interest to the perovskite field for synthesis and growth and solid solutions etc. The original T-x diagram for the system $BaO-TiO_2$ was done by Rase and Roy in 1954 [51]. It is shown in Fig. 7(a), alongside the much later one [52] [Fig. 7(b)] the significant changes are all in the high TiO_2 region where some new phases have been detected, which resulted in very minor changes in the melting temperatures involved.

3 Major applications in electroceramics

As mentioned earlier (Fig. 2) in an ideal perovskite structure the corner-shared oxygen octahedra linked in the three dimensions is the basic feature of the perovskite structure. The origin of ferroelectricity is linked with the characteristics of the oxygen octahedron unit not only in this structure but also in other derivative structures, e.g., tungsten bronzes and the bismuth titanate structure. Within the perovskite subgroup there are many possible variations of ferroics and phase transitions, e.g., ferroelectric, antiferroelectric, ferroelastics (Table 5 [53]).

In a simple composition when the octahedra are linked in a regular fashion in a cubic material a high temperature or prototype m3m point symmetry perovskite is formed. Various A-site substitutions result in a large family of simple perovskite ferroelectrics, which at present numbers over 100 ferroelectrics. The variation of these corner linked octahedra such as tilt, (1,2,3 axis) [54] rotations give the possibility of several new families of ferroelectrics. Two of those which are worth mentioning here are the tungsten bronze structure (tilting of the octahedra in the a-b plane) and Bi-layer structures (where corner linked oxygen octahedra layers are separated by $Bi_2O_2^{2+}$ layers in the structure). The former family has about the same number of solid solution ferroelectric tungsten bronze compositions and the latter one, well over 50 compounds though the number increases to very large numbers when these are modified or the solid solution compositions are designed by using the simple principles of crystal chemistry.

Fig. 7 (a) Phase equilibria in the system BaO-TiO₂ (Rase and Roy 1954); and (b) later version of the diagram (ref [52])

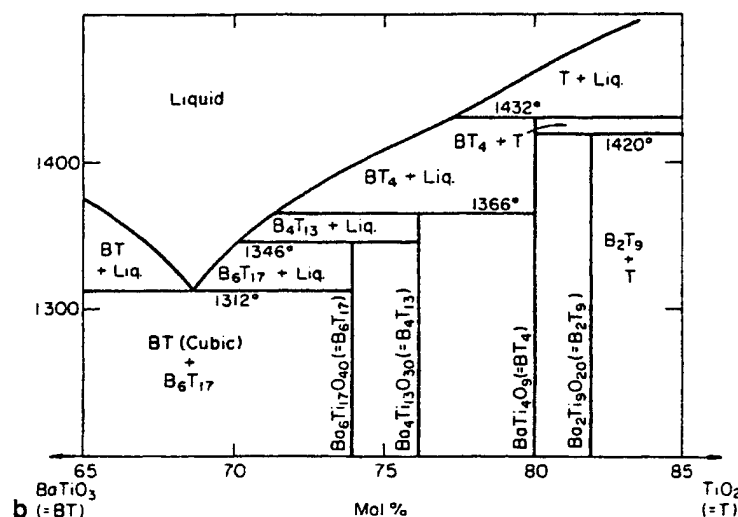
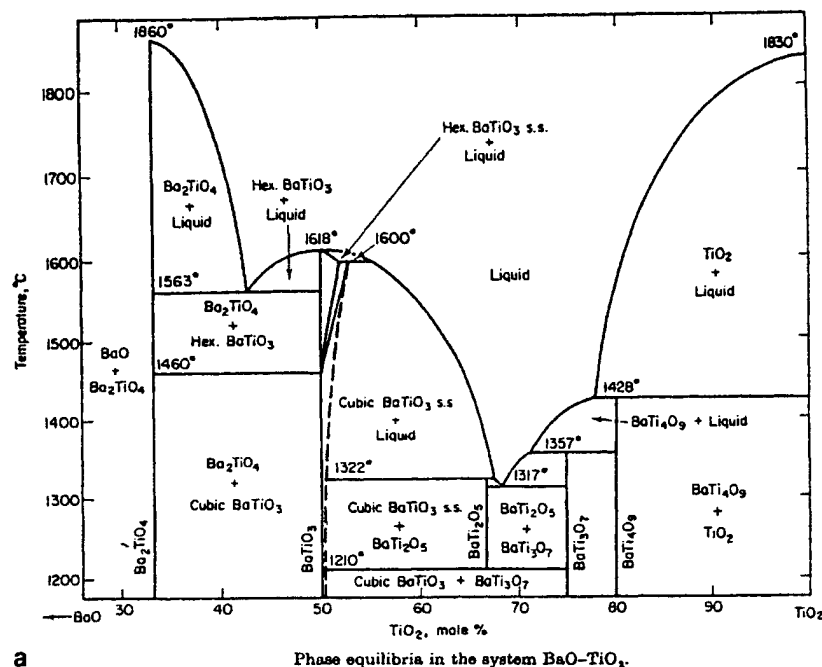


Table 5 Primary and secondary ferroics (Newnham and Cross)

Ferroic class	Orientation states differ in	Switching force	Example
Primary:			
Ferroelectric	Spontaneous polarization	Electric field	BaTiO ₃
Ferroelastic	Spontaneous strain	Mechanical stress	CaAl ₂ Si ₂ O ₈
Ferromagnetic	Spontaneous magnetization	Magnetic field	Fe ₃ O ₄
Secondary:			
Ferroelectric	Dielectric susceptibility	Electric field	SrTiO ₃ (?)
Ferrobimagnetic	Magnetic susceptibility	Magnetic field	NiO
Ferrobielastic	Elastic compliance	Mechanical stress	SiO ₂
Ferroelastoelectric	Piezoelectric coefficients	Electric field and mechanical stress	NH ₄ Cl
Ferromagnetoelastic	Piezomagnetic coefficients	Magnetic field and mechanical stress	FeCO ₃
Ferromagnetolectric	Magnetolectric coefficients	Magnetic field and electric field	Cr ₂ O ₃

In the simple ferroelectrics (at room temperature) the origin of ferroelectricity in the high symmetry paraelectric perovskite is governed by the two unequal TiO¹ and TiO² (and thus reduction of m3m symmetry to 4mm)

bond distances. At a suitable temperature (T_c) when TiO¹=TiO², the distorted perovskite (or ferroelectric) transforms back to the cubic high symmetry m3m perovskite structure.

Fig. 8 Other variants of perovskite structure

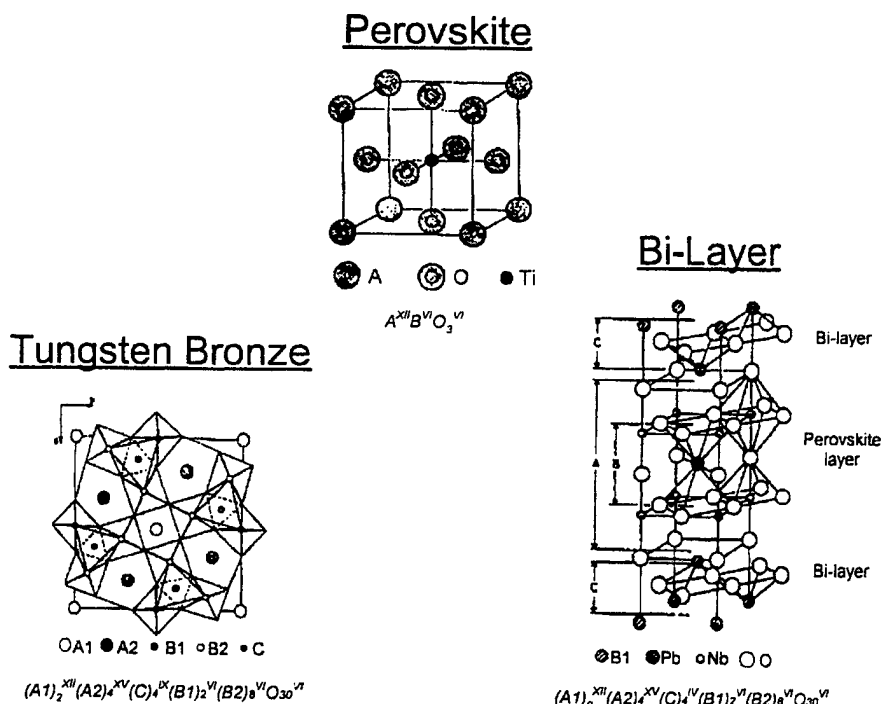


Table 6 Prime device materials in the field of electroceramics

Device applications	Perovskite materials
Microwave dielectrics	$Ba(Zn_{1/3}Nb_{2/3})O_3$, $Ba(Mg_{1/3}Ta_{2/3})O_3$ and Large number of modified compositions
Microwave dielectric substrates for HTSC	$LaAlO_3$, $NdGaO_3$, $Sr(Al_{0.5}Ta_{0.5})O_3$, $Sr(Al_{0.5}Nb_{0.5})O_3$
NOx sensors	$LaFeO_3$
Dielectric resonators	$BaZrO_3$
Resistors	$BaRuO_3$
Conducting electrodes	$SrRuO_3$, $LaCoO_3$
Superconductors	YBCO, BiSCO, $Ba(Pb,Bi)O_3$
Laser host	$YAlO_3$
Magnetic bubble	$GdFeO_3$
Ferromagnetics	$(Ca,La)MnO_3$

Table 7 Some of the practical uses of simple ferroic perovskites and their solid solutions (non ferroelectric and ferroelectrics) are listed

Ferroic perovskite	Comments/applications
$BaTiO_3$	Capacitors, PTC (for hair driers, etc.)
$PbTiO_3$	Pyroelectric detectors, hydrophone, high d_{33} , d_{31}
$Pb(Zr_{1-x}Ti_x)O_3$	Piezoelectric applications of all kind. Simple modifications of compositions or dopants are used for obtaining the suitable material for a specific application, e.g., transducers, hydrophones, actuators, x-y translator, e.g., AFM
$PbLa(ZrTi)O_3$ -8/65/35	Transparent ceramics, electrooptic shutters, EO goggles, etc. for high altitude flying pilots
$LiNbO_3$	Variant of perovskite: Optical modulators
$LiTaO_3$	Variant of perovskite: pyroelectric sensors
$KNbO_3$	Best second harmonic generator
Doped Rh: $BaTiO_3$, $KNbO_3$, Fe: $LiNbO_3$	Photorefractive materials
$SrTiO_3$, $(KTaO_3)$	Tunable microwave devices

There are some other variants of the perovskite structures with other special arrangements (Fig. 8) and which have the limited number of compounds. $LiNbO_3$ and $LiTaO_3$ and their solid solutions along with a few substituents are the most important materials. Because of the versatility of the perovskite structure in exhibit-

ing the vast range of conduction behaviors (as shown below).

Insulator	FE	AFE	Conductor	Superconductor
$SrTiO_3$	$BaTiO_3$	$NaNbO_3$	$La(Cr,Mn,Ni)O_3$	YBCO, etc.

Table 8 Comparison of relaxor and normal ferroics

Property	Normal	Relaxor
Permittivity temperature dependence	Sharp 1st or 2nd order transition about Curie temperature (T_c)	Broad-diffuse phase transition $\epsilon=\epsilon(T)$ about Curie maxima (T_{max})
Permittivity temperature and frequency dependence $\epsilon=\epsilon(T, \omega)$	Weak frequency dependence	Strong frequency dependence
Permittivity behavior in paraelectric range ($>T_c$)	Follow Curie-Weiss law Equation: $1/K=C/(T-T_c)$	Follow Curie-Weiss square law Equation: $1/K=1/K_{max}+(T-T_{max})^2/2K_{max}\delta^2$
Remanent polarization	Strong remanent polarization	Weak remanent polarization
Scattering of light	Strong anisotropy (birefringent)	Very weak anisotropy to light (pseudo-cubic)
Diffraction of x-rays	Line splitting owing to spontaneous deformation from paraelectric to ferroelectric phase	No x-ray line splitting giving a pseudo-cubic structure

the compounds of this family are the prime device materials in the field of electroceramics (Table 6). Some of the practical uses of these simple ferroic perovskites and their solid solutions are listed in Table 7.

3.1 Relaxors

A special family of substituted perovskites which have extraordinarily high dielectric constants have been called "relaxors." From the crystal chemistry point of view the perovskite structure can accept a large number of ionic substitutions to form new simple or complex compounds as well as solid solutions amongst the various oxide or complex oxide compositions (Fig. 9). In particular lead based complex perovskites with the formula $PbA'B'O_3$, $PbB'B''O_3$, $PbA'B'B''O_3$ where $A'=La^{3+}$, etc., $B'=Fe^{2+}$, Mg^{2+} , Zn^{2+} , In^{3+} , Sc^{3+} , and $B''=Nb^{5+}$, Ta^{5+} , W^{6+} result in nanoscale ordered regions in a disordered matrix (Fig. 10). In some cases the material can be converted in to an ordered state. Also the characteristics of the substitutions are not limited to the ionic species listed above but these are some which so far have been prepared, studied, and used in a wide range of applications. The degree of ordering in some of these materials can be adjusted by simple processing and thermal annealing approach whereas in most materials the structure remains in the highly disordered state. These materials have some characteristics which normal perovskite ferroelectrics do not exhibit (Fig. 11). Table 8 shows the comparison of relaxor and normal ferroics.

All the unusual characteristics observed in these materials have been associated with the order-disorder behavior and the degree of order present in these materials. Also perovskites (and some of the related tungsten bronze structure materials) are the only materials so far which have demonstrated this characteristic. Such ferroelectric compositions are categorized as "relaxor ferroelectrics" [55, 56]. Structurally most perovskite based relaxors, due to the presence of slight lattice distortion are in the rhombohedral symmetry. Relaxor materials have shown great promise in most ferroelectric-related application arenas (Table 9).

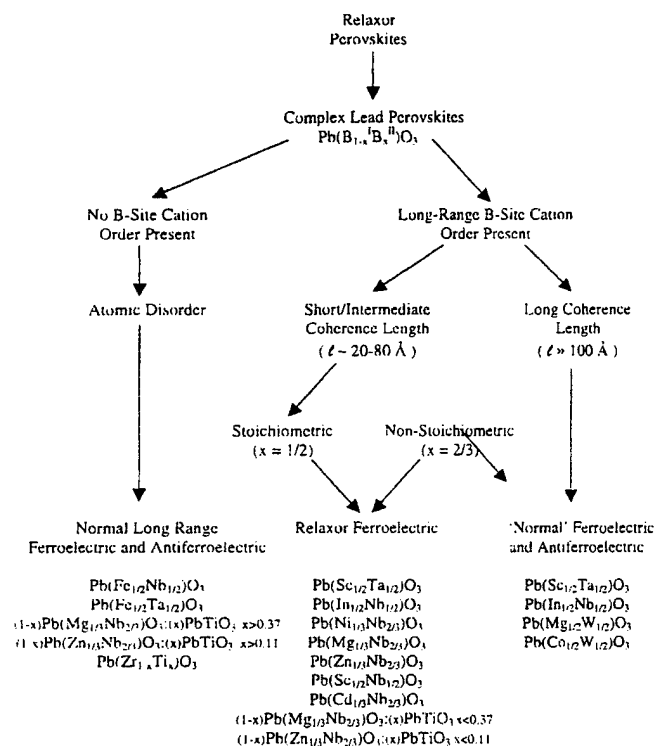


Fig. 9 Various relaxors perovskite combinations and their classification based on short and long range ordering (after Randall and Bhalla)

3.2 Morphotropic phase boundary compositions

It is quite interesting to note that a further expansion of the perovskite ferroelectrics list is possible by the route of solid solution between various classes of perovskite ferroelectric and relaxor (Table 10; [57, 58]). In most cases a morphotropic phase boundary [59] (Fig. 12) occurs at which point several ferroelectric properties change drastically in favor of device applications (Table 11; [56]).

The morphotropic phase boundary (MPB) represents an abrupt structural change within a solid solution with variation in composition but nearly independent of temperature. Usually it occurs because of the instability of one phase against the other at a critical composition

where two phases are energetically very similar but elastically different. It is noticed that the dielectric constant, piezoelectric and electromechanical characteristics, spontaneous polarization and pyroelectric behavior attain maxima whereas the elastic constants tend to be softer in the vicinity of the MPB. Because of such high property coefficients and unique structural characteristics of MPB compositions, a vast number of publications and patents (Table 12) covering various device applications of this class of ferroelectric have been added in the field of electroceramics. Bhalla et al. [60] have recently compiled the vast literature on the structure property diagrams of the relaxor MPB systems. Figure 13 shows the current trend and increased interest in the relaxor based MPB systems [60].

3.3 Microwave dielectrics

Dielectric resonators are the prime components in various communication and microwave systems as those provide for very effective size reduction for microwave components ($\text{size} \propto 1/\sqrt{\text{dielectric constant}}$) compared to that for air filled cavities. In such applications, the material should fulfill the following stringent requirements (Table 13): (1) high dielectric constant, κ (at microwave frequencies); (2) minimum possible dielectric loss, $\tan\delta$; (3) temperature stability of the dielectric properties; (4)

very low thermal expansion coefficients (which is related to (3)).

In a high quality microwave dielectric material the requirements (2), (3) and (4) should be as close to zero as possible. To have such an ideal material available is highly improbable, but suitable materials can be de-

Table 9 Areas of applications for relaxor ferroelectrics and solid solutions

Application:	Example:
Pyroelectrics	$\text{Pb}(\text{Sc}_{1/2}\text{Ta}_{1/2})\text{O}_3$ $(\text{Ba}_{0.60}\text{Sr}_{0.40})\text{TiO}_3$
Capacitors/dielectrics	$\text{Pb}(\text{Mg}_{1/3}\text{Nb}_{2/3})\text{O}_3$ (see patent list)
Electrostriction/actuators	$\text{Pb}(\text{Mg}_{1/3}\text{Nb}_{2/3})\text{O}_3$ $\text{Pb}(\text{Zn}_{1/3}\text{Nb}_{2/3})\text{O}_3$ $\text{Pb}[(\text{Mg}_{1/3}\text{Nb}_{2/3})_{1-x}\text{Ti}_x]\text{O}_3$
Medical ultrasound/high efficiency transducers	$\text{Pb}[(\text{Zn}_{1/3}\text{Nb}_{2/3})_{1-x}\text{Ti}_x]\text{O}_3$ $\text{Pb}[(\text{Sc}_{1/2}\text{Nb}_{1/2})_{1-x}\text{Ti}_x]\text{O}_3$
Piezoelectrics	$\text{Pb}(\text{Zr}_{1-x}\text{Ti}_x)\text{O}_3$ $\text{Pb}[(\text{Zn}_{1/3}\text{Nb}_{2/3})_{1-x}\text{Ti}_x]\text{O}_3$ $\text{Pb}[(\text{Sc}_{1/2}\text{Nb}_{1/2})_{1-x}\text{Ti}_x]\text{O}_3$
Electrooptics	$(\text{Pb}_{1-x}\text{La}_{2x/3})(\text{Zr}_{1-y}\text{Ti}_y)\text{O}_3$

Table 10 Summary of important relaxors based on MPB systems (Bhalla et al.)

System: ^a	Example:
Antiferroelectric : proper ferroelectric	PbZrO_3 : PbTiO_3
Relaxor : proper ferroelectric	$\text{Pb}(\text{Zn}_{1/3}\text{Nb}_{2/3})\text{O}_3$: PbTiO_3
Relaxor (short range order) : proper ferroelectric	$\text{Pb}(\text{Mg}_{1/3}\text{Nb}_{2/3})\text{O}_3$: PbTiO_3
Relaxor (order-disorder) : proper ferroelectric	$\text{Pb}(\text{Sc}_{1/2}\text{Nb}_{1/2})\text{O}_3$: PbTiO_3
Relaxor : antiferroelectric	$\text{Pb}(\text{Zn}_{1/3}\text{Nb}_{2/3})\text{O}_3$: PbZrO_3
Relaxor (short range order) : relaxor (order-disorder)	$\text{Pb}(\text{Mg}_{1/3}\text{Nb}_{2/3})\text{O}_3$: $\text{Pb}(\text{Sc}_{1/2}\text{Nb}_{1/2})\text{O}_3$
Relaxor (o - d) : relaxor (o-antiferroelectric - d-ferroelectric)	$\text{Pb}(\text{Sc}_{1/2}\text{Ta}_{1/2})\text{O}_3$: $\text{Pb}(\text{In}_{1/2}\text{Nb}_{1/2})\text{O}_3$
Relaxor (sro) : relaxor (o-antiferroelectric - d-ferroelectric)	$\text{Pb}(\text{Mg}_{1/3}\text{Nb}_{2/3})\text{O}_3$: $\text{Pb}(\text{In}_{1/2}\text{Nb}_{1/2})\text{O}_3$

^a o: order, d: disorder, sro: short range order

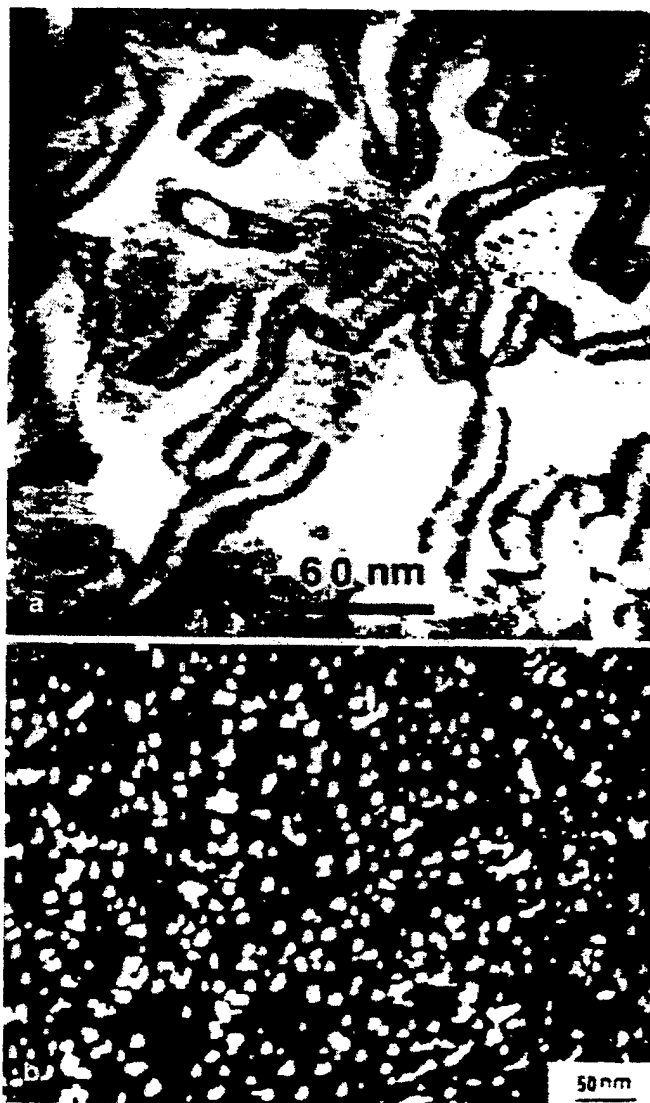


Fig. 10a, b Nanoscale ordered regions in a disordered matrix. (a) $\text{PbSc}_{1/2}\text{Ta}_{1/2}\text{O}_3$ (Harmer, Bhalla); and (b) $\text{PbMg}_{1/3}\text{Nb}_{2/3}\text{O}_3$ (Randall et al.)

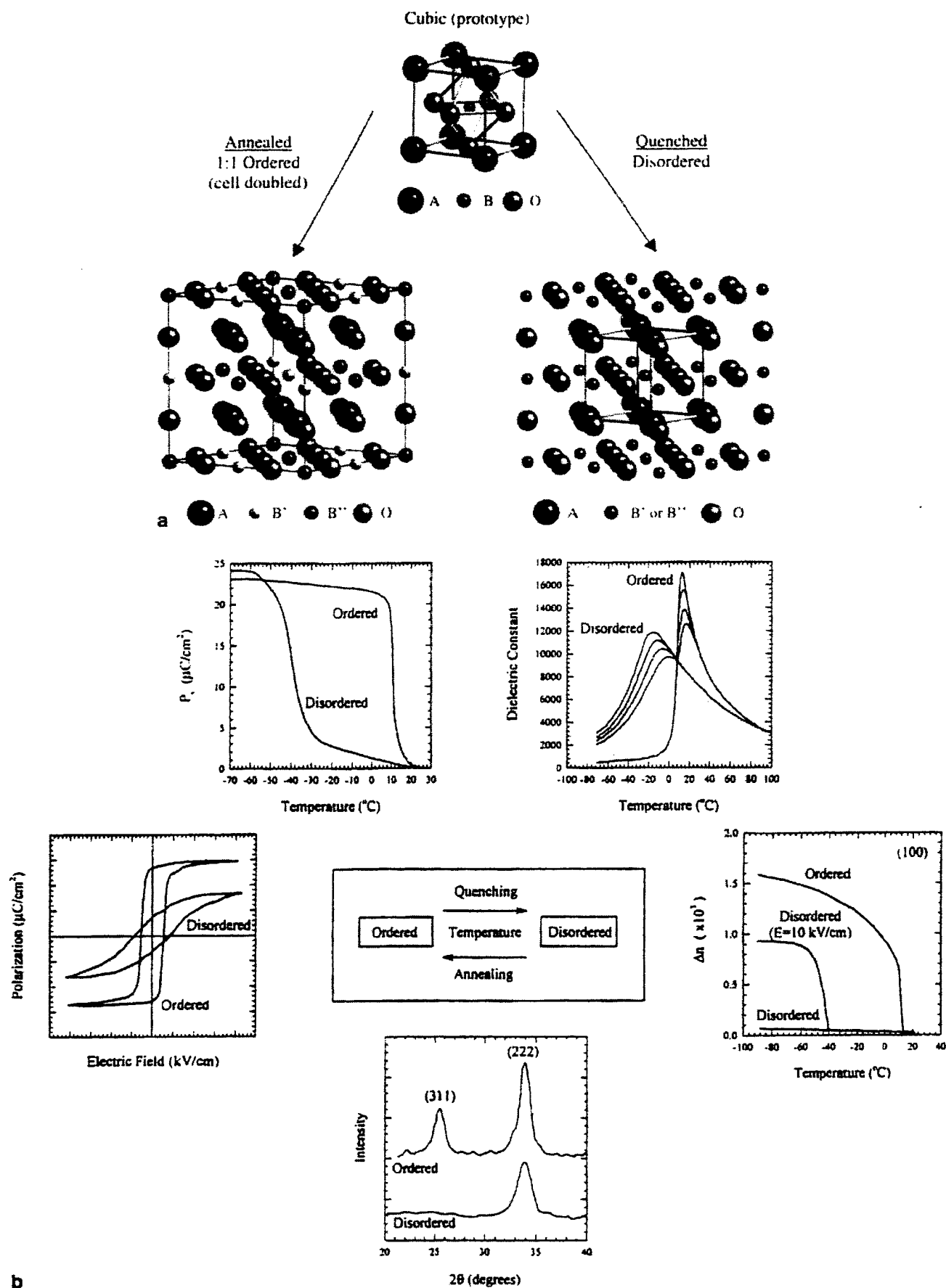


Fig. 11 (a) o-d structure in perovskites, and (b) properties in relation to o-d structure

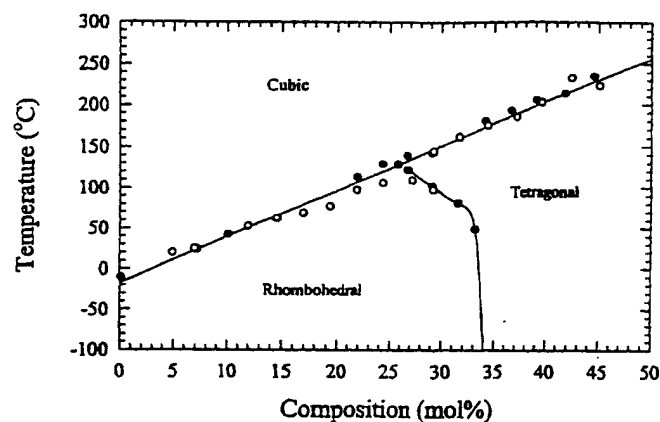


Fig. 12 Phase diagram for the (1-x)PMN:xPT system (Choi et al.)

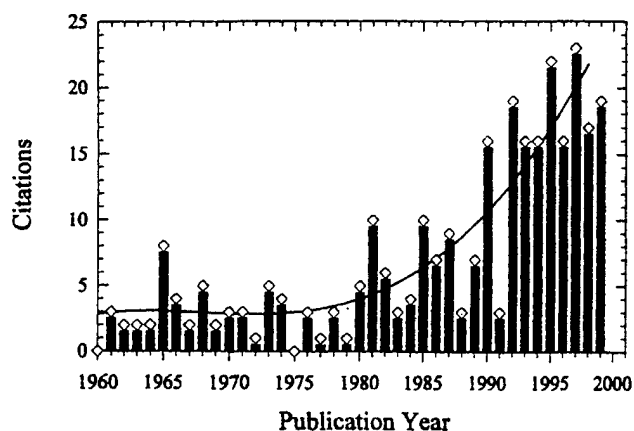


Fig. 13 Number of new relaxor-based solid solution citations reviewed by year

Table 11 Commonly employed perovskite end members for relaxors

Complex perovskites	T_c (°C)	Behavior ^a	Simple Perovskites	T_c (°C)	Behavior
$\text{Pb}(\text{Mg}_{1/3}\text{Nb}_{2/3})\text{O}_3$	-10	RFE	PbTiO_3	190	FE
$\text{Pb}(\text{Zn}_{1/3}\text{Nb}_{2/3})\text{O}_3$	140	RFE	PbZrO_3	230	AFE
$\text{Pb}(\text{Ni}_{1/2}\text{Nb}_{1/2})\text{O}_3$	-120	RFE	BaTiO_3	130	FE
$\text{Pb}(\text{Fe}_{1/2}\text{Nb}_{1/2})\text{O}_3$	110	FE	SrTiO_3	-	PE
$\text{Pb}(\text{Fe}_{2/3}\text{W}_{1/3})\text{O}_3$	-95	RFE			
$\text{Pb}(\text{Mg}_{1/2}\text{W}_{1/2})\text{O}_3$	38	AFE			
$\text{Pb}(\text{Nb}_{1/2}\text{W}_{1/2})\text{O}_3$	17	AFE			

^a FE: ferroelectric, AFE: anti-ferroelectric, RFE: relaxor-ferroelectric, PE: para-electric

Table 12 List of a few relaxor-based compositions for MLC

Composition	EIA specification	Manufacturer	Patents
PLZT-Ag	X7R	Sprague	U.S. Pat. 4,027,209 (1973)
PMW-PT-ST	X7R	DuPont	U.S. Pat. 4,048,546 (1973)
PfN-PFW	Y5V	NEC	U.S. Pat. 4,078,938 (1978)
PfN-PFW-PZN	Y5V	NEC	U.S. Pat. 4,236,928 (1980)
PfN-PMT	-	TDK	U.S. Pat. 4,216,103 (1980)
PMN-PT	Y5V	TDK	U.S. Pat. 4,265,668 (1981)
PMN-PfN	Y5V	TDK	U.S. Pat. 4,216,102 (1980)
PMN-PfN-PMW	Y5V	TDK	U.S. Pat. 4,287,075 (1981)
PFW-PZ	Z5U	TDK	U.S. Pat. 4,235,635 (1980)
PFW-PT-MN	Z5U	Hitachi	U.S. Pat. 4,308,571 (1981)
PMN-PZT-PT	Z5U	Murata	U.S. Pat. 4,339,544 (1982)
PfN-PFW-PbGe	X7R	-	-
PfN-PfN-PNN	Z5U, Y5V	Ferro	U.S. Pat. 4,379,319 (1983)
PMW-PT-PNN	Z5U	NEC	U.S. Pat. 4,450,240 (1984)
PfN-BaCa(CuW)-PFW	Y5V	Toshiba	U.S. Pat. 4,544,644 (1985)
PMN-PZN	Z5U	STL	U.K. Pat. 2,127,187A (1984)
PMN-PfN-PT	Z5U	STL	U.K. Pat. 2,2126,575 (1984)
PMN-PZN-PfN	Z5U	Matshshita	Japan Pat. 59-107959 (1984)
PMN-PFW-PT	-	Matshshita	Japan Pat. 59-203759 (1984)
PNN-PfN-PFW	Y5V	Matshshita	Japan Pat. 59-111201 (1984)
PZN-PT-ST	-	Toshiba	-
PMN-PfN-PbGe	Z5U	Union Carbide	U.S. Pat. 4,550,088 (1985)
PfN-PNN	Y5V	-	-
PFW-PfN	-	NTT	-
PMN-PT-PNW	Z5U	Matshshita	-
PMW-PT-PZ	X7R	NEC	-
PZN-PMN-PT-BT-ST	Z5U	Toshiba	Japan Pat. 61-155245 (1986)
PZN-PT-BT-ST	X7R	Toshiba	Japan Pat. 61-250904 (1986)
PZN-PMN-BT	Z5U, Y5S	Toshiba	-
PMN-PLZT	Z5U	MMC	U.S. Pat. 4,716,134 (1987)
PMN-CT,ST,BT	Z5U	Matshshita	Japan Pat. 62-115817 (1986)
PFW-PfN-PT	Y5V	-	-
BT-PMN-PZN	X7R, X7S	Toshiba	U.S. Pat. 4,767,732 (1988)
PMN-PS-PNW-Ca (base metal)	Z5U	Matsushita	-

Table 13 Microwave dielectrics (a) and (b) (Table based on [64])

	ϵ_r	Q (4 GHz)	T_f	f_0 (GHz)	$Q \times f (\times 10^3)$	Refs ^a
Temperature coefficients						
Ba ₂ Ti ₉ O ₂₀	40	9000	+2			4, 5
(Zr,Sn)TiO ₄	34–37	9000	+/-20			6
(Sr,Ca)[(Li,Nb)Ti]O ₃	38–46	3500 at 9 GHz	+30/-70			7
BaTi ₄ O ₉	38	8500	+15			4, 5, 8
(Ca,Sr)(Ba,Zr)O ₃	29–32	2500 at 11 GHz	+/- 50			9
MgTiO ₃	17	22000 at 7 GHz	-45			23, 24, 25
CaTiO ₃	170	1800 at 7 GHz	+800			
Qxf characteristics						
MgTiO ₃ -CaTiO ₃	21	8000		7	56	14
Ba(Sn,Mg,Ta)O ₃	24	43,000		10	430	15
Ba(Zn,Ta)O ₃	30	14,000		12	168	16, 17
Ba(Zr,Zn,Ta)O ₃	30	10,000		10	100	17, 18
(Zr,Sn)TiO ₄	38	10,300		5	51	19, 20
Ba ₂ Ti ₉ O ₂₀	40	8000		4	32	21, 22
BaO-PbO-Nd ₂ O ₃ -TiO ₂	90	5000		1	5	19, 23

^a number refers to that of in original paper

signed by using the simple guidelines of crystal chemistry as described in the following sections 5.1 and 6, also in the paper by Guo et al. [61].

Several compounds such as TiO₂, spinels and perovskites (Table 13) have been examined for microwave dielectric resonators but the perovskites provided the wide range of suitable materials, possibility of tailoring the parameters to meet the device requirements. In addition, several approaches like eutectics, composites (macro, micro and nanoscale) [62, 63] and solid solutions have been made to design optimum materials for specific applications.

While telecommunications are revolutionizing our lifestyle, the demand for new microwave dielectrics with the multifunctionality-feature is also increasing. The present technology in addition to the above listed requirements, demands tunable microwave dielectrics. To our surprise, so far, it appears that it is the perovskite family which provides the best materials e.g., SrTiO₃, KTaO₃, CaTiO₃, and several solid solutions e.g., (BaSr)TiO₃, (PbSr)TiO₃ etc. and their doped and modified compositions, for the frequency and field agile microwave electronics.

4 Perovskites as superconductors

4.1 Conductors and superconductors

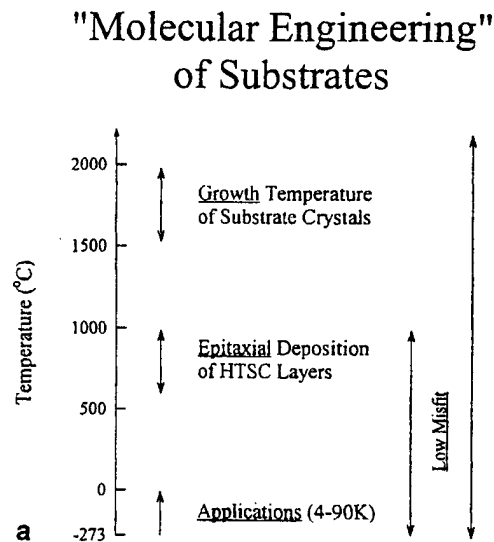
While for 30 years the perovskite structure dominate the world of dielectrics, it was soon noted that a combination of 4f ions in the A-site, and 3d ions in the B-site give rise to reasonably conducting phases, at room temperature and at very high temperatures. For example, LaCrO₃ was a typical candidate for MHD electrodes, Rao et al. [65] vigorously followed up on cuprate conductors including "BaCuO₃" phases. But it was not their argument which led to the first superconductive perovskite. In 1975, Sleight et al. [66] developed the highest temperature oxide superconductor in a BaBiPbO_x perovskite. In the late seventies Gilbert [67] and Gilbert and Roy [68] performed the usual substitutions in the structure to see if the T_C could be

raised. All substitutions lowered the T_C. A self-imposed constraint of not using Cu²⁺ because of the variability of valence states, had them avoid the winner. Bednorz and Muller's early work [69] was on the K₂NiF₄ structure and the first perovskite phase with T_C over 30K was BaLaCuO_x [70]. When James Ashburn [71] at the University of Alabama (Wu [72]) by sheer empirical mixing of "rare earth" and Ba, Sr, and Cu oxides discovered the "YBC" superconductor in a mixture of "green and black phases" the authors did not immediately connect the perovskite phase to the high T_C. In the event a highly defective perovskite YBa₂Cu₃O_{7-δ} was identified as the true high T_C material. Since then some billions of dollars (literally) have been spent in sheer empirical substitution of every easily conceivable combination of ions – the best work following well established crystal chemical principles in the perovskite structure. It is unlikely that any structure will ever receive the same detailed chemical manipulation again. It is significant to note that in this enormous international search the principles of physics could contribute nothing. The highest T_C materials at present are BiSCO and Hg-HTSC and represent another intercalated family not much unlike the Roddlesden-Popper phases.

4.2 Perovskite substrates for high-T_C superconductors

While the search for new superconductors by crystal chemical manipulation was intense for a dozen years, and relatively obvious substitutions increased the T_C some 30 °C, the selection of useful substrate materials for the deposition of high T_C superconductors (HTSC) is of prime importance and is subjected to a number of more difficult constraints, and has received much less attention. In several microwave applications of the "ceramic dielectric substrates," important considerations have been given to the (a) materials' thermal properties such as thermal expansion and thermal conductivity, and (b) the electrical characteristics such as low dielectric loss, dielectric constants and dielectric coefficient with

Fig. 14 (a) Temperature scale of substrates between their melting (growth) temperature and the application temperature (ranges 4 to 90 K). The regions of required low misfit and of required absence of twinning due to structural phase transitions are indicated. **(b)** Structural and compatible aspects of substrates needed for the applications of HTSC films; selection criterion and improvement of substrate materials over the characteristics of well known LaAlO_3 crystals



CHARACTERISTICS			
$x \approx 2-25$, $Q \approx 10,000$ at liq. N_2 & 10GHz ($\tan \delta \approx 10^{-4}$)	M.P. $\approx 2100^\circ\text{C}$, Crystal growth: 2" dia. Crystal available	Heavy twinning; phase transition $\approx 500^\circ\text{C}$ (rhomb.) 012 edge 3.792Å	Processability of HTSC thin film: α , a O.K. but not perfect; no buffer layer needed
CONSIDERING IT AS A MATERIAL			
TO BE IMPROVED UPON		COMMENTS & APPROACH	
Lower x and $\tan \delta$ at liq. N_2 & freq. $\geq 10\text{GHz}$	Lower M.P. (congruent), if possible the feasibility of crystal growth from Pt-crucible or other suitable/practical growth technique, sizes 4" desirable	No twinning, if there is a T_c - it should be below liq. N_2 (?)	α , a match in temperature range 500 K - liq. N_2

Table 14 Substrate parameters required for HTSC film applications

	Multi-chip-modules (MCM)	Millimeter wave devices
Applications	Digital receivers, IR detectors, high performance computers	Oscillators; frequency discriminators; phase shifters; delay lines etc.
Requirements	High speed, $\propto 1/(x)^{1/2}$; satisfy characteristic impedance $1/Z\alpha(W/d)(x)^{1/2}$; high packing density (thinner film); low crosstalk (thinner film)	Narrow bandpass filters high Q); low temperature coefficient of capacitance; compact designs (moderate x values)
Dielectric constant	$x \approx 20$ or less is acceptable, however, for film thickness $d = 1 \mu\text{m}$, $x < 10$ is required	$x \approx 20-25$ desirable
Dielectric loss	$\tan \delta < 10^{-3}$ to maintain the dielectric loss much lower than the conductor loss	Ultra low loss, $\tan \delta < 10^{-4}$ ($Q > 10,000$)
Type of substrates	Single crystal films (2 μm) in multi-layer integrated structure with HTSC films	Single crystal substrates 3" or 4" in diameter

temperature. The main heart of the selection criteria are intended for the speed (in MCM devices) and the reduction of thermal effects on the signals. In case of the resonators the values of the constants are adjusted with the size of the required device. If we look for HTSC uses in such applications, the additional requirement from the

substrates are also demanded. For example, additional crystallographic matching parameters are required to deposit high quality oriented (preferably epitaxial) and hence high J_C high temperature superconducting films on the single crystal perovskite substrates. These parameters are summarized in Table 14.

Table 15 Potential candidate materials for substrates for HTSC (Guo et al.)

Substance	@ 10 KHz, 90K	
	K	D
LaAlO ₃	21.5	7.47×10 ⁻⁵
Ba(Mg _{1/3} Ta _{2/3})O ₃		
hot-pressed ceramic	25.0	1.93×10 ⁻⁵
ceramic	24.7	<1×10 ⁻⁵
crystal fiber	25.0*	<1×10 ⁻⁵
(Ba _{0.9} Sr _{0.1})(Mg _{1/3} Ta _{2/3})O ₃	26.04	2.34×10 ⁻⁴
(Ba _{0.8} Sr _{0.2})(Mg _{1/3} Ta _{2/3})O ₃	26.6	1.96×10 ⁻⁴
MgLaAl ₁₁ O ₁₉	14.0	1.51×10 ⁻⁴
MgNdGaAl ₁₀ O ₁₉	15.6	1.75×10 ⁻⁴
CaGa ₆ Al ₆ O ₁₉	20.9	3.20×10 ⁻⁴
CaGa ₁₂ O ₁₉	9.4	1.81×10 ⁻⁴
Sr(Al _{1/2} Nb _{1/2})O ₃	18.7	2.20×10 ⁻⁴
Sr(Al _{1/2} Nb _{1/2})O ₃ , Sol-Gel	17.2	6.57×10 ⁻⁴
0.7SAN:0.3LaAlO ₃	25.7	2.79×10 ⁻⁴
0.7SAN:0.3NdGaO ₃	23.0	5.15×10 ⁻⁴
Sr(Al _{1/2} Ta _{1/2})O ₃	11.8	4.24×10 ⁻⁵
Sr(Al _{1/2} Ta _{1/2})O ₃ , Sol-Gel	11.5	6.05×10 ⁻⁴
0.7SAT:0.3LaAlO ₃	21.7	7.47×10 ⁻⁵
0.7SAT:0.3NdGaO ₃	16.0	4.25×10 ⁻⁴
1/3SAN:1/3SAT:1/3NdGaO ₃	22.3	5.11×10 ⁻⁴
La(Mg _{2/3} Ta _{1/3})O ₃	23.4	4.22×10 ⁻⁴
La(Mg _{1/2} Ti _{1/2})O ₃	27.1	1.82×10 ⁻⁴
La(Al _{1/4} Mg _{1/2} Ta _{1/4})O ₃	24.1	1.17×10 ⁻⁴
YBa ₂ Al ₂ TaO ₉	11.2	8.33×10 ⁻⁴
KMgF ₃	5.8	1.65×10 ⁻⁴

Numerous candidate materials have been suggested for such purposes to achieve useful HTSC based devices. The most widely used candidate has been LaAlO₃. The serious problem of ferroelastic twinning in this material however, seriously affects the quality of HTSC film and the device performance. An additional factor, i.e., thermal expansion, must also be considered rather seriously in selection of the single crystal substrate materials for HTSC. In this case, the films are deposited and oxidized at ≈500 °C and the devices operate at liquid nitrogen temperatures. Therefore, for the lower aging effects and high performance from the device point of view, thermal expansion matching over the temperature range from the deposition temperature to liquid nitrogen are highly recommended. These features are illustrated in Fig. 14(a).

The goal has been to design and develop new highly suitable substrates which are better than that of LaAlO₃. Thus the considerations for the selection was based on the approach illustrated in Fig. 14(b) [73].

Investigations on the design and engineering of candidate substrate materials suitable for high T_C superconductor thin film deposition and application have yielded several interesting new hosts such as Ba(Mg_{1/3}Ta_{2/3})O₃ (BMT), Sr(Al_{1/2}Ta_{1/2})₃ (SAT); Sr(Al_{1/2}Nb_{1/2})O₃ (SAN). These complex perovskite phases and their associated solid solutions provide new options for ultra low losses; low permittivity substrates with close structural and thermal matching to the high T_C oxide superconductors. In this work it was necessary to develop a predictive capability for the dielectric constants of mixed oxide perovs-

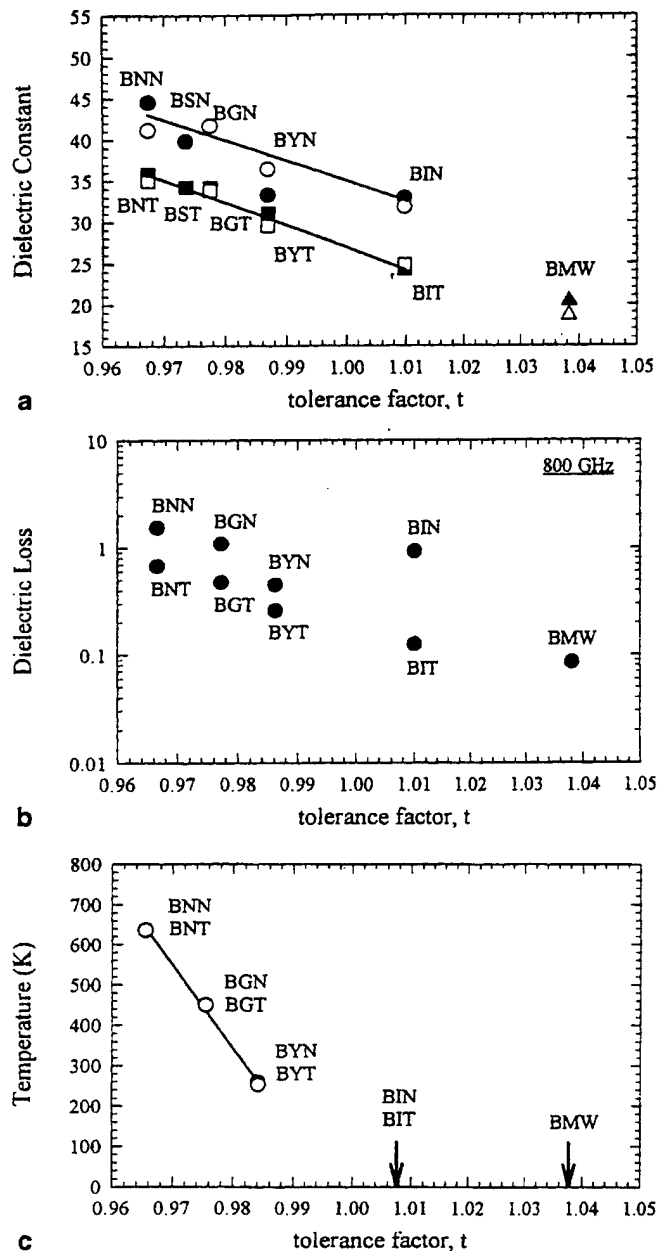


Fig. 15 (a) Dielectric constant vs. tolerance factor (Zumuhlen); (b) Dielectric loss vs. tolerance factor (Zumuhlen); and (c) Transition temperature vs. tolerance factor

kites by extending Shannon's approach. Our approach is described later in Sect. 6.2 of this paper and some of the potential candidates developed are listed in Table 15.

5 Some specific features

5.1 Revisiting the tolerance factor and its new and added significance

The tolerance factor (T.F.), a simple geometrical number which was worked out by Goldschmidt, appears now to be a very useful figure. Recently, in trying to control the

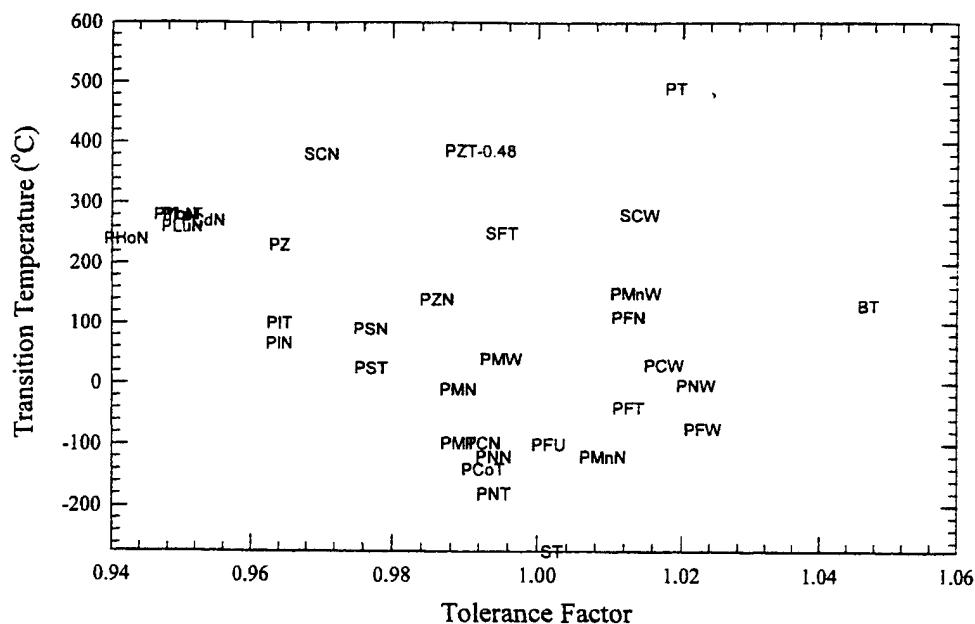
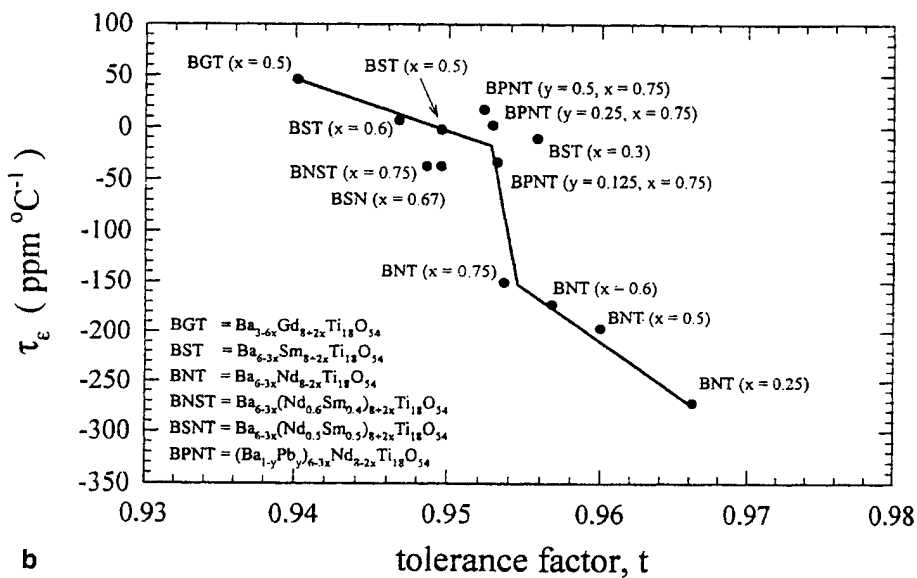
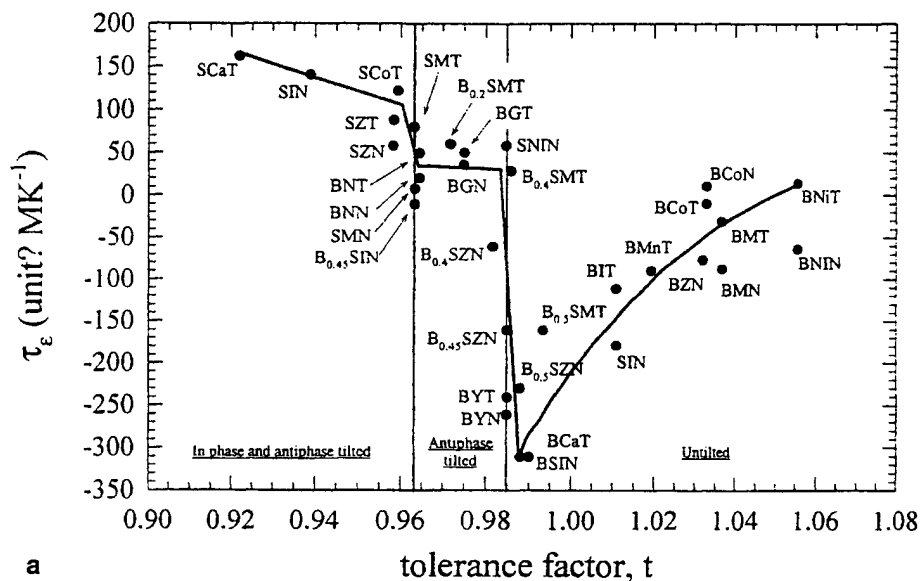


Fig. 17 (a) Temperature coefficients vs. tolerance factor at room temperature for some microwave dielectrics and (b) τ_f vs. T for BNT compounds



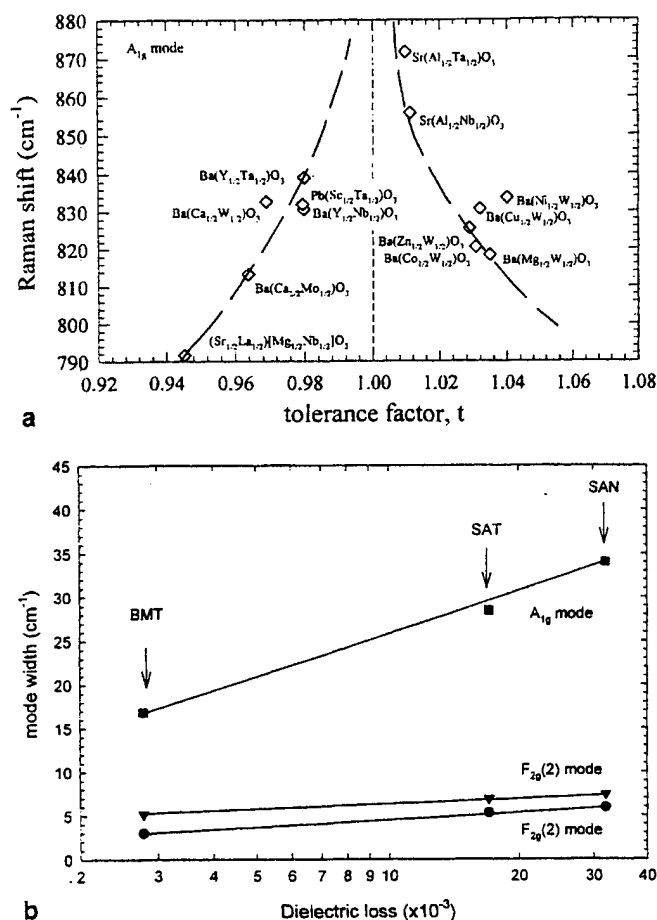


Fig. 18 (a) A_{1g} Raman mode shift vs. tolerance factor in perovskite structure; and (b) Raman mode width vs. dielectric loss in perovskites microwave dielectrics

various device-oriented properties of the perovskite structure again and again useful correlations have been found with this simple parameter. The T.F. shows how far from ideal packing the ionic sizes can move and still be "tolerated" by the perovskite structure. It reflects the structural distortion, force constants of binding, rotation and tilt of the octahedrons, etc.. These in turn affect the dielectric properties, transition temperature, temperature coefficient of the dielectric constant of material, and even the dielectric loss behavior in a perovskite dielectric.

For $t < 1$, the size of the unit cell is governed by the B-site ion and as a result the A-site ions have too much room for vibration. For $t > 1$, just the opposite situation occurs in the unit cell, i.e., in this case, B-site ions have too much room to vibrate. The $t = 1$ condition represents the "close-packing" in the perovskite structure. It is important to mention here that all these calculations hold only when the radii of the ions used for calculating "*t*" are taken constantly from within the same tables e.g., Roy/Müller, or Shannon/Prewitt, or Goldschmidt, or Pauling. Therefore, various A- and B-site substitutions may influence properties involving restoring forces, bond strength, dipolar behavior, etc. Several properties especially related to the dielectric, phase transition be-

havior etc. in electronic materials correlate significantly with this simple tolerance factor approach. A few examples [74–76] (without going into details) are illustrated in Fig. 15(a), (b), and (c).

Zumuhlen et al. [74] suggested that restoring force constant of the lowest polar mode is highly influenced by the values of tolerance factors and the binding energy and consequently reflects on the magnitude of dielectric constant of a compound.

Figure 15 shows the relation of dielectric constant and transition temperature with tolerance factor in several perovskite structures. Figure 16 further expands the plots for the MPB composition materials to correlate the T_C s of various compounds.

In Figure 17 there are plotted the temperature coefficients of a dielectric in relation to the tolerance factor.

As mentioned above, the tolerance factor may also correlate well with the peak width and frequency of a typical A_{1g} mode in Raman scattering (Fig. 18). Such features can subsequently be related back to the intrinsic dielectric losses in the perovskite family compounds in the microwave frequency region. The foregoing illustrates again the enormous value and power of the true first principles approach in science¹: relying on the facts (empirical data) *not* the theories.

5.2 Quantum paraelectrics

Quantum paraelectric behavior is the tendency of materials to exhibit a behavior that suggests an impending phase transition at low temperatures, but the temperatures are low enough to activate quantum effects in these materials and thus the impending ferroelectric phase transition may not be realized in these cases [77]. So far the effect has been associated with only some perovskites, e.g., SrTiO₃ [78], KTaO₃, CaTiO₃ [79] and possibly several solid solution (RE,Na)TiO₃, where RE=La, Nd, Sm, Gd [80, 81]. When a small amount of impurities (a few ppm) are added, this class of perovskites shows a typical ferroelectric-like behavior and are thus classified as incipient ferroelectrics.

Quantum paraelectrics by virtue of their field tunability, frequency agility and low loss tangent values are promising candidates for applications in next generation communication devices. Also these materials are ideal for tunable microwave resonator and filter designs when integrated with high T_C superconductor microwave devices.

¹ Aristotle, in the Nicomachean Ethics I, vii, 20–22, clearly defines first principles in science thus: "Nor again must we in all matters alike demand an explanation of the reason why things are what they are; in some cases it is enough if the fact that they are so is satisfactorily established. This is the case with first principles; and the fact is the primary thing – it is a first principle. And principles are studied – some by induction, others by perception, others by some form of habituation, and also others otherwise; so we must endeavour to arrive at the principles of each kind in their natural manner, and must also be careful to define them correctly."

5.3 Unexpected application niches

5.3.1 Giant magnetoresistance (GMR)/colossal magnetoresistance (CMR)

The phenomenon is recognized as a change in resistance of a material by more than a factor of ten in the presence of magnetic field. It is interesting to note that a large number of compounds related to perovskite family $R_{1-x}A_x\text{MnO}_{3+y}$ where R refers to rare earth elements and A refers to alkaline-earth elements (Sr, Ca, etc.) are the prime oxide compositions exhibiting giant magnetoresistance/colossal magnetoresistance effect and metal:insulator type transitions [82, 83]. Several compounds belonging to both ABO_3 and K_2NiF_4 structures exhibiting the GMR effect have been synthesized and studied in the past decade, e.g., $\text{La}_{1-x}\text{Sr}_x\text{MnO}_3$, $\text{LaMnO}_3\text{:Ca}$, $(\text{La,Pr})(\text{Sr,Ca})\text{MnO}_3$, $(\text{La,Sr})\text{CoO}_3$, LaNiO_3 , etc.

GMR oxide compounds find tremendous applications such as underwater sonar, high pressure pumps, active vibration control, damage analysis and sensors related area. These materials also have potential in high density magnetic storage technologies.

5.3.2 Catalysis

Since the 1980s perovskites have appeared in catalysis application [84, 85]. Mixed oxides of transition and rare-earth metals possessing perovskite structure appear to be suitable for such high-temperature processes as catalytic combustion, methane reforming, ammonia oxidation, sulfur dioxide reduction, etc., due to their well-known thermal stability in a broad range of oxygen partial pressures and resistance to catalytic poison [84, 85]. Recently the fact that perovskite can be both the substrate and the wash-coat, and also the active element has led to new advances by Isupova et al. [86].

Up to the present, catalytic properties of pure bulk perovskites or supported perovskites have been mainly studied and reported [86–88]. Suitable systems are rather limited but the content of the active component, and chemical interaction between active component and support at enhanced temperatures often cause loss of activity and mechanical strength. At the same time, bulk catalysts with homogeneous distribution of the structural additives and/or promoters are known to be the most thermally stable under real high-temperature conditions. Moreover, catalysts with a high content of the active component are more resistant to such catalytic poisons such as Cl, F, S-containing compounds. To minimize the pressure drop across the catalytic bed especially for gas streams with high linear velocities honeycomb monoliths are required (Fig. 19).

Pauli et al. [89, 90] developed the technology of perovskite monolith honeycomb catalyst production, the methods of preparation of highly dispersed, chemically active powders with uniform phase composition and narrow partial size distribution. Two techniques: mechano-

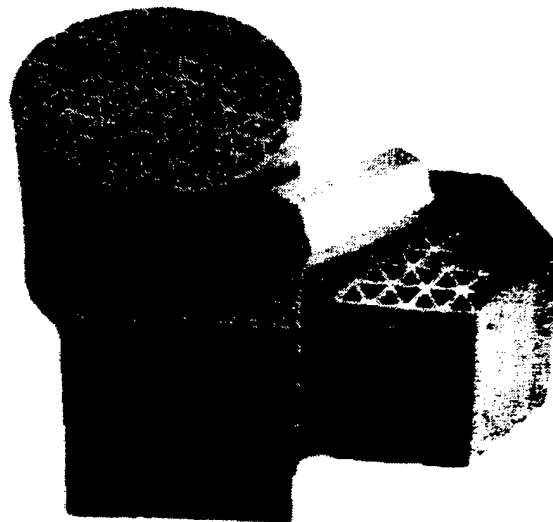


Fig. 19 Typical shapes of monolithic perovskite catalysts

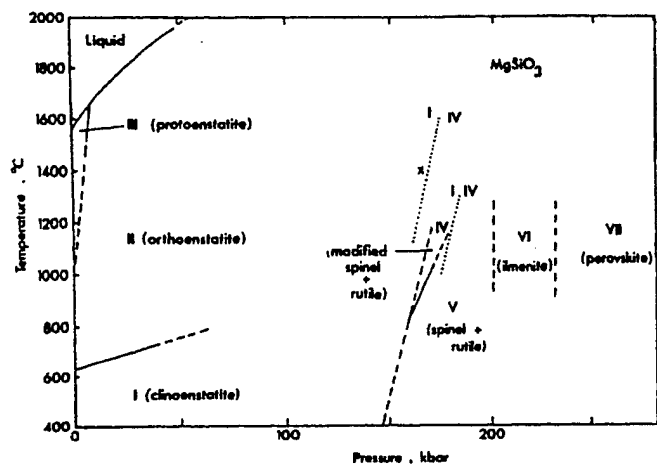
chemical activation (MA) of solid starting compounds in high powered ball mills with a subsequent thermal treatment [89, 90] and arc plasma thermolysis (APT) of the mixed solutions of rare-earth and transition metals nitrates were both shown to work [91].

5.3.3 Major materials of the Earth's mantle

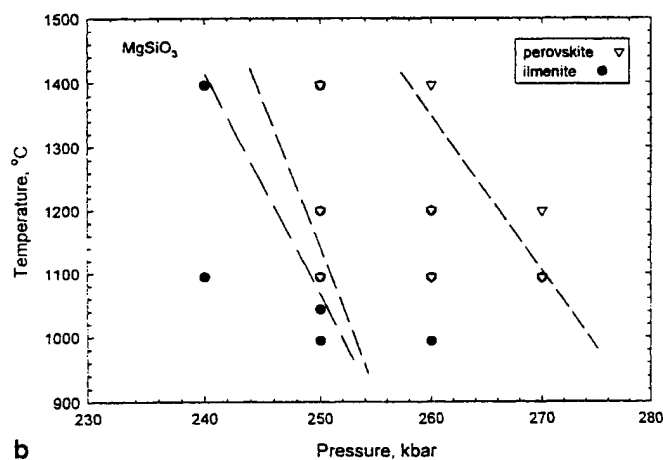
Speculation as to what the inner layers of the Earth are made of are an intriguing aspect of high pressure crystal chemistry. It is now a wide belief that the major component of the lower mantle of the earth may be a perovskite- $(\text{Mg,Fe})\text{SiO}_3$ [92]. Several experimental data on the conversion of ilmenite structure, MgSiO_3 , to perovskite at pressures ~250 kbars and temperature ~1000–1400 °C strongly supports the hypothesis. Figure 20(a) and (b) shows the ilmenite-perovskite stability range in the case of MgSiO_3 [52], which predominantly occurs as a substituted $(\text{Mg}_{1-x}\text{A}_x)\text{SiO}_3$ perovskite of the earth mantle. The pressure and temperature range are in the vicinity of the conditions existed at the mantle.

5.3.4 Ultrahigh melting point materials: $\text{Ba}(\text{Mg}_{1/3}\text{Ta}_{2/3})\text{O}_3$

Ceramics of the complex perovskite oxide, $\text{Ba}(\text{Mg}_{1/3}\text{Ta}_{2/3})\text{O}_3$, which crystal chemically are also analogues of PMN, have been studied extensively as potential microwave dielectrics. We have shown [73] that the BMT compound is one of the most refractory oxides so far known to science. Its refractory characteristics were not known till our attempts to grow the single crystals of BMT from its melt using the laser heated pedestal growth technique [93]. It grows congruently from the melt in the temperature range of 2900–3100 °C. A typical high temperature cubic perovskite phase was obtained at



a

Phase diagram of MgSiO_3 .

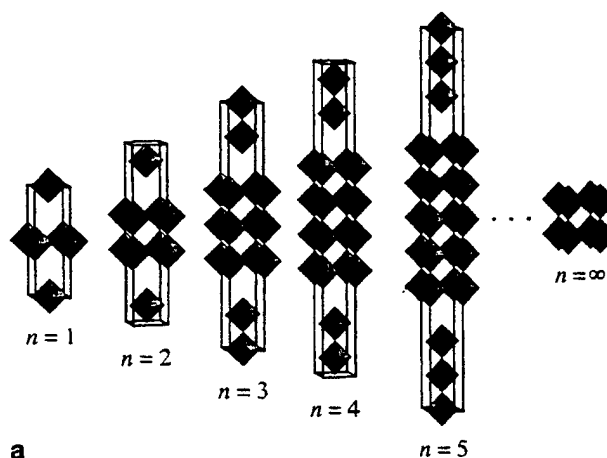
b

Fig. 20 (a) Phase diagram of MgSiO_3 ; (b) experimental data for the ilmenite-perovskite

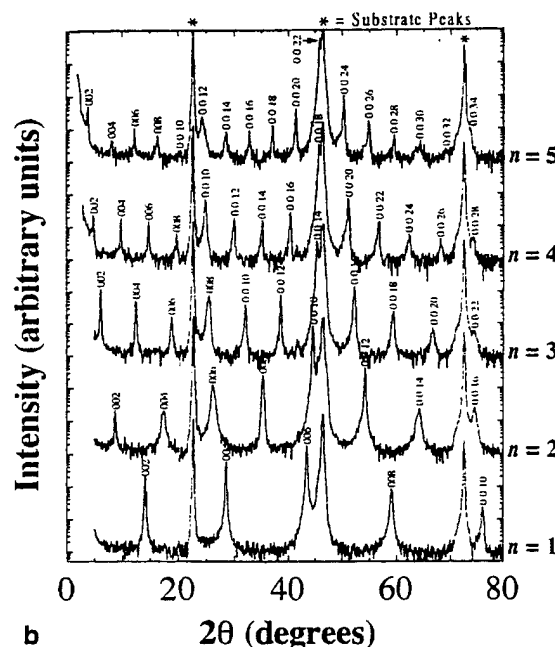
room temperature, in comparison to the hexagonal, ordered perovskite ceramics usually obtained via solid state sintering. Vicker's indentation hardness test suggests the hardness of BMT single crystals are comparable to or slightly harder than Al_2O_3 . These findings are highly unexpected, since the anisodesmicity caused by half-breeding of a divalent (Mg^{2+}) and pentavalent (Ta^{5+}) would have been expected to strongly *lower* the melting point.

6 Molecular engineering and design of new phases (compounds) with desired properties

It has been illustrated in earlier sections (5.1) that while simple structural descriptions such as the tolerance factor in a given perovskite compound can correlate and predict various property characteristics, such as transition temperature, temperature coefficient of dielectrics, dielectric loss, etc., it is likely that several simple crystal chemical guidelines can guide us to design the new phases/compounds with targeted electrical and mechanical properties within the perovskite family of materials. In this context we will



a



b

Fig. 21 $\text{AO}(\text{ABO}_3)_n$ structure - Ruddlesden and Popper phase (Schlom et al.)

provide a few examples which are of high technical importance and in which this approach has been exploited by us to design unique perovskites with desired properties.

6.1 Ruddlesden-popper phases and molecular engineering

The K_2NiF_4 structure in simple terms can be represented as KF layers separating the corner shared perovskite blocks. Ruddlesden and Popper [94,95] designed a series of homologous compounds with the general formula $\text{AO}(\text{ABO}_3)_n$ where AO represents the rock salt structure layer separating the blocks of perovskite layers characterized by $n=1, 2, 3, \dots, \infty$. Such phases exhibit properties ranging from a typical insulator or ferroelectric to a conductor or superconductor. As n increases, the phases tend to be more perovskite in nature and finally reaches the pure perovskite structure for $n=\infty$ (Fig. 21).

Table 16 Some Ruddlesden and Popper type phases studied by various researchers (Sharma et al.)

Compound	Lattice type/symmetry
RE ₂ CuO ₄ (RE = rare earth)	T, T', T'', T*
La _{n+1} Ni _n O _{3n+1} (n=1, 2, 3)	Tetragonal/monoclinic (n=1) Orthorhombic (n=2, 3)
La _{n+1} Co _n O _{3n+1}	Orthorhombic (n=1, 3) Pseudo monoclinic/tetragonal Symmetry for n=1 also suggested
Sr _{n+1} Ti _n O _{3n+1}	Tetragonal
Sr _{n+1} Fe _n O _{3n+1}	Tetragonal
Sr _{n+1} Ir _n O _{3n+1}	Tetragonal
Sr _{n+1} Cr _n O _{3n+1}	Tetragonal, I4 ₁ /acd (n=1)
Sr _{n+1} V _n O _{3n+1}	Tetragonal
Sr _{n+1} Ru _n O _{3n+1} (n=1, 2)	Tetragonal
LaSr ₃ Fe ₃ O _{10-δ}	Tetragonal
Ca _{n+1} Mn _n O _{3n+1}	I4 ₁ /acd (n=1)
A ₂ Ln ₂ Ti ₂ O ₁₀ (A=Na, K)	Tetragonal
Sr ₃ MnM'O ₇ (M'=Ru, Fe)	Tetragonal
(A,A') _{n+1} M _n O _{3n+1} (n=1, 2, 3) (A,A' = rare earth/alkaline earth M=Cr, Al, Ni, Fe, Mn, Ru, Ga)	Tetragonal/orthorhombic
Ln ₂ Li _{0.5} Au _{0.5} O ₄	Tetragonal
La ₂ PdO ₄	Tetragonal
Sr ₂ RhO ₄	I4 ₁ /acd
Ba ₂ ZrS ₄ /Ba ₂ HfS ₄	I4/mmm
Bs ₄ Zr ₃ S ₁₀	Fmmm

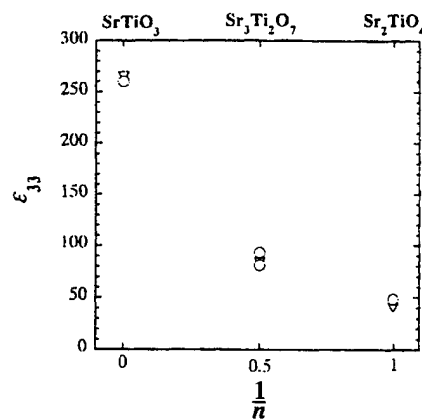
Recently, with the popularity of reactive MBE, it is now possible to engineer these complex phases in high structural purity. Interesting electronic properties are envisaged from such materials. Schlom et al. [96, 97] have synthesized (SrO)(SrTiO₃) series and measured the targeted dielectric constant of various single crystal phases (Fig. 22). Rao et al. [98, 99] have synthesized successfully the (LaO)(LaNiO₃)_n compounds. Table 16 lists some of the RP type phases studied by various workers. Such molecularly engineered materials may find applications in catalysis, electrochemistry, proton exchange and several other interesting fields [100].

6.2 Shannon's approach to designing microwave dielectrics

The macroscopic dielectric constant and the polarizability of a molecule are known to be related through the Clausius-Mosotti relation:

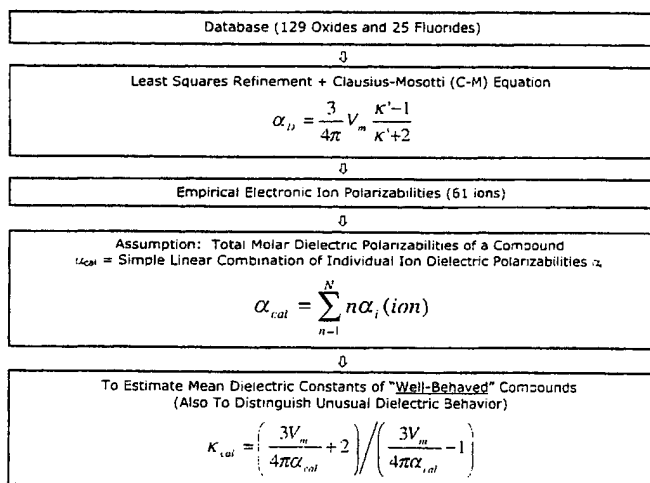
$$\alpha_D = \frac{3}{4\pi} V_m \frac{k-1}{k+2} \quad (3)$$

where α_D is the dielectric polarizability and V_m is the molar volume in Å³. While there has been no major breakthroughs in local field calculations for complex ionic solids, there has been a steadily increasing pool of experimentally measured dielectric constants of substances of various compositions and structures. An Aristotelian first principles approach will continue to dominate the high-science approach here. Dielectric polarizabilities and hence the dielectric constants of new mate-

**Fig. 22** Dielectric constant vs. AO(ABO₃)_n structure series (Schlom et al.)

Dielectric Properties: Theoretical Approach: Ion Polarizability Additivity Model

(ref.: R.D. Shannon, *J. Appl. Phys.*, **73**(1), 348 (1993))

**Fig. 23** Shannon's crystal chemical approach to calculate dielectric constant of materials

rials and compounds whose dielectric constants have not been measured are potentially predictable by linear addition of the molecular polarizabilities of simpler substances (molecular polarizability additivity rule) [101–103] or ion polarizabilities of individual ions (ion polarizability additivity rule) [103, 104]. A review and comments about the application of polarizability additivity rules can be found in Shannon's paper [105].

Thus the κ of compositions developed by the crystal chemical approach can be calculated by the method illustrated in Fig. 23. However, in the case of complex oxide perovskites containing Ta⁵⁺, Nb⁵⁺, and rare earths, we have found large discrepancies between calculated and observed values. Guo et al. [106, 107] analyzed the origin of these discrepancies and expanded the Shannon model for tantalates and niobates to correctly predict the dielectric constants which agree well with the measured

Table 17 Measured and calculated dielectric constants of some tailored compositions (perovskites and complex oxides) (Guo et al.)

Substance	Symmetry	V_m	K'_{exp}	K'_{calc}	$\Delta\alpha$ (%)
Ba(Mg _{1/3} Ta _{2/3})O ₃	Hexagonal	68.59	24.60	24.29	0.15
(Ba _{0.8} Sr _{0.2})(Mg _{1/3} Ta _{2/3})O ₃	Cubic	67.48	25.90	21.74	2.11
(Ba _{0.9} Sr _{0.1})(Mg _{1/3} Ta _{2/3})O ₃	Cubic	67.84	25.30	23.48	0.88
CaNdAlO ₄	Tetragonal	82.30	19.65, 17.65	18.34	-0.29
CaYAlO ₄	Tetragonal	78.88	21.44, 16.12	22.44	1.97
LaAlO ₃	Rhombohedral	54.40	21.90	22.39	-0.87
Nd _{0.39} Sr _{0.61} Al _{0.695} Ta _{0.305} O ₃		24.04	22.17	1.01	
PrAlO ₃	Rhombohedral	53.25	25.00	25.99	0.44
Sr(Al _{0.5} Ta _{0.5})O ₃ ordered	Cubic	59.09	11.78	17.10	-7.76
Sr(Al _{0.5} Ta _{0.5})O ₃ - 0.3 LaAlO ₃	Cubic	58.08	21.90	22.75	-0.50
Sr(Al _{0.5} Ta _{0.5})O ₃ - 0.3 NdGaO ₃	Cubic	57.90	16.30	21.89	-4.59
SrLaAlO ₄	Tetragonal	89.15	16.81, 20.02	18.77	0.61

values. Table 17 lists (along with some other complex oxides) some examples of tailored perovskite compositions and their measured and predicted (calculated) dielectric constants. The agreement in values is remarkable.

In addition, if the compositions are designed with the appropriate tolerance factor value, then engineered materials will also exhibit the low loss in the microwave frequency range.

7 Summary

The history of the utilization of perovskite-structured phases is an object lesson in the value of crystal chemistry. It is quite clear from the examples given or referred to in this article that the perovskite structure is an extraordinarily versatile one. It provides an essential family of materials for a wide variety of present day technologies and is likely to be an integral part of the future developments needed in high frequency communication and several other integrated technologies. The diversity of perovskite structure compounds which can be synthesized, provides the extreme range of electrical, magnetic, optical and mechanical properties over a wide temperature range. This could be a special boon to the integrated technologies where compatibility of the structure of various materials, with different functional properties is a major concern, since the structural mismatch often leads to various ageing, failure and impractical operating limitations for devices. By using the vast crystal chemistry resources and principles (e.g., ionic radii, valence, tolerance factor, etc.) innumerable perovskite compounds with variety of properties can be designed and yet provide the structural identity to facilitate superior integrated devices. As mentioned in this article, several highly technologically important properties from macro to nanoscale have already been identified in this class of materials. Perovskite structure compounds, no doubt, are and will be an integral part of the important commercial and strategic/special technologies of the future. As we step into the future nanoscale technologies such as high density packaging, low and ultra-low temperature and HTSC based electronics, spintronics, high Q and com-

pact microwave components etc., the unique perovskite structure has the potential to provide a wealth of new compounds with unique properties. With the availability of new nanoscale deposition and fabrication tools for material preparation, a perovskite material can be engineered which can exhibit more than one desirable property for new device concepts.

Acknowledgements We are thankful to many of our colleagues and students for invaluable contributions in various aspects of the related research. Financial support from federal, state, and industry for various projects throughout the years were also instrumental for some of the findings.

References

1. Muller O, Roy R (1974) The Major Ternary Structural Families. Springer, Berlin Heidelberg New York
2. Swanson HE et al. (1953-1960) NBS Circ 549, vol 1-10
3. Perovskite R (1839) Ann Phys 48:558; 2:128
4. Perovskite R (1877) Dysanolyte Knop Zs Kr 1:284
5. Goldschmidt VM (1927) Geochemische Verwertungsgesetze der Elemente. Norske Videnskap. Oslo
6. Pauling L (1960) Nature of the Chemical Bond. Cornell University Press, Ithaca NY
7. Wainer E, Solomon S (1942) Titanium Alloy Manufacturing Co. Report 8-9
8. Wul BM, Goldman IM (1945) Doki Akad. Nauk SSSR 46:154
9. Ogawa. see in Miyake S, Ueda R (1946) J Phys Soc Jpn 1:32
10. Newnham RE, Cross LE (1990) In Kyoui no Chitabari (on BaTiO₃) p 325, published by Murata Co. Japan
11. Sheldrake R, Bohm D (1982) "Morphogenetic fields and the implicate order," ReVision 5:41
12. von Hippel A (1959) Molecular Science and Molecular Engineering, MIT Press, Cambridge, MA
13. Ginsberg VL (1945) J Expt Theor Phys SSR 15:739 (in Russian)
14. Megaw H (1945) Nature (London) 155:484
15. Blattner H, Matthias B, Merz W (1947) Helv Phys Acta 20:225
16. Matthias B, von Hippel A (1948) Phys Rev 73:1378
17. Cross LE, Dennison AT, Nicholson M (1949) Proc Leeds, Phil Soc 5:199
18. Blattner H, Kaenzig W, Merz W (1949) Helv Phys. Acta 22:35
19. Devonshire AF (1949) Phil Mag 40:1040
20. Kay HF, Vousden P (1949) Phil Mag 40:1019
21. Roy R (1956) J Am Ceram Soc 49:145
22. DeVries RC, Roy R (1955) J Am Ceram Soc 38:142
23. DeVries RC, Roy R, Osborn EF (1955) J Am Ceram Soc 38:158

24. Rase DE, Roy R (1955) *J Am Ceram Soc* 38:389
25. Roy R, Osborn EF (1954) *Am Mineralogist* 39:853
26. Komarneni S, Roy R, Brevet E, Ollinen M, Suwa Y (1986) *Advanced Ceramic Materials* 1:87
27. Roy R (1996) Fifty-Year Perspective on Hydrothermal Research. In *Proceedings 1st Intl Workshop on Solvothermal and Hydrothermal Reactions*, Takamatsu, Japan, p 1
28. Ravichandran D, Meyer R Jr, Roy R, Guo R, Bhalla AS, Cross LE (1996) *Materials Research Bulletin* 31:817
29. Ravichandran D, Yamakawa K, Bhalla AS, Roy R (1997) *J Sol-gel Science and Technology* 9:95
30. Yamakawa K, Ravichandran D, Trolier-McKinstry S, Dougherty JP, Roy R, Bhalla AS (1997) *Ferroelec Lett* 22:41
31. Roy R, Tuttle OF (1956) Investigations Under Hydrothermal Conditions. In *Physics and Chemistry of the Earth* 1:138-180, Pergamon Press
32. DeVries RC, Roy R (1958) *Econ Geol.* 59:958
33. Moon J, Li T, Randall C, Adair JH (1997) *J Mat Res* 12:189
34. Kutty TRN, Balachandran R (1984) *Mat Res Bull* 19:1479
35. Phule PP et al (1990) *Ceram Transact* 12:725
36. Hawkins DB, Roy R (1963) *Geochim Cosmochim Acta* 27:1047
37. Yoshimura M, Yoo S-E, Hayashi M, Ishizawa M (1989) *Jpn J Appl Phys* 28:L2007
38. Cheng JP, Agrawal DK, Komarneni S, Mathis M, Roy R (1997) *Mater Res Innov* 1:44
39. Bhalla AS, Nair KM (eds) (1992) *Ferroelectric Films*. Ceramic Transactions. Am Ceram Soc, Westerville, OH
40. "Modeling and simulation of thin-film processing", *Materials Research Society Symposia Proceedings*, V. 389, Pittsburgh, PA, Materials Research Society (1995)
41. *Journal of Integrated Ferroelectrics*, Gordon and Breach Publication (1981-)
42. Roy R (1954) *J Am Ceram Soc* 37:581
43. Keith ML, Roy R (1954) *Am Mineralogist* 39:1
44. Galasso F (1970) *Structure and Properties of Inorganic Solids*. Pergman Press, Oxford, New York
45. Stability of Metallic Structures (1967) In: *Phase Stability in Metals and Alloys*. McGraw-Hill, New York, chap 3
46. Zunger A, Engelsi N (1964) *ASM Transac* 57:610
47. Phillips JC (1970) *Physics Today* 23:23
48. Phillips JC (1969) *Phys Rev Letters* 22:649
49. Muller O, White WB, Roy R (1964) *J Inorg Nuc Chem* 26:2075
50. Sleight WA (1968) *Inorg Chem* 7:1704
51. Rase DE, Roy R (1955) *J Am Ceram. Soc* 38:102
52. See *Phase Diagrams for Ceramists: bibliographic update through January 1, 1989 and cumulative indexes for volumes I-VIII.* American Ceramic Society (1990)
53. Newnham RE, Cross LE (1974) *Mat Res Bull* 9:92
54. Lines ME, Glass AM (1977) *Principles and Applications of Ferroelectrics and Related Materials*. Oxford University Press, London
55. Smolenski GA, Isupov VA, Agranovskaya AI (1959) *Sov Phys Sol State* 1:909
56. Cross LE (1987) *Ferroelectrics* 76:241
57. Bhalla AS (1993) Presented at ONR Workshop, University of Maryland
58. Randall CA, Bhalla AS (1990) *Jpn J Appl Phys* 29:327
59. Jaffe B, Cook WR Jr, Jaffe H (1971) *Piezoelectric Ceramics*. Academic Press, London and New York
60. Alberta E, Guo R, Bhalla AS (2000) *Ferroelectrics Rev* 3 (to be published)
61. Guo R, Bhalla AS, Roy R, Cross LE (1994) *Epitaxial Oxide Thin Films and Heterostructures* 341:215. MRS Publications
62. Newnham RE, Skinner DP, Cross LE (1978) *Mat Res Bull* 13:525
63. Roy R (1996) Widespread Occurrence of the Nano Composite State and Principles for Its Exploitations. In *Frontier Nano-structured Ceramics*. Tohwa Univ. Press, Fukuoka, Japan, p 3
64. Freer R (1993) *Silicates Industries* 9:191
65. Ganguly P, Rao CNR (a) *Mat Res Bull* 8:408 (1973); (b) *J Sol State Chem* 24:820 (1979)
66. Sleight AW, Gilson JL, Bierstedt PE (1975) *Sol State Commun* 17:27
67. Gilbert LR (1980) PhD Thesis, The Pennsylvania State University
68. Gilbert LR, Messier R, Roy R (1978) *Thin Solid Films* 54:129
69. Bednorz JG, Muller KA (1986) *Z Phys B* 64:189
70. See Bhalla AS, Roy R, Cross LE (1988) In *Chemistry of Oxide Superconductors*. Blackwell Scientific Publications, p 71
71. Ashburn JR (private communication)
72. Wu MK, Ashburn JR, et al (1987) *Phys Rev Lett* 58:908
73. Bhalla A, Guo R (1997) *Acta Physica Polonica A* 92:7
74. Zumhulen R, et al (1995) *J Appl Phys* 77:5341; 77:5351
75. Katiyar R, Siny IG, Guo R, Bhalla AS (1990) *Materials Transac* 511:165
76. Siny IG, Katiyar R, Bhalla A (to be published) *J Phys Chem Sol*
77. Weaver HE (1959) *J Phys Chem Solids* 11:274
78. Möller KA, Burkhard H (1979) *Phys Rev B* 19:3593
79. Bhalla AS, Jiang Y, Guo R, *Ferroelect Lett* (to be published).
80. Venkateshwaran B, Guo R, Bhalla AS (1999) *J Inorg Matls* 1:395
81. Bhalla A (1999) Presentation at the Am Ceram Soc Meeting, Cincinnati, OH
82. Rao CNR et al (a) *J Sol State Chem* 22:353 (1977); (b) *Science* 272:369 (1996)
83. Von Helmos R et al (1993) *Phys Rev Lett* 71:2332
84. Trimm DL (1983) *Appl Catal* 7:249
85. Tejuca LG, Fierro JLG, Tascon JMD (1989) *Adv Catal* 36:237
86. Isupova LA, Sadykov VA, Tikhov SF, Kimkhai ON, Kovalenko ON, Kustova GN, Ovsyannikova IA, Dovbii ZA, Kryukova GN, Rozovskii AY, Tretyakov VF, Lumin VV (1994) *React Kinet Catal Lett* 53:223
87. Baran ET (1990) *Catalysis Today* 8:133
88. Yamaoe V, Tekaoka J (1990) *Catalysis Today* 8:175
89. Pauli IA, Avvakumov EG, Isupova LA, Poluboyarov VA, Sadykov VA (1992) *Sib Khim Zhurn* 3:133 (Russian)
90. Isupova LA, Sadykov VA, Solovyova LP, Andrianova MP, Ivanov VP, Kryukova GN, Kolomiichuk VN, Avvakumov E, Pauli IS, Andryushkova OV, Poluboyarov VA, Rozovskii AY, Tretyakov VF (1994) *Proc 6th Intl Symp Scientific Bases for the Preparation of Heterogeneous Catalysts* 2:231. Louvain-la-Neuve, 5-8 Sept
91. Tikhov SF, Sadykov VA, Pack EA, Kimkhai ON, Moroz EM, Ivanov VP, Kustova GN, Alikina GM (1991) *Proc 7th Intl Symp Heterogeneous Catalysis* 2:423. Bourgas
92. Tschauner O, Zerr A, et al (1999) *Nature*, April 15
93. Guo R, Bhalla AS, Cross LE (1994) *J Appl Phys* 75:4704
94. Ruddlesden SN, Popper P (1957) *Acta Cryst* 10:538
95. Ruddlesden SN, Popper P (1958) *Acta Cryst* 11:54
96. Schlom D, Theis CD, Hawley ME (1998) *Ceram Transac* 86:41
97. Haeni JH, Theis CD, Schlom D (to be published) *Appl Phys Lett*
98. Rao CNR (1985) *Bull Mat Sci* 1:155
99. Rao, CNR, Thomas JM (1988) *Acc Chem Res* 18:113
100. Sharma JB, Singh D (1998) *Bull Mat Sci* 21:363 (and references therein)
101. Heydweille AR (1920) *Z Phys* 3:308
102. Narayana Rao DAAS (1949) *Proc Ind Acad Sci* 30A:317
103. Langa AC, Cygan RT (1942) *Am Mineral* 67:328
104. Roberts R (1949) *Phys Rev* 76:1215
105. Shannon RD (1993) *J Appl Phys* 73:348
106. Guo R, Bhalla AS, Roy R, Cross LE (1994) *Ferroelectrics* 155:43
107. Guo R, Bhalla AS (1998) *Ceramic Transactions* 84:139

APPENDIX 6

Structure-Property Diagrams of Ferroic Solid Solutions. Part I: Perovskite Relaxor Ferroelectrics with Morphotropic Phase Boundaries

EDWARD F. ALBERTA, RUYAN GUO and AMAR S. BHALLA*

Materials Research Laboratory The Pennsylvania State University University Park, PA 16802 USA

(Received September 20, 2000)

Contents

1. Introduction	1
A. Relaxors	2
B. Morphotropic Phase Boundaries	5
2. Some Comments on MPBs	7
3. Properties Associated with the MPB – A Case History: PZT	9
4. Organization	10
5. Symbols and Units	12
6. Property Diagrams	21
1 Lead Based Systems - $\text{Pb}(\text{B}^{\text{I}}\text{B}^{\text{II}})\text{O}_3$	21
1.1 Niobates - $\text{Pb}(\text{B}^{\text{I}}\text{Nb})\text{O}_3$	21
1.1.1 $\text{Pb}(\text{In}_{1/2}\text{Nb}_{1/2})\text{O}_3$ [PIN]	23
1.1.2 $\text{Pb}(\text{Fe}_{1/2}\text{Nb}_{1/2})\text{O}_3$ [PFN]	38
1.1.3 $\text{Pb}(\text{Sb}_{1/2}\text{Nb}_{1/2})\text{O}_3$ [PSbN]	51
1.1.4 $\text{Pb}(\text{Sc}_{1/2}\text{Nb}_{1/2})\text{O}_3$ [PSN]	54
1.1.5 $\text{Pb}(\text{Yb}_{1/2}\text{Nb}_{1/2})\text{O}_3$ [PYN]	78
1.1.6 $\text{Pb}(\text{Co}_{1/3}\text{Nb}_{2/3})\text{O}_3$ [PCN]	78
1.1.7 $\text{Pb}(\text{Mg}_{1/3}\text{Nb}_{2/3})\text{O}_3$ [PMN]	91
1.1.8 $\text{Pb}(\text{Mn}_{1/3}\text{Nb}_{2/3})\text{O}_3$ [PMnN]	129
1.1.9 $\text{Pb}(\text{Ni}_{1/3}\text{Nb}_{2/3})\text{O}_3$ [PNN]	130
1.1.10 $\text{Pb}(\text{Zn}_{1/3}\text{Nb}_{2/3})\text{O}_3$ [PZN]	141
1.2 Tantalates - $\text{Pb}(\text{B}^{\text{I}}\text{Ta})\text{O}_3$	172
1.2.1 $\text{Pb}(\text{Fe}_{1/2}\text{Ta}_{1/2})\text{O}_3$ [PFT]	173
1.2.2 $\text{Pb}(\text{In}_{1/2}\text{Ta}_{1/2})\text{O}_3$ [PIT]	179
1.2.3 $\text{Pb}(\text{Sc}_{1/2}\text{Ta}_{1/2})\text{O}_3$ [PST]	187
1.2.4 $\text{Pb}(\text{Mg}_{1/3}\text{Ta}_{2/3})\text{O}_3$ [PMT]	193
1.3 Tungstates - $\text{Pb}(\text{B}^{\text{I}}\text{W})\text{O}_3$	219
1.3.1 $\text{Pb}(\text{Cd}_{1/2}\text{W}_{1/2})\text{O}_3$ [PCdW]	220
1.3.2 $\text{Pb}(\text{Co}_{1/2}\text{W}_{1/2})\text{O}_3$ [PCW]	222

1.3.3	Pb(Mg _{1/2} W _{1/2})O ₃ [PMW].....	227
1.3.4	Pb(Fe _{2/3} W _{1/3})O ₃ [PFW]	234
1.3.5	Pb(Mn _{2/3} W _{1/3})O ₃ [PMnW].....	241
1.3.6	Pb(Y _{2/3} W _{1/3})O ₃ [PYW]	243
1.4	Miscellaneous - Pb(B ^I B ^{II})O ₃	254
1.4.1	Pb(Sn _{1/2} Sb _{1/2})O ₃ [PSnSb]	255
1.4.2	Pb(Mn _{1/3} Sb _{2/3})O ₃ [PMnSb].....	255
1.4.3	Pb(Fe _{2/3} U _{1/3})O ₃ [PFU]	262
2	Strontium Based Systems - Sr(B ^I B ^{II})O ₃	264
2.1	Niobates - Sr(B ^I Nb)O ₃	264
2.1.1	Sr(La _{1/2} Nb _{1/2})O ₃ [SLN].....	265
2.1.2	Sr(Cu _{1/3} Nb _{2/3})O ₃ [SCN].....	268
2.2	Tantalates - Sr(B ^I Ta)O ₃	271
2.2.1	Sr(Fe _{1/2} Ta _{1/2})O ₃ [SFT]	271
2.3	Tungstates - Sr(B ^I W)O ₃	272
2.3.1	Sr(Cu _{1/2} W _{1/2})O ₃ [SCW]	272
2.3.2	Sr(Li _{2/5} W _{3/5})O ₃ [SLW]	273
2.4	Miscellaneous - Sr(B ^I B ^{II})O ₃	273
2.4.1	Sr(Sn _{1/3} Mn _{2/3})O ₃ [SSM]	273
3	Bismuth Based Systems - Bi(B ^I B ^{II})O ₃	275
2.1	Niobates - Bi(B ^I Nb)O ₃	275
2.1.1	Bi(Mg _{2/3} Nb _{1/3})O ₃ [BMN]	276
2.1.2	Bi(Zn _{1/3} Nb _{2/3})O ₃ [BZN].....	277
2.2	Miscellaneous - Bi(B ^I B ^{II})O ₃	279
2.2.1	Bi(Zn _{1/2} Zr _{1/2})O ₃ [BZZ]	279
2.2.2	(Bi _{1/2} Na _{1/2})TiO ₃ [BNT].....	281
4	Barium Based Systems - Ba(B ^I B ^{II})O ₃	290
4.1	Niobates - Ba(B ^I Nb)O ₃	290
4.1.1	Ba(Ca _{1/3} Nb _{2/3})O ₃ [BCN].....	291
4.1.2	Ba(Zn _{1/3} Nb _{2/3})O ₃ [BZN].....	295
4.1.3	Ba(Li _{1/4} Nb _{3/4})O ₃ [BLN].....	297
4.2	Tantalates - Ba(B ^I Ta)O ₃	301
4.2.1	Ba(Zn _{1/3} Ta _{2/3})O ₃ [BZnTa]	301
5	Lanthanum Based Systems - La(B ^I B ^{II})O ₃	303
5.1	Niobates - La(B ^I Nb)O ₃	303
5.1.1	La(Mg _{1/3} Nb _{2/3})O ₃ [LMN]	304
5.1.2	La(Zn _{1/3} Nb _{2/3})O ₃ [LZN]	305
5.2	Miscellaneous - La(B ^I B ^{II})O ₃	309
5.2.1	La(Zn _{1/2} Ti _{1/2})O ₃ [LZT]	309
6	Calcium Based Systems - Ca(B ^I B ^{II})O ₃	310
6.1	Niobates - Ca(B ^I Nb)O ₃	310
6.1.1	Ca(Fe _{1/2} Nb _{1/2})O ₃ [CFN].....	311
7.	Cross Reference.....	313
	Acknowledgements	318
	References	319

APPENDIX 7

ARTICLES

Tetragonal-to-monoclinic phase transition in a ferroelectric perovskite: The structure of $\text{PbZr}_{0.52}\text{Ti}_{0.48}\text{O}_3$

B. Noheda* and J. A. Gonzalo

Departamento de Física de Materiales, UAM, Cantoblanco, 28049 Madrid, Spain

L. E. Cross, R. Guo, and S.-E. Park

Materials Research Laboratory, The Pennsylvania State University, Pennsylvania 16802-4800

D. E. Cox and G. Shirane

Department of Physics, Brookhaven National Laboratory, Upton, New York 11973-5000

(Received 11 October 1999; revised manuscript received 27 December 1999)

The perovskitelike ferroelectric system $\text{PbZr}_{1-x}\text{Ti}_x\text{O}_3$ (PZT) has a nearly vertical morphotropic phase boundary (MPB) around $x=0.45$ – 0.50 . Recent synchrotron x-ray powder diffraction measurements by Noheda *et al.* [Appl. Phys. Lett. **74**, 2059 (1999)] have revealed a monoclinic phase between the previously established tetragonal and rhombohedral regions. In the present work we describe a Rietveld analysis of the detailed structure of the tetragonal and monoclinic PZT phases on a sample with $x=0.48$ for which the lattice parameters are, respectively, $a_t=4.044$ Å, $c_t=4.138$ Å, at 325 K, and $a_m=5.721$ Å, $b_m=5.708$ Å, $c_m=4.138$ Å, $\beta=90.496^\circ$, at 20 K. In the tetragonal phase the shifts of the atoms along the polar [001] direction are similar to those in PbTiO_3 but the refinement indicates that there are, in addition, local disordered shifts of the Pb atoms of ~ 0.2 Å perpendicular to the polar axis. The monoclinic structure can be viewed as a condensation along one of the $\langle 110 \rangle$ directions of the local displacements present in the tetragonal phase. It equally well corresponds to a freezing-out of the local displacements along one of the $\langle 100 \rangle$ directions recently reported by Corker *et al.* [J. Phys.: Condens. Matter **10**, 6251 (1998)] for rhombohedral PZT. The monoclinic structure therefore provides a microscopic picture of the MPB region in which one of the “locally” monoclinic phases in the “average” rhombohedral or tetragonal structures freezes out, and thus represents a bridge between these two phases.

I. INTRODUCTION

Perovskitelike oxides have been at the center of research on ferroelectric and piezoelectric materials for the past fifty years because of their simple cubic structure at high temperatures and the variety of high symmetry phases with polar states found at lower temperatures. Among these materials the ferroelectric $\text{PbZr}_{1-x}\text{Ti}_x\text{O}_3$ (PZT) solid solutions have attracted special attention since they exhibit an unusual phase boundary which divides regions with rhombohedral and tetragonal structures, called the morphotropic phase boundary (MPB) by Jaffe *et al.*¹ Materials in this region exhibit a very high piezoelectric response, and it has been conjectured that these two features are intrinsically related. The simplicity of the perovskite structure is in part responsible for the considerable progress made recently in the determination of the basic structural properties and stability of phases of some important perovskite oxides, based on *ab initio* calculations (see, e.g., Refs. 2–9). Recently, such calculations have also been used to investigate solid solutions and, in particular, PZT, where the effective Hamiltonian includes both structural and compositional degrees of freedom.^{10–12}

The PZT phase diagram of Jaffe *et al.*,¹ which covers only temperatures above 300 K, has been accepted as the basic

characterization of the PZT solid solution. The ferroelectric region of the phase diagram consists mainly of two different regions: the Zr-rich rhombohedral region, (F_R) that contains two phases with space groups $R3m$ and $R3c$, and the Ti-rich tetragonal region (F_T), with space group $P4mm$.¹³ The two regions are separated by a boundary that is nearly independent of temperature, the MPB mentioned above, which lies at a composition close to $x=0.47$. Many structural studies have been reported around the MPB, since the early 1950's, when these solid solutions were first studied,^{13,14} since the high piezoelectric figure of merit that makes PZT so extraordinary is closely associated with this line.^{1,15} The difficulty in obtaining good single crystals in this region, and the characteristics of the boundary itself, make good compositional homogeneity essential if single phase ceramic materials are to be obtained. Because of this, the MPB is frequently reported as a region of phase coexistence whose width depends on the sample processing conditions.^{16–19}

Recently, another feature of the morphotropic phase boundary has been revealed by the discovery of a ferroelectric monoclinic phase (F_M) in the $\text{Pb}(\text{Zr}_{1-x}\text{Ti}_x)\text{O}_3$ ceramic system.²⁰ From a synchrotron x-ray powder diffraction study of a composition with $x=0.48$, a tetragonal-to-monoclinic phase transition was discovered at ~ 300 K. The monoclinic

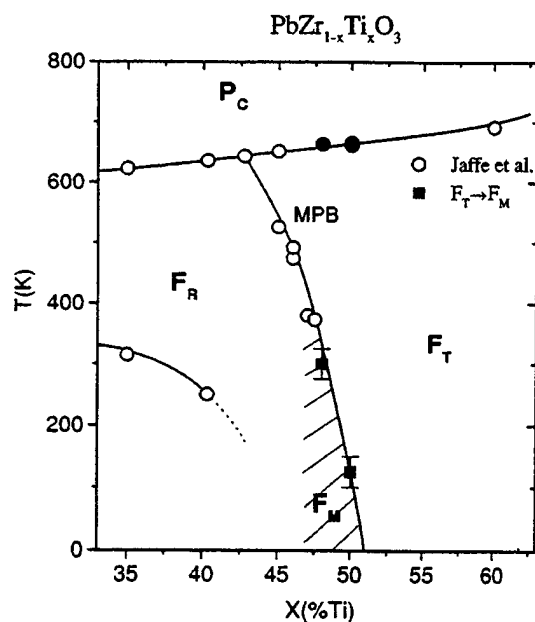


FIG. 1. Preliminary modification of the PZT phase diagram. The data of Jaffe *et al.* (Ref. 1) are plotted as open circles. The F_T - F_M and P_C - F_T transition temperatures for $x=0.48$ and $x=0.50$ are plotted as solid symbols. The F_T - F_M transition for $x=0.50$ is reported in Ref. 22.

unit cell is such that a_m and b_m lay along the tetragonal $[1\bar{1}0]$ and $[1\bar{1}0]$ directions ($a_m \approx b_m \approx a_t/\sqrt{2}$), and c_m deviates slightly from the $[001]$ direction ($c_m \approx c_t$).²¹ The space group is Cm , and the temperature dependence of the monoclinic angle β gives immediately the evolution of the order parameter for the tetragonal-monoclinic (F_T - F_M) transition. The polar axis of the monoclinic cell can in principle be directed along any direction within the ac mirror plane, making necessary a detailed structural study to determine its direction.

In the present work we present such a detailed structure determination of the monoclinic phase at 20 K and the tetragonal phase at 325 K in PZT with $x=0.48$. The results show that the polarization in the monoclinic plane lies along a direction between the pseudocubic $[001]_c$ and $[111]_c$ directions, corresponding to the first example of a species with $P_x^2 = P_y^2 \neq P_z^2$. A tentative phase diagram is presented in Fig. 1, which includes data for the $x=0.48$ composition together with those of the recently studied $x=0.50$ composition.²² The most striking finding, however, is that the monoclinic cation displacements found here correspond to one of the three locally disordered sites reported by Corker *et al.*²³ for rhombohedral compositions in the region $x=0.1-0.4$, and thus provide a microscopic model of the rhombohedral-to-monoclinic phase transition. This, together with the fact that the space group of the new phase, Cm , is a subgroup of both $P4mm$ and $R3m$, suggests that F_M represents an intermediate phase connecting the well-known F_T and F_R PZT phases.

II. EXPERIMENTAL

A PZT sample with $x=0.48$ was prepared by conventional solid-state reaction techniques using appropriate amounts of reagent-grade powders of lead carbonate, zirco-

num oxide, and titanium oxide, with chemical purities better than 99.9%. Pellets were pressed and heated to 1250 °C at a ramp rate of 10 °C/min, held at this temperature in a covered crucible for 2 h, and furnace cooled. During sintering, $PbZrO_3$ was used as a lead source in the crucible to minimize volatilization of lead.

High-resolution synchrotron x-ray powder diffraction measurements were made at beam line X7A at the Brookhaven National Synchrotron Light Source. In the first set of measurements, an incident beam of wavelength 0.6896 Å from a Ge(111) double-crystal monochromator was used in combination with a Ge(220) crystal and scintillation detector in the diffraction path. The resulting instrumental resolution is about 0.01° on the 2θ scale, an order of magnitude better than that of a laboratory instrument. Data were collected from a disk in symmetric flat-plate reflection geometry over selected angular regions in the temperature range 20–736 K. Coupled θ - 2θ scans were performed over selected angular regions with a 2θ step interval of 0.01°. The sample was rocked 1–2° during data collection to improve powder averaging.

Measurements above room temperature were performed with the disk mounted on a BN sample pedestal inside a wire-wound BN tube furnace. The furnace temperature was measured with a thermocouple mounted just below the pedestal and the temperature scale calibrated with a sample of CaF_2 . The accuracy of the temperature in the furnace is estimated to be within 10 K, and the temperature stability about 2 K. For low-temperature measurements, the pellet was mounted on a Cu sample pedestal and loaded in a closed-cycle He cryostat, which has an estimated temperature accuracy of 2 K and stability better than 0.1 K. The diffracted intensities were normalized with respect to the incident beam monitor.

For the second set of measurements aimed at the detailed determination of the structure, a linear position-sensitive detector was mounted on the 2θ arm of the diffractometer instead of the crystal analyzer, and a wavelength of 0.7062 Å was used. This configuration gives greatly enhanced counting rates which make it feasible to collect accurate data from very narrow-diameter capillary samples in Debye-Scherrer geometry, with the advantage that systematic errors due to preferred orientation or texture effects are largely eliminated. A small piece of the sintered disk was carefully crushed and sealed into a 0.2 mm diameter glass capillary. The latter was loaded into a closed-cycle cryostat, and extended data sets were collected at 20 and 325 K while the sample was rocked over a 10° range. With this geometry the instrumental resolution is about 0.03° on the 2θ scale. Because lead is highly absorbing, the data were corrected for absorption effects²⁴ based on an approximate value of $\mu_r = 1.4$ determined from the weight and dimensions of the sample.

III. PHASE TRANSITIONS

The evolution of the lattice parameters with temperature was briefly summarized in Ref. 20, and a more complete analysis is presented below. The results of the full structure analysis are described later.

A transition from the cubic to the tetragonal phase was observed at ~660 K, in agreement with the phase diagram

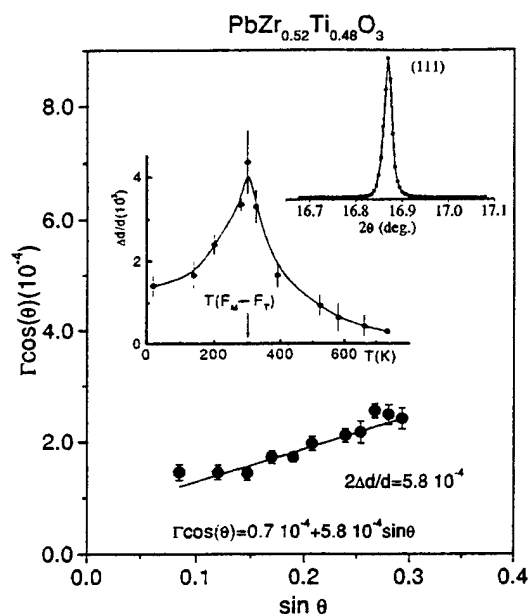


FIG. 2. The Williamson-Hall plot for PZT ($x=0.48$) derived from the measured diffraction peak widths in the cubic phase ($T=736$ K). Particle size and microstrain are estimated from a linear fit (solid line). The plot for the (111) reflection in the cubic phase demonstrates the excellent quality of the ceramic sample (peak width $\sim 0.02^\circ$). The plot of $\Delta d/d$ vs temperature is also shown as an inset.

shown in Fig. 1. The measurements made on the pellet in the cubic phase at 736 K demonstrate the excellent quality of the sample, which exhibits diffraction peaks with full-widths at half-maximum (FWHM) ranging from 0.01° to 0.03° as shown for the (111) reflection plotted as the upper-right inset in Fig. 2. The FWHM's (Γ) for several peaks were determined from least-squares fits to a pseudo-Voigt function with the appropriate corrections for asymmetry effects,²⁵ and corrected for instrumental resolution. The corrected values are shown in Fig. 2 in the form of a Williamson-Hall plot²⁶

$$\Gamma \cos \theta = \lambda/L + 2(\Delta d/d) \sin \theta, \quad (3.1)$$

where λ is the wavelength and L is the mean crystallite size. From the slope of a linear fit to the data, the distribution of d spacings, $\Delta d/d$, is estimated to be $\sim 3 \times 10^{-4}$, corresponding to a compositional inhomogeneity Δx of less than ± 0.003 . From the intercept of the line on the ordinate axis the mean crystallite size is estimated to be $\sim 1 \mu\text{m}$.

A tetragonal-to-monoclinic phase transition in PZT with $x=0.48$ was recently reported by Noheda *et al.*²⁰ Additional data have been obtained near the phase transition around 300 K which have allowed a better determination of the phase transition to be made, as shown by the evolution of the lattice parameters as a function of temperature in Fig. 3. The tetragonal strain c_t/a_t increases as the temperature decreases from the Curie point ($T \approx 660$ K), to a value of 1.0247 at 300 K, below which peak splittings characteristic of a monoclinic phase with $a_m \approx b_m \approx a_t/\sqrt{2}$, $\beta \neq 90^\circ$, are observed (Fig. 3). As the temperature continues to decrease down to 20 K, a_m (which is defined to lie along the $[\bar{1}\bar{1}0]$ tetragonal direction) increases very slightly, and b_m (which lies along the $[1\bar{1}0]$ tetragonal direction) decreases. The c_m lattice parameter

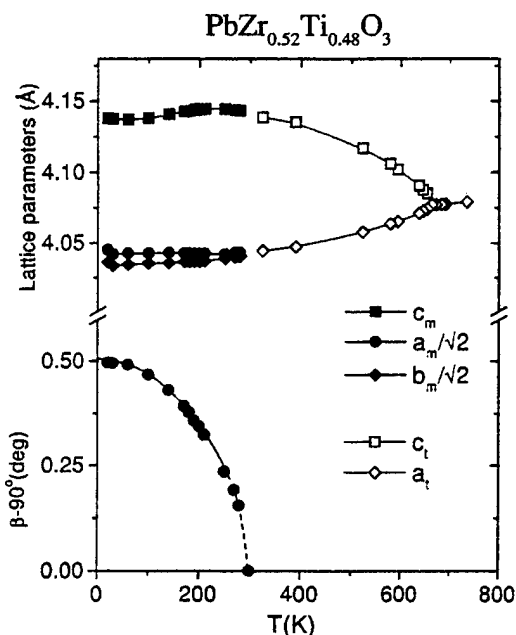


FIG. 3. Lattice parameters versus temperature for PZT ($x=0.48$) over the whole range of temperatures from 20 to 750 K showing the evolution from the monoclinic phase to the cubic phase via the tetragonal phase.

reaches a broad maximum value of 4.144 \AA between 240–210 K and then reaches a shallow minimum value of 4.137 \AA at 60 K. Over the same temperature region there is a striking variation of $\Delta d/d$ determined from Williamson-Hall plots at various temperatures, as shown in the upper-left inset in Fig. 2. $\Delta d/d$ increases rapidly as the temperature approaches the F_T - F_M transition at 300 K, in a similar fashion to the tetragonal strain, and then decreases rapidly below this temperature in the monoclinic region. Thus the microstrain responsible for the large increase in $\Delta d/d$ is an important feature of the phase transition, which may be associated with the development of local monoclinic order, and is very likely responsible for the large electromechanical response of PZT close to the MPB.¹

The deviation of the monoclinic angle β from 90° is an order parameter of the F_T - F_M transition, and its evolution with temperature is also depicted in Fig. 3. This phase transition presents a special problem due to the steepness of the phase boundary (the MPB in Fig. 1). As shown in the previous section, the compositional fluctuations are quite small in these ceramic samples ($\Delta x \approx \pm 0.003$) but, even in this case, the nature of the MPB implies an associated temperature uncertainty of $\Delta T \approx 100$ K. There is, therefore, a rather wide range of transition temperatures instead of a single well-defined transition, so that the order parameter is smeared out as a function of temperature around the phase change, thereby concealing the nature of the transition.

Scans over the $(220)_c$ region for several different temperatures are plotted in Fig. 4, which shows the evolution of phases from the cubic phase at 687 K (upper-left plot) to the monoclinic phase at 20 K (lower-right plot), passing through the tetragonal phase at intermediate temperatures. With decreasing temperature, the tetragonal phase appears at ~ 660 K and the development of the tetragonal distortion can be observed on the left side of the figure from the splitting of

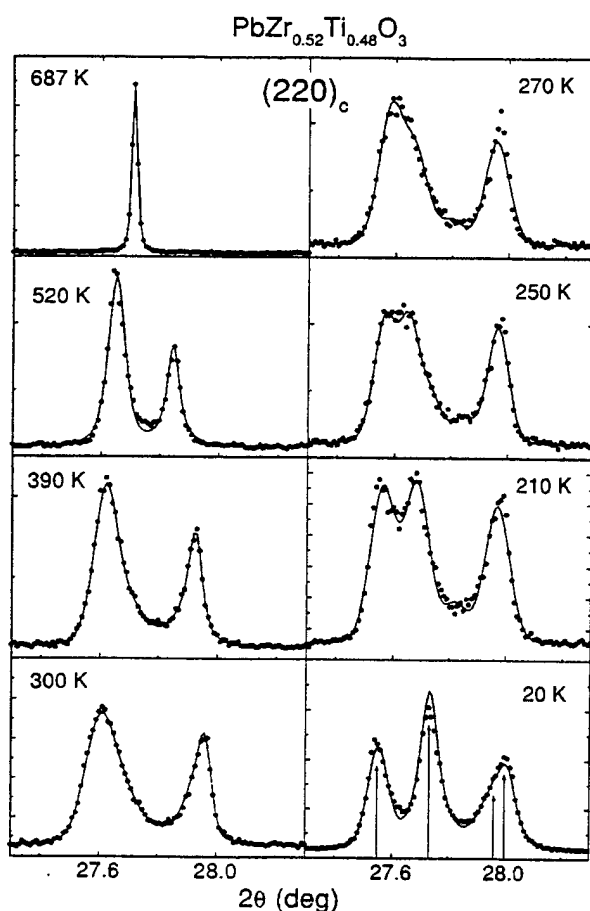


FIG. 4. Temperature evolution of the pseudocubic (220) peak from the cubic (top left) to the monoclinic (bottom right) phase.

the (202), and (220), reflections. On the right side of the figure, the evolution of the monoclinic phase, which appears below ~ 300 K, is shown by the splitting into the $(22\bar{2})_m$, $(222)_m$, $(400)_m$, and $(040)_m$ monoclinic reflections. It is quite evident from Fig. 4 that the (202), peak is much broader than the neighboring (220), peak, for example, and this "anisotropic" peak broadening is a general feature of the diffraction data for both phases. Another feature of the patterns is the presence of additional diffuse scattering between neighboring peaks, which is particularly evident between tetragonal (00 l) and (h 00) pairs, and the corresponding monoclinic (00 l) and (h h 0) pairs.

IV. STRUCTURE DETERMINATION

A detailed analysis of the 325 K tetragonal and 20 K monoclinic structures of $\text{PbZr}_{0.52}\text{Ti}_{0.48}\text{O}_3$ was carried out by Rietveld refinement using the GSAS program package.²⁷ The pseudo-Voigt peak shape function option was chosen²⁵ and background was estimated by linear interpolation between fixed values. An important feature of the refinements was the need to allow for the anisotropic peak broadening mentioned above. This was accomplished by the use of the recently incorporated generalized model for anisotropic peak broadening proposed by Stephens,²⁸ which is based on a distribution of lattice parameters. It was also necessary to take into account some additional diffuse scattering by modeling with a second, cubic, phase with broad, predominately Gaussian,

peaks. A similar strategy has been adopted by Muller *et al.*²⁹ in a recent study of $\text{PbHf}_{0.4}\text{Ti}_{0.6}\text{O}_3$. Although in principle this could represent a fraction of untransformed cubic phase, we suspect that the diffuse scattering is associated with locally disordered regions in the vicinity of domain walls. The refinements were carried out with the atoms assigned fully ionized scattering factors.

A. Tetragonal structure at 325 K

At 325 K the data show tetragonal symmetry similar to that of PbTiO_3 . This tetragonal structure has the space group $P4mm$ with Pb in 1(a) sites at (0,0, z); Zr/Ti and O(1) in 1(b) sites at (1/2,1/2, z) and O(2) in 2(c) sites at (1/2, 0, z). For the refinement we adopt the same convention as that used in Refs. 30 and 31 for PbTiO_3 , with Pb fixed at (0,0,0). However, instead of thinking in terms of shifts of the other atoms with respect to this origin, it is more physically intuitive to consider displacements of Pb and Zr/Ti from the center of the distorted oxygen cuboctahedra and octahedra, respectively. We shall take this approach in the subsequent discussion.

The refinement was first carried out with individual isotropic (U_{iso}) temperature factors assigned. Although a reasonably satisfactory fit was obtained ($R_F^2 = 8.9\%$), U_{iso} for O(1) was slightly negative and U_{iso} for Pb was very large, 0.026 \AA^2 , much larger than U_{iso} for the other atoms. Similarly high values for Pb(U_{iso}) in Pb-based perovskites are well known in the literature, and are usually ascribed to local disordered displacements, which may be either static or dynamic. Refinement with anisotropic temperature factors³² (U_{11} and U_{33}) assigned to Pb (Table I, model I) gave an improved fit ($R_F^2 = 6.1\%$) with $U_{11}(=U_{22})$ considerably larger than U_{33} (0.032 and 0.013 \AA^2 , respectively) corresponding to large displacements perpendicular to the polar [001] axis. A further refinement based on local displacements of the Pb from the 1(a) site to the 4(d) sites at ($x,x,0$), with isotropic temperature factors assigned to all the atoms, gave a small improvement in the fit ($R_F^2 = 6.0\%$) with $x = 0.033$, corresponding to local shifts along the $\langle 110 \rangle$ axes, and a much more reasonable temperature factor (Table I, model II). In order to check that high correlations between the temperature factor and local displacements were not biasing the result of this refinement, we have applied a commonly used procedure consisting of a series of refinements based on model II in which Pb displacements along $\langle 110 \rangle$ were fixed but all the other parameters were varied.^{34,35} Figure 5 shows unambiguously that there is well-defined minimum in the R factor for a displacement of about 0.19 \AA , consistent with the result in Table I. A similar minimum was obtained for shifts along $\langle 100 \rangle$ directions with a slightly higher R factor. Thus, in addition to a shift of 0.48 \AA for Pb along the polar [001] axis towards four of its O(2) neighbors, similar to that in PbTiO_3 ,^{30,31,36} there is a strong indication of substantial local shifts of $\sim 0.2 \text{ \AA}$ perpendicular to this axis. The Zr/Ti displacement is 0.27 \AA along the polar axis, once again similar to the Ti shift in PbTiO_3 . Attempts to model local displacements along $\langle 110 \rangle$ directions for the Zr/Ti atoms were unsuccessful due to the large correlations between these shifts and the temperature factor. Further attempts to refine the z parameters of the Zr and Ti atoms independently,

TABLE I. Structure refinement results for tetragonal $\text{PbZr}_{0.52}\text{Ti}_{0.48}\text{O}_3$ at 325 K, space group $P4mm$, lattice parameters $a_s = 4.0460(1)$ Å, $c_s = 4.1394(1)$ Å. Fractional occupancies N for all atoms taken as unity except for Pb in model II, where $N = 0.25$. Agreement factors, R_{wp} , R_F^2 , and χ^2 are defined in Ref. 33.

	Model I				Model II			
	anisotropic lead temperature factors				local $\langle 110 \rangle$ lead shifts			
	x	y	z	$U(\text{\AA}^2)$	x	y	z	$U_{iso}(\text{\AA}^2)$
Pb	0	0	0	$U_{11} = 0.0319(4)$ $U_{33} = 0.0127(4)$	0.0328(5)	0.0328(5)	0	0.0127(4)
Zr/Ti	0.5	0.5	0.4517(7)	$U_{iso} = 0.0052(6)$	0.5	0.5	0.4509(7)	0.0041(6)
O(1)	0.5	0.5	-0.1027(28)	$U_{iso} = 0.0061(34)$	0.5	0.5	-0.1027(28)	0.0072(35)
O(2)	0.5	0	0.3785(24)	$U_{iso} = 0.0198(30)$	0.5	0	0.3786(24)	0.0197(30)
R_{wp}	4.00%				3.99%			
R_F^2	6.11%				6.04%			
χ^2	11.4				11.3			

as Corker *et al.* were able to do,²³ were likewise unsuccessful, presumably because the scattering contrast for x rays is much less than for neutrons.

From the values of the atomic coordinates listed in Table I, it can be inferred that the oxygen octahedra are somewhat more distorted than in PbTiO_3 , the O(1) atoms being displaced 0.08 Å towards the O(2) plane above. The cation displacements are slightly larger than those recently reported by Wilkinson *et al.*³⁷ for samples close to the MPB containing a mixture of rhombohedral and tetragonal phases, and in excellent agreement with the theoretical values obtained by Bellaiche and Vanderbilt³⁸ for PZT with $x = 0.50$ from first principles calculations. As far as we are aware no other structural analysis of PZT compositions in the tetragonal region has been reported in the literature.

Selected bond distances for the two models are shown in Table II. For model I, Zr/Ti has short and long bonds with O(1) of 1.85 and 2.29 Å, respectively, and four intermediate-length O(2) bonds of 2.05 Å. There are four intermediate-length Pb-O(1) bonds of 2.89 Å, four short Pb-O(2) bonds

of 2.56 Å and four much larger Pb-O(2) distances of 3.27 Å. For model II, the Zr/Ti-O distances are the same, but the Pb-O distances change significantly. A Pb atom in one of the four equivalent $(x, x, 0)$ sites in Table I now has a highly distorted coordination, consisting of two short and two intermediate Pb-O(2) bonds of 2.46 and 2.67 Å, and one slightly longer Pb-O(1) bond of 2.71 Å (Table II). The tendency of Pb^{+2} , which has a lone *sp* electron pair, to form short covalent bonds with a few neighboring oxygens is well documented in the literature.^{23,39-41}

The observed and calculated diffraction profiles and the difference plot are shown in Fig. 6 for a selected 2θ range between 7° and 34° (upper figure). The short vertical markers represent the calculated peak positions. The upper and lower sets of markers correspond to the cubic and tetragonal phases, respectively. We note that although agreement between the observed and the calculated profiles is considerably better when the diffuse scattering is modeled with a cubic phase, the refined values of the atomic coordinates are not significantly affected by the inclusion of this phase. The anisotropic peak broadening was found to be satisfactorily

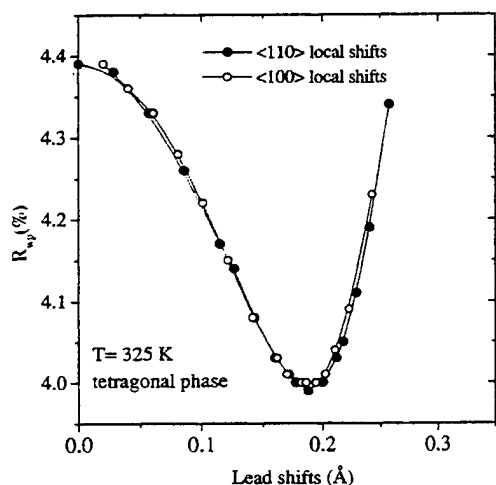


FIG. 5. Agreement factor R_{wp} as a function of Pb displacements for refinements with fixed values of x along tetragonal $\langle 110 \rangle$ and $\langle 100 \rangle$ directions as described in text. The well-defined minimum at $x \sim 0.19$ Å confirms the result listed in Table I for model II.

TABLE II. Selected Zr/Ti-O and Pb-O bond lengths in the tetragonal and monoclinic structures. Models I and II refer to the refinements with anisotropic temperature factors and local $\langle 110 \rangle$ displacements for Pb, respectively (see Table I). The standard errors in the bond lengths are ~ 0.01 Å.

	Bond lengths (Å)		
	tetragonal model I	tetragonal model II	monoclinic
Zr/Ti-O(1)	1.85×1	1.85×1	1.87×1
	2.29×1	2.29×1	2.28×1
Zr/Ti-O(2)	2.05×4	2.05×4	2.13×2
			1.96×2
Pb-O(1)	2.89×4	2.90×2	2.90×2
		2.71×1	2.60×1
Pb-O(2)	2.56×4	2.67×2	2.64×2
		2.46×2	2.46×2

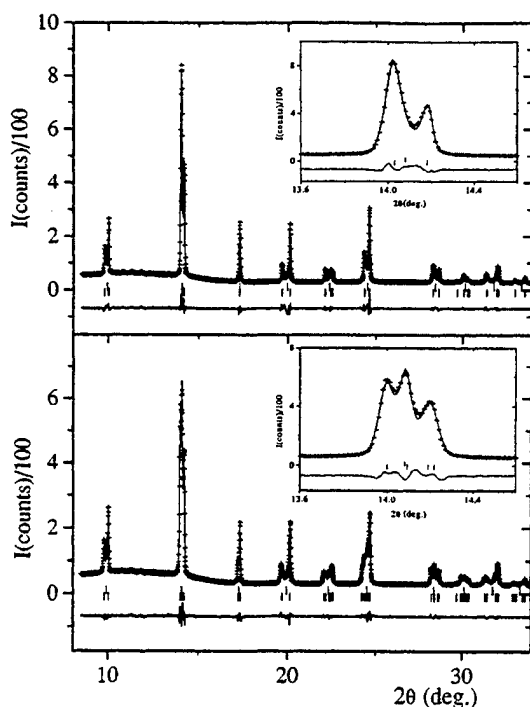


FIG. 6. Observed and calculated diffraction profiles from the Rietveld refinement of the tetragonal (top) and monoclinic (bottom) phases of PZT ($x=0.48$) at 325 and 20 K, respectively. The difference plots are shown below, and the short vertical markers represent the peak positions (the upper set correspond to the cubic phase as discussed in text). The insets in each figure highlight the differences between the tetragonal and the monoclinic phase for the pseudocubic (110) reflection, and illustrate the high resolution needed in order to characterize the monoclinic phase.

described by two of the four parameters in the generalized model for tetragonal asymmetry.²⁸

B. Monoclinic structure at 20 K

As discussed above, the diffraction data at 20 K can be indexed unambiguously on the basis of a monoclinic cell with the space group Cm . In this case Pb, Zr/Ti, and O(1) are in $2(a)$ sites at $(x,0,z)$, and O(2) in $4(b)$ sites at (x,y,z) . Individual isotropic temperature factors were assigned, and Pb was fixed at $(0,0,0)$. For monoclinic symmetry, the generalized expression for anisotropic peak broadening contains nine parameters, but when all of these were allowed to vary the refinement was slightly unstable and did not completely converge. After several tests in which some of the less significant values were fixed at zero, satisfactory convergence was obtained with three parameters ($R_{wp}=0.036$, $\chi^2=11.5$). During these tests, there was essentially no change in the refined values of the atomic coordinates. A small improvement in the fit was obtained when anisotropic temperature factors were assigned to Pb ($R_{wp}=0.033$, $\chi^2=9.2$). The final results are listed in Table III, and the profile fit and difference plot are shown in the lower part of Fig. 6.

From an inspection of the results in Tables I and III, it can be seen that the displacements of the Pb and Zr/Ti atoms along $[001]$ are very similar to those in the tetragonal phase at 325 K, about 0.53 and 0.24 Å, respectively. However, in the monoclinic phase at 20 K, there are also significant shifts

TABLE III. Structure refinement results for monoclinic $\text{PbZr}_{0.52}\text{Ti}_{0.48}\text{O}_3$ at 20 K, space group Cm , lattice parameters $a_m=5.72204(15)$ Å, $b_m=5.70957(14)$ Å, $c_m=4.13651(14)$ Å, $\beta=90.498(1)^\circ$. Agreement factors $R_{wp}=3.26\%$, $R_F=4.36\%$, $\chi^2=9.3$.

	x_m	y_m	z_m	$U_{iso}(\text{\AA}^2)$
Pb	0	0	0	0.0139 ^a
Zr/Ti	0.5230(6)	0	0.4492(4)	0.0011(5)
O(1)	0.5515(23)	0	-0.0994(24)	0.0035(28)
O(2)	0.2880(18)	0.2434(20)	0.3729(17)	0.0123(22)

^aFor Pb, U_{iso} is the equivalent isotropic value calculated from the refined anisotropic values [$U_{11}=0.0253(7)$ Å², $U_{22}=0.0106(6)$ Å², $U_{33}=0.0059(3)$ Å², $U_{13}=0.0052(4)$ Å²].

of these atoms along the monoclinic $[\bar{1}00]$, i.e., pseudocubic $[110]$, towards their O(2) neighbors in adjacent pseudocubic (110) planes, of about 0.24 and 0.11 Å, respectively, which corresponds to a rotation of the polar axis from $[001]$ towards pseudocubic $[111]$. The Pb shifts are also qualitatively consistent with the local shifts of Pb along the tetragonal $\langle 110 \rangle$ axes inferred from the results of model II in Table I, i.e., about 0.2 Å. Thus it seems very plausible that the monoclinic phase results from the condensation of the local Pb displacements in the tetragonal phase along one of the $\langle 110 \rangle$ directions.

Some selected bond distances are listed in Table II. The Zr/Ti-O(1) distances are much the same as in the tetragonal structure, but the two sets of Zr/Ti-O(2) distances are significantly different, 1.96 and 2.13 Å, compared to the single set at 2.04 Å in the tetragonal structure. Except for a shortening in the Pb-O(1) distance from 2.71 to 2.60 Å, the Pb environment is quite similar to that in the tetragonal phase, with two close O(2) neighbors at 2.46 Å, and two at 2.64 Å.

V. DISCUSSION

In the previous section, we have shown that the low-temperature monoclinic structure of $\text{PbZr}_{0.52}\text{Ti}_{0.48}\text{O}_3$ is derived from the tetragonal structure by shifts of the Pb and Zr/Ti atoms along the tetragonal $[110]$ axis. We attribute this phase transition to the condensation of local $\langle 110 \rangle$ shifts of Pb which are present in the tetragonal phase along one of the four $\langle 110 \rangle$ directions. In the context of this monoclinic structure it is instructive to consider the structural model for rhombohedral PZT compositions with $x=0.08$ – 0.38 recently reported by Corker *et al.*²³ on the basis of neutron powder diffraction data collected at room temperature. In this study and also an earlier study⁴² of a sample with $x=0.1$, it was found that satisfactory refinements could only be achieved with anisotropic temperature factors, and that the thermal ellipsoid for Pb had the form of a disk perpendicular to the pseudocubic $[111]$ axis. This highly unrealistic situation led them to propose a physically much more plausible model involving local displacements for the Pb atoms of about 0.25 Å perpendicular to the $[111]$ axis and a much smaller and more isotropic thermal ellipsoid was obtained. Evidence for local shifts of Pb atoms in PZT ceramics has also been demonstrated by pair-distribution function analysis by Teslic and co-workers.³⁹

TABLE IV. Comparison of refined values of atomic coordinates in the monoclinic phase with the corresponding values in the tetragonal and rhombohedral phases for both the "ideal" structures and those with local shifts, as discussed in text.

	tetragonal $x=0.48$, 325 K		monoclinic $x=0.48$, 20 K as refined	rhombohedral (Ref. 43) $x=0.40$, 295 K	
	ideal	local shifts ^a		local shifts ^b	ideal
$x_{\text{Zr/Ti}}$	0.500	0.530	0.523	0.520	0.540
$z_{\text{Zr/Ti}}$	0.451	0.451	0.449	0.420	0.460
$x_{\text{O}(1)}$	0.500	0.530	0.551	0.547	0.567
$z_{\text{O}(1)}$	-0.103	-0.103	-0.099	0.093	-0.053
$x_{\text{O}(2)}$	0.250	0.280	0.288	0.290	0.310
$y_{\text{O}(2)}$	0.250	0.250	0.243	0.257	0.257
$z_{\text{O}(2)}$	0.379	0.379	0.373	0.393	0.433
$a_m(\text{\AA})$	5.722		5.722	5.787	
$b_m(\text{\AA})$	5.722		5.710	5.755	
$c_m(\text{\AA})$	4.139		4.137	4.081	
$\beta(^{\circ})$	90.0		90.50	90.45	

^aTetragonal local shifts of (0.03,0.03,0).

^bHexagonal local shifts of (-0.02,0.02,0).

We now consider the refined values of the Pb atom positions with local displacements for rhombohedral PZT listed in Table IV of Ref. 23. With the use of the appropriate transformation matrices, it is straightforward to show that these shifts correspond to displacements of 0.2–0.25 Å along the direction of the monoclinic [100] axis, similar to what is actually observed for $x=0.48$. It thus seems equally plausible that the monoclinic phase can also result from the condensation of local displacements perpendicular to the [111] axis.

The monoclinic structure can thus be pictured as providing a "bridge" between the rhombohedral and tetragonal structures in the region of the MPB. This is illustrated in Table IV, which compares the results for PZT with $x=0.48$ obtained in the present study with earlier results⁴³ for rhombohedral PZT with $x=0.40$ expressed in terms of the monoclinic cell.⁴⁴ For $x=0.48$, the atomic coordinates for Zr/Ti, O(1) and O(2) are listed for the "ideal" tetragonal structure (model I) and for a similar structure with local shifts of (0.03,0.03,0) in the first two columns, and for the monoclinic structure in the third column. The last two columns describe the rhombohedral structure for $x=0.40$ assuming local shifts of (-0.02,0.02,0) along the hexagonal axes and the as-refined "ideal" structure, respectively. It is clear that the condensation of these local shifts gives a very plausible description of the monoclinic structure in both cases. It is also interesting to note the behavior of the corresponding lattice parameters; metrically the monoclinic cell is very similar to the tetragonal cell except for the monoclinic angle, which is close to that of the rhombohedral cell.

Evidence for a tetragonal-to-monoclinic transition in the ferroelectric material $\text{PbFe}_{0.5}\text{Nb}_{0.5}\text{O}_3$ has also been reported by Bonny *et al.*⁴⁵ from single crystal and synchrotron x-ray powder diffraction measurements. The latter data show a cubic-tetragonal transition at ~ 376 K, and a second transition at ~ 355 K. Although the resolution was not sufficient to reveal any systematic splitting of the peaks, it was concluded that the data were consistent with a very weak monoclinic

distortion of the pseudorhombohedral unit cell. In a recent neutron and x-ray powder study, Lampis *et al.*⁴⁶ have shown that Rietveld refinement gives better agreement for the monoclinic structure at 80 and 250 K than for the rhombohedral one. The resulting monoclinic distortion is very weak, and the large thermal factor obtained for Pb is indicative of a high degree of disorder.

The relationships between the PZT rhombohedral, tetragonal and monoclinic structures are also shown schematically in Fig. 7, in which the displacements of the Pb atom are shown projected on the pseudocubic (110) mirror plane. The four locally disordered $\langle 110 \rangle$ shifts postulated in the present paper for the tetragonal phase are shown superimposed on the [001] shift at the left [Fig. 7(a)] and the three locally disordered $\langle 100 \rangle$ shifts proposed by Corker *et al.*²³ for the rhombohedral phase are shown superimposed on the [111]

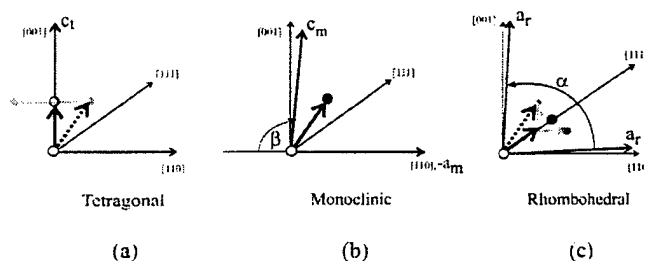


FIG. 7. Schematic illustration of the tetragonal (a), monoclinic (b), and rhombohedral (c) distortions of the perovskite unit cell projected on the pseudocubic (110) plane. The solid circles represent the observed shifts with respect to the ideal cubic structure. The light grey circles represent the four locally disordered $\langle 100 \rangle$ shifts in the tetragonal structure (a) and the three locally disordered shifts in the rhombohedral structure (c) described by Corker *et al.* (Ref. 23). The heavy dashed arrows represent the freezing-out of one of these shifts to give the monoclinic observed structure. Note that the resultant shifts in the rhombohedral structure can be viewed as a combination of a [111] shift with local $\langle 100 \rangle$ shifts, as indicated by the light grey arrows.

shift at the right [Fig. 7(c)]. It can be seen that both the condensation of the [110] shift in the tetragonal phase and the condensation of the [001] shift in the rhombohedral phase leads to the observed monoclinic shift shown at the center [Fig. 7(b)]. We note that although Corker *et al.* discuss their results in terms of $\langle 100 \rangle$ shifts and a [111] shift smaller than that predicted in the usual refinement procedure, they can be equally well described by a combination of shifts perpendicular to the [111] axis and the [111] shift actually obtained in the refinement, as is evident from Fig. 7(c).

We conclude, therefore, that the F_M phase establishes a connection between the PZT phases at both sides of the MPB through the common symmetry element, the mirror plane, and suggest that there is not really a morphotropic phase boundary, but rather a "morphotropic phase," connecting the F_T and F_R phases of PZT. In the monoclinic phase the difference vector between the positive and negative centers of charge defines the polar axis, whose orientation, in contrast to the case of the F_T and F_R phases, cannot be determined on symmetry grounds alone. According to this, from the results shown in Table III, the polar axis in the monoclinic phase is found to be tilted about 24° from the [001] axis towards the [111] axis. This structure represents the first example of a ferroelectric material with $P_x^2 = P_y^2 \neq P_z^2$, (P_x, P_y, P_z) being the Cartesian components of the polarization vector. This class corresponds to the so-called $m3m(12)A2Fm$ type predicted by Shuvalov.⁴⁷ It is possible that this new phase is one of the rare examples of a two-dimensional ferroelectric⁴⁸ in which the unit cell dipole moment switches within a plane containing the polar axis, upon application of an electric field.

This F_M phase has important implications; for example, it might explain the well-known shifts of the anomalies of many physical properties with respect to the MPB and thus help in understanding the physical properties in this region, of great interest from the applications point of view.¹ It has been found that the maximum values of d_{33} for rhombohedral PZT with $x=0.40$ are not obtained for samples polarized along the [111] direction but along a direction close to the perovskite [001] direction.⁴⁹ This points out the intrinsic importance of the [001] direction in perovskites, whatever the distortion present, and is consistent with Corker *et al.*'s model for the rhombohedral phase,²³ and the idea of the rhombohedral-tetragonal transition through a monoclinic phase.

It is also to be expected that other systems with morphotropic phase boundaries between two nonsymmetry-related phases (e.g., other perovskites or tungsten-bronze mixed systems) may show similar intermediate phases. In fact, an indication of symmetry lowering at the MPB of the PZN-PT system has been recently reported by Fujishiro *et al.*⁵⁰ From a different point of view, a monoclinic ferroelectric perovskite also represents a new challenge for first-principles theorists, until now used to dealing only with tetragonal, rhombohedral and orthorhombic perovskites.

A structural analysis of several other PZT compositions with $x=0.42$ – 0.51 is currently in progress in order to determine the new PZT phase diagram more precisely. In the preliminary version shown in Fig. 1 we have included data for a sample with $x=0.50$ made under slightly different conditions²² at the Institute of Ceramic and Glass (ICG) in Madrid, together with the data described in the present work for a sample with $x=0.48$ synthesized in the Materials Research Laboratory at the Pennsylvania State University (PSU). As can be seen the results for these two compositions show consistent behavior, and demonstrate that the F_M - F_T phase boundary lies along the MPB of Jaffe *et al.* Preliminary results for a sample from PSU with $x=0.47$ show unequivocally that the monoclinic features are present at 300 K. However, measurements on an ICG sample with the same nominal composition do not show monoclinicity unambiguously, but instead a rather complex poorly defined region from 300–400 K between the rhombohedral and tetragonal phases.²² The extension of the monoclinic region and the location of the F_R - F_M phase boundary are still somewhat undefined, although it is clear that the monoclinic region has a narrower composition range as the temperature increases. The existence of a quadruple point in the PZT phase diagram is an interesting possibility.

ACKNOWLEDGMENTS

We wish to gratefully acknowledge B. Jones for the excellent quality of the $x=0.48$ sample used in this work, and we thank L. Bellaiche, A. M. Glazer, E. Moshopoulou, C. Moure, and E. Sawaguchi for their helpful comments. Support by NATO (Grant No. R.C.G. 970037), the Spanish CICYT (Project No. PB96-0037), and the U.S. Department of Energy, Division of Materials Sciences (Contract No. DE-AC02-98CH10886) is also acknowledged.

*Visiting scientist at Brookhaven National Laboratory.

¹B. Jaffe, W.R. Cook, and H. Jaffe, *Piezoelectric Ceramics* (Academic Press, London, 1971).

²R.E. Cohen, *Nature* (London) **358**, 136 (1992).

³R.D. King-Smith and D. Vanderbilt, *Phys. Rev. B* **49**, 5828 (1994).

⁴W. Zhong, D. Vanderbilt, and K. Rabe, *Phys. Rev. Lett.* **73**, 1861 (1994); *Phys. Rev. B* **52**, 6301 (1995).

⁵W. Zhong and D. Vanderbilt, *Phys. Rev. Lett.* **74**, 2587 (1995).

⁶A. Garcia and D. Vanderbilt, *Phys. Rev. B* **54**, 3817 (1996).

⁷K.M. Rabe and U.W. Waghmare, *Phys. Rev. B* **55**, 6161 (1997).

⁸K.M. Rabe and E. Cockayne, in *First-Principles Calculations for Ferroelectrics*, AIP Conf. Proc. No. 436, edited by R. Cohen (AIP, New York, 1998), p. 61.

⁹Ph. Ghosez, E. Cockayne, U.V. Waghmare, and K.M. Rabe, *Phys. Rev. B* **60**, 836 (1999).

¹⁰L. Bellaiche, J. Padilla, and D. Vanderbilt, *Phys. Rev. B* **59**, 1834 (1999).

¹¹L. Bellaiche, J. Padilla, and D. Vanderbilt, *First-principles Calculations for Ferroelectrics: 5th Williamsburg Workshop*, edited by R. Cohen (AIP, Woodbury, 1998), p. 11.

¹²G. Soghi-Szabo and R. E. Cohen, *Ferroelectrics* **194**, 287 (1997).

¹³G. Shirane and K. Suzuki, *J. Phys. Soc. Jpn.* **7**, 333 (1952).

¹⁴E. Sawaguchi, *J. Phys. Soc. Jpn.* **8**, 615 (1953).

¹⁵Y. Xu, *Ferroelectric Materials and their Applications* (North Holland, Amsterdam, 1991).

¹⁶K. Kakewaga, O. Matsunaga, T. Kato, and Y. Sasaki, *J. Am. Ceram. Soc.* **78**, 1071 (1995).

- ¹⁷J.C. Fernandes, D.A. Hall, M.R. Cockburn, and G.N. Greaves, *Nucl. Instrum. Methods Phys. Res. B* **97**, 137 (1995).
- ¹⁸M. Hammer, C. Monty, A. Endriss, and M.J. Hoffmann, *J. Am. Ceram. Soc.* **81**, 721 (1998).
- ¹⁹W. Cao and L.E. Cross, *Phys. Rev. B* **47**, 4825 (1993).
- ²⁰B. Noheda, D.E. Cox, G. Shirane, J.A. Gonzalo, L.E. Cross, and S-E. Park, *Appl. Phys. Lett.* **74**, 2059 (1999).
- ²¹The $[\bar{1}\bar{1}0]$ and $[1\bar{1}0]$ directions are chosen so that the monoclinic angle $\beta > 90^\circ$ to conform with usual crystallographic convention.
- ²²B. Noheda, J.A. Gonzalo, A.C. Caballero, C. Moure, D.E. Cox, and G. Shirane, cond-mat/9907286, *Ferroelectrics* (to be published).
- ²³D.L. Corker, A.M. Glazer, R.W. Whatmore, A. Stallard, and F. Fauth, *J. Phys.: Condens. Matter* **10**, 6251 (1998).
- ²⁴C.W. Duggins Jr., *Acta Crystallogr., Sect. A: Cryst. Phys., Diffraction, Theor. Gen. Crystallogr.* **31**, 146 (1975).
- ²⁵L.W. Finger, D.E. Cox, and A.P. Jephcoat, *J. Appl. Crystallogr.* **27**, 892 (1994).
- ²⁶G.K. Williamson and W.H. Hall, *Acta Metall.* **1**, 22 (1953).
- ²⁷A.C. Larson and R.B. Von Dreele (unpublished).
- ²⁸P.W. Stephens, *J. Appl. Crystallogr.* **32**, 281 (1999).
- ²⁹C. Muller, J.-L. Baudour, V. Madigou, F. Bouree, J.-M. Kiat, C. Favotto, and M. Roubin, *Acta Crystallogr., Sect. B: Struct. Sci.* **55**, 8 (1999).
- ³⁰A.M. Glazer and S.A. Mabud, *Acta Crystallogr., Sect. B: Struct. Crystallogr. Cryst. Chem.* **34**, 1065 (1978).
- ³¹R.J. Nelmes and W.F. Kuhs, *Solid State Commun.* **54**, 721 (1985).
- ³²The structure factor correction is defined in terms of the anisotropic u_{ij} thermal factors as $\exp\{-[2\pi^2(\sum_i j u_{ij} a_i^* a_j^*)]\}$, a_i^* being the lattice vectors of the reciprocal unit cell.
- ³³L.B. McCusker, R.B. von Dreele, D.E. Cox, D. Louër, and P. Scardi, *J. Appl. Crystallogr.* **32**, 36 (1999).
- ³⁴K. Itoh, L.Z. Zeng, E. Nakamura, and N. Mishima, *Ferroelectrics* **63**, 29 (1985).
- ³⁵C. Malibert, B. Dkhil, J.M. Kiat, D. Durand, J.F. Berar, and A. Spasojevic-de Bire, *J. Phys.: Condens. Matter* **9**, 7485 (1997).
- ³⁶G. Shirane, R. Pepinski, and B.C. Frazer, *Acta Crystallogr.* **9**, 131 (1956).
- ³⁷A.P. Wilkinson, J. Xu, S. Pattanaik, and J.L. Billinge, *Chem. Mater.* **10**, 3611 (1998).
- ³⁸L. Bellaiche and D. Vanderbilt, *Phys. Rev. Lett.* **83**, 1347 (1999).
- ³⁹S. Teslic, T. Egami, and D. Viehland, *J. Phys. Chem. Solids* **57**, 1537 (1996); *Ferroelectrics* **194**, 271 (1997).
- ⁴⁰D.L. Corker, A.M. Glazer, W. Kaminsky, R.W. Whatmore, J. Dec. and K. Roleder, *Acta Crystallogr., Sect. B: Struct. Sci.* **54**, 18 (1998).
- ⁴¹S. Teslic and T. Egami, *Acta Crystallogr., Sect. B: Struct. Sci.* **54**, 750 (1998).
- ⁴²A.M. Glazer, S.A. Mabud, and R. Clarke, *Acta Crystallogr., Sect. B: Struct. Crystallogr. Cryst. Chem.* **34**, 1060 (1978).
- ⁴³A. Amin, R.E. Newnham, L.E. Cross, and D.E. Cox, *J. Solid State Chem.* **37**, 248 (1981).
- ⁴⁴The rhombohedral unit cell can be expressed in terms of a monoclinic one by $a_m = 2a_r \cos(\alpha/2)$, $b_m = 2a_r \sin(\alpha/2)$, $c_m = a_r$, $\beta = 180^\circ - \phi$, where $\cos \phi = 1 - 2\sin^2(\alpha/2)/\cos(\alpha/2)$ and a_r and α are the $R3m$ cell parameters. Note that a_r in Ref. 43 refers to the doubled cell.
- ⁴⁵V. Bonny, M. Bonin, P. Sciau, K.J. Schenk, and G. Chapuis, *Solid State Commun.* **102**, 347 (1997).
- ⁴⁶N. Lampis, P. Sciau, and A.G. Lehmann, *J. Phys.: Condens. Matter* **11**, 3489 (1999).
- ⁴⁷L.A. Shuvalov, *J. Phys. Soc. Jpn.* **28**, 38 (1970).
- ⁴⁸S.C. Abrahams and E.T. Keve, *Ferroelectrics* **2**, 129 (1971).
- ⁴⁹X-h Du, J. Zheng, U. Belegundu, and K. Uchino, *Appl. Phys. Lett.* **72**, 2421 (1998).
- ⁵⁰K. Fujishiro, R. Vlokh, Y. Uesu, Y. Yamada, J.-M. Kiat, B. Dkhil, and Y. Yamashita, *Ferroelectrics* (to be published).

APPENDIX 8

Stability of the monoclinic phase in the ferroelectric perovskite $\text{PbZr}_{1-x}\text{Ti}_x\text{O}_3$

B. Noheda,* D. E. Cox, and G. Shirane

Physics Department, Brookhaven National Laboratory, Upton, New York 11973

R. Guo, B. Jones, and L. E. Cross

Materials Research Laboratory, The Pennsylvania State University, University Park, Pennsylvania 16802

(Received 9 June 2000; published 12 December 2000)

Recent structural studies of ferroelectric $\text{PbZr}_{1-x}\text{Ti}_x\text{O}_3$ (PZT) with $x=0.48$, have revealed a monoclinic phase in the vicinity of the morphotropic phase boundary (MPB), previously regarded as the boundary separating the rhombohedral and tetragonal regions of the PZT phase diagram. In the present paper, the stability region of all three phases has been established from high-resolution synchrotron x-ray powder-diffraction measurements on a series of highly homogeneous samples with $0.42 \leq x \leq 0.52$. At 20 K, the monoclinic phase is stable in the range $0.46 \leq x \leq 0.51$, and this range narrows as the temperature is increased. A first-order phase transition from tetragonal to rhombohedral symmetry is observed only for $x=0.45$. The MPB, therefore, corresponds not to the tetragonal-rhombohedral phase boundary, but instead to the boundary between the tetragonal and monoclinic phases for $0.46 \leq x \leq 0.51$. This result provides important insight into the close relationship between the monoclinic phase and the striking piezoelectric properties of PZT; in particular, investigations of poled samples have shown that the monoclinic distortion is the origin of the unusually high piezoelectric response of PZT.

DOI: 10.1103/PhysRevB.63.014103

PACS number(s): 77.84.Dy, 61.10.-i

I. INTRODUCTION

Exceptionally striking dielectric and piezoelectric properties are found in $\text{PbZr}_{1-x}\text{Ti}_x\text{O}_3$ (PZT), the perovskite-type oxide system that is the basis of practically all transducers and other piezoelectric devices. This solid solution is cubic at high temperatures but becomes slightly distorted at lower temperatures, where it is ferroelectric. Except for a narrow region close to PbZrO_3 , the ferroelectric phase is divided in two regions of different symmetry, rhombohedral for Zr-rich compositions and tetragonal for Ti-rich compositions. The highest piezoelectric response in this system is found at the boundary between these two phases, at $x \approx 0.47$; the so-called morphotropic phase boundary (MPB). The term "morphotropic" was coined by Jaffe *et al.*¹ and means literally "the boundary between two forms." However, it is usually assumed to mean nearly vertical, i.e., composition independent. The PZT phase diagram for compositions around the MPB is shown in Fig. 1, where the open circles represent the data of Jaffe *et al.*,¹ which define the MPB above room temperature. The sharpness of this line is such that a composition fluctuation of $\Delta x = 0.01$ corresponds to a temperature uncertainty of $\Delta T \approx 90$ K. Recently, high-resolution x-ray diffraction measurements on extremely homogeneous samples by Noheda *et al.* showed that an intermediate monoclinic phase exists between the rhombohedral and tetragonal PZT phases.²⁻⁴ The observation of this monoclinic phase in two different compositions, $x = 0.48$ ^{2,4} and $x = 0.50$,³ has allowed a preliminary modification of the phase diagram, as shown in Fig. 1. Furthermore, the discovery of this phase around the MPB in PZT answers many of the questions raised by previous investigators⁵⁻¹⁰ about the nature of the MPB and the underlying basis for the special physical properties of PZT in this region of the phase diagram, especially in the context of the coexistence of rhombohedral and tetragonal phases.

The monoclinic unit cell is doubled with respect to the tetragonal one and has b as the unique axis. a_m and b_m are directed along the pseudocubic $[\bar{1}\bar{1}0]$ and $[1\bar{1}0]$ directions, respectively, while c_m is close to the tetragonal c axis, along $[001]$, but tilted away from it such that the angle β between a_m and c_m is slightly larger than 90° . This monoclinic phase has unique characteristics in comparison to all other ferroelectric perovskite phases. The polar axis is not determined by symmetry and can be directed anywhere within the monoclinic ac plane; that is, the polar axis is allowed to rotate within this plane. In the case of PZT, the pseudocubic $[111]$ and $[001]$ directions are contained within the monoclinic plane and the monoclinic polar axis is tilted away from the polar axis of the tetragonal phase $[001]$ towards that of the rhombohedral phase $[111]$.⁴ As has already been pointed out by other authors,¹¹⁻¹³ the diffraction data show clearly that the local structure of PZT differs from that of the average one. A structure analysis of rhombohedral PZT by Corker *et al.*¹³ indicated that the Pb and Zr/Ti cations in the Zr-rich compositions are distributed among three locally disordered sites with monoclinic symmetry (see the gray circles in the top left plot of Fig. 1), resulting in average rhombohedral symmetry (black circle in the top left plot of Fig. 1).⁴ In a similar structure analysis of tetragonal PZT close to the MPB,⁴ the diffraction data were shown to be consistent with Pb and Zr/Ti cations distributed among four locally disordered cation sites with monoclinic symmetry, resulting in average tetragonal symmetry.⁴

In recent years, the development of first-principles calculations applied to the study of ferroelectric perovskites has contributed greatly to the understanding of the physical properties of these materials (see, e.g., Refs. 14-19). The incorporation of a compositional degree of freedom to allow for the study of solid solutions has been an important advance, which has opened up the possibility of investigating more

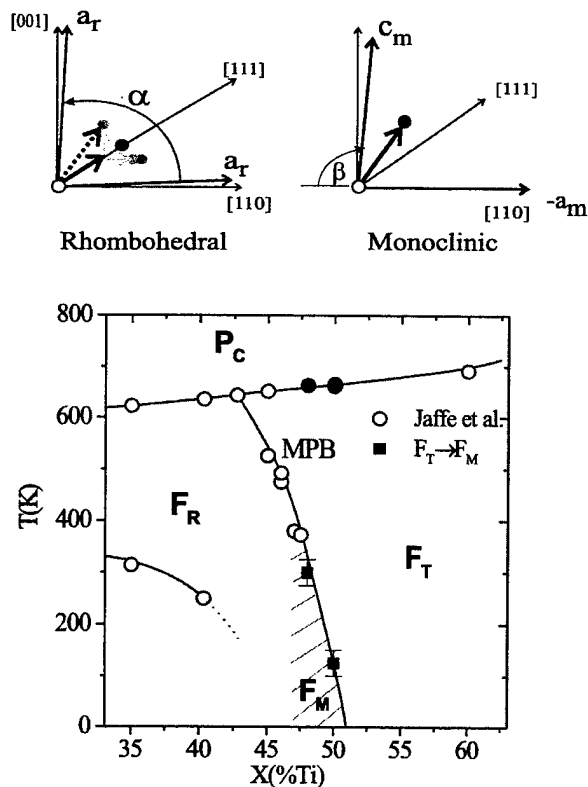


FIG. 1. The lower part of the figure shows the PZT phase diagram close to the MPB reported by Jaffe *et al.* (Ref. 1) (open symbols), and the preliminary modification proposed in Ref. 3, including the monoclinic phase. The solid symbols represent the observed phase transitions for $x=0.48$ (Ref. 4) and $x=0.50$ (Ref. 3). The upper part of the figure depicts the microscopic model proposed for the rhombohedral and the monoclinic phases in Ref. 4 (see text).

complex ferroelectric materials such as PZT and related systems.^{20–26} Very recently, Bellaiche *et al.*²⁷ have succeeded in deriving the monoclinic phase of PZT from first-principles calculations. These authors also show that the value of the piezoelectric coefficient calculated, taking into account rotation of the polarization vector in the monoclinic plane, is in good agreement with the high values observed in PZT.

In the present paper, the stability region of the monoclinic phase in PZT is characterized by means of synchrotron x-ray powder-diffraction measurements made on PZT compositions at closely spaced intervals in the range $x=0.42–0.52$. The monoclinic phase is observed at 20 K for $0.46 \leq x \leq 0.51$, and this composition range narrows as the temperature increases. The transition temperature between the tetragonal and monoclinic phases is very steep as a function of composition and coincides with the previously mentioned MPB of Jaffe *et al.*¹ above ambient temperature.

II. EXPERIMENT

PZT samples with $x=0.42, 0.45, 0.46, 0.47, 0.50, 0.51$, and 0.52 were prepared by conventional solid-state reaction techniques similar to those used previously for PZT with $x=0.48$.⁴ During the calcination, two steps were used. First,

the desired solid solution was formed at 900°C using the appropriate amounts of reagent-grade powders of lead carbonate, zirconium oxide, and titanium oxide with chemical purity better than 99.9%. Second, the formed product was pulverized and allowed to reach homogeneity by heating for 6 h at 850°C (lower than the temperature at which PbO evaporates). Pellets were then pressed using an organic binder and, after burnout of the binder, heated to 1250°C at a ramp rate of 10°C/min , held at this temperature in a covered crucible for 2 h, and cooled to room temperature. During sintering, PbZrO_3 was used as a lead source to maintain a PbO -rich atmosphere.

Several sets of high-resolution synchrotron x-ray powder-diffraction measurements were made on different occasions at beam line X7A at the Brookhaven National Synchrotron Light Source. Data were collected from the ceramic disks in symmetric flat-plate reflection geometry using θ - 2θ scans over selected angular regions in the temperature range 20–750 K. The sample was rocked $1^\circ–2^\circ$ during data collection to improve powder averaging. In all these experiments a $\text{Ge}(111)$ double-crystal monochromator was used to provide an incident beam with a wavelength close to 0.7 \AA . A $\text{Ge}(220)$ crystal analyzer and scintillation detector were mounted in the diffracted beam, giving an instrumental resolution of about 0.01° on the 2θ scale. As described in Ref. 4, measurements above room temperature were performed with the disk mounted inside a wire-wound BN tube furnace. The accuracy of the temperature in the furnace is estimated to be about 10 K. For low-temperature measurements, the pellet was loaded in a closed-cycle He cryostat, which has an estimated temperature accuracy of 2 K. With this type of diffraction geometry, it is not always possible to eliminate preferred orientation and texture effects, but the peak positions, on which the present results are based, are not affected.

In many cases the peak profiles were quite complex, necessitating a very detailed and careful peak-fitting analysis. The peak positions were determined from least-squares fits to the profile recorded for each of the selected regions. A pseudo-Voigt peak shape function with an asymmetry correction was used,²⁸ and factors such as anisotropic peak widths, coexisting phases, and diffuse scattering between peaks were taken into account. The lattice parameters of individual phases were obtained from fits to the observed peak positions for several reflections. Because of the complicated peak shapes, we found that the above procedure gave more consistent results than standard profile-fitting programs.

Examples of selected regions of the diffraction patterns for the three PZT phases, tetragonal (top), monoclinic (center), and rhombohedral (bottom), around the morphotropic phase boundary are shown in Fig. 2. The narrow width of the peaks demonstrates the excellent quality of the ceramic samples and allows the specific characteristics of each phase to be clearly distinguished. In particular, the monoclinic phase exhibits unique features that cannot be accounted for by either of the other phases or a mixture of them. In the monoclinic phase, the unit cell is doubled in volume with respect to the tetragonal one, with a_m and b_m lying along the tetragonal $[1\bar{1}0]$ and $[11\bar{0}]$ directions, and c_m tilted slightly

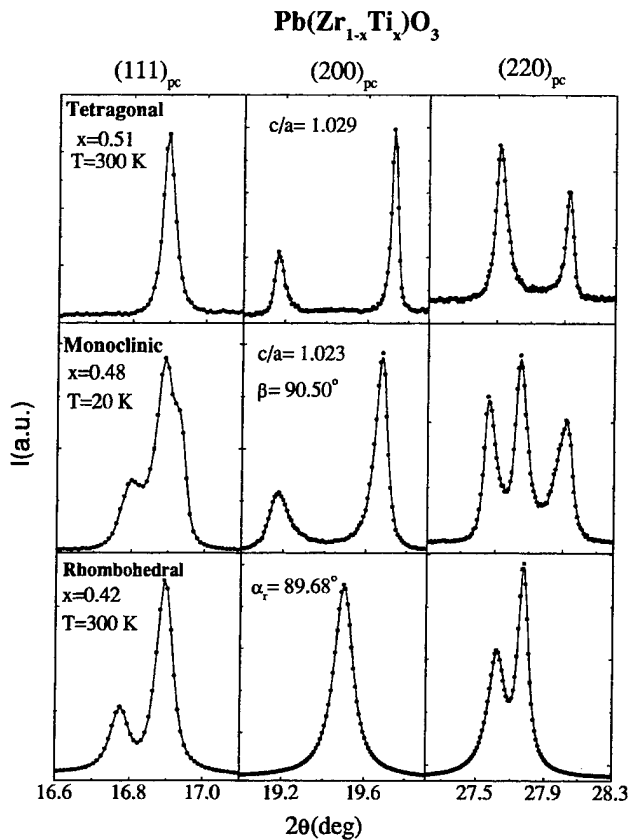


FIG. 2. Pseudocubic (111), (200), and (220) reflections for PZT with $x=0.51$ at 300 K (top), $x=0.48$ at 20 K (center), and $x=0.42$ at 300 K (bottom), showing the distinctive features of the tetragonal, monoclinic, and rhombohedral PZT phases, respectively.

away from the [001] direction. The monoclinic phase illustrated in this figure corresponds to the composition $x=0.48$ at 20 K, described in detail in Ref. 4, with $a_m=5.721$ Å, $b_m=5.708$ Å, $c_m=4.138$ Å, and $\beta=90.50^\circ$. The c/a value in Fig. 2 (center) is defined as $2\sqrt{2}c_m/(a_m+b_m)$, in order to correspond to the c_t/a_t ratio in the tetragonal case (top).

III. PHASE TRANSITIONS

The evolution of the different structures as a function of temperature has been determined for all the PZT samples in the present study ($x=0.42, 0.45, 0.46, 0.47, 0.51$, and 0.52) and combined with previous data obtained for $x=0.48$ and $x=0.50$.²⁻⁴ These results give a complete picture of the phase transitions occurring around the morphotropic phase boundary from 20 to 700 K. Three different low-temperature phases, with rhombohedral, monoclinic, and tetragonal symmetry, are observed. An important result is that the MPB defined by Jaffe *et al.*¹ is shown to correspond to the limit of the monoclinic phase rather than that of the rhombohedral phase and is a very robust line that is reproduced for all the samples under investigation. Both the tetragonal-monoclinic and the tetragonal-rhombohedral phase transitions will be described in this section, as well as the rhombohedral-rhombohedral phase transitions observed for $x=0.42$ at lower temperatures.

A. Tetragonal-monoclinic phase transition

The tetragonal phase in PZT is very similar to that of pure PbTiO_3 .²⁹⁻³¹ The effects of Zr substitution on the structure of the tetragonal phase are basically two: first, as the Zr content increases, the tetragonal strain c_t/a_t decreases, and, second, the cubic-to-tetragonal phase transition evolves from first order to second-order. Figure 3 (top) shows the lattice parameters of PZT with $x=0.51$ as a function of temperature. The paraelectric-ferroelectric phase transition at $T \approx 660$ K is of second order, as expected,³² and the ferroelectric phase is purely tetragonal down to 100 K. Below this temperature, structural changes can be noticed; in particular, the tetragonal $(h0h)_t$ and $(hhh)_t$ reflections broaden markedly. This is apparent in the lower part of Fig. 3, where the pseudocubic $(220)_{pc}$ reflections are shown at high temperature (right), at an intermediate temperature (center), and at low temperature (left). Based on a careful peak-fitting analysis, the broadening at low temperatures of these reflections can be attributed to two separated peaks, consistent with the monoclinic symmetry observed in PZT with $x=0.48$,⁴ also illustrated in Fig. 2. However, the monoclinic distortion is quite small, with $a_m \approx b_m$ and $\beta \approx 90.2^\circ$. Similar behavior was observed for a sample of PZT with $x=0.50$ (Ref. 3) prepared under slightly different conditions, to be discussed later. As seen from Fig. 3, the monoclinic angle β is small, and the tetragonal-to-monoclinic transition temperature can only be approximately defined at $T_{T-M} \approx 50$ K. On the other hand, data collected from PZT with $x=0.52$ show a well-defined tetragonal phase down to 20 K.

The evolution of the lattice parameters with temperature for PZT with $x=0.46$ is shown in Fig. 4 (top). The features displayed by this composition are similar to those of PZT with $x=0.48$.⁴ A comparison with the latter data at low temperatures shows that the monoclinic angle β is larger for $x=0.46$ than for $x=0.48$. With decreasing x (Ti content), the differences between a_m and b_m also increase, while the difference between a_m and c_m decreases, corresponding to the evolution to a rhombohedral phase in which " $a_m=b_m=c_m$ ".⁴ The monoclinic phase is very well defined at low temperatures, as shown by the pseudocubic $(110)_{pc}$ reflections plotted at the bottom left of Fig. 4. The evolution of $\beta-90^\circ$ shows a transition to a tetragonal phase at $T_{T-M} \approx 450$ K, in agreement with the MPB of Jaffe *et al.* However, the characteristic features of the tetragonal phase also appear well below this temperature, and there is a wide region of phase coexistence between the tetragonal and monoclinic phases, as shown in the central plot at the bottom of the figure. In this plot, the peak positions for the pseudocubic $(110)_{pc}$ reflections corresponding to the monoclinic and tetragonal phases are shown together with the experimental data. From the observed data, a reliable peak-fitting analysis can be carried out and the lattice parameters determined for both phases in this region, as plotted as a function of temperature at the top of Fig. 4. The measurements on PZT with $x=0.47$ show similar behavior, but with a narrower coexistence region ($300 \text{ K} < T < 400 \text{ K}$). For this composition the evolution of the order parameter, $(\beta-90^\circ)$, suggests a tetragonal-to-monoclinic phase transition at $T_{T-M} \approx 310$ K,

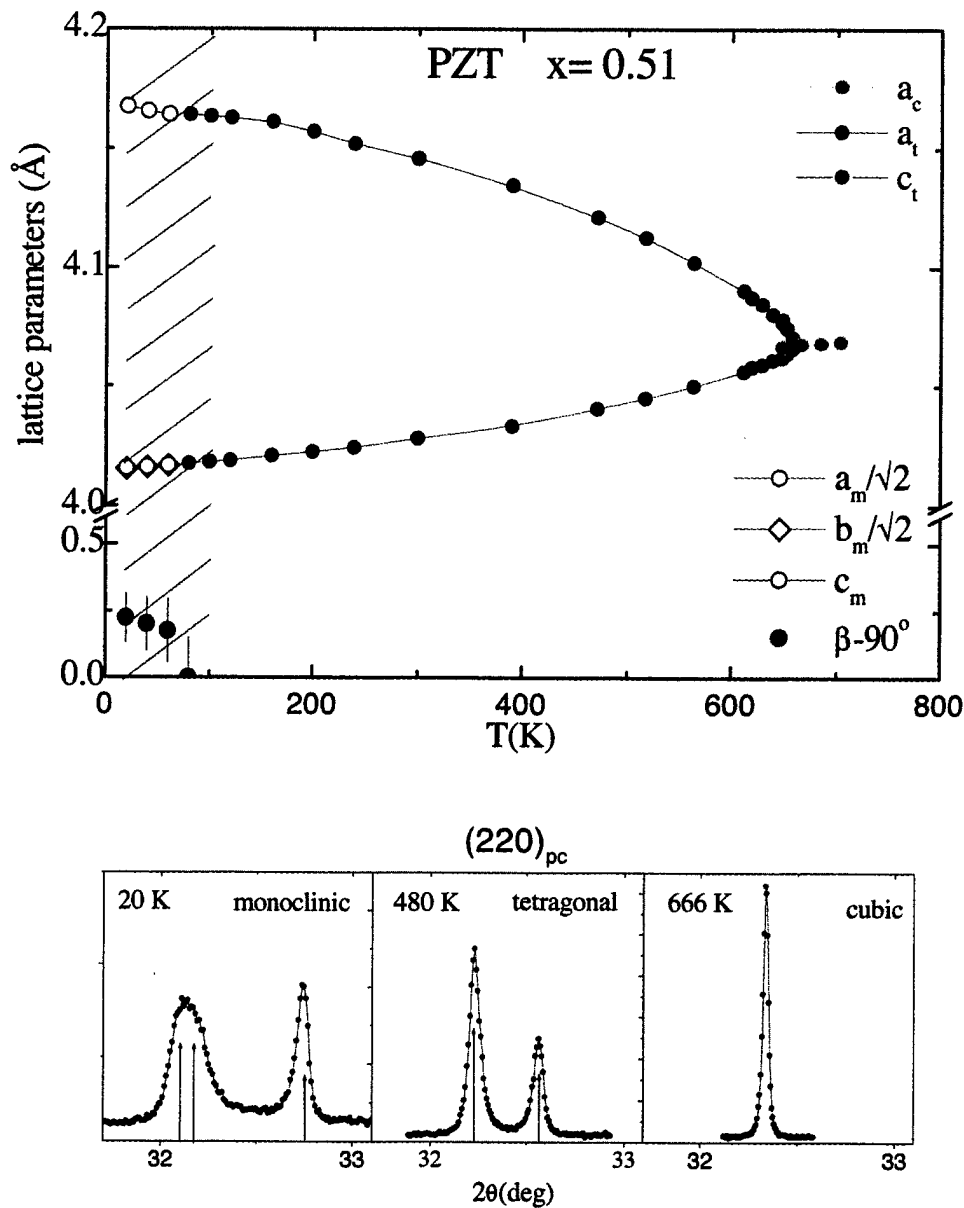


FIG. 3. (Color) Temperature evolution of the lattice parameters of PZT with $x=0.51$ from 20 K to 700 K, for the monoclinic, a_m , b_m , c_m , and β ; tetragonal, a_t and c_t ; and cubic, a_c , phases. The dashed region in the figure represents the uncertainty in the tetragonal-monoclinic phase transition. At the bottom of the figure, the pseudocubic (220) reflection is plotted at 20 K (monoclinic), 480 K (tetragonal), and 666 K (cubic) to illustrate the differences between the three phases.

very close to that observed for $x=0.48$, but the sample is not fully tetragonal until the temperature is greater than 400 K, corresponding to the MPB of Jaffe *et al.* for this composition.

B. Tetragonal-rhombohedral phase transition

A similar analysis for PZT with $x=0.45$ yields completely different results, as shown by the evolution of the $(200)_{pc}$ reflection in the lower part of Fig. 5. At low temperature the sample is rhombohedral (left) and remains rhombohedral up to $T \approx 500$ K, while for $T > 550$ K, this composition is tetragonal. Some diffuse scattering is observed between the tetragonal peaks, as shown in the bottom right of Fig. 5. This feature is present in all compositions in

the study, as previously noted in Ref. 4, and is associated with the existence of twin boundaries in the tetragonal ferroelectric phase.³³ From the evolution of the order parameter ($90^\circ - \alpha_r$), it is possible to determine that the tetragonal-rhombohedral phase transition is complete at $T_{T-R} \approx 580$ K. A coexistence region is observed in the interval $500 \text{ K} < T < 580 \text{ K}$. In the central plot at the bottom of the figure, the $(200)_{pc}$ reflection in this region is depicted together with the calculated peak positions for both phases.

C. Low-temperature rhombohedral phase

The data obtained for the PZT sample with $x=0.42$ show that this composition has rhombohedral symmetry all the

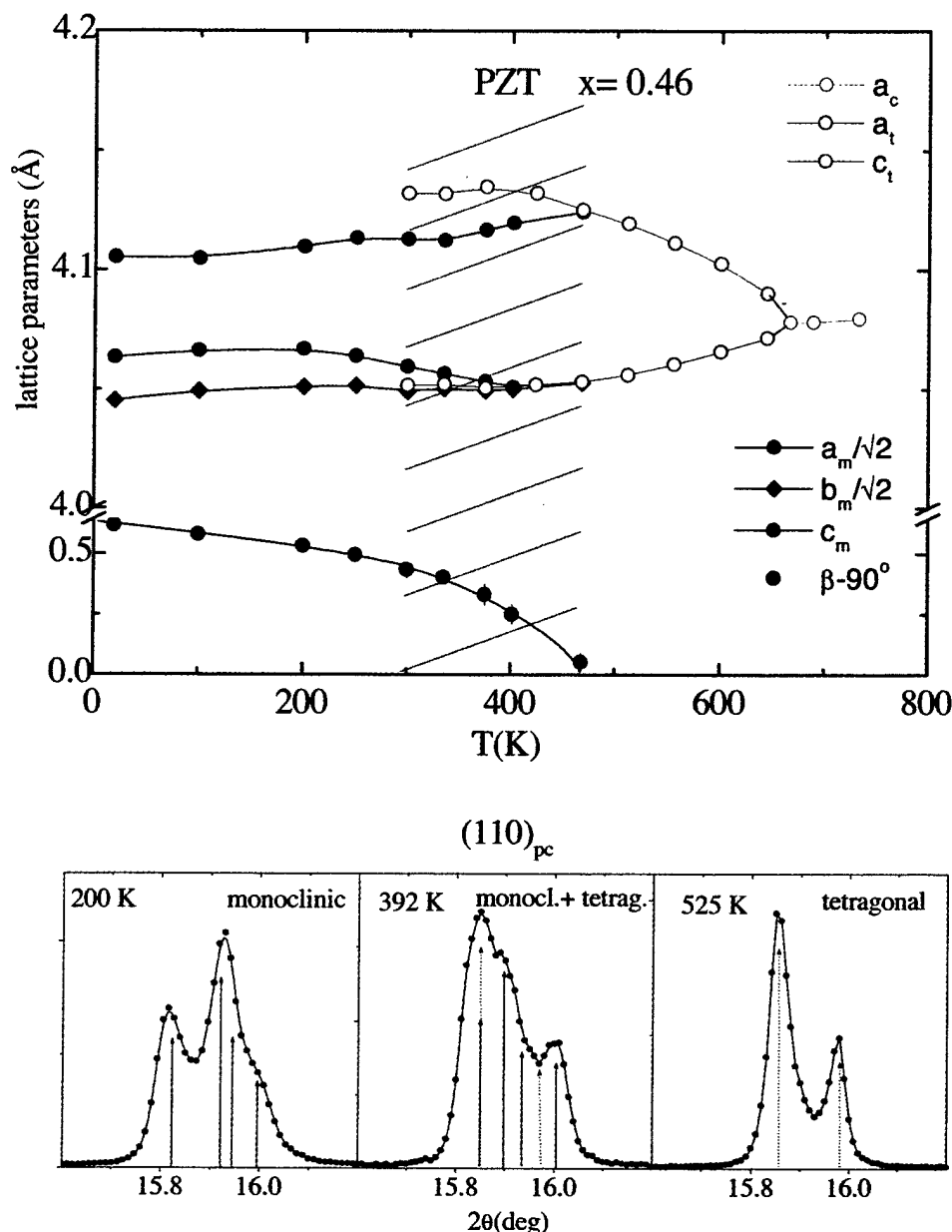


FIG. 4. (Color) Temperature evolution of the lattice parameters of PZT with $x=0.46$ from 20 K to 710 K, for the monoclinic, a_m , b_m , c_m , and β ; tetragonal, a_t and c_t ; and cubic, a_c , phases. The dashed area in the figure represents the region of tetragonal and monoclinic phase coexistence. At the bottom of the figure, the pseudocubic (110) reflection is plotted at 200 K (monoclinic phase), 392 K (tetragonal-monoclinic phase coexistence), and 525 K (tetragonal phase), where the calculated peak positions are indicated by solid arrows in the monoclinic phase and dashed arrows in the tetragonal phase.

way down to 20 K from the Curie point at $T_c \approx 650$ K. At 20 K, the rhombohedral lattice parameters are $a = 4.0921$ Å and $\alpha_r = 89.61^\circ$. With increasing temperature, the rhombohedral angle α_r increases gradually until the cubic phase is reached, while a remains practically constant.

Two different rhombohedral phases have been observed in PZT: a high-temperature phase ($F_{R(HT)}$) and a low-temperature rhombohedral phase ($F_{R(LT)}$),³⁴ which have space groups $R3m$ and $R3c$, respectively. In the latter phase, adjacent oxygen octahedra along the $[111]$ polar axis are rotated about this axis in opposite directions, so that the unit cell is doubled with respect to the high-temperature

phase.^{35,36} The corresponding phase boundary was also determined by Jaffe *et al.*¹ in the region of the phase diagram above room temperature. An extension of this boundary below room temperature was reported in a neutron powder-diffraction study by Amin *et al.*,³⁷ who investigated the superlattice peaks from a sample with $x=0.40$ and found the transition temperature to occur at about 250 K. In the present work, we were also able to observe very weak superlattice peaks from a composition with $x=0.42$ below room temperature in the synchrotron x-ray patterns. The phase boundary in this case was found to lie at approximately 175 K (see Fig. 6).

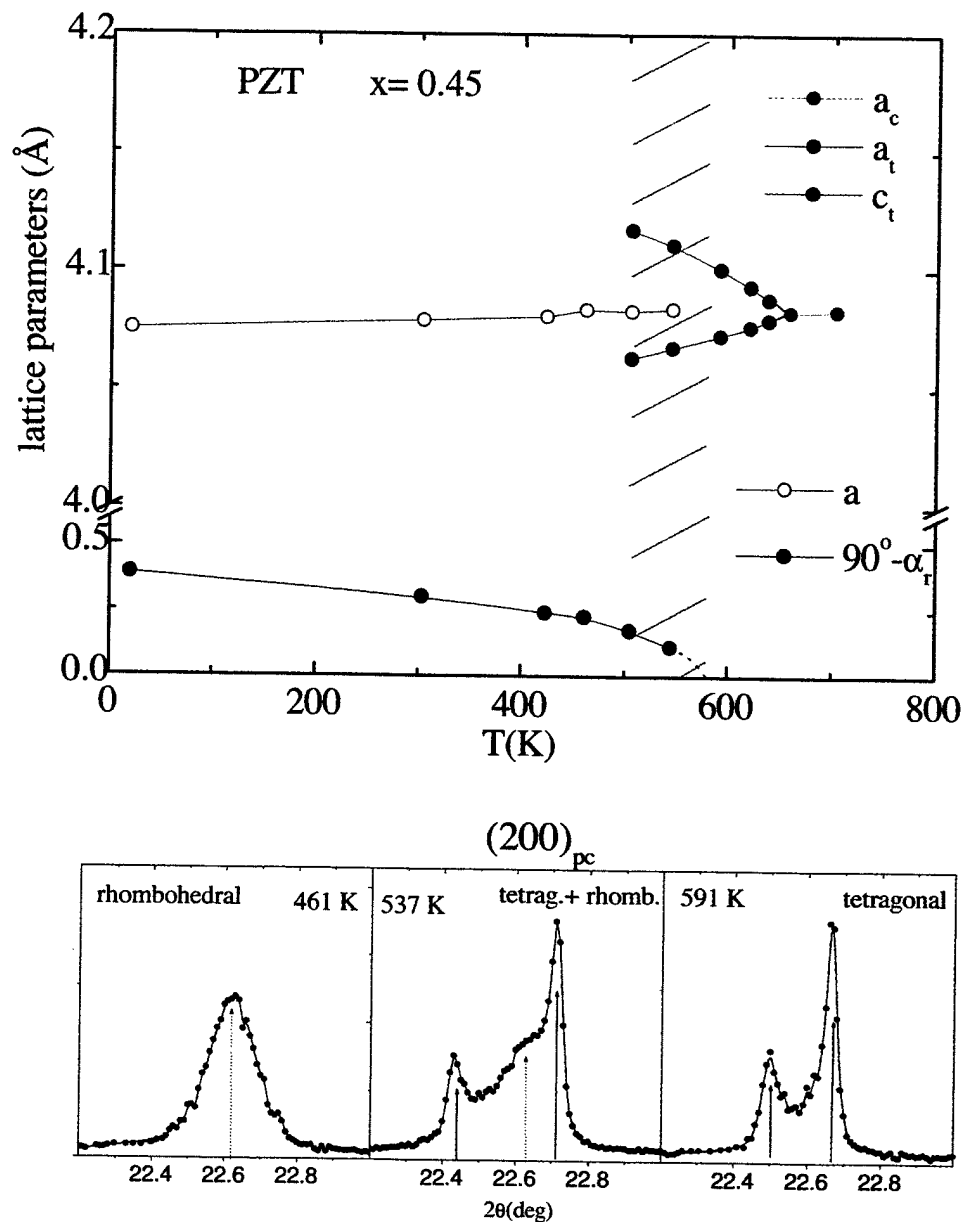


FIG. 5. (Color) Temperature evolution of the lattice parameters of PZT with $x=0.45$ from 20 K to 710 K, for the rhombohedral, a and α_r ; tetragonal, a_t and c_t ; and cubic, a_c , phases. The dashed area in the figure represents the region of tetragonal and rhombohedral phase coexistence. At the bottom of the figure, the pseudocubic (200) reflection is plotted at 461 K (rhombohedral phase), 537 K (tetragonal-rhombohedral phase coexistence), and 591 K (tetragonal phase), where the calculated peak positions are indicated by dashed arrows in the rhombohedral phase and solid arrows in the tetragonal phase.

We have also observed one very weak superlattice peak in a recent neutron diffraction study of a sample with $x=0.48$ at 20 K. This peak can be indexed in terms of a monoclinic cell with a doubled c axis, but the nature of the distortion and any possible relationship with that in the low-temperature rhombohedral phase has not yet been determined.

IV. DISCUSSION

The results presented above are summarized and compared with previous data from $x=0.48$ and $x=0.50$ in Fig. 6, which represents the new PZT phase diagram around the MPB. The data obtained for the tetragonal-(monoclinic/

rhombohedral) transition temperatures for $0.45 < x < 0.51$ are very consistent and lie on a well-defined line, which reproduces the MPB of Jaffe *et al.*¹ above ambient temperature. The boundary between the rhombohedral and monoclinic regions is shown as a vertical line between $0.45 < x < 0.46$, since no evidence of a monoclinic-rhombohedral phase transition has been observed. The lattice parameters at 20 and 300 K for the compositions under study are listed in Table I, which also shows clearly the widening of the monoclinic region at lower temperatures. Figure 7 shows the evolution of the lattice parameters of the different phases as a function of composition at 300 K, from the rhombohedral to the tetragonal PZT phases via the monoclinic phase. At the top of

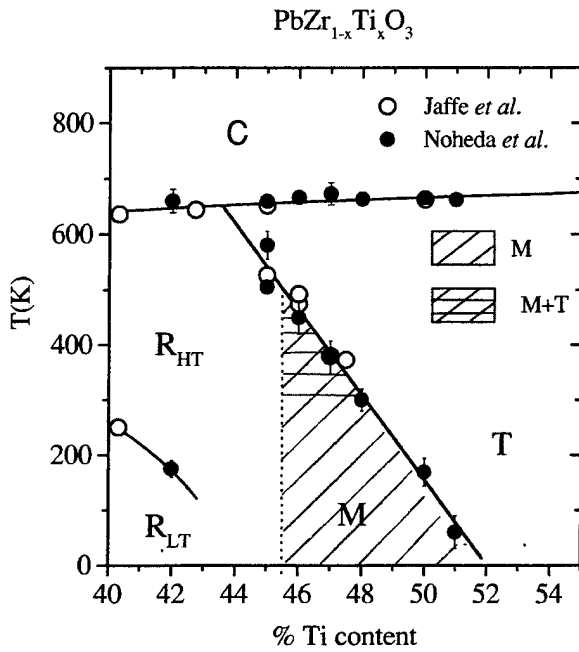


FIG. 6. New PZT phase diagram around the MPB. The solid symbols are the results from the current work, together with those in Ref. 3 ($x=0.50$) and Ref. 4 ($x=0.48$). Data from Jaffe *et al.* (Ref. 1) and Amin *et al.* (Ref. 37) are represented by open circles. The monoclinic region is shaded with diagonal lines. Horizontal lines are superimposed in the region of tetragonal-monoclinic phase coexistence. For $x=0.45$, the solid symbols represent the limits of the tetragonal-rhombohedral coexistence region.

the figure, the unit-cell volume shows an essentially linear behavior with composition in the range studied. The monoclinic angle β and lattice strain c/a at 300 K are also plotted as a function of composition in Fig. 7, where the rhombohedral cell with lattice parameters a and α_r (see Table I) has been expressed in terms of the monoclinic cell.³⁸ c/a corresponds to c_t/a_t , $2\sqrt{2}c_m/(a_m+b_m)$, and 1, in the tetragonal, monoclinic, and rhombohedral cases, respectively. β is 90° for a tetragonal cell and is the monoclinic angle for the monoclinic cell. The role of the monoclinic phase as a "bridge" between the tetragonal and rhombohedral phases

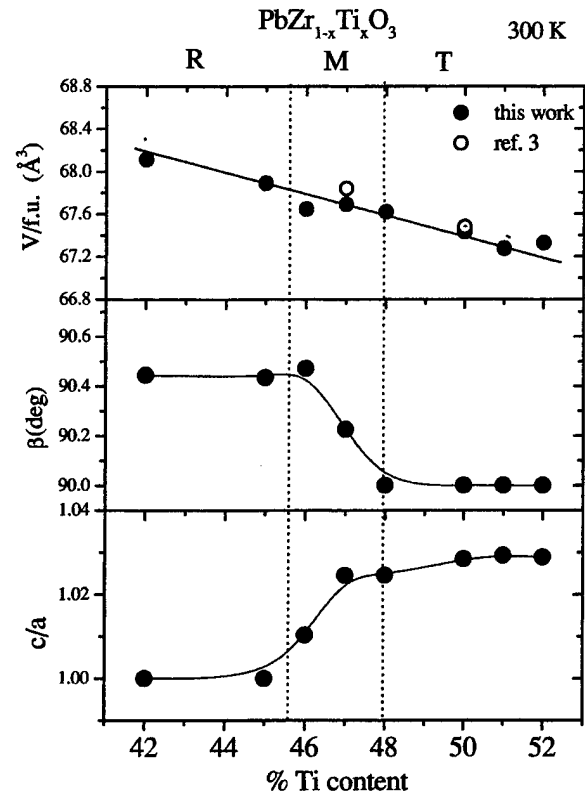


FIG. 7. The structural evolution with composition from the rhombohedral to the tetragonal PZT phases, through the monoclinic phase, as illustrated by the cell volume per formula unit, V (top), the monoclinic angle β (center) (Ref. 38), and the lattice strain c/a (bottom) for PZT with $0.42 \leq x \leq 0.52$ at 300 K. The cell volumes of the samples in Ref. 3 are also plotted as open circles at the top of the figure.

in PZT is clearly demonstrated in these plots. The monoclinic phase has also been observed by Raman scattering in a very recent paper by Souza Filho *et al.*³⁹

The structural studies reported here, together with those in Refs. 2–4, comprise data from ten samples from two different origins spanning the composition range $0.42 \leq x \leq 0.52$. Only one of these samples was inconsistent with the picture

TABLE I. Lattice parameters at 20 and 300 K for PZT, with x in the range 0.42–0.52. The symmetry S of the unit cell, rhombohedral (R), monoclinic (M), or tetragonal (T) is indicated in each case. For rhombohedral symmetry $a=b=c$, and α_r is the rhombohedral angle. In the monoclinic case, β is the monoclinic angle. In the tetragonal case $a=b=a_t$, and $\beta=90^\circ$.

%Ti	S	20 K					S	300 K				
		a (Å)	b (Å)	c (Å)	α_r (°)	β (°)		a (Å)	b (Å)	c (Å)	α_r (°)	β (°)
42	R	4.078			89.61		R	4.084			89.68	
45	R	4.075			89.61		R	4.079			89.69	
46	M	5.747	5.721	4.104		90.62	M	5.754	5.731	4.103		90.47
47	M	5.731	5.713	4.123		90.58	M	5.720	5.715	4.142		90.22
48	M	5.717	5.703	4.143		90.53	T	4.041		4.140		
50	M	5.693	5.690	4.159		90.35	T	4.032		4.147		
51	M	5.681	5.680	4.169		90.22	T	4.028		4.146		
52	T	4.009		4.158			T	4.030		4.145		

shown in Fig. 6, namely, PZT with $x=0.47$ described in Ref. 3. For this composition, it was found that the tetragonal phase transformed to a rhombohedral phase at low temperatures, while at intermediate temperatures, a poorly defined region of coexisting phases was observed. On the other hand, the data for the $x=0.47$ sample studied in the present work shows, as described above, characteristics similar to those of $x=0.46$ or $x=0.48$; in particular, the existence of a monoclinic phase at low temperatures and no traces of a rhombohedral phase. It is noteworthy that an analysis of the peak widths in the cubic phase shows clear differences in the microstructure of the two sets of samples. The microstrain $\Delta d/d$, and crystallite size of the samples used in the present study are estimated to be about 3×10^{-4} and $1 \mu\text{m}$, respectively.⁴ A similar analysis for the $x=0.47$ sample described in Ref. 3 yields values of 5×10^{-4} and $0.2 \mu\text{m}$, respectively. One possible explanation is that because of the smaller crystallite size in the ceramic samples in Ref. 3, the inhomogeneous internal stress "prematurely" induces the tetragonal-rhombohedral phase transitions and inhibits the formation of the intermediate monoclinic phase. With a larger crystallite size, the internal strain is more easily relieved,^{40,41} presumably through the formation of non-180° domains,⁴² and the monoclinic phase is stabilized.

It is interesting to address the question of why the monoclinic phase was not observed in any of the previous studies. One important factor is the very superior resolution of synchrotron powder-diffraction equipment compared to that of laboratory equipment. A second is the presence of wide regions of rhombohedral-tetragonal phase coexistence in many of these studies, due to compositional fluctuations and/or small grain sizes,^{8,43-46} which would obscure the evidence for monoclinic symmetry. For samples prepared by conventional "dry" solid-state techniques, a much narrower range of compositional fluctuations and large grain size can be achieved by the use of a final heat treatment at 1250 °C, as in the present case, or by the use of "semiwet" methods of

synthesis and lower firing temperatures.⁴⁷⁻⁵⁰ However, perhaps the key element for clarifying the phase diagram is to carry out the structural studies at low temperatures, as clearly demonstrated in Fig. 6.

Very recently, experiments on poled samples by Guo *et al.*⁵¹ have further underlined the crucial role of the monoclinic phase in PZT. These experiments have revealed that poling induces the monoclinic distortion. The application of an electric field causes the rotation of the polar axis and an associated monoclinic distortion, which is retained after the field is removed. These features are shown to be the origin of the high piezoelectric response in PZT. It is observed that for rhombohedral PZT close to the MPB, the region of stability of the monoclinic phase increases after an electric field is applied. The field-induced monoclinic phase is found to be considerably wider on the Zr side of the phase diagram, at room temperature, extending at least to a Ti content of $x=0.42$. These experiments⁵¹ validate the microscopic model for the MPB proposed in Ref. 4; i.e., the application of a field would favor one of the local sites, which corresponds exactly to the observed monoclinic distortion (see the dashed arrow in the top left plot of Fig. 1), and induces the monoclinic phase (see the top right plot in Fig. 1). Further studies of the poled samples are in progress, and will be reported in a subsequent publication.

ACKNOWLEDGMENTS

The authors are especially grateful to J. A. Gonzalo and S.-E. Park, who were collaborators in the initial stages of this investigation, for their advice and encouragement. We also wish to thank L. Bellaiche, T. Egami, E. Salje, B. A. Tuttle, D. Vanderbilt, and T. Vogt for very helpful discussions. Financial support by the U.S. Department of Energy, Division of Materials Sciences (Contract No. DE-AC02-98CH10886) and ONR (MURI Project No. N00014-96-1-1173) is also acknowledged.

*Corresponding author. On leave from U. Autonoma de Madrid, Spain. Email address: noheda@bnl.gov

¹B. Jaffe, W.R. Cook, and H. Jaffe, *Piezoelectric Ceramics* (Academic Press, London, 1971).

²B. Noheda, D.E. Cox, G. Shirane, J.A. Gonzalo, L.E. Cross, and S.-E. Park, *Appl. Phys. Lett.* **74**, 2059 (1999).

³B. Noheda, J.A. Gonzalo, A.C. Caballero, C. Moure, D.E. Cox, and G. Shirane, *Ferroelectrics* **237**, 237 (2000).

⁴B. Noheda, J.A. Gonzalo, L.E. Cross, R. Guo, S.-E. Park, D.E. Cox, and G. Shirane, *Phys. Rev. B* **61**, 8687 (2000).

⁵G. Shirane and K. Suzuki, *J. Phys. Soc. Jpn.* **7**, 333 (1952).

⁶E. Sawaguchi, *J. Phys. Soc. Jpn.* **8**, 615 (1953).

⁷L. Hanh, K. Uchino, and S. Nomura, *Jpn. J. Appl. Phys.* **17**, 637 (1978).

⁸W. Cao and L.E. Cross, *Phys. Rev. B* **47**, 4825 (1993).

⁹S.K. Mishra, D. Pandey, and A. Singh, *Appl. Phys. Lett.* **69**, 1707 (1996).

¹⁰X.-h Du, J. Zheng, U. Belegundu, and K. Uchino, *Appl. Phys. Lett.* **72**, 2421 (1998).

¹¹S. Teslic, T. Egami, and D. Viehland, *J. Phys. Chem. Solids* **57**,

1537 (1996); *Ferroelectrics* **194**, 271 (1997).

¹²J. Ricote, D.L. Corker, R.W. Whatmore, S.A. Impey, A.M. Glazer, J. Dec, and K. Roleder, *J. Phys.: Condens. Matter* **10**, 1767 (1998).

¹³D.L. Corker, A.M. Glazer, R.W. Whatmore, A. Stallard, and F. Fauth, *J. Phys.: Condens. Matter* **10**, 6251 (1998).

¹⁴R.E. Cohen, *Nature (London)* **358**, 136 (1992).

¹⁵R.D. King-Smith and D. Vanderbilt, *Phys. Rev. B* **49**, 5828 (1994).

¹⁶W. Zhong, D. Vanderbilt, and K.M. Rabe, *Phys. Rev. Lett.* **73**, 1861 (1994); *Phys. Rev. B* **52**, 6301 (1995).

¹⁷A. Garcia and D. Vanderbilt, *Phys. Rev. B* **54**, 3817 (1996).

¹⁸A. Garcia and D. Vanderbilt, *Appl. Phys. Lett.* **72**, 2981 (1998).

¹⁹U.V. Waghmare and K.M. Rabe, *Phys. Rev. B* **55**, 6161 (1997).

²⁰K.M. Rabe and E. Cockayne, in *First-Principles Calculations for Ferroelectrics*, edited by Ronald E. Cohen, AIP Conf. Proc. No. 436 (AIP, Woodbury, NY, 1998), p. 61.

²¹Ph. Ghosez, E. Cockayne, U.V. Waghmare, and K.M. Rabe, *Phys. Rev. B* **60**, 836 (1999).

²²L. Bellaiche, J. Padilla, and D. Vanderbilt, *Phys. Rev. B* **59**, 1834 (1999).

- ²³G. Saghi-Szabo, R.E. Cohen, and H. Krakauer, *Phys. Rev. B* **59**, 12 771 (1999).
- ²⁴B.P. Burton and E. Cockayne, *Phys. Rev. B* **60**, R12 542 (1999).
- ²⁵H. Fu and R. Cohen, *Nature (London)* **403**, 281 (2000).
- ²⁶L. Bellaiche and D. Vanderbilt, *Phys. Rev. Lett.* **83**, 1347 (1999).
- ²⁷L. Bellaiche, A. Garcia, and D. Vanderbilt, *Phys. Rev. Lett.* **84**, 5427 (2000).
- ²⁸L.W. Finger, D.E. Cox, and A.P. Jephcoat, *J. Appl. Crystallogr.* **27**, 892 (1994).
- ²⁹A.M. Glazer and S.A. Mabud, *Acta Crystallogr., Sect. B: Struct. Crystallogr. Cryst. Chem.* **34**, 1065 (1978).
- ³⁰R.J. Nemes and W.F. Kuhs, *Solid State Commun.* **54**, 721 (1985).
- ³¹G. Shirane, R. Pepinski, and B.C. Frazer, *Acta Crystallogr.* **9**, 131 (1956).
- ³²G.A. Rosetti, Jr. and A. Navrotsky, *J. Solid State Chem.* **144**, 188 (1999).
- ³³A.I. Ustinov, J.-C. Niepce, C. Valot, L.A. Olikhovska, and F. Bernard, *Mater. Sci. Forum* **321-324**, 109 (2000).
- ³⁴H.M. Barnett, *J. Appl. Phys.* **33**, 1606 (1962).
- ³⁵C. Michel, J.-M. Moreau, G.D. Achenbach, R. Gerson, and W.J. James, *Solid State Commun.* **7**, 865 (1969).
- ³⁶A.M. Glazer, S.A. Mabud, and R. Clarke, *Acta Crystallogr., Sect. B: Struct. Crystallogr. Cryst. Chem.* **34**, 1060 (1978).
- ³⁷A. Amin, R.E. Newnham, L.E. Cross, and D.E. Cox, *J. Solid State Chem.* **37**, 248 (1981).
- ³⁸The rhombohedral unit cell with lattice parameters a and α , can be expressed in terms of a monoclinic unit cell as follows: $a_m = 2a \cos(\alpha/2)$, $b_m = 2a \sin(\alpha/2)$, $c_m = a$ and $\beta = 180^\circ - \arccos[\{1 - 2 \sin^2(\alpha/2)\}/\cos(\alpha/2)]$.
- ³⁹A.G. Souza Filho, K.C.V. Lima, A.P. Ayala, I. Guedes, P.T.C. Freire, J. Mendes Filho, E.B. Araujo, and J.A. Eiras, *Phys. Rev. B* **61**, 14 283 (2000).
- ⁴⁰W.R. Buessem, L.E. Cross, and A.K. Goswami, *J. Am. Ceram. Soc.* **49**, 33 (1966).
- ⁴¹B. Tuttle and D.A. Payne, *Ferroelectrics* **37**, 603 (1981).
- ⁴²R.W. Cahn, *Adv. Phys.* **3**, 363 (1954).
- ⁴³P. Ari-Gur and L. Benguigui, *J. Phys. D* **8**, 1856 (1975).
- ⁴⁴J.C. Fernandes, D.A. Hall, M.R. Cockburn, and G.N. Greaves, *Nucl. Instrum. Methods Phys. Res. B* **97**, 137 (1995).
- ⁴⁵A.P. Wilkinson, J. Xu, S. Pattanaik, and S.J.L. Billinge, *Chem. Mater.* **10**, 3611 (1998).
- ⁴⁶E.R. Leite, M. Cerqueira, L.A. Perazoli, R.S. Nasar, and E. Longo, *J. Am. Ceram. Soc.* **79**, 1563 (1996).
- ⁴⁷K. Kakegawa, J. Mohri, T. Takahashi, H. Yamamura, and S. Shirasaki, *Solid State Commun.* **24**, 769 (1977).
- ⁴⁸K. Kakegawa, J. Mohri, S. Shirasaki, and K. Takahashi, *J. Am. Ceram. Soc.* **65**, 515 (1982).
- ⁴⁹A.P. Singh, S.K. Mishra, D. Pandey, Ch.D. Prasad, and R. Lal, *J. Mater. Sci.* **28**, 5050 (1993).
- ⁵⁰A. Cüneyt Taş, *J. Am. Ceram. Soc.* **82**, 1582 (1999).
- ⁵¹R. Guo, L.E. Cross, S.-E. Park, B. Noheda, D.E. Cox, and G. Shirane, *Phys. Rev. Lett.* **84**, 5423 (2000).

APPENDIX 9

Origin of the high piezoelectric response in $\text{PbZr}_{1-x}\text{Ti}_x\text{O}_3$

R. Guo¹, L.E. Cross¹, S.-E. Park¹, B. Noheda^{2,3}, D.E. Cox³, and G. Shirane³

¹Mat. Res. Lab., Pennsylvania State University, PA 16802-4800

²Universidad Autonoma de Madrid, 28049-Madrid, Spain

³Brookhaven National Laboratory, Upton, NY 11973-5000

High resolution x-ray powder diffraction measurements on poled $\text{PbZr}_{1-x}\text{Ti}_x\text{O}_3$ (PZT) ceramic samples close to the rhombohedral-tetragonal phase boundary (the so-called morphotropic phase boundary, MPB) have shown that for both rhombohedral and tetragonal compositions, the piezoelectric elongation of the unit cell does not occur along the polar directions but along those directions associated with the monoclinic distortion. This work provides the first direct evidence for the origin of the very high piezoelectricity in PZT.

The ferroelectric $\text{PbZr}_{1-x}\text{Ti}_x\text{O}_3$ (PZT) system has been extensively studied because of its interesting physical properties close to the morphotropic phase boundary (MPB), the nearly vertical phase boundary between the tetragonal and rhombohedral regions of the phase diagram close to $x = 0.50$, where the material exhibits outstanding electromechanical properties [1]. The existence of directional behavior for the dielectric and piezoelectric response functions in the PZT system has been predicted by Du *et al.* [2], [3] from a phenomenological approach [4]. These authors showed that for rhombohedral compositions the piezoelectric response should be larger for crystals oriented along the [001] direction than for those oriented along the [111] direction. Experimental confirmation of this prediction was obtained [5,6,7] for the related ferroelectric relaxor system $\text{PbZn}_{1/3}\text{Nb}_{2/3}\text{-PbTiO}_3$ (PZN-PT), which has a rhombohedral-to-tetragonal MPB similar to that of PZT, but it has not been possible to verify similar behavior in PZT due to the lack of single crystals. Furthermore, *ab initio* calculations based on the assumption of tetragonal symmetry, that have been successful for calculating the piezoelectric properties of pure PbTiO_3 [8,9,10,11], were unable to account for the much larger piezoelectric response in PZT compositions close to the MPB. Thus, it is clear that the current theoretical models lack some ingredient which is crucial to understanding the striking piezoelectric behavior of PZT.

The stable monoclinic phase recently discovered in the ferroelectric $\text{PbZr}_{1-x}\text{Ti}_x\text{O}_3$ system (PZT) close to the MPB [12], provides a new perspective to view the rhombohedral-to-tetragonal phase transformation in PZT and in other systems with similar phase boundaries as PMN-PT and PZN-PT [13]. This phase plays a key role in explaining the high piezoelectric response in PZT and, very likely, in other systems with similar MPBs. The polar axis of this monoclinic phase is contained in the (110) plane along a direction between that of the tetragonal and rhombohedral polar axes [12]. An investigation of several compositions around the MPB has suggested a modification of the PZT phase diagram [1] as shown in Fig. 1(top right) [13].

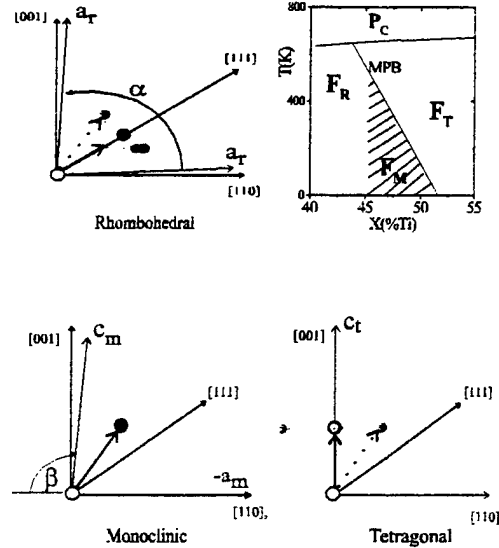


FIG. 1. Schematic view of the PZT phase diagram in the vicinity of the MPB showing the monoclinic region (top right). A projection of the rhombohedral (top left), monoclinic (bottom left) and tetragonal (bottom right) unit cells on the pseudo-cubic (110) plane is sketched. The solid circles represent the observed lead shifts with respect to the ideal cubic structure and the grey circles the locally-disordered shifts, four in the tetragonal phase and three in the rhombohedral phase. The heavy dashed arrows represent the freezing-out of one of these shifts to give the observed long-range monoclinic structure [13].

A local order different from the long-range order in the rhombohedral and tetragonal phases has been proposed from a detailed structural data analysis. Based on this, a model has been constructed in which the monoclinic distortion (Fig. 1, bottom-left) can be viewed as either a condensation along one of the $\langle 110 \rangle$ directions of the local displacements present in the tetragonal phase [13] (Fig. 1 bottom-right), or as a condensation of the local displacements along one of the $\langle 100 \rangle$ directions present in the rhombohedral phase [14] (Fig. 1 top-left). The monoclinic structure, therefore, represents a bridge between

these two phases and provides a microscopic picture of the MPB region [13].

In the present work experimental evidence of an enhanced elongation along [001] for rhombohedral PZT and along [101] for tetragonal PZT ceramic disks revealed by high-resolution x-ray diffraction measurements during and after the application of an electric field is presented. This experiment was originally designed to address the question whether poling in the MPB region would simply change the domain population in the ferroelectric material, or whether it would induce a permanent change in the unit cell. As shown below, from measurements of selected peaks in the diffraction patterns, a series of changes in the peak profiles from the differently oriented grains are revealed which provide key information about the PZT problem.

$\text{PbZr}_{1-x}\text{Ti}_x\text{O}_3$ ceramic samples with $x = 0.42$, 0.45 and 0.48 were prepared by conventional solid-state reaction techniques using high purity (better than 99.9%) lead carbonate, zirconium oxide and titanium oxide as starting compounds. Powders were calcined at 900°C for six hours and recalcined as appropriate. After milling, sieving, and the addition of the binder, the pellets were formed by uniaxial cold pressing. After burnout of the binder, the pellets were sintered at 1250°C in a covered crucible for 2 hours, and furnace-cooled. During sintering, PbZrO_3 was used as a lead source in the crucible to minimize volatilization of lead. The sintered ceramic samples of about 1 cm diameter were ground to give parallel plates of 1 mm thickness, and polished with $1\ \mu\text{m}$ diamond paste to a smooth surface finish. To eliminate strains caused by grinding and polishing, samples were annealed in air at 550°C for five hours and then slow-cooled. Silver electrodes were applied to both surfaces of the annealed ceramic samples and air-dried. Disks of all compositions were poled under a DC field of $20\ \text{kV/cm}$ at 125°C for 10 minutes and then field-cooled to near room temperature. The electrodes were then removed chemically from the $x = 0.42$ and 0.48 samples. For the $x = 0.45$ sample (which had been ground to a smaller thickness, about $0.3\ \text{mm}$), the electrodes were retained, so that diffraction measurements could be carried out under an electric field.

Several sets of high-resolution synchrotron x-ray powder diffraction measurements were made at beam line X7A at the Brookhaven National Synchrotron Light Source. A $\text{Ge}(111)$ double-crystal monochromator was used in combination with a $\text{Ge}(220)$ analyser, with a wavelength of about $0.8\ \text{\AA}$ in each case. In this configuration, the instrumental resolution, $\Delta 2\theta$, is an order-of-magnitude better than that of a conventional laboratory instrument (better than 0.01° in the 2θ region $0-30^\circ$). The poled and unpoled pellets were mounted in symmetric reflection geometry and scans made over selected peaks in the low-angle region of the pattern. It should be noted that since lead is strongly absorbing, the penetra-

tion depth below the surface of the pellet at $2\theta = 20^\circ$ is only about $2\ \mu\text{m}$. In the case of the $x = 0.45$ sample, the diffraction measurements were carried out with an electric field applied in-situ via the silver electrodes.

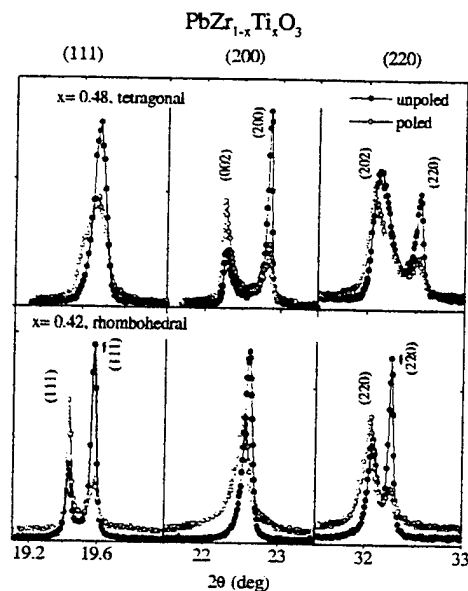


FIG. 2. (Color) Comparison of (111), (200) and (220) pseudo-cubic reflections for the $x = 0.48$ (tetragonal), and $x = 0.42$ (rhombohedral) PZT compositions before and after poling

Powder diffraction measurements on a flat plate in symmetric reflection, in which both the incident and the diffracted wave vectors are at the same angle, θ , with the sample plate, ensures that the scattering vectors are perpendicular to the sample surface. Thus only crystallites with their scattering vector parallel to the applied electric field are sampled. Scans over selected regions of the diffractogram, containing the (111), (200) and (220) pseudo-cubic reflections, are plotted in Fig. 2 for poled and unpoled PZT samples with the compositions $x = 0.48$ (top) and $x = 0.42$ (bottom), which are in the tetragonal and rhombohedral region of the phase diagram, respectively. The diffraction profiles of the poled and unpoled samples show very distinctive features. For the tetragonal composition (top), the (200) pseudo-cubic reflection (center) shows a large increase in the tetragonal $(002)/(200)$ intensity ratio after poling due to the change in the domain population, which is also reflected in the increased $(202)/(220)$ intensity ratio in the right side of the figure. In the rhombohedral composition with $x = 0.42$ (bottom of Fig. 2), the expected change in the domain population can be observed from the change of the intensity ratios of the rhombohedral (111) and $(11\bar{1})$ reflections (left side) and the (220) and $(2\bar{2}0)$ reflections

(right side).

In addition to the intensity changes, the diffraction patterns of the poled samples show explicit changes in the peak positions with respect to the unpoled samples, corresponding to specific alterations in the unit cell dimensions. In the rhombohedral case ($x=0.42$), the electric field produces no shift in the (111) peak position (see bottom-left plot in Fig.2), indicating the absence of any elongation along the polar directions after the application of the field. In contrast, the poling does produce a notable shift of the (001) reflections (center plot), which corresponds to a very significant change of d-spacing, with $\Delta d/d = 0.32\%$, $\Delta d/d$ being defined as $(d_p - d_u)/d_u$, where d_p and d_u are the d-spacings of the poled and unpoled samples, respectively. This provides experimental confirmation of the behavior predicted by Du *et al.* [3] for rhombohedral PZT, as mentioned above. The induced change in the dimensions of the unit cell is also reflected as a smaller shift in the (202) reflection (right side plot), corresponding to a $\Delta d/d$ along [101] of 0.12%.

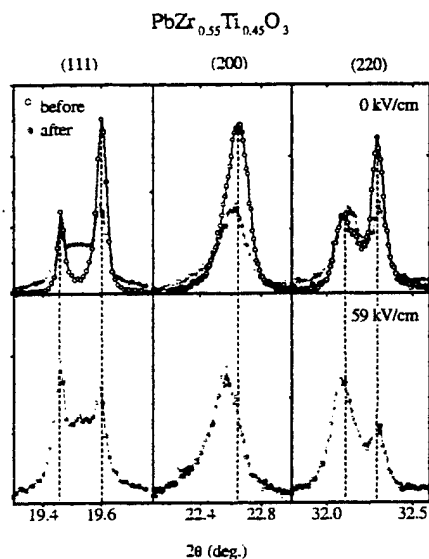


FIG. 3. (Color), (111), (200) and (220) pseudocubic reflections for PZT with $x=0.45$ measured on an unpoled sample (open circles) and on a similar sample after the application and removal of a field of 59 kV/cm at room temperature (solid circles) are plotted in the upper part of the figure. The scattered intensity at $2\theta = 19.52^\circ$ from the second sample corresponds to the (111) reflection from the silver electrode. Measurements on the latter sample under an electric field of 59 kV/cm applied *in situ* are plotted in the lower part of the figure.

In the tetragonal case for $x=0.48$ (top of Fig.2), there is no peak shift observed along the polar [001] direction (center plot), but the (202) and the (111) reflections exhibit striking shifts (right and left sides, respectively).

Furthermore, this composition, which at room temperature is just at the monoclinic-tetragonal phase boundary, shows, after poling, a clear tendency towards monoclinic symmetry, in that the (111) and (202) reflections, already noticeably broadened in the unpoled sample and indicative of an incipient monoclinicity, are split after poling. These data clearly demonstrate, therefore, that whereas the changes induced in the unit cell after the application of an electric field do not increase either the rhombohedral or the tetragonal strains, a definite elongation is induced along those directions associated with the monoclinic distortion.

In addition to the measurements on the poled and unpoled samples, diffraction measurements were performed *in situ* on the rhombohedral PZT sample with $x=0.45$ as a function of applied electric field at room temperature. The results are shown in Fig.3 where the (111), (200) and (220) pseudo-cubic reflections are plotted with no field applied (top) and with an applied field of 59 kV/cm field (bottom). The top part of the figure also shows data taken after removal of the field. As can be seen, measurements with the field applied show no shift along the polar [111] direction but, in contrast, there is a substantial shift along the [001] direction similar to that for the poled sample with $x=0.42$ shown in Fig. 2, proving that the unit cell elongation induced by the application of a field during the poling process corresponds to the piezoelectric effect induced by the in-situ application of a field. Comparison of the two sets of data for $x=0.45$ before and after the application of the field shows that the poling effect of the electric field at room temperature is partially retained after the field is removed, although the poling is not as pronounced as for the $x=0.42$ sample in Fig. 2.

A quantification of the induced microstrain along the different directions has been made by measuring the peak shifts under fields of 31 and 59 kV/cm. In Fig. 4, $\Delta d/d$ is plotted *versus* the applied field, E , for the (200) and (111) reflections. These data show an approximately linear increase in $\Delta d/d$ for (200) with field, with $\Delta d/d = 0.30\%$ at 59 kV/cm, corresponding to a piezoelectric coefficient $d_{33} \approx 500$ pm/V, but essentially no change in the d-spacing for (111).

It is interesting to compare in Fig.4 the results of dilatometric measurements of the macroscopic linear elongation ($\Delta l/l$) on the same pellet, which must also reflect the effects of domain reorientation. At higher fields, this contribution diminishes and one could expect the $\Delta l/l$ vs. E curve to fall off between those for the [100] and [111] oriented grains, typical of the strain behaviour of polycrystalline ceramics [15]. Although such a trend is seen above 30 kV/cm, it is intriguing to note that below this value, the macroscopic behavior is essentially the same as the microscopic behavior for the (200) reflection.

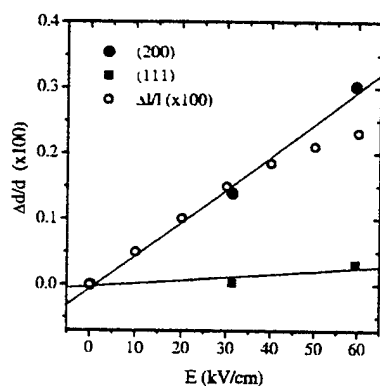


FIG. 4. Fractional change of d-spacing, $\Delta d/d$ for PZT with $x=0.45$ from the rhombohedral (200) and (111) reflections as a function of electric field (closed symbols). Dilatometric measurements of the macroscopic $\Delta l/l$ for the same pellet are also shown (open circles)

It is of interest to relate our observations to the more conventional description of piezoelectric effects in ceramics, in which the dielectric displacements would be attributed to tilts of the polar axis. What we actually observe in the diffraction experiment is an intrinsic monoclinic deformation of the unit cell as a consequence of the rotation of the polar axis in the monoclinic plane. However, large atomic displacements can only occur in compositions close to the MPB, and it is this feature which accounts for the sharp peak in the piezoelectric d constants for compositions close to 52:48 Zr/Ti [1].

We therefore conclude that the piezoelectric strain in PZT close to the morphotropic phase boundary, which produces such striking electromechanical properties, is not along the polar directions but along those directions associated with the monoclinic distortion. This work supports a model based on the existence of local monoclinic shifts superimposed on the rhombohedral and tetragonal displacements in PZT which has been proposed from a detailed structural analysis of tetragonal [13] and rhombohedral [14] PZT samples. Very recent first-principles calculations by L. Bellaiche et al. [16] have been able not only to reproduce the monoclinic phase but also to explain the high piezoelectric coefficients by taking into account rotations in the monoclinic plane.

As demonstrated above, these high resolution powder data provide key information to understanding the piezoelectric effect in PZT. In particular, they allow an accurate determination of the elongation of the unit cell along the direction of the electric field, although they give no information about the dimensional changes occurring along the perpendicular directions, which would give a more complete characterization of the new structure induced by the electric field. It is interesting to note that in the case of the related ferroelectric system PZN-PT, the availability of single crystals has allowed Durbin

et al. [7] to carry out diffraction experiments along similar lines at a laboratory x-ray source. Synchrotron x-ray experiments by the present authors are currently being undertaken on PZN-PT single crystals with Ti contents of 4.5 and 8% under an electric field, and also on other ceramic PZT samples. Preliminary results on samples with $x=0.46$ and 0.47 , which are monoclinic at room temperature, have already been obtained. In these cases, the changes of the powder profiles induced by poling are so drastic that further work is needed in order to achieve a proper interpretation.

We thank L. Bellaiche, A. M. Glazer, J.A. Gonzalo and K. Uchino for their stimulating discussions, B. Jones and E. Alberta for assisting in the sample preparation, and A. L. Langhorn for his invaluable technical support. Financial support by the U.S. Department of Energy under contract No. DE-AC02-98CH10886, and by ONR under project MURI (N00014-96-1-1173) is also acknowledged.

- [1] B. Jaffe, W.R. Cook, and H. Jaffe, *Piezoelectric Ceramics*, Academic Press, London (1971).
- [2] X-h Du, U. Belegundu, and K. Uchino, *Jpn. J. Appl. Phys.* **36**, 5580 (1997).
- [3] X-h Du, J. Zheng, U. Belegundu, and K. Uchino, *Appl. Phys. Lett.* **72**, 2421 (1998).
- [4] M. J. Haun, E. Furman, S-J. Jang, and L.E. Cross, *Ferroelectrics* **72**, 13(1989).
- [5] J. Kuwata, K. Uchino, and S. Nomura, *Jpn. J. Appl. Phys.* **21**, 1298(1982).
- [6] S-E. Park and T. R. Shrout, *J. Appl. Phys.* **82**, 1804 (1997).
- [7] M. K. Durbin, E.W. Jacobs, J.C. Hicks, and S.-E. Parks, *Appl. Phys. Lett.* **74**, 2848 (1999).
- [8] K.M. Rabe and E. Cockayne, in *First-Principles Calculations for Ferroelectrics: Fifth Williamsburg Workshop*, edited by R.E. Cohen (AIP, Woodbury, 1998), p. 61.
- [9] G. Saghi-Szabo, R.E. Cohen, and H. Krakauer, *Phys. Rev. Lett.* **80**, 4321 (1998).
- [10] G. Saghi-Szabo, R.E. Cohen, and H. Krakauer, *Phys. Rev. B* **59**, 12771 (1999).
- [11] L. Bellaiche and D. Vanderbilt, *Phys. Rev. Lett.* **83**, 1347 (1999).
- [12] B. Noheda, D.E. Cox, G. Shirane, J.A. Gonzalo, L.E. Cross, and S-E. Park, *Appl. Phys. Lett.* **74**, 2059 (1999).
- [13] B. Noheda, J. A. Gonzalo, L.E. Cross, R. Guo, S-E. Park, D.E. Cox, and G. Shirane, *Phys. Rev. B*, (01-April-2000) in press, e-print: cond-mat/9910066.
- [14] D.L. Corker, A.M. Glazer, R.W. Whatmore, A. Stallard, and F. Fauth, *J. Phys.:Condens. Matter* **10**, 6251 (1998).
- [15] S.-E. Park, T.R. Shrout, P. Bridenbaugh, J. Rottenberg, and G. Loiacono, *Ferroelectrics* **207**, 519 (1998).
- [16] L. Bellaiche, A. Garcia, and D. Vanderbilt. To be published.

APPENDIX 10

Nonlinear properties of lead zirconate–titanate piezoceramics

Wenhua Jiang

Materials Research Laboratory, The Pennsylvania State University, University Park, Pennsylvania 16802

Wenwu Cao^{a)}

Department of Mathematics, Materials Research Laboratory, The Pennsylvania State University, University Park, Pennsylvania 16802

(Received 6 July 2000; accepted for publication 22 September 2000)

Nonlinear properties of lead zirconate–titanate (PZT) piezoceramics are investigated using ultrasonic second harmonic generation technique. When a sinusoidal ultrasonic wave of frequency ω_0 is sent into a nonlinear material, the second harmonic wave with frequency $2\omega_0$ is generated. Through measuring the absolute amplitude of the fundamental (ω_0) and of the second harmonic ($2\omega_0$) waves, the ultrasonic nonlinearity parameter β can be determined, which involves certain combinations of the third-order elastic constants and piezoelectric coefficients. We report the measured nonlinear parameters for four types of doped PZT ceramics, PZT-4, PZT-5A, PZT-5H, and PZT-5H HD, which are widely used in practice. We found that the nonlinear parameter is much more sensitive than the linear parameter in responding to microstructural changes in piezoceramics. It could be used to distinguish unpoled samples from depoled samples, which are undistinguishable in terms of the linear parameters. © 2000 American Institute of Physics. [S0021-8979(01)02001-1]

I. INTRODUCTION

The lead zirconate–titanate (PZT) ceramics are widely used in ultrasonic transducers, resonators, sensors, ultrasonic motors, actuators, and many other electromechanical devices. Although their linear material properties have been well characterized, little has been reported on their nonlinear elastic properties. The knowledge on the nonlinear elastic properties of PZT materials is very important for devices operating at high field levels, such as many increasingly popular miniaturized piezoelectric devices, which are being driven way out of the linear regime. Under high field, nonlinear effects will have strong impact on device operations and must be taken into account, including frequency-amplitude effect, acoustic power saturation, waveform distortion, and higher harmonic generation. These nonlinear effects can greatly degrade the performance of many electromechanical devices if not being handled carefully. On the other hand, nonlinear acoustic signal processing devices¹ and ultrasonic imaging techniques can employ nonlinear effects as an advantage.

Literature concerning the nonlinear elastic properties of PZT piezoceramics is scarce. Beige measured the nonlinear elastic compliance s_{333}^E and the nonlinear dielectric coefficient ϵ_{333}^T as well as their temperature dependence for modified lead zirconate–titanate ceramics (type Piezolan S_2 , L , T_m), by means of resonance method.² It was found that the nonlinear coefficients depend strongly on the microstructures of the materials. Na and Breazeale reported the third-order elastic constants c_{111}^E and c_{333}^D of PZT ceramics types K1 and S1 by means of ultrasonic second harmonic generation technique.³ They reported that the nonlinear coefficients could change several orders of magnitude when the tempera-

ture varies from room temperature to temperatures above the Curie temperature.

Our present work is devoted to study the nonlinear properties of the popular PZT ceramics, PZT-4, PZT-5A, conventional PZT-5H (Valpey–Fisher, 75 South St. Hopkinton, MA 01748), and high density PZT-5H HD (Motorola) at room temperature. By means of the ultrasonic second harmonic generation technique, the third-order elastic constants c_{111}^E and c_{333}^D for poled samples and c_{111} for the unpoled and depoled samples are measured. Distinctive nonlinear coefficients were found among these samples.

This article is structured as the following: In Sec. II, a general description will be given to discuss the propagation of ultrasonic waves in poled nonlinear piezoelectric ceramics; in Sec. III the experimental setup and method are described; Sec. IV reports the experimental results together with brief discussions; and Sec. V gives the summary and conclusions.

II. ULTRASONIC SECOND HARMONIC GENERATION IN A PIEZOELECTRIC MATERIAL

Although most materials are assumed to be linear, solid materials are inherently nonlinear, and these nonlinearities will cause anharmonic effects. It was found that ignoring anharmonic terms of phonon vibrations could result in failure of the interpretation of many static and transport properties of solids, such as thermal expansion, temperature dependence of elastic constants, and thermal conductivity.⁴ Owing to the anharmonicity, stored energy expansion of a piezoelectric crystal in terms of the elastic strain and the electric field will deviate from a parabolic formulation. Consequently, linear piezoelectricity and elasticity must be modi-

^{a)}Electronic mail: cao@math.psu.edu

fied, particularly at high field and strain levels. When the energy expansion includes cubic terms of the strain and electric field, bilinear constitutive relations, and bilinear electroacoustic equations are obtained. For such a nonlinear medium, if an initially sinusoidal ultrasonic wave of finite amplitude propagates through it, the waveform will be distorted and a second harmonic wave will be generated.

McMahon had discussed ultrasonic second harmonic generation in piezoelectric crystals with $3m$ symmetry,⁵ and Nelson had provided a description for three-field interactions in more general dielectric materials.⁶ It can be verified that the quasistatic bilinear electromechanical equations can be written, in terms of the material coordinates, as:

$$\rho_0 \ddot{u}_i = (P_{ij}^L + P_{ij}^{NL})_{,j} \quad (i, j = 1, 2, 3), \quad (1a)$$

$$D_{k,k}^L + D_{k,k}^{NL} = 0 \quad (i, j = 1, 2, 3). \quad (1b)$$

Here the bilinear constitutive relations are

$$P_{ij} = P_{ij}^L + P_{ij}^{NL} = c_{ijkl}^E u_{k,l} - e_{kij} E_k + \frac{1}{2} (c_{ijklmn}^E + \delta_{ik} c_{ijlmn}^E + \delta_{il} c_{ijkmn}^E + \delta_{im} c_{ijnkl}^E + \delta_{km} c_{ijln}^E) u_{k,l} u_{m,n} - (e_{kijmn} + \delta_{im} e_{knj}) u_{m,n} E_k - \frac{1}{2} m_{kl ij} E_k E_l, \quad (2b)$$

$$D_k = D_k^L + D_k^{NL} = \epsilon_{kl} E_l + e_{klm} u_{l,m} + \frac{1}{2} (e_{klmij} + \delta_{li} e_{kmj}) \times u_{l,m} u_{i,j} + m_{klmn} E_l u_{m,n} + \epsilon_{klm} E_l E_m. \quad (2d)$$

The relation of finite strain η_{ij} and particle displacement gradient $\eta_{ij} = \frac{1}{2}(u_{i,j} + u_{j,i} + u_{k,i} u_{k,j})$ is employed in deriving the equations. In Eqs. (1) and (2) the dot above a letter stands for material time derivative, the indices after the comma in the subscript stand for material spatial derivatives, δ_{ij} is the Kronecker delta, P_{ij} is the Piola-Chirrhoff stress tensor, D_k is material electric displacement, ρ_0 is the mass density of the material in unstrained state, c_{ijkl} , e_{ijk} , and ϵ_{ij} are the second-order elastic constants, piezoelectric coefficients and dielectric constants, c_{ijklmn} , e_{ijklm} , and ϵ_{ijk} are the third-order elastic constants, nonlinear piezoelectric coefficients and nonlinear dielectric constants, and m_{ijkl} are the electrostriction constants.

Generally speaking, Eq. (1) can be solved subject to appropriate boundary conditions for any wave propagation direction in the crystal. Here we are only interested in those pure-mode longitudinal waves, which we have also measured experimentally. These longitudinal waves will couple to the piezoelectric effect if the particle displacement direction coincides with the polarization direction. For an anisotropic crystal, the directions allowing pure mode longitudinal wave to propagate are limited.⁷ Poled PZT ceramics have a conic ∞m symmetry, which can be treated as $6mm$ symmetry while deriving the differential equations. Pure longitudinal modes exist in the X_3 and X_1 directions (X_3 is the poling direction) for such systems.⁷ The longitudinal wave propagating along X_1 does not couple to the piezoelectric effect. Hence, its nonlinear behavior can be described by the equations developed for the nonpiezoelectric solid medium.⁸ The longitudinal wave along the X_3 direction is a piezoelectric stiffened wave, and the piezoelectric and dielectric nonlin-

earities will also contribute to the ultrasonic second harmonic wave generation,⁵ which results in effective nonlinear constants as defined below.

For a pure-mode longitudinal wave along X_3 , Eq. (1) can be simplified to:

$$\rho_0 \ddot{u}_3 = P_{33,3}, \quad (3a)$$

$$D_{3,3} = 0, \quad (3b)$$

where

$$P_{33} = c_{33}^E u_{3,3} - e_{33} E_3 + \frac{1}{2} (c_{333}^E + 3c_{33}^E) u_{3,3}^2 - \frac{1}{2} m_{33} E_3^2 - (e_{33} + e_{333}) u_{3,3} E_3, \quad (4a)$$

$$D_3 = \epsilon_{33} E_3 + e_{33} u_{3,3} + \frac{1}{2} \epsilon_{333} E_3^2 + m_{33} E_3 u_{3,3} + \frac{1}{2} (e_{33} + e_{333}) u_{3,3}^2. \quad (4b)$$

Substituting Eq. (4) into (3) yields

$$\rho_0 \ddot{u}_3 = c_{33}^E u_{3,33} - e_{33} E_{3,3} + (c_{333}^E + 3c_{33}^E) u_{3,3} u_{3,33} - m_{33} E_3 E_{3,3} - (e_{33} + e_{333}) (u_{3,3} E_{3,3} + u_{3,33} E_3), \quad (5a)$$

$$\epsilon_{33} E_{3,3} + e_{33} u_{3,33} + \epsilon_{333} E_3 E_{3,3} + m_{33} (E_{3,3} u_{3,3} + E_3 u_{3,33}) + (e_{33} + e_{333}) u_{3,3} u_{3,33} = 0. \quad (5b)$$

Because the nonlinear effect is generally much smaller compared to the linear effect, it may be considered as a perturbation to the linear effects and we can use the successive approximation technique to solve Eq. (5). Let us assume

$$u_3 = \lambda u_3^{(0)} + \lambda^2 u_3^{(1)} + \dots, \quad (6a)$$

$$E_3 = \lambda E_3^{(0)} + \lambda^2 E_3^{(1)} + \dots, \quad (6b)$$

where λ is a parameter less than one, which indicates the order of magnitude of the successive terms in Eq. (6). The terms higher than λ^2 are ignored since we only deal with the quadratic nonlinearity and the third order nonlinear constants. Substituting Eq. (6) into Eq. (5) and equating the terms of the same order in λ , we can obtain, respectively, the equations for different orders of the successive approximations in Eq. (6). Among them the first order correction equation for a piezoelectric stiffened longitudinal wave can be written as:

$$\rho_0 \ddot{u}_3^{(1)} - K_2 u_{3,33}^{(1)} = (K_3 + 3K_2) u_{3,3}^{(0)} u_{3,33}^{(0)}. \quad (7)$$

Equation (7) has the same form as that of the nonpiezoelectric longitudinal wave⁸ except the second order coefficient K_2 has been redefined as

$$K_2 = c_{33}^D = c_{33}^E + \frac{e_{33}^2}{\epsilon_{33}}, \quad (8)$$

and the third order coefficient K_3 is redefined as

$$K_3 = c_{333}^D = c_{333}^E + \epsilon_{333} \left(\frac{e_{33}}{\epsilon_{33}} \right)^3 - 3m_{33} \left(\frac{e_{33}}{\epsilon_{33}} \right)^2 + 3e_{333} \left(\frac{e_{33}}{\epsilon_{33}} \right). \quad (9)$$

Since the zeroth order equation is simply the linear piezoelectric stiffened wave equation, $u_3^{(0)}$ has the general wave solution:

$$u_3^{(0)} = A_1 \sin(\omega t - kz). \quad (10)$$

Here z is the coordinate along the wave propagation direction. Substituting Eq. (10) into Eq. (7) leads to the second harmonic solution:

$$u_3^{(1)} = A_2 \cos 2(\omega t - kz) = \frac{1}{8} \beta k^2 z A_1^2 \cos 2(\omega t - kz), \quad (11)$$

which is the first order correction to the linear solution. The solution (11) satisfies the boundary condition $u_3^{(1)} = 0$ at $z = 0$. In Eqs. (10) and (11), A_1 and A_2 are amplitudes of the fundamental and second harmonic waves, respectively, ω is the angular frequency, $k = (\omega/v)$ is the wave number and v is the wave velocity given by

$$v = \sqrt{\frac{K_2}{\rho_0}}, \quad (12)$$

β is the nonlinearity parameter defined as

$$\beta = -\frac{3K_2 + K_3}{K_2}. \quad (13)$$

It can be seen from Eq. (11) that the amplitude of the second harmonic wave (degree of waveform distortion for the traveling wave) is proportional to β , which is directly related to Gruneisen parameter of materials⁸ and is a measure of the material nonlinearity.

III. EXPERIMENTAL DETERMINATION OF NONLINEARITY PARAMETER β

From Eq. (11), if the amplitudes of the fundamental and the second harmonic waves A_1 and A_2 are known, the nonlinearity parameter β can be calculated from the formula:

$$\beta = \frac{8}{k^2 L} \frac{A_2}{A_1^2}, \quad (14)$$

where L is the distance of wave propagation or sample length. Once the β is determined, K_3 can be calculated from Eq. (13) since K_2 has been measured. Generally speaking, K_2 and K_3 are associated with different combinations of the second- and third-order elastic constants, respectively. For different wave propagation directions in PZT materials, K_2 and K_3 are listed in Table I. Note: poled PZT ceramic has a conic symmetry of ∞m , which is equivalent to a $6mm$ system when calculating the independent elastic constants,⁹ while the unpoled and depoled PZT ceramic have isotropic symmetry so that K_2 and K_3 in Table I are equal to c_{11} and c_{111} , respectively.

TABLE I. Directions allowing pure mode longitudinal wave and the corresponding second- and third-order elastic constants of materials with $6mm$ and ∞m symmetries.

K parameters	Z direction	X direction*
K_2	c_{33}^D	c_{11}^E
K_3	c_{333}^D	c_{111}^E

*For isotropic materials (e.g., unpoled and depoled PZT ceramics), there is no difference between the elastic constants under constant electric displacement D and constant electric field E , the superscript E is therefore ignored in most literatures.

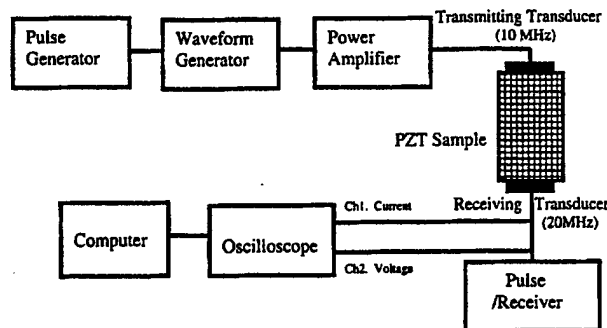


FIG. 1. Experimental setup for the second harmonic measurements.

The determination of β by the second harmonic generation technique needs to measure the absolute amplitude of the first and second harmonic waves. The existing absolute amplitude measurement methods are: (1) capacitive detector,⁸ (2) contact transducer,¹⁰ and (3) optic interferometer.¹¹ PZT ceramics are fairly lossy materials due to the existence of porosity. They exhibit large ultrasonic attenuation at higher frequencies.¹² On the other hand, using lower working frequencies will result in an increase of the sample size for obtaining a reasonable signal to noise ratio since the amplitude of the second harmonic wave is proportional to the propagation distance and the inverse of wavelength square. Considering all these factors, the contact transducer method was chosen for our experiments. Comparing the capacitive detector and optic interferometer, the contact transducer has higher sensitivity since a narrower band receiver was used. In our experiments, either 5 or 10 MHz is chosen as the fundamental frequency so that the corresponding second harmonic frequency is either 10 or 20 MHz. The experimental setup is schematically shown in Fig. 1. A toneburst signal from an arbitrary waveform generator (AWG 2021, Tektronix) is fed into a power amplifier (LogiMetrics). The output of the amplifier is applied to the transmit transducer (5 or 10 MHz) and the acoustic wave arriving at the end of the sample is detected by a receive transducer (10 or 20 MHz).

In order to obtain the absolute amplitude of the fundamental and second harmonic waves, the receive transducer must be calibrated. We have followed the calibration prin-

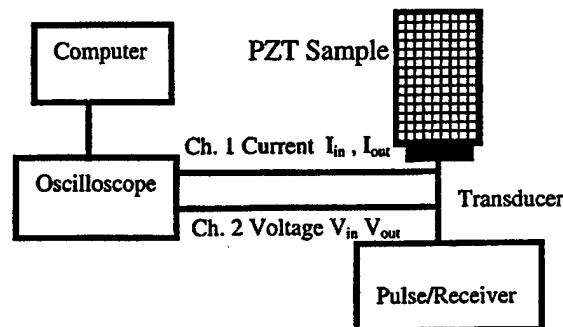


FIG. 2. Illustration of the calibration procedure of the receive transducer by the pulse-echo technique.

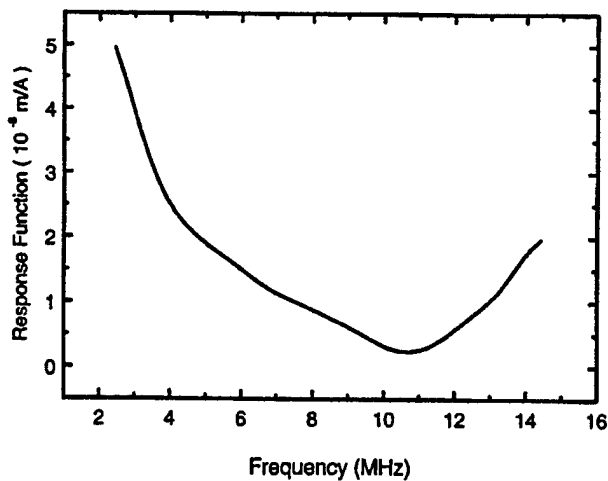


FIG. 3. Typical response function of the receive transducer.

ciple described in Ref. 10. As shown in Fig. 2, before bonding the transmit transducer to the sample, an electric pulse from a DPR35 pulser/receiver is applied to the receive transducer. Then, the current I_{in} , voltage V_{in} applied to the transducer as well as the current I_{out} , voltage V_{out} from the first back wall echo are recorded by a digital oscilloscope (Tek TDS 460 A). The data are then transferred to a PC computer where FFT of all four signals is performed. Finally, a so-called response function $H(\omega)$ of the receive transducer with surface area a is obtained,

$$|H(\omega)| = \sqrt{\frac{I_{in}(\omega) \left(\frac{V_{out}(\omega)}{I_{out}(\omega)} \right) + V_{in}(\omega)}{2\omega^2 \rho v a |I_{out}(\omega)|}} \quad (15)$$

The acoustic wave amplitude can be simply calculated using the response function multiplied by the output current:

$$|A(\omega)| = |H(\omega)| |I_{out}(\omega)|. \quad (16)$$

A typical response function is shown in Fig. 3. The transducer is a 36° Y cut LiNbO₃ disk with a diameter of 0.5"

and nominal center frequency of 10 MHz. It is bonded to the PZT samples by Salol. From the figure it is seen that the receive transducer can respond to both the fundamental and second harmonic waves. Thus, A_1 and A_2 can be measured at the same time. In our experiments, the output current from the receive transducer is recorded in the digital oscilloscope and then transferred to the computer. Through FFT of the waveform the electric current amplitudes corresponding to the fundamental and second harmonic waves are obtained and the A_1 and A_2 can be calculated using Eq. (16).

Since the $H(\omega)$ was obtained at a given electric load, during the nonlinear measurements, the DPR35 pulser/receiver with power off is connected with the receiver transducer in order to keep the electric load of the transducer unchanged from the calibration stage. The whole system is carefully checked to exclude the nonlinearities that may come from the system itself. The electric current probe used in our experiment is the Tek P6022 with a sensitivity of 1 mV/mA and has a good linear response within the range of the electric current in our experiments. We also checked the system with an aluminum test sample to obtain a value of $\beta=5$, which is consistent with those reported in Ref. 10 ($\beta=4.5$ and $\beta=5.1$).

IV. EXPERIMENTAL RESULTS AND DISCUSSIONS

The ultrasonic nonlinearity parameter β and corresponding third-order elastic constants are measured for PZT-4, PZT-5A, PZT-5H, and PZT-5H HD. The size and geometry of the samples are listed in Table II.

Figure 4 gives the relation between the second harmonic amplitude A_2 and the square of the fundamental amplitude A_1^2 for one of the measurements. A good linear relation between A_2 and A_1^2 was found, which is expected from Eq. (11). From the slope of the straight line the β value can be calculated since the length and sound velocity of the sample as well as the wave frequency are known. The measured results for the four types of PZT ceramics are also listed in Table II.

TABLE II. Sample parameters and measured results for PZT-4, PZT-5A, PZT-5H HD, and PZT-5H. K_2 and K_3 correspond to different second- and third-order elastic constants as defined in Table I.

Sample	PZT-4			PZT-5A			PZT-5H HD		PZT-5H	
	Poled	Unpoled		Poled	Unpoled		Poled	Depoled	Poled	Depoled
orientation	Z cut	X cut	isotropic	Z cut	X cut	isotropic	Z cut	isotropic	Z cut	isotropic
shape	cubic ^a	cubic ^a	cubic ^a	cubic ^a	cubic ^a	cubic ^a	plate ^b	plate ^b	cylinder ^c	cylinder ^c
ρ (kg/m ³)	7600	7600	7600	7500	7500	7500	7800	7800	7500	7500
porosity	0.95	0.95	0.95	0.94	0.94	0.94	0.98	0.98	0.94	0.94
K_2^d	14.7	13.2	13.2	14.1	11.7	11.7	17.1	13.5	13.4	10.6
β_u	7	16.4	13.4	5.7	4.8	3	3.1	10.4	14.9	17.4
β_c	7.03	19.5	16	5.1	4.5	2.9	3.2	8.3	15	18.3
K_{3u}^e	-14.7	-25.6	-21.6	-12.3	-9.1	-7	-10.4	-18.1	-24	-21.6
K_{3c}^e	-14.7	-29.7	-25.1	-11.4	-8.8	-6.9	-10.6	-15.3	-24.1	-22.6

^aSample size is 2.54 cm cube.

^bSample size is 2.54 cm×2.54 cm×0.64 cm.

^cCylinder sample with 2.54 cm diameter and thickness 1.27 cm.

^dUnit: 10^{10} N/m².

^eUnit: 10^{11} N/m².

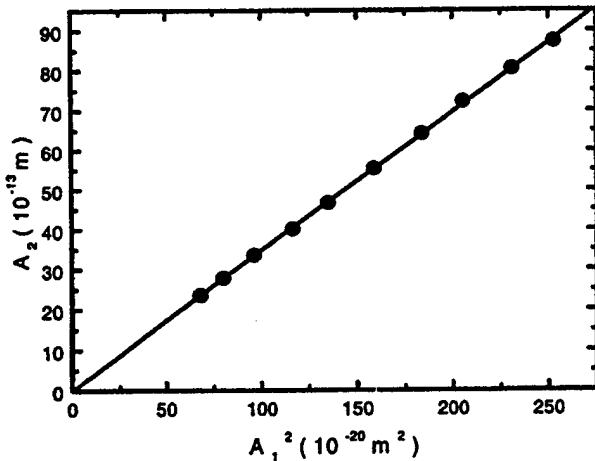


FIG. 4. Variation of the second harmonic amplitude vs the square of the fundamental amplitude.

Without taking into account the ultrasonic attenuation, the first-order approximation Eq. (7) leads to a secular solution, which states that the amplitude of the second harmonic wave will linearly increase with the wave propagation distance as indicated by Eq. (11). Obviously, this solution cannot be valid for arbitrary large amplitude of the second harmonic wave. The attenuation of PZT materials used in our experiment is fairly strong, which will reduce the amplitude of the second harmonic wave as it propagates. When both the nonlinearity and dissipation of the medium are simultaneously taken into account, it can be verified¹³ that the linear accretion of the second harmonic wave with propagation distance only holds at the beginning stage of wave propagation. The general equation for the second harmonic displacement must be modified:

$$u_3^{(1)} = \frac{1}{8} \beta k^2 A_1^2 \frac{\exp[-2\alpha(\omega)z] - \exp[-\alpha(2\omega)z]}{\alpha(2\omega) - 2\alpha(\omega)} \times \cos 2(\omega t - kz), \quad (17)$$

where $\alpha(\omega)$ and $\alpha(2\omega)$ are attenuation coefficients at ω and 2ω , respectively. Thus,

$$\beta = \frac{8A_2}{k^2 A_1^2} \frac{\alpha(2\omega) - 2\alpha(\omega)}{1 - \exp\{-[\alpha(2\omega) - 2\alpha(\omega)]L\}}, \quad (18)$$

where L is the sample length, A_1' is the attenuated fundamental amplitude measured at $z=L$. For PZT ceramics, the attenuation mainly comes from the scattering of ultrasonic wave at grain boundaries. The frequency dependence of attenuation can be obtained by using the ultrasonic spectroscopy technique.¹²

The diffraction effect associated with the finite size of the transducers also needs to be considered. If A_u and A_c are the ultrasonic wave amplitudes without and with correction of the diffraction effect, respectively, it is known that they obey the following relationship,¹⁴

$$A_c = A_u q^{-1}(\omega, z), \quad (19)$$

where

$$q = \{[\cos \xi - J_0(\xi)]^2 + [\sin \xi - J_1(\xi)]^2\}^{1/2}, \quad (20)$$

$\xi = \omega R^2/vz$, v is the wave velocity, R is the radius of the transducer, and z is the propagation distance of ultrasonic wave,¹⁴ which is the sample length L in our experiments.

Taking into account both the effects of attenuation and diffraction, the response function of the receive transducer becomes

$$|H_c(\omega)| = |H(\omega)| \{\exp[-\alpha(\omega)z] q(\omega, z)\}^{1/2}. \quad (21)$$

(Note: during calibration, z is twice of the sample length because the reflected echoes were used.) Then, the corrected acoustic wave amplitude is

$$A_c(\omega) = |H_c(\omega)| |I(\omega)|. \quad (22)$$

In Table II, β_u and K_{3u} are the nonlinearity parameter and the K_3 value, respectively, without the attenuation and diffraction correction, while β_c and K_{3c} are the corresponding values after the correction. One can see that the corrections are not always significant due to the cancellation of the above two effects.

Although PZT ceramics contain porosity, the β values in the X_3 direction of poled PZT-4 and PZT-5A and PZT 5H HD are comparable with that of typical single crystals,⁸ which agrees with the conclusion of Ref. 3. The porosity of PZT materials measured in our experiment is also listed in Table II. It was found that the poled high density PZT-5H HD has the lowest porosity of only 2%. Its nonlinearity parameter β is the smallest among all of the Z-cut PZT ceramics. The regular PZT-5H has 6% porosity and its β value is five times as large as that of the PZT-5H HD. Since the chemical composition of PZT 5H and PZT 5H HD are the same, it seems that more porous material also has larger nonlinearity. As pointed out by Donskoy *et al.* that the β values of some porous materials, such as rocks, could be as large as 10^3 – 10^4 (Ref. 15) compared to the β values of single crystals in the range of 2–14.⁸

On the other hand, different dopants in PZT ceramics definitely have strong influence to the nonlinearity, which can be seen from the β value of the PZT-4 and PZT-5A ceramics. Although PZT-5A is more porous, its β value in the X_3 direction is smaller than PZT-4, which also has much stronger nonlinearity in the X_1 direction of poled and unpoled samples.

For PZT-4 and PZT-5A we found that the sound velocity in the X_1 direction of a poled sample is the same as that of an unpoled sample (isotropic). But the nonlinearity parameter β of an unpoled sample is a little less than the β value in the X_1 direction of a corresponding poled sample. This is to say that the polarization process does not influence the linear properties of the material in the X_1 direction but the nonlinear properties have noticeable change from the poling process. This is indirect proof that the poling process seems to generate some degree of mechanical damage in the sample due to the switching of domains.

In order to further investigate the influence of the poling process to the nonlinearity parameter, the originally poled PZT-5H HD and regular PZT-5H samples were thermally depoled. The measured nonlinearity parameters for the depoled samples are also listed in Table II. It was observed that the depoled samples have the same ultrasonic velocity as that

of the velocity along the X_1 direction of the poled samples (the same as that of unpoled samples). However, as shown in Table II, the nonlinearity parameter of the depoled samples increased about three times compared to the poled samples for PZT-5H HD. This means that the depoling process also creates microstructural changes in the ceramic. It further reveals the fact that the nonlinear parameters are much more sensitive to microstructural changes than the linear parameters. Specifically, we may use the nonlinearity parameter to distinguish an unpoled sample from a depoled sample for the PZT-5H HD. The same trend was also observed in the regular PZT-5H ceramic, but it is far less drastic than what occurred in PZT-5H HD. This may be understood by the fact that the regular PZT-5H already contains much higher porosity and the depoling process does not create significant change to its porous structure.

V. SUMMARY AND CONCLUSIONS

The nonlinear properties of lead zirconate-titanate piezoceramics PZT-4, PZT-5A, PZT-5H and PZT-5H HD have been investigated by means of the ultrasonic second harmonic generation method. In the X_1 direction, the ultrasonic nonlinearity parameter β represents solely the elastic nonlinearity associated with c_{111} , but in the piezoelectric stiffened direction (X_3 direction), the contributions of piezoelectric and dielectric nonlinearities are also included in the ultrasonic nonlinearity parameter β . Therefore, only the effective third-order elastic constant c_{333}^D can be determined.

Due to different porosities and different dopants in these PZT ceramics, the observed nonlinearity parameter β covers a wide range from 3 to 19. For poled PZT ceramics, the β values in the X_3 direction are comparable to that of other single crystals, but the nonlinearity in the X_1 direction is higher than the typical value for single crystals. An impor-

tant finding from our study is that the nonlinearity parameter is much more sensitive to internal structural changes than the linear parameters. We could use the nonlinearity parameter to discriminate unpoled and depoled PZT samples because the poling and depoling process both cause damages to the microstructure inside the ceramics,¹⁶ which are invisible to linear effects.

ACKNOWLEDGMENT

The research was sponsored by the NIH under Grant No. P41 RR 11795-010A and the ONR MURI Grant No. N00014-96-1-1173.

- ¹Y. Cho and K. Yamanouchi, J. Appl. Phys. **61**, 1728 (1987).
- ²H. Beige, Ferroelectrics **51**, 113 (1983).
- ³J. K. Na and M. A. Breazeale, J. Acoust. Soc. Am. **95**, 3213 (1994).
- ⁴Neil W. Ashcroft and N. David Mermin, in *Solid State Physics* (Saunders College, Philadelphia, PA, 1976).
- ⁵D. H. McMahon, J. Acoust. Soc. Am. **44**, 1007 (1968).
- ⁶D. F. Nelson, in *Electric, Optic and Acoustic Interactions in Dielectrics* (Wiley, New York, 1979).
- ⁷B. A. Auld, in *Acoustic Fields and Waves in Solids* (Wiley, New York, 1973).
- ⁸M. A. Breazeale and J. Philip, in *Physical Acoustics* edited by W. P. Mason (Academic, New York, 1984), Vol. XVII, pp. 1–60.
- ⁹J. F. Nye, in *Physical Properties of Crystals* (Clarendon, Oxford, 1985).
- ¹⁰G. E. Dace, R. B. Thompson, L. J. H. Brasche, D. K. Rehbein, and O. Buck, in *Review of Progress in Quantitative Nondestructive Evaluation*, edited by D. O. Thompson and D. E. Chimenti (Plenum, New York, 1991), Vol. 10B, p. 1685.
- ¹¹A. Moreau, J. Acoust. Soc. Am. **98**, 2745 (1995).
- ¹²H. Wang, W. Jiang, and W. Cao, J. Appl. Phys. **85**, 8083 (1999).
- ¹³B. T. Beyer, in *Nonlinear Acoustic*, Naval Sea System Command, 1974.
- ¹⁴W. Cao, G. Barch, W. Jiang, and M. A. Breazeale, Phys. Rev. B **38**, 10244 (1988).
- ¹⁵D. M. Donsky, K. Khashanah, and T. G. McKee, Jr., J. Acoust. Soc. Am. **102**, 2521 (1997).
- ¹⁶E. C. Subbarao, V. Srikanth, W. Cao, and L. E. Cross, Ferroelectrics **145**, 271 (1993).

APPENDIX 11



Substituent Effects in $0.65\text{Pb}(\text{Mg}_{1/3}\text{Nb}_{2/3})\text{O}_3$ - 0.35PbTiO_3 Piezoelectric Ceramics

YUN-HAN CHEN & KENJI UCHINO

*International Center for Actuators and Transducers, Material Research Laboratory
The Pennsylvania State University, University Park, PA 16802*

DWIGHT VIEHLAND

Code 2132; Naval Undersea Warfare Center, Newport, RI 02835

Submitted March 29, 2000. Revised July 28, 2000; accepted September 8, 2000

Abstract. $\text{Pb}(\text{Mg}_{1/3}\text{Nb}_{2/3})\text{O}_3$ - PbTiO_3 (PMN-PT) ceramics with base compositions close to the morphotropic phase boundary are potential materials for many applications such as transducers and actuators due to their high dielectric constants and electromechanical coupling factors. However, their dielectrical and mechanical losses are too high for high-power applications. In this paper, the dielectric and electromechanical properties of piezoelectric PMN-PT ceramics were investigated in specimens containing various A-site and B-site substituents with the goal of developing lower loss materials for wider applications. Emphasis was placed on various transition metal cation substituents of both lower and higher valences. Mn substituent was found to be the most promising substituent investigated for developing high power low loss piezoelectric PMN-PT ceramics.

Keywords: PMN-PT, substituents, dielectric and electromechanical properties

I. Introduction

Since the discovery of relaxor behavior in $\text{Pb}(\text{Mg}_{1/3}\text{Nb}_{2/3})\text{O}_3$ (PMN) by Smolenskii and Agronovskaya [1], many investigations of mixed B-site cation relaxor ferroelectrics, of the $\text{Pb}(\text{B}_{1/3}\text{B}_{2/3})\text{O}_3$ -type perovskites, have been performed, due to their excellent dielectric and electromechanical properties. A characteristic feature of these materials is that they possess B-site cation sublattices which are occupied by ionic species of various valencies. In the stoichiometric case, charge compensation requires that the average valence of the B-site be +4, however in $\text{Pb}(\text{B}_{1/3}\text{B}_{2/3})\text{O}_3$ this occurs by a mixture of higher ($>+4$) and lower ($<+4$) valent cation species on the octahedral B-site sublattice. In PMN, electron microscopy investigations by Chen and Harmer have shown the presence of short-range B-site cation ordering [2]. The size of the short-range ordered regions was observed to be ~ 30 to 50 Angstroms and were character-

ized by the presence of $(1/21/21/2)$ superlattice reflections in the selected area electron diffraction patterns. Investigations by Setter and Cross [3] have demonstrated that the electrical properties of relaxor ferroelectrics are influenced to a large degree by the manner in which B-site cations (BI and BII ions) are distributed amongst the B-site sublattices. Specimens which were quenched and possessed very low B-site cation ordering had relaxor ferroelectric characteristics, whereas specimens which were annealed and possessed a high degree of B-site cation ordering had normal ferroelectric characteristics.

The structure of PMN is pseudo-cubic with an average space group symmetry of $\text{Pm}3\text{m}$ at room temperature. The degree of short-range B-site cation ordering in PMN is quite small [3], thus the relaxor characteristics are pronounced, and the dominant electromechanical coupling mechanism is electrostriction [4]. In crystalline solutions of $(1-x)\text{PMN}$ - $x\text{PbTiO}_3$ (PMN-PT), a piezoelectric state with a remanent polarization can be

achieved. The PMN-PT crystalline solid solution system possesses a morphotropic phase boundary (MPB) between pseudo-cubic and tetragonal ferroelectric phases at about 30–35 at. % PT ($T = 25^\circ\text{C}$) [5]. The dielectric and piezoelectric constants for these PMN-PT compositions ($0.3 < x < 0.35$) are significantly high, as reported by many researchers such as Lejeune [6]. The high piezoelectric, dielectric, and electromechanical coupling coefficients in the MPB compositions of PMN-PT are very attractive for applications in high-power transducer devices. However, one of the limitations of PMN-PT in these applications is that the mechanical quality factor Q_m is quite low, in addition to the dielectric loss being quite high.

The purpose of this investigation was to study the effect of various substituents on the properties of PMN-PT ceramics. It was hoped that a trend in the substituent types and classes might be identified, so that a wider range of materials might be developed for high power transducer applications. Both A-site and B-site substituents, as well as higher and lower valent substituents, have been investigated.

II. Sample Preparation and Experimental Procedure

In order to eliminate the formation of a parasitic pyrochlore phase ($\text{Pb}_3\text{Nb}_4\text{O}_{13}$), the columbite precursor method proposed by Swartz and Shrout [7] was used to prepare PMN-PT 65/35 ceramics. In the first stage, MgO and Nb_2O_5 were mixed in a stoichiometric ratio, and a precursor columbite phase MgNb_2O_6 was formed after calcination at 1200°C for 4 hrs. (X-ray diffraction patterns were then taken to check phase formation). In the second stage, the precursor was mixed in stoichiometric ratios with PbO and TiO_2 . To insure proper mixing, both steric hinderence and electrostatic repulsion (pH adjustment by ammonia), dispersion mechanisms were required to prepare a 30 vol.% slurry with de-ionized water. The slurry was vibratory milled, then dried and calcined at 700°C for 4 hr. Calcined powders were examined by x-ray diffraction to insure phase purity. To control PbO volatility, sintering was performed in a lead rich atmosphere by placing a small amount of mixed powder of PbO and ZrO_2 in a closed crucible. Sintering was performed at $1000\text{--}1200^\circ\text{C}$ for 4 hours depending on the different doping elements and concentration.

Specimens with both A-site and B-site substituents,

including higher valence and lower valence ones, were fabricated. The various substituents investigated include La, Li, Na, K, Mn, In, Fe, Cu and Co. Specimens with excess Mg and Nb were also fabricated for comparisons. For each composition, two batches were prepared and at least three samples were made and measured from each batch. After sintering, the samples were polished, and gold-sputtering was used for the electrodes on both surfaces.

The dielectric properties were measured with a computer controlled automated-measurement system (HP4284A) from room temperature to 250°C for dielectric measurement in an oven with temperature controlling (FLUKE8840). The electromechanical properties were determined with the resonance-antiresonance method by measurement of the admittance spectrum using a HP4194.

III. Results and Discussions

Table 1 summarizes the dielectric and electromechanical properties of PMN-PT 65/35 with 1 at.% of various A-site substituents. Data taken from previous studies of various substituents in PZT, and the radii of $\text{Pb}(2+)$ and $\text{Ti}(4+)$, have also been included in this table [8]. $\text{La}(3+)$ has previously been studied in PMN and PMN-PT [9], as well as in PZT [10]. In La modified PMN-PT, it was found that lead vacancies are not a favorable defect, unlike that in PZT [9]. PMN prefers to restore the A/B ratio by precipitating out magnesium niobate. Compensation is thus achieved by self-adjustment of the Mg/Nb ratio.

The effects of Na and K substituents can be seen to be almost the same in Table 1. Both substituents are from the same element group (s-orbital with a 1+ valance state) and substitute onto the A^{2+} (Pb) sites, which are 12-fold coordinated. Hence, they effectively act as acceptors. It is necessary to charge compensate for a Na^{1+} occupying a Pb^{2+} site. This was achieved by reducing the Mg:Nb ratio. Consequently, these substituents should decrease the degree of short-range B-site cation ordering, as previously reported by Chen and Harner [4]. Both of these substituents were found to somewhat increase the mechanical quality factor Q_m and reduce the piezoelectric constant, as shown in Table 1. Temperature dependent dielectric constant data are shown in Fig. 1 (b) for these composition.

Li is also from the same chemical group (s-orbital with a 1+ valence state), yet the effect of Li on the di-

Table 1. Electromechanical properties of 0.65PMN-0.35PT + 1 at.% A-site Doping.

Element	La	K	Na	Li
Substitute site	A-site	A-site	A-site	
Valency	+3	+1	+1	+1
Behavior in PZT	Donor-like	Acceptor-like	Acceptor-like	?
Ionic radii (Å)	1.20	1.52	1.16	0.90
Density (g/cc)	7.95	8.10	8.02	7.81
Curie T (°C)	149.40	181.23	178.00	178.29
Dielectric constant (1kHz)	3700	3990	4140	3260
Maximum dielectric constant (1kHz)	16000	34800	34800	25600
Dielectric loss (1kHz)	0.031	0.012	0.011	0.031
s_{11}^E (10^{-9} m ² /N)	0.015	0.013	0.014	0.020
k_{31}	0.220	0.280	0.278	0.310
d_{33} (pC/N)	340	373	360	546
Q_m	64	143	150	68
	Used to adjust Curie temperature			Used to improve the electrical resistance, reduce the sintering temperature and reduce the temperature coefficient of capacitance

Pb (+2) 1.330Å, Ti (+4) 0.745Å

A-site cation : 12-coordinated

B-site cation : 6-coordinated

electric and electromechanical properties were significantly different than those for Na and K, as can be seen in Table 1. Li substitution also reduced the sharpness of the temperature dependent dielectric constant, as can be seen in Fig. 1. The ionic radius of Li is smaller (0.90Å) than that of either Na (1.16Å) or K (1.52Å). However, according to the tolerance factor

$$t = \frac{(r_{A(12-CN)} + r_{O(6-CN)})}{\sqrt{2}(r_{B(6-CN)} + r_{O(6-CN)})},$$

Li still is too large for it to go onto the B-sites.

Table 2 summarizes the properties of B-site substituents. Indium is the only non-transitional metal cation listed in this table. Indium substitution resulted in the highest electromechanical coupling (0.36) and one of the highest piezoelectric (571 pC/N) coefficients. The ionic radius of In³⁺ is quite large (0.94). Interestingly, Pb(In_{1/3}Nb_{2/3})O₃ exists as a stable mixed B-site cation perovskite, which is known to be a relaxor antiferroelectric [11].

As shown in Table 2, four transition metal cations were chosen as substituents. Interests were placed on these substituents because transition metal cations often have multiple valence states. For example, in the

PZT system, Fe is known to increase Q_m to more than 1000 [12]. Analogously, it was hoped that Fe-substituents might have a similar effect in PMN-PT, however this was not the case. Fe-substituents were found not to change the properties of PMN-PT significantly. In PZT, all B-site cation sites are occupied by 4+ species. Whereas, in PMN-PT, two distinct B-site cation sublattices exist whose occupancies are composed of multiple valent species, i.e., 2+ (Mg), 5+ (Nb), and 4+ (Ti). In consideration of the ionic size of Fe, it will most probably substitute onto the Mg sites in PMN-PT, rather than the Nb ones. If this is the case, then Fe is either a 3+ (or 2+) species on a 2+ site. It will then act either as an isovalent or as a donor-type substituent, rather than an acceptor-type one as it does in PZT. Consequently, the electromechanical properties of Fe-substituted PZT and PMN-PT will be different. Fe-substituted PZT will be a "hard" piezoelectric, whereas Fe-substituted PMN-PT will be a "soft" piezoelectric.

Similar arguments can also be used to understand the effects of Co-substituents, which have a smaller ionic radius than Fe. Again, based on the ionic radius consideration, Co²⁺ and/or Co³⁺ will most probably

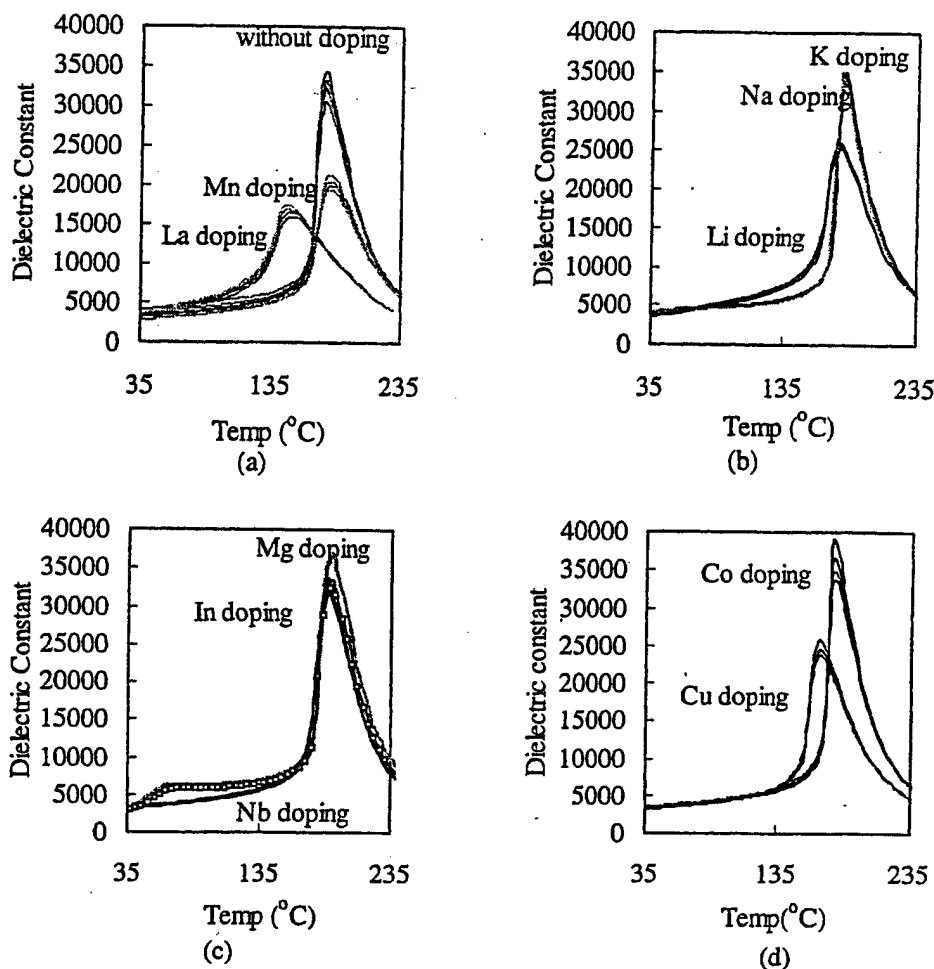


Fig. 1. The temperature and frequency dependence (100, 1k, 10k, 100k from high to low) of dielectric constant of 0.65PMN-0.35PT + 1 at.% (a) pure and La, and Mn; (b) Li, Na, and K; (c) In, Mg and Nb; (d) Co and Cu.

substitute onto the Mg sites. Co also has an additional valance state (+4) which has a smaller ionic radius (0.67\AA). This valance state is not common, but it is accessible. Consequently, it may be possible for Co to go onto the Nb site and behave as an acceptor. This would result in "harder" piezoelectric characteristics. Interestingly, Co-substituent resulted in higher values of Q_m (~ 152) and lower values of dielectric losses (0.008) ($Q_e \sim 125$), as can be seen in Table 2. But, yet, Co did not result in any significant decrease in either the piezoelectric or dielectric constants, as would be expected of a "harder" piezoelectric response.

The ionic radius of copper is significantly larger than that of the other substituents investigated. Interestingly, Cu^{1+} and Cu^{2+} are too small for the A-site, but yet too big for the B-site. However, Cu^{3+} is of the

right ionic size and maybe suitable for substitution onto the Nb sites. If this were the case, then Cu substituents should act as an effective acceptor in PMN-PT, making the piezoelectric characteristics "harder". Cu substituents resulted in a much lower value of the dielectric loss (0.004 , $Q_e \sim 250$). Interestingly, its mechanical quality factor was not increased dramatically, furthermore the piezoelectric constant was significantly increased (~ 570 pC/N). Temperature dependent dielectric data (Fig. 1(d)) revealed a decrease in the peak dielectric constant and a decrease in the phase transition temperature.

Of all the substituents investigated in this study, Mn was the only one which was found to impart "harder" characteristics in both the dielectric and electromechanical properties. As shown in Table 2, upon Mn

Table 2. Dielectric and electromechanical properties of 0.65PMN-0.35PT+1at.% B-site doping.

Element	Cu	Co	Mn	Fe	In
Substitute site	B-site	B-site	B-site	B-site	B-site
Valency	+1, +2	+2, +3	+2, +3, +4, +7	+2, +3	+3
Behavior in PZT	Acceptor-like	Acceptor-like	Acceptor-like	Acceptor-like	Acceptor-like
Ionic radii(Å)	(+1)0.91 (+2)0.87	(+2,LS)0.79 (+2,RS)0.89 (+3,LS)0.69 (+3,RS)0.75	(+2,LS)0.81 (+2,HS)0.97 (+3,LS)0.72 (+3,HS)0.79 (+4)0.67 (+7)0.60	(+2,LS)0.75 (+2,HS)0.92 (+3,LS)0.69 (+3,HS)0.79	0.94
Density (g/cc)	8.04	7.45	7.67	7.70	7.72
Curie T (°C)	166.98	177.00	175.00	178.00	187.62
Dielectric constant (1kHz)	2500	3200	2100	3100	3140
Maximum dielectric constant (1kHz)	23600	33600	21000	33000	33400
Dielectric loss (1kHz)	0.004	0.008	0.009	0.012	0.012
s_{11}^E ($10^{-9}\text{m}^2/\text{N}$)	0.012	0.013	0.011	0.015	0.018
k_{31}	0.25	0.26	0.29	0.30	0.36
d_{33} (pC/N)	571	499	350	500	564
Q_m	132	152	300	80	88
		Can form PCN	1. Used as similar reason of Li. 2. Change the age effect.	Can form PFN	Can form PIN

LS: Low spin

HS: High spin

modification, the piezoelectric constant, dielectric constant and dielectric loss were all decreased, however the quality factor Q_m was increased significantly. The coupling coefficient k_{31} was not significantly affected by Mn modification and had a constant value of ~ 0.3 . Due to the many valent states available to Mn (which range from +2 to +7), it is difficult to ascertain based upon simple crystal symmetry arguments which sites Mn most probably occupies. The data presented in Table 1 indicates that whichever site Mn does occupy it is acting as a lower valent species on a higher valent site. Furthermore, the changes in properties that occur upon Mn modification make the material more suitable for high power transducer applications.

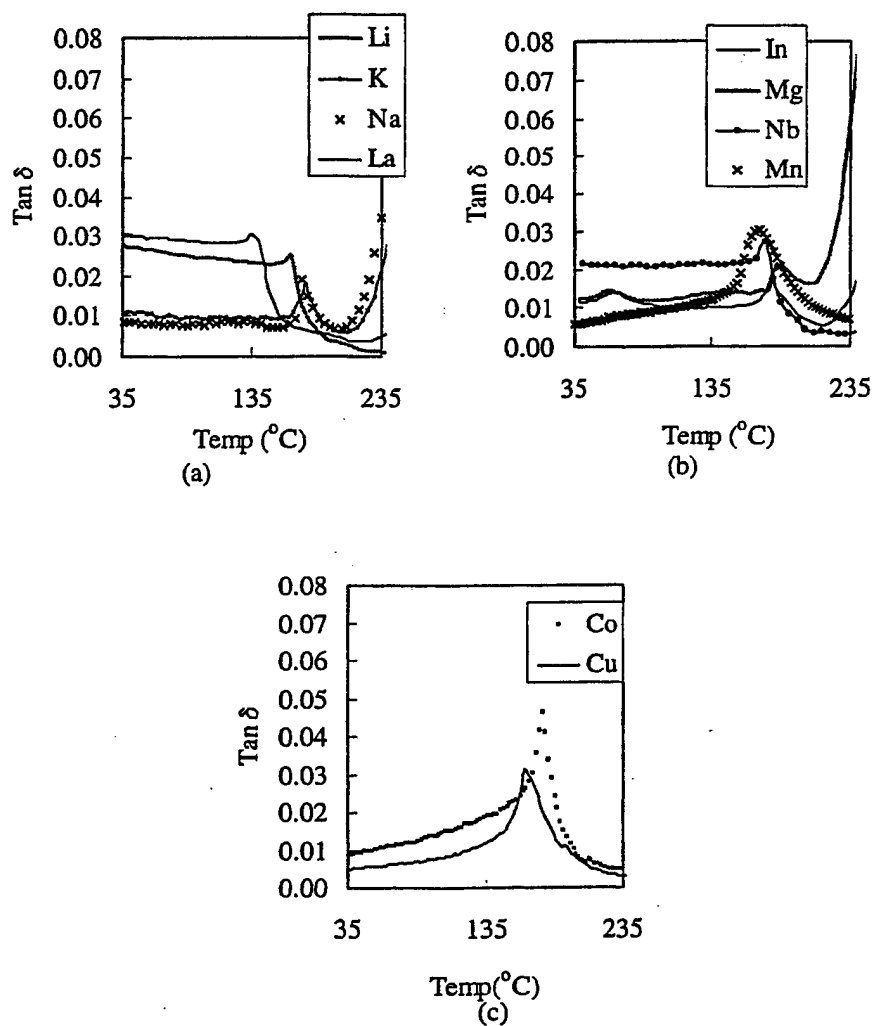
Beck et al. have previously investigated Mn-substituted PMN-PT [11]. They studied specimens modified with 1 at.% Mn in a base composition of PMN-PT 95/5. This base composition has pronounced relaxor ferroelectric behavior, however addition of 1 at.% resulted in a conversion of the dielectric response into a

normal, non-dispersive ferroelectric [13]. Mn substitution has been found to induce unique changes not only in PMN-PT, but also in BaTiO_3 . In BaTiO_3 , Mn substituents influence the orthorhombictetrahedral ferroelectric transition [14]. It was conjectured that a mixed Mn valent state (Mn^{3+} and Mn^{2+} coexisting) destabilizes the orthorhombic phase at a temperature T_2 . Similarly, a combination of Mn^{4+} and Mn^{3+} was conjectured to be responsible for the destabilization of the rhombohedral phase at a temperature T_3 , for specimens that had been treated under higher oxygen partial pressures during densification. Lattice distortion caused by Mn ions appeared to be a factor in this case [15].

Table 3 shows data for specimens prepared with excess Mg and Nb. Neither excess Mg nor excess Nb resulted in any significant effects on the properties. Variations in the ratio of the octahedral site occupancies within a single-phase would be equivalent to aliovalent substituent modification. An excess of the lower-valent constituent, i.e., Mg^{2+} in PMN, would be

Table 3. Dielectric and electromechanical properties of 0.65PMN-0.35PT with 1 at.% Mg or Nb excess.

Element	Nb	Mg			
Substitute site	B-site	B-site	Maximum dielectric constant (1kHz)	33600	38100
Valency	+5	+2	Dielectric loss (1kHz)	0.024	0.020
Behavior in PZT	Donor-like	Acceptor-like	s_{11}^E ($10^{-9}\text{m}^2/\text{N}$)	0.020	0.019
Density (g/cc)	7.82	7.66	k_{31}	0.296	0.281
Ionic radii(Å)	0.64	0.72	d_{33} (pC/N)	583	540
Curie T (°C)	185.90	189.00	Q_m	75	78
Dielectric constant (1kHz)	4050	3500		Form pyrochlore	Sintering aid but grain growth

*Fig. 2.* The temperature dependence of $\tan \delta$ at 1kHz of 0.65PMN-0.35PT + 1 at.% (a) pure and La, and Mn; (b) Li, Na, and K; (c) In, Mg and Nb; (d) Co and Cu.

the equivalent to lower valent substitution on a higher valent site (effective acceptor). Whereas, an excess of the higher-valent constituent, i.e., Nb^{5+} in PMN, would be the equivalent to a higher valent substitution on a lower valent site (effective donor). However, we found that control of the Mg/Nb stoichiometry is difficult to achieve in practice, in particular with respect to changing the electromechanical properties (i.e., "harder" and "softer"). Variations in the Mg/Nb ratio tended to result in secondary phase formation in PMN-PT, instead of inducing lattice vacancy formation. However, excess MgO can be seen in Table III to increase the dielectric constant. This may be due to the excess MgO reacting with pyrochlore on the grain boundaries.

Temperature dependent dielectric loss data are shown in Fig. 2 for the various specimens investigated in this study. Specimens with excess Mg and those modified with Na, In or K had significant losses at high temperatures. This kind of loss usually is contributed by the conduction loss [15]. However, specimens with Mn, Co, and Cu resulted in decreased dielectric losses at all temperatures except near the Curie temperature. In each case the dielectric loss factor had a pronounced peak near the temperature of the dielectric constant maximum. These results again indicate the importance of transition metal cation modifications on the properties of PMN-PT. IV.

IV. Summary

In this paper, MPB compositions of PMN-PT with various substituents were studied. Unlike previous results for PZT, the effect of substituents on the mechanical quality factor was quite small. However, Mn substituents were found to be unique. Mn substituents

were found to reduce the total loss (including mechanical and dielectric) while keeping the electromechanical quality constant. These changes make PMN-PT more suitable for high-power transducer. It appears that Mn substituents behave as effective acceptors in PMN-PT ceramics, resulting in "harder" piezoelectric characteristics.

Acknowledgements

This research is supported by USA Office of Naval Research through the grant no. N00014-96-1-1173.

References

1. G.A. Smolenskii and Agranovskaya, *Sov. Phys. Tech. Phys.*, **3**, 1380 (1958).
2. J. Chen, H.M. Chan, and M.P. Harmer, *J. Amer. Cer. Soc.*, **72**(4), 593 (1989).
3. N. Setter and L.E. Cross, *J. Appl. Phys.*, **51**(8) 4356 (1980).
4. K. Uchino, K. Nomura, L.E. Cross, S.-J. Jang, and R.E. Newnham, *J. Appl. Phys.*, **51**(2), 1142 (1980).
5. S. Tashiro, M. Ikehiro, and H. Igarashi, *Jpn. J. Appl. Phys.*, **36**, 3004 (1997).
6. M. Lejeune and J.P. Boilot, *Mater. Res. Bull.*, **20**, 493 (1985).
7. S. Swartz and T. Shrout, *Mat. Res. Bull.*, **17**, 1245 (1982).
8. R.D. Shannon and C.T. Prewitt, *Acta. Cryst.*, **B25**, 925 (1969).
9. N. Kim, W. Huebner, S.J. Jang, and T.R. Shrout, *Ferroelectrics*, **93**, 341 (1989).
10. G.H. Haerling and C.E. Land, *J. Am. Ceram. Soc.*, **54**(1), 1 (1971).
11. Yohachi Yamashita, *Jpn. J. Appl. Phys.*, **33**, 5328 (1994).
12. S. Takahashi and S. Hirose, *Jpn. J. Appl. Phys.*, **32**, 2422 (1993).
13. C.M. Beck, N.W. Thomas, and I. Thompson, *J. Europ. Ceram. Soc.*, **18**, 1685 (1998).
14. Ian Burn, *J. Mater. Sci.*, **14**, 1979, 2453 (1979).
15. R.E. Newnham, *Structure-Properties Relations*, R.E. Newnham, ed. (Springer-Verlag, New York, 1975), pp. 148.

APPENDIX 12

Intrinsic and coupling-induced elastic nonlinearity of lanthanum-doped lead magnesium niobate–lead titanate electrostrictive ceramic

Wenhua Jiang and Wenwu Cao^{a)}

Materials Research Laboratory, Pennsylvania State University, University Park, Pennsylvania 16802

(Received 15 May 2000; accepted for publication 5 July 2000)

The elastic nonlinearity of lanthanum-doped lead magnesium niobate–lead titanate electrostrictive ceramic has been investigated by using ultrasonic second-harmonic generation technique and field-induced strain measurement. A large ultrasonic nonlinearity parameter, $\beta = 30$, was observed at room temperature, which is more than twice of the values for lead zirconate–lead titanate piezoelectric ceramics. The third-order elastic constant c_{111} has been calculated from the β value. By introducing an effective nonlinearity parameter β_e that includes both the intrinsic and the electromechanical coupling generated elastic nonlinearities, the nonlinearity parameter can be accurately characterized. The strong field dependence of the nonlinearity parameter shows excellent potential for designing field tunable nonlinear devices using this material. © 2000 American Institute of Physics. [S0003-6951(00)04335-7]

The solid solution $\text{Pb}_{0.985}\text{La}_{0.01}(\text{Mg}_{0.3}\text{Nb}_{0.6}\text{Ti}_{0.1})\text{O}_3$ [La-doped PMN-PT] is a relaxor material, which has a giant dielectric constant at room temperature and gives rise to large field-induced strain through the electrostriction effect. It was reported that a strain of 10^{-4} could be obtained under an electric field of less than 1 kV/cm.¹ The strong electrostrictive properties of this material make it a good material for transducers, sensors, and actuators.² This intrigued interest in both the materials and physical communities to study its elastic, dielectric, electrostrictive properties^{3,4} and electromechanical coupling coefficients.⁵ In those studies, however, linear elasticity of the material was assumed, although very strong nonlinear behavior was observed under electric field.⁴ The assumption of linear elasticity is only conditionally valid since solids are inherently nonlinear and the PMN-PT system is inherently a strong nonlinear material.⁶ The knowledge of elastic nonlinearity is important in fundamental studies as well as device designs. In the present letter we report the measurement results on the elastic nonlinearity of PMN-PT and their field dependence.

The lanthanum-doped PMN-PT ceramic was manufactured by TRS Ceramics (State College, PA 16801) and the measured sample is a cylinder with a diameter of 2.54 cm and 2.16 cm long. The ultrasonic second-harmonic generation setup used in the experiment is shown in Fig. 1. A 5 MHz toneburst signal from a function generator is amplified by a power amplifier, then, applied to the transmitting transducer, which sends a finite amplitude acoustic wave into the sample. When the ultrasonic wave arrives at the other end of the sample, its wave form is distorted due to the material nonlinearity and the second-harmonic wave is generated. The nonlinear ultrasonic phenomenon is originated from several sources: nonlinearity of the interatomic forces, geometrical nonlinearity, and nonlinear electromechanical coupling effects. For a general dielectric, the dynamical process is

described by the nonlinear electroacoustic coupling equations in material reference frame.

$$\rho_0 \ddot{u}_i = T_{ij,j}, \quad (1a)$$

$$D_{k,k} = 0, \quad (i, j, k = 1, 2, 3), \quad (1b)$$

and the nonlinear constitutive relations are given by

$$T_{ij} = c_{ijkl}^E u_{k,l} - e_{kij} E_k + \frac{1}{2} (c_{ijklmn}^E + \delta_{ik} c_{ljmn}^E + \delta_{im} c_{njl}^E + \delta_{km} c_{ijln}^E) u_{k,l} u_{m,n} - (e_{kijmn} + \delta_{im} e_{knj}) u_{m,n} E_k - \frac{1}{2} m_{klj} E_k E_l, \quad (2a)$$

$$D_k = \epsilon_{kl} E_l + e_{klm} u_{l,m} + \frac{1}{2} (e_{klmij} + \delta_{li} e_{kmj}) u_{l,m} u_{i,j} + m_{klmn} E_l u_{m,n} + \epsilon_{klm} E_l E_m, \quad (2b)$$

where ρ_0 is mass density in unstrained state, u is particle displacement, D is material electric displacement, T is the stress tensor, c_{ijkl} , e_{ijk} , and ϵ_{ij} are the second-order elastic constants, piezoelectric coefficients, and dielectric constants, respectively. The coefficients c_{ijklmn} , e_{ijklm} , and ϵ_{ijk} are tensor components of the third-order elastic constant, nonlinear piezoelectric coefficient, and nonlinear dielectric constant, respectively, and m_{ijkl} are the electrostriction coefficients. The second harmonic generation is a special case of

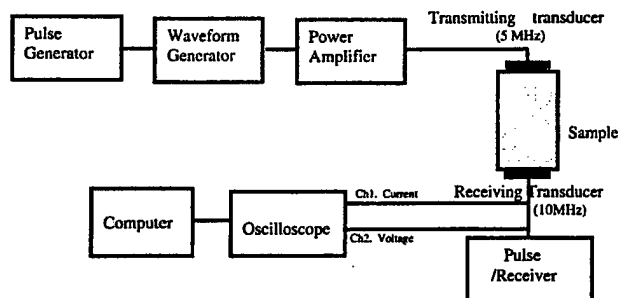


FIG. 1. Experimental setup for measure the absolute amplitudes of the first and second harmonic ultrasonic waves.

^{a)}Electronic mail: cao@math.psu.edu

TABLE I. The ultrasonic nonlinearity parameter β and the third-order elastic constant c_{111} of $\text{Pb}_{0.985}\text{La}_{0.01}(\text{Mg}_{0.3}\text{Nb}_{0.6}\text{Ti}_{0.1})\text{O}_3$ ceramic.

β	$c_{11} (10^{10} \text{ N/m}^2)$	$c_{111} (10^{10} \text{ N/m}^2)$
30	14.1	-465.3

three-phonon interactions in solids, i.e., the self-interaction of one fundamental phonon that generates another phonon with twice of the frequency.⁷ Because the amplitude of the second harmonic is much smaller compared to the fundamental wave, only quadratic nonlinearity is considered in Eqs. (2a) and (2b).

Our second-harmonic generation measurements were conducted at room temperature without bias field. In this case, there is no electromechanical coupling to the fundamental acoustic wave but only electrostrictive coupling. The ceramic sample can be treated as isotropic. For a longitudinal wave propagating in an isotropic medium, the Eqs. (1a)–(2b) can be simplified as

$$\rho_0 \ddot{u}_1 = T_{11,1}, \quad (3)$$

$$T_{11} = c_{11} u_{1,1} + \frac{1}{2} (3c_{11} + c_{111}) u_{1,1}^2. \quad (4)$$

This is a pure elastic nonlinear equation. The solution of Eq. (3) is

$$u_1 = A_1 \sin(\omega t - kx) - \frac{1}{8} \beta k^2 x A_1^2 \cos 2(\omega t - kx), \quad (5)$$

where A_1 and A_2 are the amplitudes of fundamental and second-harmonic waves, respectively, k is the wave number, ω is the angular frequency, x is the distance in the wave propagation direction, and β is the ultrasonic nonlinearity parameter of the material defined as

$$\beta = -\frac{3c_{11} + c_{111}}{c_{11}}. \quad (6)$$

From Eq. (5), it is seen that β can be experimentally determined if the absolute amplitudes of A_1 and A_2 are known

$$\beta = \frac{8}{k^2 L} \frac{A_2}{A_1^2}, \quad (7)$$

where L is the sample length. In order to measure A_1 and A_2 , the receiving transducer is calibrated by following the calibration procedure given in Ref. 8. Once β is determined, the third-order elastic constant c_{111} can be calculated by

$$c_{111} = -(3 + \beta)c_{11}, \quad (8)$$

where the second-order elastic constant $c_{11} = \rho_0 v^2$ can be determined by the material density ρ_0 and the longitudinal wave velocity v .

The measured results are listed in Table I. It is seen that the nonlinearity parameter β of La-doped PMN-PT is twice as large as that of common single crystals ($\beta = 2 - 14$)⁹ and normal ferroelectric lead zirconate-lead titanate (PZT) ceramics ($\beta = 3 - 18$).^{10,11}

Usually, the electromechanical devices using electrostrictive material as the active part are biased by an external electric field. Under this situation there is an electromechanical coupling nonlinearity in addition to the pure elastic nonlinearity mentioned above. Macroscopically, relaxor sys-

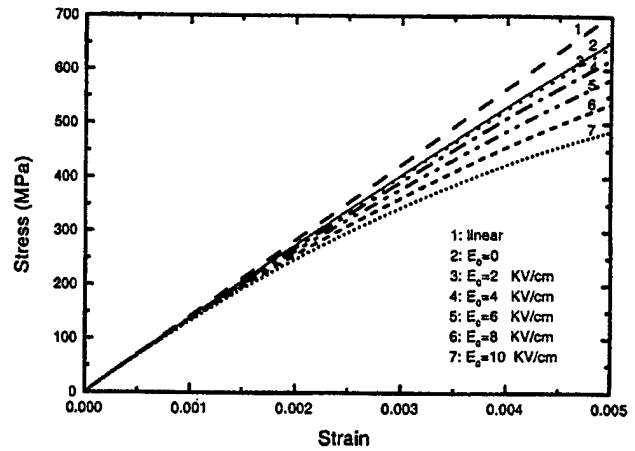


FIG. 2. Strain-stress relation for lanthanum doped PMN-PT under different bias field. The solid line is for the case without coupling nonlinearity.

tems, such as the PZN-PT system under study, have a center of symmetry, therefore, the third order tensors coefficients are all vanished and the constitutive equations for a biased electrostrictive material can be expressed as

$$T_{11} = c_{11}^E u_{1,1} + \frac{1}{2} (3c_{111}^E + c_{111}) u_{1,1}^2 - \frac{1}{2} m_{11} E_1^2, \quad (9)$$

$$D_1 = \epsilon_{11} E_1 + m_{11} E_1 u_{1,1}, \quad (10)$$

and

$$E_1 = E_0 + E(x, t), \quad (11)$$

where E_0 and $E(x, t)$ are applied bias and electrostrictively generated internal electric fields, respectively. From equation (1b), i.e., $D_{1,1} = 0$, the electrostrictively generated fundamental electric field $E(x, t) [\ll E_0]$ can be calculated as

$$E(x, t) \approx -\frac{m_{11} E_0}{\epsilon_{11}} u_{1,1}. \quad (12)$$

Substituting the result into Eq. (9), the nonlinear strain-stress relation can be obtained as

$$T_{11} = \left(\bar{c}_{11} + \frac{m_{11}^2 E_0^2}{\epsilon_{11}} \right) u_{1,1} + \frac{1}{2} \left(3c_{11} + c_{111} - \frac{m_{11}^3 E_0^2}{\epsilon_{11}^2} \right) u_{1,1}^2. \quad (13)$$

Thus, one can define an effective nonlinearity parameter

$$\beta_e = -\frac{3c_{11} + \bar{c}_{111}}{\bar{c}_{11}}, \quad (14)$$

where

$$\bar{c}_{11} = c_{11} + \frac{m_{11}^2 E_0^2}{\epsilon_{11}},$$

$$\bar{c}_{111} = c_{111} - \frac{m_{11}^3 E_0^2}{\epsilon_{11}^2}.$$

Using the measured values of $m_{11} = 8.5 \times 10^{-5} \text{ F/m}$, $\epsilon_{11} = 2 \times 10^4 \epsilon_0$ ($\epsilon_0 = 8.86 \times 10^{-12} \text{ F/m}$), and $c_{11} = 14.1 \text{ N/m}^2$,¹² we can calculate the effective nonlinearity parameter β_e and the effective third order elastic constant \bar{c}_{111} . Then, the nonlinear strain-stress relation for the PMNPT sample can be calculated. Figure 2 shows a few curves for several values of the bias field. The solid line is for the case of zero external

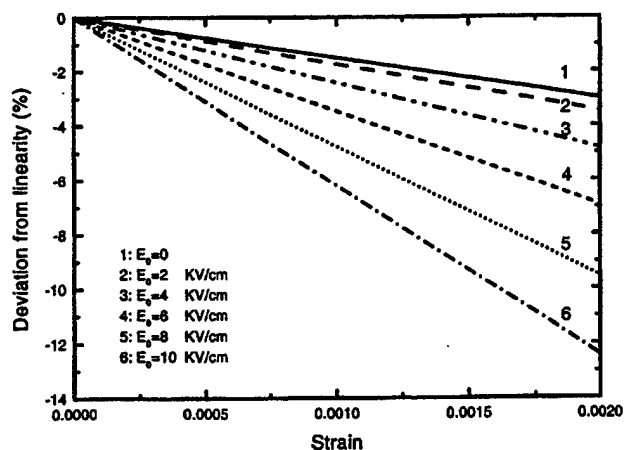


FIG. 3. Relative deviation from linear strain-stress relation for lanthanum doped PMN-PT under different bias field.

fields. We can see that the system is quite nonlinear. This nonlinearity increases with bias field level and the adjustability is fairly large. We show the relative change of the nonlinearity caused by the applied electric field in Fig. 3.

By defining an effective nonlinearity parameter, we have also successfully quantified the relative change of the nonlinearity induced by the application of electric field. The strong dependence of β_e on the bias-electric field suggests a

way to the control nonlinearity of PMN-PT, which may be used to design field tunable nonlinear electroacoustic devices.

This research was sponsored by the NIH under Grant No. P41 RR 11795-010A and the ONR MURI Grant No. N 00014-96-1-1173.

- ¹R. E. Newnham, Proc. of International Conference on Chemistry of Electronic Ceramic Materials, 1991 (unpublished), p. 39.
- ²H. Takeuchi, H. Masuzawa, and C. Nakaya, 1990 IEEE Ultrasonics Symposium Proceedings, 1990 (unpublished), p. 697.
- ³K. Uchino, L. E. Cross, and R. E. Newnham, J. Appl. Phys. 51, 1142 (1981).
- ⁴J. T. Fielding, Ph.D. Thesis, The Pennsylvania State University, University Park, Pennsylvania (1993).
- ⁵S. P. Leary and S. M. Pilgrim, IEEE Trans. Ultrason. Ferroelectr. Freq. Control 46, 1155 (1999).
- ⁶Neil W. Ashcroft and N. David Mermin, in *Solid State Physics* (Saunders College, Philadelphia, 1976).
- ⁷A. C. Holt and J. Ford, J. Appl. Phys. 40, 142 (1969).
- ⁸G. E. Dace, R. B. Thompson, and O. Buck, *Review of Progress in Quantitative Nondestructive Evaluation*, edited by D. O. Thompson and D. E. Chimenti (Plenum, New York, 1992), Vol. 11.
- ⁹M. A. Breazeale and J. Philip, *Physical Acoustics*, edited by W. P. Mason (Academic, New York, 1984), Vol. XVII.
- ¹⁰J. K. Na and M. A. Breazeale, J. Acoust. Soc. Am. 95, 3213 (1994).
- ¹¹W. Jiang and W. Cao (unpublished).
- ¹²Q. M. Zhang, W. Y. Pan, A. Bhalla, and L. E. Cross, J. Am. Ceram. Soc. 72, 599 (1989).